Mass balance of Icelandic glaciers in variable climate

Joaquín M.C. Belart

Faculty of Earth Sciences
University of Iceland

Laboratoire d'Etudes en Géophysique et Océanographie Spatiales (LEGOS)
University of Toulouse 3 – Paul Sabatier

2018

Mass balance of Icelandic glaciers in variable climate

Joaquín M.C. Belart

Dissertation submitted in partial fulfillment of a
Philosophiae Doctor degree in Geophysics between the University of Iceland and the University of Toulouse 3 – Paul Sabatier

PhD Committee
Eyjólfur Magnússon, University of Iceland
Etienne Berthier, LEGOS, University of Toulouse III: Paul Sabatier
Guðfinna Adalgeirsdóttir, University of Iceland
Finnur Pálsson, University of Iceland
Simon Gascoin, CESBIO, University of Toulouse III: Paul Sabatier

Opponents
Francisco José Navarro, Universidad Politécnica de Madrid
Beata Csatho, University of Buffalo

Faculty of Earth Sciences
School of Engineering and Natural Sciences
University of Iceland
Reykjavik, November 2018

Mass balance of Icelandic glaciers in variable climate
Dissertation submitted in partial fulfillment of a *Philosophiae Doctor* degree in Geophysics

Faculty of Earth Sciences
School of Engineering and Natural Sciences
University of Iceland
Sturlugata 7
101, Reykjavik
Iceland

Telephone: +354 525 4000

Bibliographic information:
Joaquín M.C. Belart, 2018, *Mass balance of Icelandic glaciers in variable climate,* PhD dissertation, Faculty of Earth Sciences, University of Iceland, 171 pp.

Author ORCID: https://orcid.org/0000-0002-0853-8935
ISBN: 978-9935-9412-1-3

Printing: Háskólaprent
Reykjavik, Iceland, November 2018

Abstract

The mass balance of a glacier is strongly connected to climate. At high latitudes, mass balance is typically controlled by snow accumulation during the winter and the glacier ablation during the summer. In Iceland, direct mass balance observations have been mostly focused on the three largest ice caps (~600 to ~8000 km^2), measured in situ for the last 25 years. There are, however, glaciers and ice caps distributed over all quarters of the country that lack mass balance observations. Remote sensing data with the capability to retrieve the glacier surface geometry through Digital Elevation Models (DEMs) are valuable tools to measure mass balance using the geodetic method. For a typical Icelandic glacier (with an area between 1 km^2 and hundreds of km^2), this can be optimally achieved from optical stereoscopic imagery, emplaced in airborne or spaceborne sensors, and from airborne lidar. This thesis focuses on remote sensing techniques to accurately measure geodetic mass balance from seasonal to decadal time spans and the relationship of mass balance to climate.

As an example of seasonal mass balance, the winter mass balance of Drangajökull was measured from satellite sub-meter stereo images at the beginning, middle and end of the 2014–2015 winter using data from the Pléiades and WorldView-2 satellites. The results were complemented with in situ snow density measurements and validated with snow thickness measurements. The study concludes that images from the sensors mentioned above may often be used to monitor seasonal mass balance without tedious field logistics.

A vast archive of aerial photographs exists for Iceland extending back to 1945. Since then, most glaciers were surveyed every 5 to 20 years. In addition, a wealth of modern satellite stereo images is available since the early 2000s as well as airborne lidar data in 2008–2013. This creates a unique dataset to construct a 70-year time series of geodetic mass balances. Eyjafjallajökull (~70 km^2) was used to develop semi-automated processing chains based on open-source software. The result is a detailed record of glacier changes resulting from climatic and volcanic forcing. Simple linear regression of the annual mass balance of Eyjafjallajökull indicates that most mass balance variations can be related to changes in summer temperature and winter precipitation. It also allows to infer the sensitivities of mass balance to these two climatic variables.

The processing chain was then applied to 14 glaciers and ice caps spatially distributed in all quarters of Iceland, resulting in a dense mass-balance record for the last 70 years. The mean and standard deviation (±SD) of mass balances of the target glaciers were –0.44±0.16 m w.e. a^{-1} in 1945–1960, 0.00±0.21 m w.e. a^{-1} in 1960–1980, 0.11±0.25 m w.e. a^{-1} in 1980–1994, –1.01±0.50 m w.e. a^{-1} in 1994–2004, –1.27±0.56 m w.e. a^{-1} in 2004–2010 and –0.14±0.51 m w.e. a^{-1} in 2010–2015. The glaciers located at the south and west coasts revealed the highest decadal variability, in contrast to glaciers located in the north. This study improves the knowledge of Icelandic glaciers prior to the warm 1990s. The obtained glacier DEMs reveals in some cases elevation changes caused by irregularities in ice motion and opens for opportunities of modelling the ice dynamics of some of these glaciers coupled with their mass balance.

Útdráttur

Afkoma jökla ræðst af veðurfari. Augljós eru tengslin við snjósöfnun vetrar, en einnig hitastig sumars sem vísbending um orku til leysingar. Hefðbundnar reglulegar afkomumælingar með mælingu þykktar vetrarsjós að hausti og sumarleysingu að hausti, á völdum mælistöðvum, hófust á þremur stærstu jöklum Íslands á níunda og tíunda áratug síðustu aldar og hefur verið haldið úti síðan. Á öðrum jöklum Íslands eru beinar afkomumælingar takmarkaðar; á langflestum hafa engar slíkar mælingar verið gerðar. Upplýsingar um afkomu jökla má einnig meta með því að bera saman hæðarkort af yfirborði þeirra á mismunandi tímum. Í þessu skyni eru fjarkönnunargögn eins og loftmyndir, gervihnattaljósmyndir og leysihæðarskönnun (lidar) sem nýtast við gerð hæðarkorta einkar gagnleg. Viðfangsefni ritgerðarinnar er úrvinnsla slíkra gagna og hvernig má nýta þau til að fá sem nákvæmasta mælinga á afkomu jökla á tímabilum sem spanna allt frá árstíð til áratuga, auk þess sem vensl afkomu og veðurfars eru greind.

Til að kanna notagildi fjarkönnunargagna við rannsóknir á árstíðabundinni afkomu jökla voru yfirborðshæðarkort af Drangajökli unnin eftir háupplausnarljósmyndum frá Pléiades og WorldView-2 gervitunglunum við upphaf, miðbik og lok vetursins 2014–2015. Mælingar á eðlismassa vetrarsnjós að vori voru nýttar til að skorða betur vetrarafkomu jökulsins auk þess sem niðurstöðurnar voru bornar saman við mælda snjóþykkt í afkomumælistöðum. Niðurstöður rannsóknarinnar sýna ótvírætt að oft er hægt að nýta myndir frá áðurnefndum gervitunglum við mælingu vetrarákomu jökla í stað þess að leggja í og erfiða mælileiðangra.

Gríðarmikið safn loftmynda er til af íslenskum jöklum allt aftur til ársins 1945. Síðan þá hafa þeir flestir verið myndaðir á 5 til 20 ára fresti. Einnig hefur verulegu magni gervihnattaljósmynda sem nýtast til vinnslu hæðarkorta af jöklum verið aflað eftir 2000 auk hæðarkorta eftir leysimælingum úr flugvél af flestum jöklum landsins frá 2008 til 2013. Þessi yfirgripsmiklu gögn gera mögulega vinnslu 70 ára afkomusögu margra jökla. Með slíka vinnslu að markmiði var sett saman hálfsjálfvirk úrvinnslulína (flæðilína úrvinnsluþátta) sem byggist á opnum hugbúnaðarlausnum. Hún var þróuð fyrir og fyrst beitt á öll tiltæk gögn af Eyjafjallajökli (~70 km^2). Úrvinnslan skilaði ítarlegri sögu um hæðarbreytingar, afkomu og umfang Eyjafjallajökuls sem bæði veðurfar og eldgos hafa stjórnað. Útfrá afkomuröðinni var bestað línulegt fall sem lýsir venslum ársafkomu við sumarhita og vetrarúrkomu auk leiðréttingarliðs vegna breytilegs umfangs jökulsins. Þetta fall sýnir að stór þáttur breytileika afkomu jökulsins má skýra með breytileika í þessum veðurfarsþáttum. Það gerir einnig kleift að meta hversu næm afkoma jökulsins er fyrir breytingum í þeim.

Úrvinnslulínan var síðan notuð til að setja saman afkomusögu 14 íslenska jökla á um 70 ára tímabili. Jöklar í öllum landsfjórðungum sem og á miðhálendinu voru rannsakaðir. Meðaltal og staðalfrávik afkomu jöklanna á hverju tímabili fyrir sig var -0.44±0.16 m v.g. ár^{-1} (metrar vatnsígildis á ári) 1945–1960, 0.00±0.21 m v.g. ár^{-1} 1960–1980, 0.11±0.25 m v.g. ár^{-1} 1980–1994, -1.01±0.50 m v.g. ár^{-1} 1994–2004, -1.27±0.56 m v.g. ár^{-1} 2004–2010 og -0.14±0.51 m v.g. ár^{-1} 2010–2015. Jöklar við suður og vesturströndina sýna breytilegasta afkomu frá einu tímabili til annars, ólíkt jöklum í norðri þar sem þessi breytileiki er mun minni. Þessi rannsókn eykur mjög við þekkingu okkar á íslenskum jöklum áður en mikil hlýnun varð á tíunda áratug síðustu aldar sem og hvernig afkomu íslenskra jökla breyttist í kjölfarið. Jökla-kortin sem þessi vinna hefur skilað sýna víða hæðarbreytingar sem skýrast af tímabreyti-leika eða óreglu í ísflæði frá afkomu- til leysingasvæðis jöklanna. Þau nýtast einnig sem próf fyrir framtíðarrannsóknir með samtengdum líkönum ísflæðis og afkomu þessara jökla.

Résumé

Le bilan de masse des glaciers est fortement lié au climat. Aux hautes latitudes, l'accumulation de neige pendant l'hiver et la fonte de glace pendant l'été sont les principales composantes du bilan de masse. En Islande, le bilan de masse des trois plus larges calottes glaciaires (~600-~8000 km²) a été suivi régulièrement depuis 25 ans notamment grâce à des mesures in situ. Mais les bilans de masse des autres glaciers et calottes glaciaires islandaises ont été très peu étudiés. Aujourd'hui, les données de télédétection, notamment via la comparaison des modèles numériques du terrain (MNT), permettent de mesurer le bilan de masse par la méthode géodésique. Pour ces glaciers et calottes de plus petites tailles (de 1 km² et à quelques centaines de km²), les photographies aériennes, l'imagerie satellitaire stéréoscopique sub-métriques, et le lidar aérien sont parfaitement adaptées. Cette thèse se focalise donc sur l'estimation des bilans de masse des « petits » glaciers et calottes islandaises depuis le pas de temps saisonnier jusqu'à pluri-décennal et leur relation avec les variations spatiales et temporelles du climat.

Le bilan de masse hivernal de la calotte du Drangajökull (NO-Islande) a été mesuré par des images satellitaires stéréoscopiques sub-métriques (données Pléiades et WorldView-2) acquises au début, milieu et à la fin de l'hiver 2014-2015. Les changements de volume ont été convertis en bilan de masse grâce à des mesures in situ de densité de neige, et validés avec des mesures in situ de profondeur de neige. Ce travail permet d'envisager désormais un suivi du bilan de masse saisonnier sans un laborieux travail de terrain.

Une importante archive de photographies aériennes est disponible en Islande depuis 1945. Ces données offrent une revisite de 5 à 20 ans pour la majorité des glaciers. De plus, depuis 2000, cette archive est complétée par les données des capteurs satellitaires stéréoscopiques et de lidar aérien acquis entre 2008 et 2013. Cet ensemble de données est exploité pour créer une série temporelle de 70 ans de bilan de masse en Islande. La calotte d'Eyjafjallajökull (~70 km²) sert de zone test pour la création et l'automatisation d'une chaîne de traitement, basée sur des logiciels libres. Le résultat est une série de 70 ans de bilan de masse et changements glaciaires liés au climat et au volcanisme. Les variations décennales du bilan de masse sont mises en relation avec les variations des températures estivales et les précipitations hivernales. Cette relation, quasi linéaire, sert pour le calcul de la sensibilité du bilan de masse au changement de température et précipitation.

La chaîne de traitement est alors appliquée à 14 glaciers et calottes glaciaires distribuées aux quatre coins de l'Islande. La moyenne et déviation standard (±DS) du bilan de masse des glaciers sélectionnés est : –0.44±0.16 m w.e. a^{-1} en 1945–1960, 0.00±0.21 m w.e. a^{-1} en 1960–1980, 0.11±0.25 m w.e. a^{-1} en 1980–1994, –1.01±0.50 m w.e. a^{-1} en 1994–2004, –1.27±0.56 m w.e. a^{-1} en 2004–2010 et –0.14±0.51 m w.e. a^{-1} en 2010–2015. Les glaciers maritimes situés près des côtes sud et ouest montrent une plus forte variabilité décennale que les glaciers plus continentaux situés dans le nord et nord-ouest. Notre étude améliore la connaissance des évolutions des glaciers islandais et leur relation avec le climat, en particulier avant les années 1990s et l'augmentation de température. Nos travaux montrent aussi la complexité de la réponse géométrique des glaciers (en lien avec leur dynamique) et offre des données uniques pour la calibration/validation des modèles des glaciers.

To two flightless phoenixes, pillars of my life. May they regenerate and fly again.

Preface

This dissertation was written in a collaboration between the Institute of Earth Sciences (IES) of University of Iceland and the Laboratoire d'Études en Geophisique et Oceanographie Spatiale (LEGOS, Toulouse).

Photogrammetric and remote sensing data and methods were applied to glacierized areas of Iceland, aimed at measuring geodetic mass balances, from seasonal to decadal time scales. The obtained mass balances were then correlated to climatic variables. The results of this work are summarized in three scientific papers, published, in review and to be submitted in peer-reviewed scientific journals, respectively:

I. **Belart, J.M.C.**, Berthier, E., Magnússon, E., Anderson, L. S., Pálsson, F., Thorsteinsson, T., Howat, I. M., Aðalgeirsdóttir, G., Jóhannesson, T., and Jarosch, A. H.: Winter mass balance of Drangajökull ice cap (NW Iceland) derived from satellite sub-meter stereo images, *The Cryosphere*, 11, 1501-1517, https://doi.org/10.5194/tc-11-1501-2017, 2017.

II. **Belart, J.M.C.**, Magnússon, E., Berthier, E., Pálsson, F., Aðalgeirsdóttir, G.: The geodetic mass balance of Eyjafjallajökull ice cap for 1945–2014: processing guidelines and relation to climate. In review, *Journal of Glaciology*.

III. **Belart, J.M.C.**, Magnússon, E., Berthier, E., Björnsson, H., Pálsson, F., Aðalgeirsdóttir, G.: Spatially distributed mass balance of selected Icelandic glaciers, 1945–2015. Trends and link with climate. To be submitted to *Frontiers in Earth Sciences.*

Alongside, other co-authored papers were written throughout the course of the doctoral studies, with a significant contribution from photogrammetric and remote sensing methods, DEM creation and subsequent analyses, based on similar datasets as used for this dissertation. These publications are:

- Magnússon, E., **Belart, J.M.C.**, Pálsson, F., Ágústsson, H., and Crochet, P.: Geodetic mass balance record with rigorous uncertainty estimates deduced from aerial photographs and lidar data – Case study from Drangajökull ice cap, NW Iceland, *The Cryosphere*, 10, 159-177, doi:10.5194/tc-10-159-2016, 2016.

- Guðmundsson, M.T. and 50 others: Gradual caldera collapse at Bárdarbunga volcano, Iceland, regulated by lateral magma outflow, *Science*, 353, I 6296. doi: 10.1126/science.aaf8988, 2016.

- Magnússon, E., **Belart, J.M.C.**, Pálsson, F., Anderson, L.S., Gunnlaugsson., Á. Þ., Berthier, E., Ágústsson, H and Geirsdóttir, Á. The subglacial topography of Drangajökull ice cap, NW-Iceland, deduced from dense RES-profiling. *Jökull*, 66, 1-16, 2016.

- Pedersen, G.B.M., **Belart, J.M.C.**, Magnússon, E., Vilmundaróttir, O.K., Kizel, F.,Sigurmundsson, F.S., Gílasdóttir, G., Benediktsson, J.A.: Hekla Volcano, Iceland, in the 20th Century: Lava Volumes, Production Rates, and Effusion Rates. *Geophysical Research Letters*, 45,1805-1813. doi: 10.1002/2017GL076887, 2018.

Table of Contents

List of Figures

List of Tables

Acknowledgements

Spending the last years as a foreigner in two countries made me cross paths with many people that need to be acknowledged:

I would first and foremost like to acknowledge my two supervisors, Eyfi and Etienne, for the invaluable guidance throughout the studies. Eyfi has been teaching me about glaciers since we first started looking a Drangajökull, and he's been available ever since, even by phone late at night. Etienne never missed a smile or a quick e-mail, and managed to push me even from the distance. It has been a great pleasure to work with you, as supervisors and as persons.

I would also like to express my gratitude to the glaciology group at the University of Iceland for their long support and help. Specially to Tollý, for introducing me to the glaciology group, and to Finnur and Helgi for their enthusiasm and fascination about my work, which has constantly cheered me up. Together with rest of the group, Sverrir, Alex, Hrafnhildur, Bergur, Louise, Snævarr, Ági, Tayo and Becca, they have made a perfect workplace.

This thesis could not have been done without the long and tedious scanning (and re-scanning) of photographs done by Carsten. The rest of members of Landmælingar were also incredibly charming during every visit. Tómas, Þorsteinn and the glaciology group at Veðurstofan are also acknowledged for their help and ideas.

Besides the work done in remote sensing, I also had great opportunities to assist numerous field campaigns. I'm especially grateful for sharing adventures with Gro and the rest of the EMMIRS group in Hekla. I also thank Vincent, for all the riddles in Askja, and for his help with some AWKward problems. The Icelandic Glaciological Society (Jörfi) kindly allowed me to drill and shovel, and Magnús Tumi and Dísa let me be part of some beautiful monitoring flights.

Thanks to my huge family in Askja: to the "dudejos" Tayo and Daniel for all the great adventures, and to Sydney, Dani J., Oli and Martin for even more adventures. To Jorge, Ásta, Karolina, Hannah, Will, Jed, Rannveig, Mona, Werner, Jelte, Baptiste, David, Victor, Matilda, Barbara and Maja.

In Toulouse, I would also like to acknowledge the "glacio" group, for all the coffees, pique-niques and discussions, in particular to Frédérique, Simon, Denis, Alexei, Elena and Sara. Martine and Agathe saved my life with the French administration, and Bruno and Jeoffray kept the server up and running despite my attempts to collapse it. Thanks also to Fanny, the ASP Team, and especially to Fifi, Inés, César, Antoine and Kevin for making an excellent and unforgettable work environment :)

I also thank my friends at LEGOS, LA and GET for innumerable encounters at the OMP's maze, the canteen, along the canal and by the terraces. Romain, Ernesto and Delphine are thanked for letting me squat at "la mezzanine" where we spent many nights drinking wine "comme un cheval".

Reykjavík Trad Sessions, Ínblástur Arkestra and "Les Sessiones Toulusaines" have maintained my head at the right place during these years through the music, and more important, made me meet innumerable wonderful people. So here's a health to the company and one to time passed!

I thank Deirdre, for her love and support, for the help with the English and for her patience for listening when I started to learn violin at a small cabin in Vopnafjörður.

Agradezco profundamente a los profesores de la Escuela Politécnica Superior de Jaén, cuyas enseñanzas han sido de enorme ayuda estos años en el extranjero. Por último, agradezco a mi familia, padres y hermanos, por todo su cariño y apoyo, a Carmina y Miguel Ángel, por mostrarme los glaciares y por su sabiduría, y a Ana por transmitirme su espíritu de aventura.

This work was financially supported by the University of Iceland Research Fund, the Jules Verne Fund and the Katla Kalda project. The lidar mapping of the glaciers in Iceland was funded by the Icelandic Research Fund, the Landsvirkjun research fund, the Icelandic Road Administration, the Reykjavík Energy Environmental and Energy Research Fund, the Klima- og Luftgruppen research fund of the Nordic Council of Ministers, the Vatnajökull National Park, the organization Friends of Vatnajökull, LMÍ, IMO and the UI research fund. Pléiades images were acquired at research price thanks to the CNES ISIS program. WorldView DEMs were obtained through the ArcticDEM project.

1 Introduction

Glaciers and ice caps are indicators of climate; they gain mass during periods of cold summers and/or winters of heavy snowfall and consequently start advancing, and they lose mass during warm summers and/or dry winters and begin retreating. In stable climate they approach a steady-state. These adjustments occur within human (decadal) timescales. In the last 70 years, glaciers on Earth have experienced retreat due to warm temperatures from the 1920s to the 1940s, advances or steady-state during the 1960s to the early 1990s, and a rapid decline after the 1990s, due to rapid warming, linked to anthropogenic causes (Marzeion et al., 2014). Glaciers are natural water reservoirs, used for irrigation and electric power production (Kaser et al., 2010), and contributed significantly to sea level rise in the late 20th and early 21th centuries (Gardner et al., 2013; Björnsson et al., 2013; Zemp et al., 2015). Thus monitoring and measuring glacier changes is key to understanding how the past, current and future climate have and will affect the glaciers and serves as constraints for models that project the sea level rise in the near future.

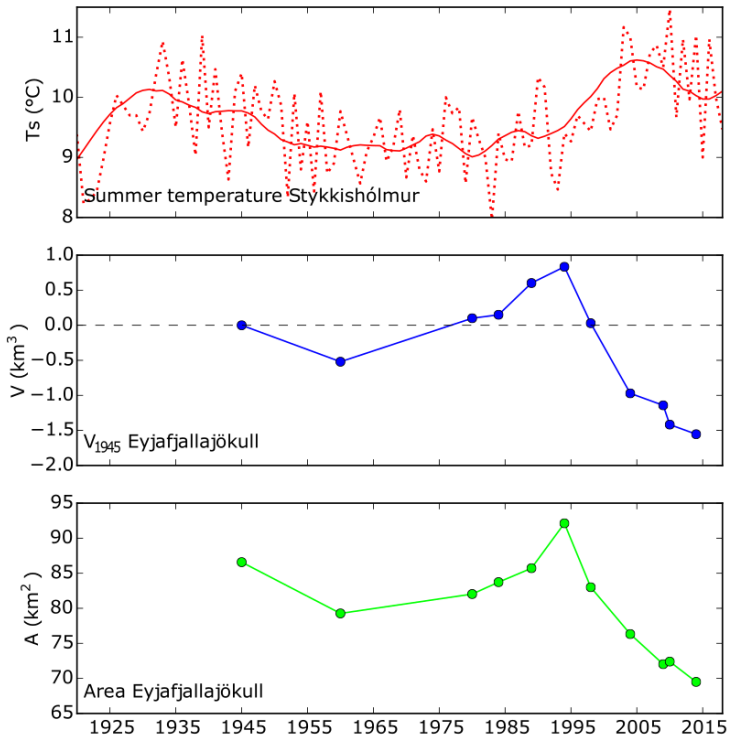

Fig. 1.1 A) Temperature records (Ts, average of June, July and August) at Stykkishólmur, 1935–2018. The solid line indicates 11-year triangular filter data. B) Cumulative volume changes during 1945–2014 of Eyjafjallajökull (S-Iceland), based on archives of aerial photographs and recent satellite imagery. C) Area changes of Eyjafjallajökull during 1945–2014. Locations of the station and glacier are shown in Fig. 1.4.

1.1 Mass balance

The mass balance is "*the change of the mass of the glacier, or part of the glacier, over a stated span of time" (Cogley et al., 2011).* It encompasses glacier accumulation and ablation processes, which makes it a robust proxy for climate change (Vaughan et al., 2013; Bojinski et al., 2014). Mass balance observations are commonly done seasonally (summer and winter), annually or multiannually (Fig. 1.2). The onset dates for the accumulation and ablation seasons are variable, both between years and as a function of elevation, which can lead to difficulties in interpreting seasonal mass balances. The *fixed-date* mass balance method is used often used for convenience. In this dissertation the defined start of the hydrological year is 1 October, the winter ends on 20 May and the summer ends on 30 September. The sum of the winter balance (typically positive) and consequent summer balance (typically negative) reveals the annual mass balance, and when integrated over an entire glacier, ice cap or ice catchment, the mass balance is *glacier-wide* $(\dot{B})$. This is commonly measured in meters of water equivalent (*m w.e.*). Further aspects of mass balance terms can be found in the glossary by Cogley et al., (2011).

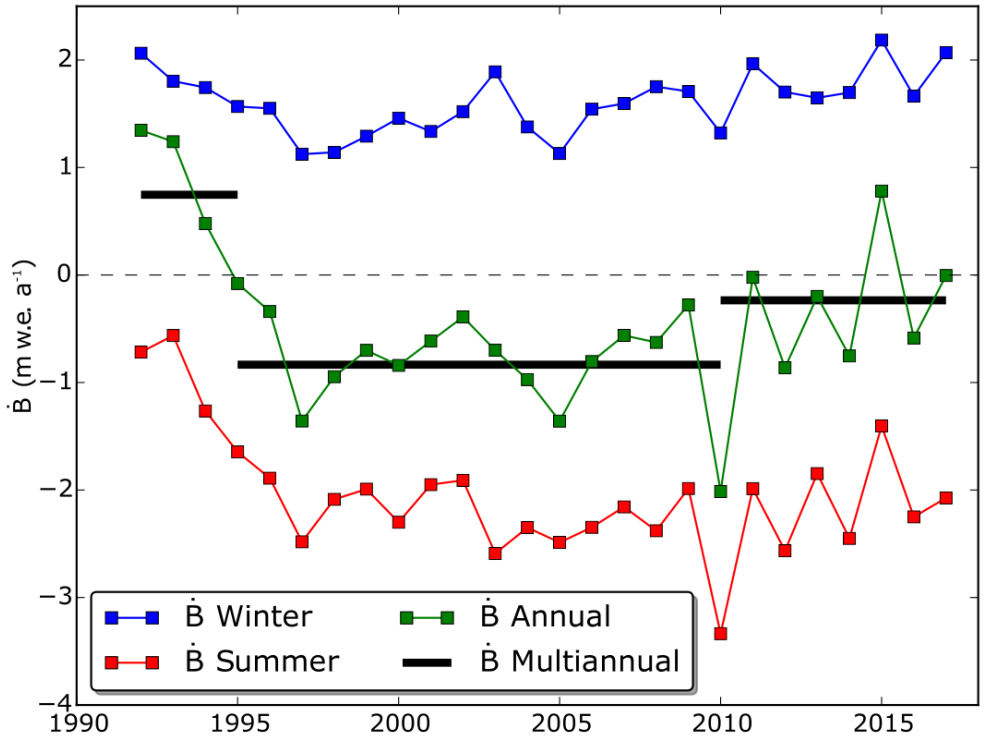

Fig. 1.2 Time series of glacier-wide mass balance for Vatnajökull, 1992–2017, based on in situ measurements. Records are presented in seasonal (red and blue lines), annual (green line) and multiannual averages of mass balance (black lines). Data from Pálsson et al. (2016),expanded to 2017.

In situ mass balance measurements (glaciological method, Fig. 1.2 and 1.3) provide seasonal observations of mass balance. With adequate sampling, the glacier-wide accuracy is typically 0.1–0.3 m w.e, (Fountain and Vecchia, 1999). Long time series of in situ measurements are available for selected glaciers worldwide (WGMS, 2017) and provide valuable trends of mass balance, which correlate well with changing temperature and precipitation (e.g. Leclercq and Oerlemans, 2012; Marzeion et al., 2014; Zemp et al., 2015).

The main limitations of the in situ method are: (1) it is a point-wise measurement $(\dot{b})$, therefore a careful location of the mass-balance points is needed in order to create an accurate representation of the glacier-wide $(\dot{B})$ mass balance (Fountain and Vecchia, 1999). The observations can be then skewed if a mass-balance point is emplaced at a location with substantially different mass balance than its surroundings, for example due to snow drift. (2) The fieldwork required for this type of observations can be logistically, economically and time-wise expensive.

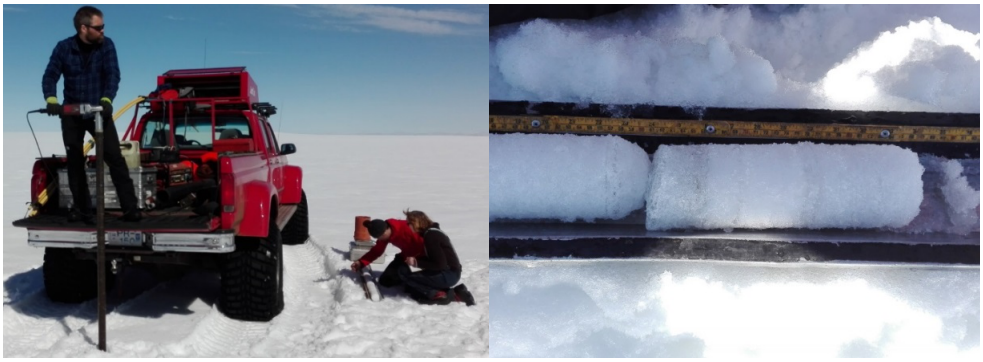

Fig. 1.3 Images from the winter mass balance measurements on Mýrdalsjökull in spring 2016, organized by the Icelandic Glaciological Society (Jörfi). Left: shallow snow core drilling over one mass-balance point. Right: Example of a snow core.

Indirect methods for measuring mass balance rely mostly on remote sensing techniques. A common approach, the so-called geodetic mass balance, consists of comparing the glacier surface over two dates, typically by differencing DEMs (dDEMs), calculating a change in volume, and converting into water equivalent with the knowledge or assumption of the density properties of the glacier (e.g. Huss, 2013). This is a useful method to calibrate in situ mass balance measurements (e.g. Zemp et al., 2013; Andreassen et al., 2016) because it can greatly expand the time series of mass balance (WGMS, 2017). Also it is usually provided as an annual rate, therefore if the calculations are derived from long time periods, the uncertainties are reduced significantly. With adequate DEMs and care for other sources of uncertainties, further described below, this method can provide multiannual, glacier-wide mass balance with uncertainties in the order of 0.1 m w.e. a^{-1} for ~10 year time steps (e.g. Fischer et al., 2015; Magnússon et al., 2016).

Another indirect satellite-based method to obtain mass balance is through gravimetry, with campaigns like GRACE (2002–2017). This method is not utilized in the presented work due to limitations in spatio-temporal resolution of these datasets, but its application for mass balance measurements of large ice caps are acknowledged, particularly after accounting for external signals affecting gravity changes, such as glacier isostatic adjustment (GIA) and influence from the large neighboring ice mass of Greenland (e.g. Sørensen et al., 2017).

1.2 Study area

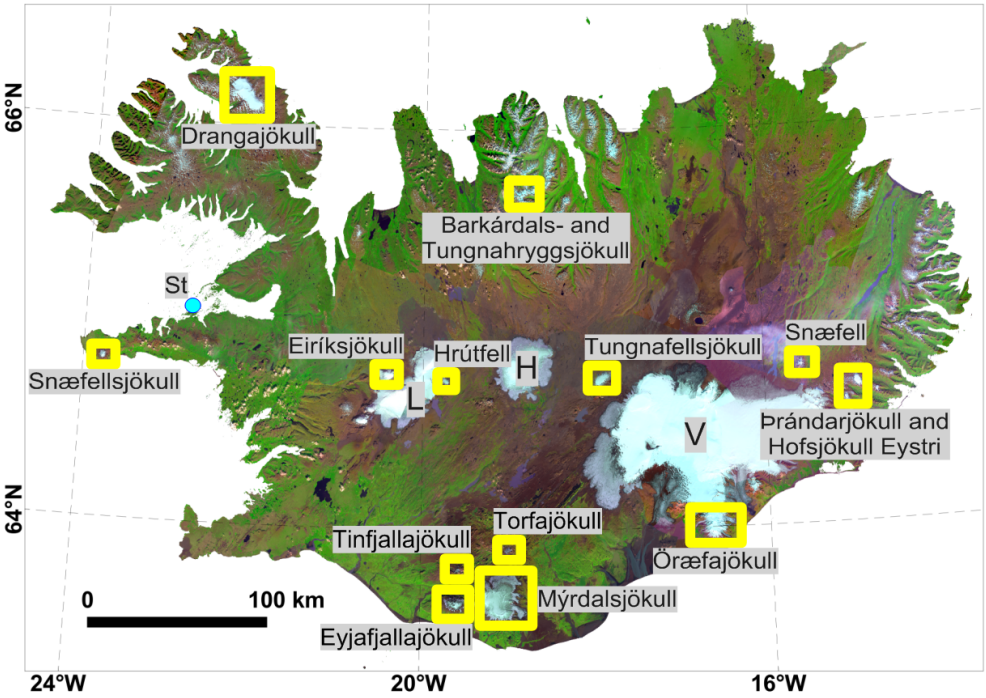

Fig. 1.4 The areas of study, marked in yellow rectangles. V, L and H represent the three largest ice caps, Vatnajökull, Langjökull and Hofsjökull, respectively. The blue dot indicates the location of the Stykkishólmur (St) weather station, data shown in the Fig. 1.1.

Iceland contains about 3.600 km^3 of ice spread over 11.000 km^2, which if melted, would contribute to a ~1 cm to sea-level rise (Björnsson and Pálsson, 2008). Rigorous field monitoring of the three largest ice caps, Vatnajökull, Langjökull and Hofsjökull (Fig. 1.4) started in the late 1980s and early 1990s. Further constraints for mass balance have been estimated for selected ice caps and catchments with geodetic measurements (Aðalgeirsdóttir et al., 2011; Pálsson et al., 2012; Björnsson et al., 2013; Jóhannesson et al., 2013). From the 20th century and up to the present, numerous glacier front measurements have been conducted in Iceland (survey program of the Icelandic Glaciological Sosciety, started in the 1930s, e.g. Sigurðsson, 1998,

http://spordakost.jorfi.is/), and geodetic mass balance has been extracted from DEM differencing at other selected, smaller ice caps (Guðmundsson et al., 2011; Jóhannesson et al., 2011; Gunnlaugsson, 2016; Magnússon et al., 2016).

The results from all combined efforts have constrained the glacier mass loss and sea-level contribution since the 1990s for the three largest ice caps (Björnsson et al., 2013). It has also shown significant glacier fluctuations throughout the 20th century, suggesting that the mass loss rates in the 1930s and 1940s were similar to the rates in the late 1990s and 2000s. However, during the period between the 1960s and early 1990s the Icelandic glaciers and many glaciers elsewhere in the world were close to equilibrium and had in some cases significant front advances.

Our study analyzes glacierized regions in Iceland outside the three main ice caps, i.e. glaciers and ice caps smaller than 600 km^2, as well as Öræfajökull (120 km^2, S-Iceland), attached to the main ice cap of Vatnajökull (Fig. 1.4). The criteria of definition to select the target areas was: (1) broad spatial distribution of glaciers over the entire country, (2) lack or sparse mass balance measurements up to date and (3) relatively small size in order to apply remote sensing techniques without the tedious mosaicking necessary for large glacierized areas.

1.3 Research objectives

This dissertation has three main objectives:

1) To develop and optimize remote sensing methods for measuring past and present geodetic mass balance with state of the art, optical remote sensing and photogrammetric techniques, retrieving accurate mass balance from seasonal to decadal time spans. This includes use of information of various physical processes in glaciers, utilizing limited amount of field observations to extract mass balance from DEM difference.

2) To constrain the mass balance of glaciers and ice caps distributed in all quarters of Iceland during the last 70 years, based on numerous sources of elevation data available.

3) To define and assess a statistical correlation between mass balance and a climate model based on summer temperature and winter precipitation and obtain sensitivities of mass balance to changes in this climate model.

2 Methods

2.1 Glacier Mapping

Glacier mapping is a practical way to observe, monitor and measure glacier changes. This can be done with multiple approaches, from glacier length (e.g. Sapiano et al., 1998) or area changes (e.g. Raup et al., 2007) to a topographic mapping of the glacier surface. The length and area measurements are nevertheless not necessarily related to mass balance changes, since they are affected by the response time of a glacier (e.g. Nye, 1960; Jóhannesson et al., 1989). A full mapping of the 3D surface geometry of the glacier, typically resulting in the production of a DEM, and its comparison with another DEM, is the basis for calculation of volume changes, and subsequently the geodetic mass balance. This section explains the different optimal methods used to create DEMs for the size of the studied glaciers (area spanning few km^2 to hundreds of km^2).

2.1.1 Optical stereo imagery

For decades, airborne optical frame stereo imagery have been the main data source to retrieve the surface topography of terrain at medium-large scales (footprint typically ~8×8 km/image for flight altitude of 7000 m a.s.l., Table 1). This relies on the principles of photogrammetry, where a passive sensor acquires two images with different perspectives over a ground object, generally illuminated by the sun. The basis of photogrammetry are well described in DeWitt and Wolf (2000) and Kraus (2011).

Airborne stereo images reach back to the 1900s, although the biggest improvements in cameras occurred in 1930s (Livingston, 1963) and extended mapping surveys were carried out worldwide after WWII (e.g. KC mapping cameras, Spriggs, 1966). The mapping cameras were also emplaced in spy satellites in the early 1960s. They collected data until 1985, which were declassified up through the 1990s and 2000s (e.g. Bindschadler and Vornberger, 1998; Surazakov and Aizen, 2010). Until the 1990s most of these data were created analogically, i.e. on films. Nowadays mapping cameras are typically digital. There are ongoing, ambitious programs worldwide to scan and preserve the historical analog data on a digital format using highly accurate photogrammetric scanners.

Digital pushbroom sensors, commonly emplaced on satellites, can also have stereoscopic capabilities (e.g. ASTER, SPOT series, Table 1). Due to the sensors' linear geometry, the strategy for stereoscopic imaging is different from frame cameras: either combining acquisitions between adjacent tracks or from two different perspectives acquired along the same track (e.g. front-nadir, nadir-back or front-back imaging, Fig. 2.1). The former was used in early satellites (e.g. since SPOT1, launched in 1986), whereas the latter is adopted in satellites since the early 2000s, like SPOT5 and ASTER, which acquire stereo images with ~1-minute delay between front and nadir images or nadir and back images.

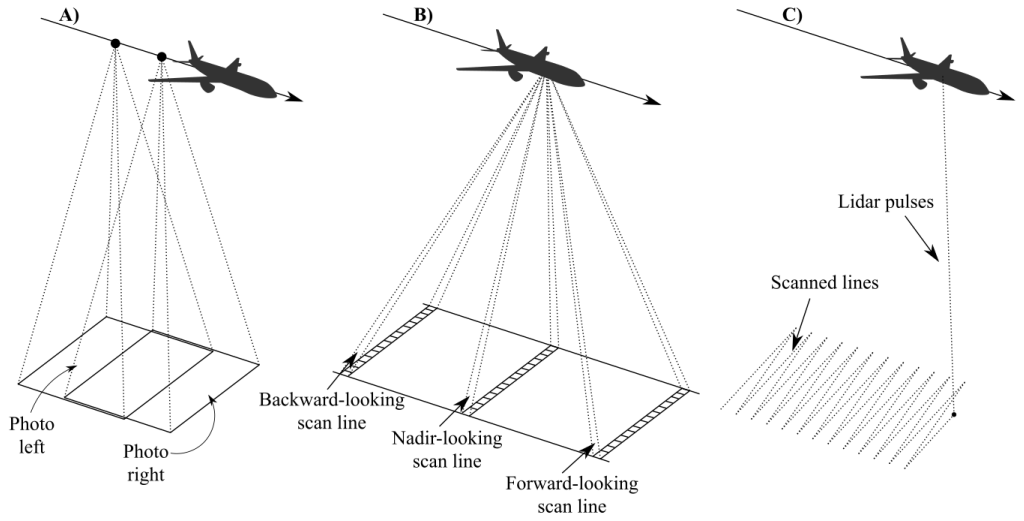

Fig. 2.1 Sketch of three types of sensors (airborne or spaceborne) utilized for topographic mapping of glaciers, modified from DeWitt and Wolf (2000). A) Frame camera collecting a couple of stereo images. B) Pushbroom sensor collecting tri-stereo imagery, based on backward, nadir and forward scans. These acquisitions do not necessarily occur simultaneously, as some pushbroom sensors have rotational capabilities for changing perspective. C) Lidar sensor scanning the terrain, explained in the following section.

The workflow for processing the stereo imagery requires a robust image orientation (e.g. Schenk et al., 2014): knowledge of sensor geometry (e.g. focal length, lens distortion), relative location of the sensor between all overlapping images and location of the block of images relative to a coordinate reference system (CRS, e.g. PROJ contributors, 2018). With the images oriented, terrain coordinates can be retrieved from any stereoscopically measured point. Integrating this over an entire stereopair, and subsequently over an entire block of images, results in a 3D pointcloud, which is interpolated into a gridded DEM. Orthorectified images are generally obtained as a last step, based on the oriented images and the DEM. Commercial photogrammetric software such as ERDAS Imagine (© Hexagon Geospatial) and SOCET-SET (© Geospatial eXploitation) are commonly used, as well as open source-based alternatives including the NASA Ames StereoPipeline (Shean et al., 2016) and MicMac (IGN, France, Pierrot Deseilligny and Clery, 2011; Rupnik et al., 2017).

The historical photographs do not contain *a priori* information about absolute image orientation. The principle of collinearity can be used to solve the orientation (e.g. DeWitt and Wolf, 2000). This relies on the conic geometry of the camera, shown in Fig. 2.2, and establishes that the two vectors in the image ($\vec{a}$) and ground ($\vec{A}$) space are collinear:

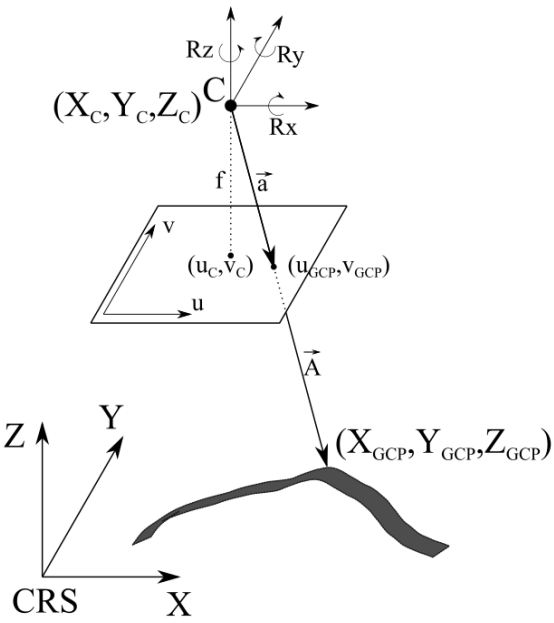

$$\begin{bmatrix} u_{GCP} - u_C \\ v_{GCP} - v_C \\ -f \end{bmatrix} = kR \begin{bmatrix} X_{GCP} - X_C \\ Y_{GCP} - Y_C \\ Z_{GCP} - Z_C \end{bmatrix} \quad (1)$$

Fig. 2.2 Sketch describing collinearity. The center of projection (C) of the camera is the origin of both vectors $\vec{a}$ and $\vec{A}$: the first one is described in the image space (u,v), and has an initial point in C (u_C, v_C, f, being the focal length), and a terminal point at the image coordinates of a feature (u_{GCP}, v_{GCP},0). The second vector is defined in the CRS, and has an initial point in C (X_C, Y_C, Z_C) and a terminal point at the coordinates of the feature ($X_{GCP}, Y_{GCP}, Z_{GCP}$). Both vectors are collinear, assuming a scale factor (k) and a 3D rotation R (defined by R_x, R_y, R_z) between them (Eq. 1).

A bundle block adjustment can be performed using Eq. 1, where the orientation of the frame stereo images is solved by least squares in a system of multiple observations of: (1) image and ground measurements of ground control points (GCPs) fixed to a CRS directly (e.g. from GPS measurements) or indirectly (e.g. based on a high-resolution, high-accuracy DEM fixed to a CRS), (2) image measurements of tie points connecting all adjacent images and (3) intrinsic camera properties, such as focal length, lens distortion and location of the center of projection relative to the image (e.g DeWitt and Wolf, 2000).

Photogrammetric and remote sensing data and methods have drastically improved in recent years. Satellite stereo images include precise orbital information, solving the image orientation either by a rigorous geometric model or via Rational Polynomial Coefficients (RPCs), which statistically links the image and ground space. Recent satellite sensors, like Pléiades (e.g. Berthier et al., 2014) and WorldView (e.g. Noh and Howat, 2015), collect sub-meter stereo images in 12 bit radiometric resolution, resulting in excellent level of details in areas previously challenging, for instance snow areas that could lead to image saturation. A temporal revisit within 1–2 days ensures a high likelihood of cloud-free acquisitions. Stereo images can be processed with automated workflows, retrieving relative image orientation (e.g. Pierrot Deseilligny and Clery, 2011), and generating 3D pointclouds with high resolution and accuracy based on digital image matching techniques (e.g. Hirschmuller, 2008).

2.1.2 Lidar

Lidar is an active sensor. It sends laser pulses at a high rate (typically >30 kHz), scanning ground features. This can be done with different scan strategies based on the sensor. A "sawtooth" line distribution (Fig. 2.1c) is commonly used in airborne mapping lidar. The sensor records the return energy and distance to each feature from which a pulse was reflected. With an accurate sensor position and orientation, dense 3D pointclouds are thus retrieved. It is a precise (e.g. Bamber et al., 2005; Farrell et al., 2012) method to survey small and medium-size glaciers areas (Table 2.1), and it works well in challenging areas for optical-based sensors, such as snow and shadow covered-areas.

In Iceland, all the major glaciers and ice caps were surveyed with airborne lidar between 2008–2013 (Jóhannesson et al., 2013), which provided a benchmark to compare the geometry of the Icelandic glaciers with both past and present glacier surfaces. These surveys covered a significant area in the vicinity of the glaciers, also serving as an excellent base for quality assessment and co-registration of other datasets (e.g. Nuth and Kääb, 2011).

Lidar sensors emplaced in other platforms are not used in this work due to the size constraint of the study areas. However, it is acknowledged that the satellite-based lidar ICESat has yielded geodetic mass balance results over the four largest Icelandic icecaps (Nilsson et al., 2015), and the recently launched ICESat-2 will overcome the coarse resolution sampling and will have further capabilities for monitoring glaciers and ice caps of the size of our study areas (Markus et al., 2017). On the other hand, terrestrial lidar is challenged by the relatively small range of measurements, and is suitable for very small mountain glaciers (e.g. area <0.5 km^2, Fischer et al., 2016; López-Moreno et al., 2016).

Table 2.1 Summary and main characteristics of sensors used in this dissertation.

Dataset	Years operative	Average footprint	Ground Sampling Distance (GSD)
Aerial photographs	1945–present	8×8 km/image*	1×1 m
KH-9 Spy photographs	1977–1984	130×155 km/image	5×5 m
ASTER	2000–present	60×60 km (stereo)	15×15 m
SPOT-5	2000–2015	60×60 km (stereo)	5×10 m
SPOT-6/7	2012–present	60×300 km (stereo)	1.5×1.5 m
Pléiades	2011–present	20×100 km (stereo)	0.7×0.7 m
WorldView-1/2	2008–present	18×100 km (stereo)	0.5×0.5 m
Airborne lidar	2008–2013	400 km^2/day**	~0.33 pt m^{-2}

*Based on a standard mapping camera of 23×23 cm, focal of 153 mm at a flight height of 7000 m above ground. **Maximum area covered in one-day survey, based on specific characteristics of the sensor used, at 2500 m above ground (Jóhannesson et al., 2013).

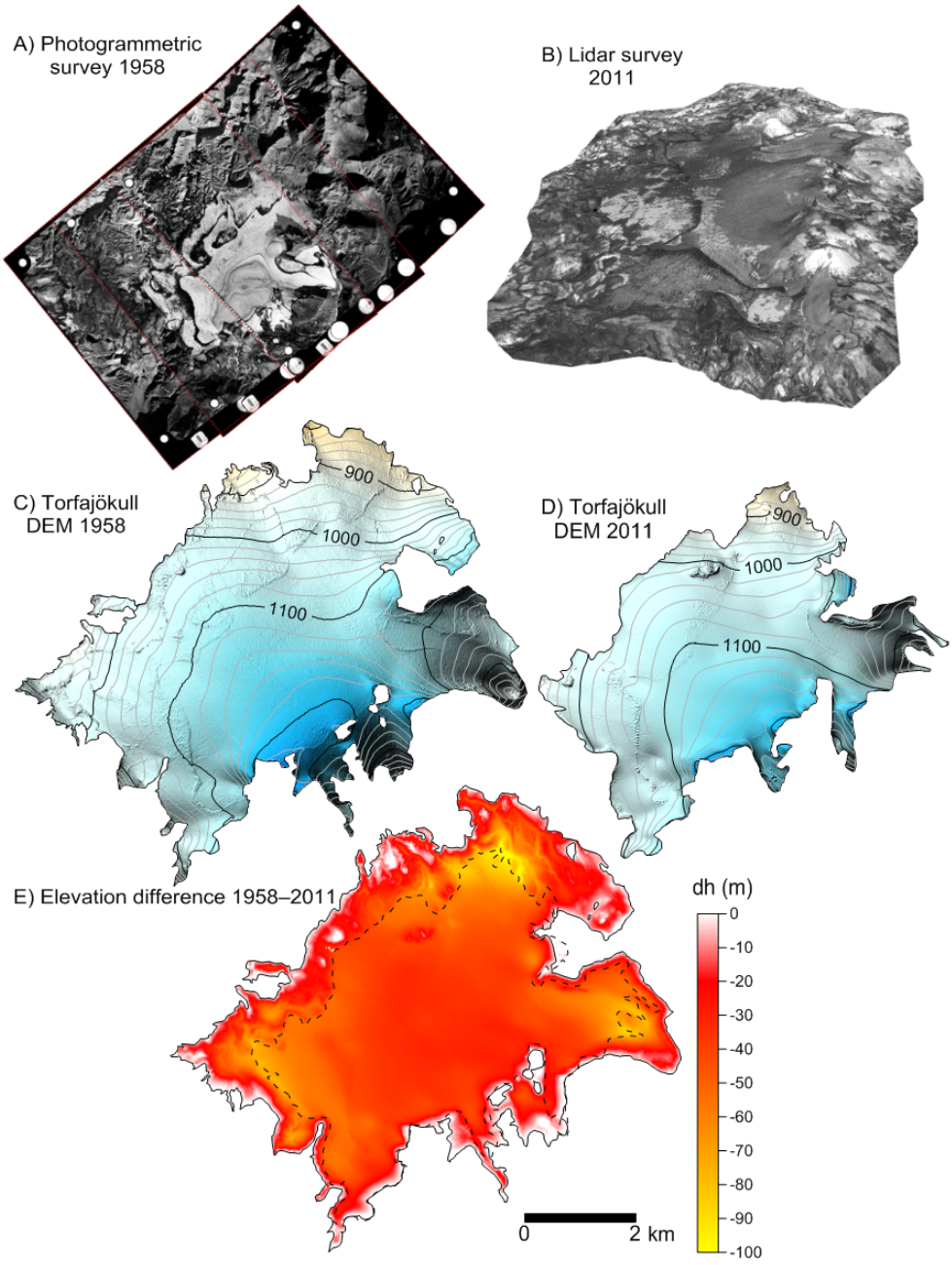

Fig. 2.3 DEM comparison of Torfajökull. A) A photogrammetric survey from October 1958. B) A lidar survey scanned Torfajökull in August 2011, producing a 3D pointcloud. C) and D) DEMs were obtained from respective sources. E) A map of the elevation change between 1958–2011 obtained by subtracting D from C. The black solid line represents the ice cap extent in 1958 and the dashed line shows the extent in 2011.

2.1.3 Other mapping methods

Traditional land survey methods based on triangulation and leveling were commonly used to produce topographic maps in the early 20th century, and have served as a base for geodetic mass balance studies, for example in the Alps and Pyrenees (Bauder et al., 2007; Marti et al., 2015). In Iceland, extensive land survey mapping was carried out in the 1900s and 1910s by the Danish Geodetic Institute, which was complemented in the 1930s with oblique aerial photographs. This resulted in topographic maps, used for example to deduce the geodetic mass balance of Langjökull between 1937–1945 (Pálsson et al., 2012). Yet the accuracy of the contours is expected to be substantially lower than obtained by photogrammetric and remote sensing methods, especially since these surveys were carried with a limited amount of points on the glacierized areas.

Synthetic Aperture Radar (SAR) is also used to create DEMs of ice masses, and modern satellites such as Tandem-X provide detailed and accurate DEMs with high (11 days) revisit time (Krieger et al., 2007). Other SAR-based satellites, e.g. CryoSAT-2, has been used to monitor larger ice masses like Greenland or Antarctica and has also been successfully used for large ice caps in Iceland (Foresta et al., 2016; Gourmelen et al., 2018). The main downside of SAR sensors is that, unlike optical or laser sensors, the radar pulses penetrate below the snow, firn and ice surfaces, causing biases, in particular on dry snow at high elevations (e.g. Dehecq et al., 2016). In Iceland, the SAR-based EMISAR DEM acquired in 1998 has also been used in geodetic studies (Magnússon et al., 2005; Guðmundsson et al., 2011). Airborne altimetric radar profiles are also used for glacier monitoring in Iceland, and have been proven especially useful to study elevation changes of glaciers related to natural hazards (e.g. Guðmundsson et al., 2016).

2.2 Geodetic mass balance

The glacier-wide geodetic mass balance between two dates, t_1 and t_2, is calculated as

$$\dot{B}_{t1}^{t2} = \frac{dV_{t1}^{t2} c}{\bar{A}_{t1}^{t2} dt} \quad (2)$$

Where dV_{t1}^{t2} is the volume change of a glacier, obtained by integrating the elevation difference between two DEMs ($dDEM_{t1}^{t2}$) over the entire glacier (Fig. 2.3), $\bar{A}_{t1}^{t2}$ is the average area of the glacier over the time period, dt is the length of the period and c is the conversion factor used to convert the obtained volume change into mass change. In this section we analyze the terms dV_{t1}^{t2} and c from Eq. 2, as they are the most relevant contributors to uncertainties in the geodetic mass balance (e.g. Magnússon et al., 2016).

2.2.1 DEM uncertainties

The dDEMs (Fig. 2.3) need a careful assessment for likely uncertainties, in order to obtain unbiased and precise volume changes with realistic error bars. Nuth and Kääb (2011) and Paul et al. (2015) describe common biases of dDEMs, mostly associated with misalignment between DEMs (horizontal and vertical shifts, and tilts in DEMs).

DEM uncertainties, and subsequent dDEM uncertainties, are dependent on the sensor sampling capabilities, topographic characteristics (slope) and image texture (e.g. low contrast from shadows or homogeneous snow produce noisier DEMs), but also on the absolute orientation of the respective sensor, i.e. sensor orientation (three-dimensional and angular) within a CRS. Sensors with on-board GPS and inertial navigation systems are fixed to a CRS and have an absolute sensor orientation *a priori*, with centimeter (airborne) to meter- (spaceborne) level accuracy. Biases between two DEMs can be removed if GCPs are used in the orientation process (e.g. James et al., 2006; Csatho et al., 2008) or by refining the approximate DEM location by using co-registration techniques, using the unchanged areas of the DEMs as reference (e.g. Berthier et al., 2007; Nuth and Kääb, 2011; Noh and Howat, 2014).

Uncertainties of a DEM are commonly assessed by descriptive statistics rather than analytically (e.g.Nuth and Kääb, 2011; Noh and Howat, 2015; Shean et al., 2016). Since the main purpose of the DEMs is to be compared to one another, the uncertainty estimates are focused on precision (relative error) rather than on accuracy (absolute error). Quantification of the dDEM precision is commonly given by comparing unchanged areas between the two analyzed DEMs (e.g. Nuth and Kääb, 2011). Simple statistical descriptors such as standard deviation, however, overestimate the uncertainty of volume change integrated from a dDEM, as they do not account for spatial autocorrelation inherent in the dDEMs (Rolstad et al., 2009 and references therein). Geostatistics, addressed in the methods presented by Rolstad et al., (2009) and by Magnússon et al., (2016), are thus a key to adequately assess the relative accuracy of the dDEMs.

2.2.2 Physical processes affecting geodetic mass balance estimates

Geodetic mass balance estimates are limited by various unobserved physical processes and properties that require consideration. Neglecting them can give misleading results.

The density of snow, firn and ice is crucial to convert between volume change and mass change. The simplest approach is to assume that the volume lost or gained has some fixed density, typically assumed to be ice, following Sorge's law (Bader, 1954). Though in recent years the term conversion factor (Huss, 2013) has been adopted rather than density. This takes into account that a glacier changing in volume does not necessarily also change in mass and vice versa, i.e. some mass change can happen without any volume change. Both cases are due to the temporal variation of the density structure, thickness and area of the firn and snow layer.

A conversion factor of 0.85±0.06 is typically used in long-term geodetic mass balance (Table 2) with the following recommendations: (1) a time period longer than 5 years between surveys, (2) a stable mass balance gradient, (3) the presence of a firn area and (4) volume changes significantly larger than zero (Huss, 2013).

When extracting seasonal mass balance from volume changes, the mean density of the snow accumulated (winter mass balance) or snow, firn and ice melted (summer mass balance) need to be known. Corresponding densities from literature and field observations of Icelandic glaciers are listed in Table 2.2 with generous error bars.

Table 2.2 Typical values of snow, firn and ice densities as well as conversion factor, based on literature.

	(kg m^{-3})	**Reference**
Ice	917	Cuffey and Paterson, 2010
Firn	650±150	Bolch et al., 2013
Winter snow*	500±100	Thorsteinsson et al., 2002; Ágústsson et al., 2013
Fresh snow*	400±100	Finnur Pálsson, Personal Communication
Ice & firn	850±60	Huss, 2013

*Based on in situ measurements in Icelandic glaciers.

The uppermost layers of the accumulation area contain firn and snow. These layers are in continuous densification due to gravitational processes (e.g. Ligtenberg et al., 2011; Sold et al., 2013). Besides increasing the density with depth, this effect leads to a continuous lowering of the surface at the accumulation area, which implies a volume change due to densification, in particular during seasonal time spans.

The glaciers dynamics also needs to be taken into account to adequately interpret remotely-sensed elevation changes. Glaciers can exhibit significant rates of displacement in the three spatial dimensions, from sub-meter to meter-level of magnitude on a daily to weekly time frames. Ice velocities are dependent on the bedrock and ice surface geometry and can be modelled numerically by finite element (e.g. Jarosch, 2008; Otero et al., 2017). For a glacier in equilibrium, meaning that its surface elevation does not change on an annual basis, the annual lowering due to the ice dynamics at a given location equals its annual mass balance, which is converted from water equivalent to meters of ice equivalent.

In glacier-wide studies of volume and mass changes, the ice dynamics can be ignored because of the continuity equation (e.g. Cuffey and Paterson, 2010); mass is transported from the accumulation to ablation area, but when integrated over the entire catchment, the net volume change equals to zero. Ice dynamics still need to be considered, specifically when studying local elevation changes in glaciers.

Due to the high mass turnover of Icelandic glaciers, the seasonal (daily to monthly) mass-balance signal can have important effects over the longer time periods analyzed. The maps of elevation changes obtained from differencing two DEMs require cautious interpretation if the dates of each survey vary substantially throughout the season. Ideally, the surveys should be fixed to similar dates and be as close as possible to the beginning of the hydrological year (1 October). However, the surveys are weather dependent; the photogrammetric campaigns during the 20th century often started in mid-July and were commonly done in August when the sun angle yields less shadows. This variability therefore requires an additional volume correction.

To correct seasonal signals and obtain a geodetic mass balance relative to a fixed date (1 October), the daily rates of melt can be estimated based on temperature records by degree-day modelling (e.g. Braithwaite and Olesen, 1989; Jóhannesson et al., 1995). This uses the basis that the melt is correlated with the sum of positive degree-days (T_+) during the analyzed time period with a degree-day factor (ddf).

On the other hand, accumulation is correlated with the precipitation falling during the time analyzed, at temperatures below a threshold, typically 1°C ($P_{(T<1°C)}$, e.g. Jóhannesson et al., 1995). Combining the melt and accumulation modelled as mentioned, and integrated over an entire glacier, this results in

$$\dot{B}_{t1}^{t2} = \sum_{t1}^{t2} \int \{\alpha \; ddf_{f\&i} \; T_+ + \beta \; ddf_s \; T_+ - P_{(T<1°C)}\}(t,x,y)dA \qquad (3)$$

Where α and β are binary switches: $\alpha = 1$ and $\beta = 0$ if the surface analyzed is firn or ice, and vice versa if the surface is snow (snow has fallen and not melted completely). Two ddf are therefore used: one for melting firn and ice ($ddf_{f\&i}$), and another for melting snow (ddf_s). The former is higher than the later, i.e. firn and ice absorb more radiation and melt faster than snow, which reflects more radiation, due to the albedo characteristics of these surfaces (e.g. Hock, 2003).

Degree-day models are obtained by deriving a link between the temperature and the observed melt. It is considered a statistical model, as the ddf is obtained from empirical data, linking measured temperature with observed melt rates. Eq. 3 parametrizes the accumulation and ablation processes into three simple variables, temperature, ddf and precipitation (Cogley et al., 2011), instead of describing the full system affecting ablation and accumulation processes as a full, energy balance model (e.g. Klok and Oerlemans, 2002). Despite this large simplification, degree-day models and precipitation below a temperature threshold have proven their efficiency to model mass balance (e.g. Braithwaite and Zhang, 2000; De Woul and Hock, 2005). Their main advantage relies on the abundant temperature and precipitation records available throughout the 20th century, while the observations needed for an energy balance model are only available from the last decades (e.g. Dee et al., 2011; Nawri et al., 2017).

2.3 Mass balance and climate

Climate variability is in general the main cause for glacier mass balance changes. A full climate model explaining mass balance changes can be given by, among others, the short and long wave radiation, turbulent fluxes, precipitation and wind and moisture transport (e.g. Hock and Holmgren, 2005). The snow accumulation is however strongly dependent on the precipitation, and the energy needed for ablation is reflected in the air temperature. Summer temperature (Ts) and winter precipitation (Pw) are thus clear proxies in formulations of glacier mass balance (e.g. Ohmura, 2001; Ohmura and Boettcher, 2018).

Mass balance sensitivities to this simplified climate model are commonly defined by the change in mass balance by a 1°C increase in summer temperature, or 10% increase in winter precipitation. In Iceland, estimated mass balance sensitivities to these variables are

among the highest worldwide (De Woul and Hock, 2005). Thus it is advantageous to use Icelandic glaciers as a study site to extract climatic signals from the mass balance, whereas the climate signal can be significantly smaller in other glacierized areas controlled by a continental climate, which exhibits lower mass balance sensitivities (De Woul and Hock, 2005; Hock et al., 2009).

The main climatic characteristics of Icelandic glaciers are well described in Björnsson and Pálsson (2008) and Björnsson et al. (2013). Surface temperatures are heavily regulated by the oceanic currents, which have small annual oscillations. The two main ocean currents have different regimes; the Irminger current, that flows along the south coast, brings warm ocean temperatures and a maritime climate, whereas the Greenlandic current is a cold stream passing near the northwest of Iceland. Precipitation in Iceland is relatively high, reaching a maxima of >8000 mm of annual precipitation on Öraefajökull (S-Iceland, Crochet et al., 2007). Precipitation is generally higher close to the coast and often discharged at areas of steep rise from the coast like Mýrdalsjökull and Öræfajökull. This causes rain shadow and dryer climate further inland.

Other forcing of mass balance, such as volcanoes, geothermal systems underneath glaciers and debris cover on glaciers, have been assumed to lead only to minor contributions to the mass balance, affecting at most one-year mass balance in case of a volcanic eruption (Björnsson, 2003; Björnsson et al., 2013).

Changes in either Ts or Pw will have an immediate effect on mass balance (Huss et al., 2012). A first order approximation of mass balance as a function of summer temperature and winter precipitation (e.g. Oerlemans and Reichert, 2000) can be presented as

$$\dot{B} = \varphi Ts + \omega Pw + k \quad (4)$$

However, changes in mass balance result in changes in the geometry of the glacier, with a time delay based on the response time of the glacier (Jóhannesson et al., 1989). This delayed adjustment has a feedback effect on the mass balance (Elsberg et al., 2001; Huss et al., 2012). A glacier, for instance, could continue to have a negative mass balance sometime after the onset of a cooler climate, and would then reach equilibrium after adjusting its geometry.

Eq. 4 is therefore only valid for a punctual span of time, or for mass balance studies shorter than the response time of the glacier. Elsberg et al. (2001) and Harrison et al. (2001) introduced the concept of *reference-surface mass balance*, which assumes a fixed reference area to estimate the mass balance, thus avoiding geometry adjustment. They introduced two correction terms for $\dot{B}$ to convert into reference-surface mass balance, resulting in

$$\dot{B} + b_g \Delta V + b_a \Delta A = \varphi Ts + \omega Pw + k \quad (5)$$

Where b_g is the mass balance gradient with elevation, b_a is the specific mass balance at the terminus and ΔV and ΔA are the differences in actual volume and area compared to the reference volume and area, respectively. The relationship between volume and area is typically assumed to be exponential (e.g. Radic et al., 2007); although their relative changes, in decadal timescales, can be approximated as linear (e.g. Pálsson et al., 2012), thereby simplifying these two terms into $\gamma \Delta A$:

$$\dot{B} = \varphi Ts + \omega Pw + \gamma \Delta A + k \quad (6)$$

This allows a simple linear relationship between mass balance and climate, that can be solved by least squares, with a minimum of four observations of geodetic mass balances together with their respective records of summer temperature, winter precipitation and glacier area.

3 Paper I: Winter mass balance derived from satellite sub-meter stereo images

3.1 Summary

Seasonal mass balance has important applications for improving measurements of climate variables. For example, measurement and modelling of winter precipitation is challenging, due to effects of wind, snow drift and complex topographic effects. Measuring the total snow deposited on glaciers at the end of the winter provides robust constraints on net winter precipitation.

The compilation of winter mass balance measurements commonly require tedious field logistics and needs adequate interpretation for interpolation from point-wise to glacier-wide winter mass balance. This study demonstrates that the winter mass balance can be measured with sub-meter satellite stereo images. This is particularly feasible when the seasonal mass-balance (winter or summer) have a large magnitude, ca. 1 m w.e. or more. This method could be applied to most Icelandic glaciers, which typically have winter mass-balances of 1–2 m w.e (Fig. 1.2), and sometimes exceed 3 m w.e. over a single winter (i.e. more than 10 meters of snow thickness, e.g. Ágústsson et al., 2013), particularly the maritime glaciers located along the south coast.

To demonstrate this, two DEMs from Pléiades, at the beginning and end of the 2014–2015 winter and an additional DEM from WorldView-2, at the middle of the same winter, were utilized to measure volume changes by snow accumulation and subsequently the winter mass balance. This calculation required knowledge of snow density and the effect of snow and firn densification, retrieved in situ. This permitted analysis of the most relevant variables and sources of uncertainty in the calculation. The field data also served as a tool for validation, by comparing the satellite-based measurements of elevation changes and the snow thickness measured in situ. Even so this comparison needs to be completed after correcting the effects of densification, time difference between surveys and ice dynamics. After applying these corrections, both in situ and remote sensing observations are in good agreement.

3.2 Main results

- The glacier-wide, seasonal mass balance can be measured from optical satellite data. The processing chain does not require external data such as GCPs, showing applicability in remote areas.

- The physical properties of the snow are essential parameters in order to infer accurate mass balance estimates. A few snow density measurements at a close date of the winter layer survey are ideal to improve the accuracy of the mass balance, and firn densification causes a minor (8%) correction of the measured mass balance. Snow density assumptions based on previous years' measurements or even from neighboring glaciers can be used with appropiate error bars.

- The elevation gain during the winter, as measured by satellite, was on average 22% smaller than the snow thickness measured in situ, which was explained by ice dynamics, firn and fresh snow densification and time difference between in situ and remote sensing observations. Correcting the satellite-based measurements for these phenomena decreased the discrepancy between remote sensing and in situ observations to 5% – 8%, depending on the method used to correct for ice dynamics.

- Our results for Drangajökull yielded 3.33±0.23 m w.e during the entire winter (14 October 2014 – 22 May 2015), and 60% of this occurred during the first four months (14 October 2014 – 15 February 2015). This ratio of accumulation agrees well with the ratios of precipitation at the same two subperiods, as measured at a nearby weather station.

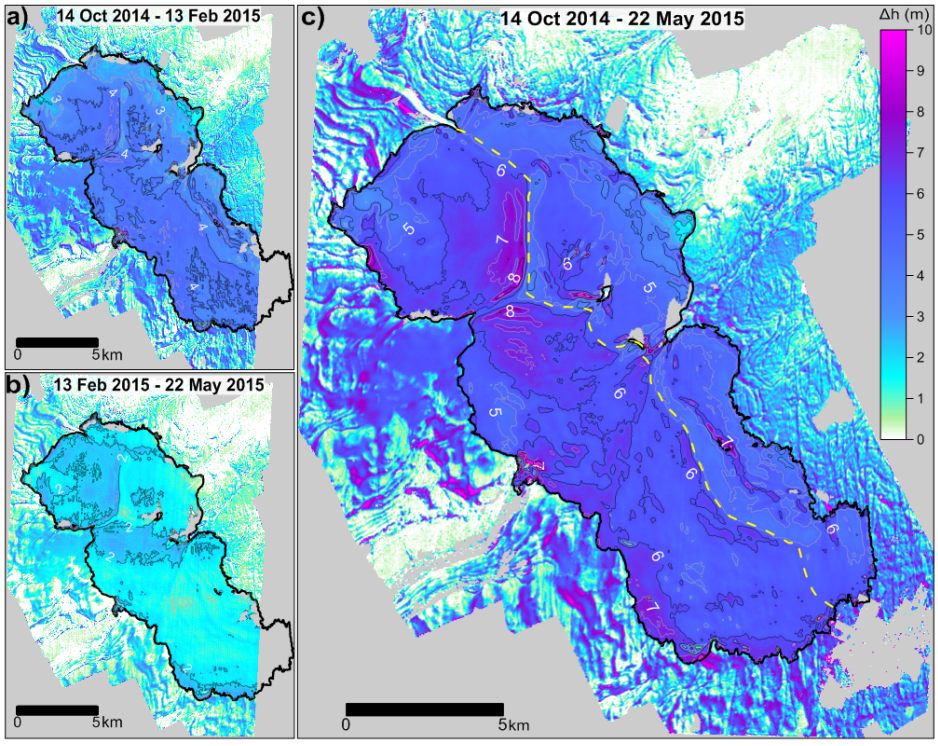

Fig. 3.1 Elevation differences over three time periods on Drangajökull during the 2014–2015 winter. A) and B) show two halves of the winter and C) the net elevation gain due to snow accumulation.

4 Paper II: The geodetic mass balance of Eyjafjallajökull ice cap for 1945–2014: processing guidelines and relation to climate

4.1 Summary

Throughout the last 70 years, there has been a vast collection of data suitable for stereo-photogrammetry in Iceland, including most glacierized areas. This is due to: (1) extensive airborne photoreconnaissance campaigns from US military in 1945/1946, repeated later in 1959–1961, and further repeated from spaceborne spy stereo images in 1977–1980, (2) Icelandic photogrammetric campaigns organized by the National Land Survey of Iceland in 1950–2000, (3) major efforts of surveys with airborne lidar in 2008–2013, (4) modern, satellite-based optical stereo images, from ASTER and SPOT5 in early 2000s and more recently with satellite sub-meter stereo images from Pléiades and WorldView. The combination of these datasets with available records of temperature and precipitation (Crochet et al., 2007; Crochet and Jóhannesson, 2011; Nawri et al., 2017) serves as the base for a study of glacier changes in relation with climate.

The focus of this work is to create a robust methodology, highly automated and repeatable, that could be applied to any glacierized area of Iceland and elsewhere, following these steps: (1) DEM processing from stereo photogrammetry, (2) robust error assessment of elevation differences based on geostatistics, (3) seasonal corrections and (4) link between geodetic mass balance and climatic variables.

We used Eyjafjallajökull as the test area (Fig. 1.4) since it contains a large amount of stereo images, is of a relatively small size for tests in processing routines and has an interesting history of changes, controlled by climate changes and volcanism.

4.2 Main results

- A highly automated workflow was developed, utilizing open source software, in order to process any source of stereoscopic optical imagery, airborne or spaceborne, with rigorous, conic-type camera model or pushbroom model, for creating DEMs and orthoimages. The main manual inputs required were (1) digitization of fiducial marks and GCPs for the processing of frame stereo images, (2) digitization of glacier outlines, (3) manual fit of semivariograms required for bias-corrections and error assessments and (4) masking of clear outliers in the dDEMs still remaining after automatic filtering.

- The use of geostatistics as a tool for bias-correction of photogrammetric DEMs proved to be more robust than other standard proxies commonly used in geodetic studies. This was inferred from intercomparison of independent historical photogrammetric datasets acquired at near dates of survey in 1960 (5 and 13 August respectively) and in 1980 (30 July and 22 August, respectively).

- A mass balance model was developed to account for seasonal corrections of the geodetic surveys, using a degree-day model to account for melt until the 1 October, combined with precipitation records to estimate the snow falling before 1 October at high elevation, run by bootstrapping in order to obtain reliable uncertainties.

- The geodetic mass balance correlated well (R^2=0.8) with the records of summer temperature and winter precipitation in overlapping time periods between 1960–2009, with a simple linear relation, which includes a reference-surface correction term (Eq. 6). This yielded static sensitivities of mass balance of –2.1±0.4 m w.e. K^{-1} and 0.5±0.3 m w.e. $(10\%)^{-1}$ to summer temperature and winter precipitation, respectively.

- The results from Eyjafjallajökull yielded an overall mass loss in 1945–1960 of –0.36±0.11 m w.e.a^{-1}, mass gain in 1960–1994 of 0.38±0.03 m w.e.a^{-1}, and mass loss in 1994–2014 of –0.86±0.06 m w.e.a^{-1}. A mass loss of –3.39±0.43 m w.e. was observed in 2009–2010, largely due to the April 2010 eruption.

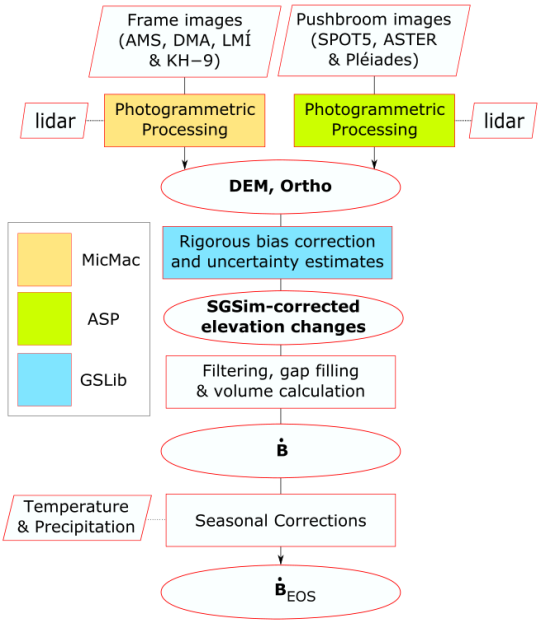

Fig. 4.1 The workflow used for DEM processing, uncertainty estimates of the dDEMs, mass balance calculations and seasonal corrections, using as input any optical stereo imagery. Trapezoids show input data, rectangles processes and ellipses results. The three colors indicate the open source tools used in the workflow.

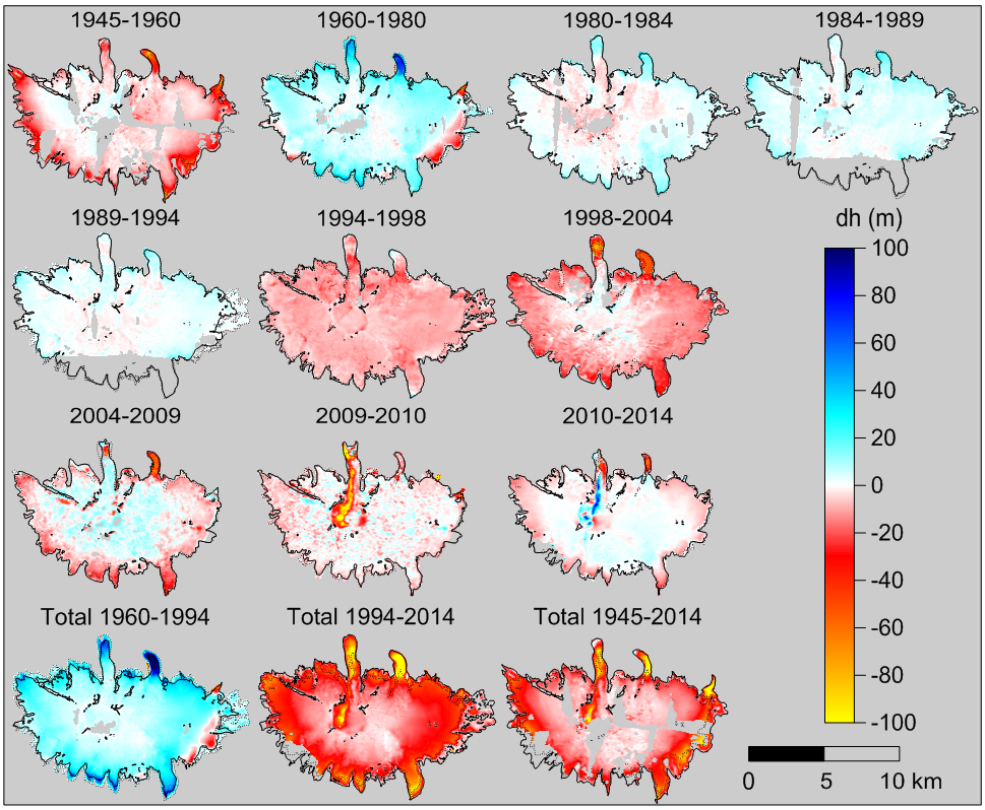

Fig. 4.2 Time series of elevation changes in Eyjafjallajökull, 1945–2014. Red colors indicate lowering and blue thickening. The last row shows three long time periods. 1960–1994 is a period of positive mass balance, glacier front advances and thickening. 1994–2014 has substantial lowering, due to climate but also due to the opening of a melt channel from the April 2010 Eyjafjallajökull eruption.

5 Paper III: Spatially-distributed mass balance of selected Icelandic glaciers, 1945–2015

5.1 Summary

In this study, a selection of 14 glaciers and ice caps distributed around all quarters of Iceland (two of them already with geodetic records: Drangajökull, Magnússon et al., 2016, and Eyjafjallajökull, from Paper II), were analyzed, using analogous datasets and methodology as described in the previous section (Paper II), obtaining geodetic mass balances in decadal time spans, and vastly expanding the knowledge and estimates of the mass balance of glaciers with previously unknown mass balance observations. Following these methodologies, a simple linear fit was used to link the mass balance with summer temperatures and winter precipitation, with a reference-surface correction (Eq. 6), which enabled obtaining region-wide sensitivities of mass balance to temperature and precipitation for the studied glaciers.

Results from the fit also allowed to estimate annual mass balances as a function of a simple climate model, which was used to homogenize the geodetic mass balance to common time intervals and perform a multitemporal mass balance comparison. The intercomparison of mass balances agrees with previous studies and shows the maritime regime of most glaciers located in the south and west coasts, which revealed high decadal mass balance variability.

The simple statistical relationship (Eq. 6) between mass balance and climate fits well for the analyzed glaciers (R^2>0.75), except Mýrdalsjökull; however the linear relationship between change in volume and area was inconsistent in some cases, specifically during 1960–1990, when the glacier advanced, likely explained by events of increased precipitation triggering increased ice flux towards the glacier margin. This encourages further study of these events; a more complete climate model coupled with ice dynamics, together with the obtained datasets, yields an ideal basis for this task.

5.2 Main results

- The mass balance of 14 glaciers and ice caps in Iceland (total >1000 km^2) was calculated from 1945–2015. The mean and standard deviation (mean±SD) of mass balances of the target glaciers were –0.44±0.16 m w.e. a^{-1} in 1945–1960, 0.00±0.21 m w.e. a^{-1} in 1960–1980, 0.11±0.25 m w.e. a^{-1} in 1980–1994, –1.01±0.50 m w.e. a^{-1} in 1994–2004, –1.27±0.56 m w.e. a^{-1} in 2004–2010 and –0.14±0.51 m w.e. a^{-1} in 2010–2015

- The glaciers and ice caps located on the south and west coasts exhibit high decadal mass balance variability, while glaciers located inland, north and northwest show more stable changes in mass balance. Exceptions to this trend may be explained by the elevation span of the glaciers. This may be explained by the influence of warm oceanic currents in the south and west of Iceland, as opposed to drier climate inland, and cold currents in the north of Iceland.

- The fit between mass balance and simple climate was robust in some glaciers, but the linear assumptions were contradicted, in particular when glaciers experienced high mass transport, lowering the accumulation area and showing front advances. This was attributed to an increase in ice flux towards the ablation area, and brings new opportunities for modelling, based on the obtained datasets.

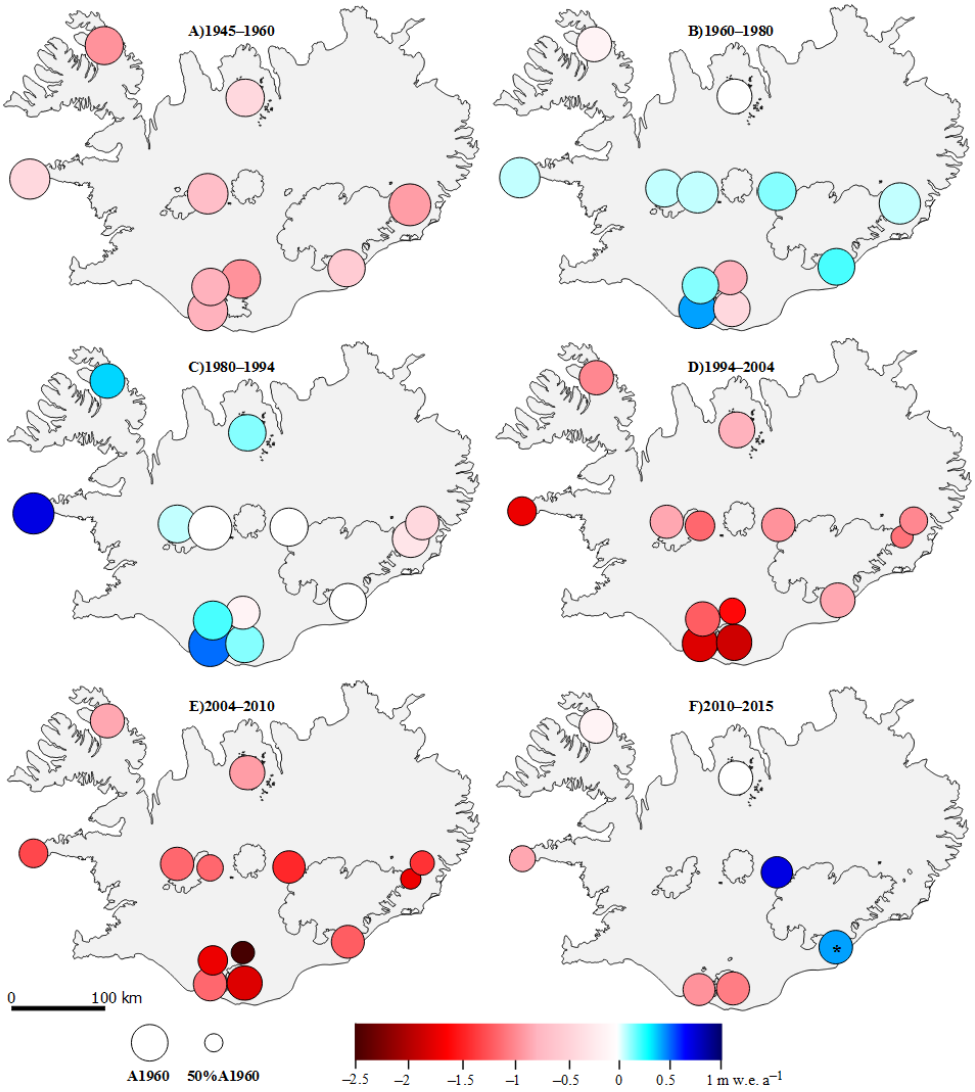

*Fig. 5.1 Region-wide mass balance in Iceland, over the 14 sites, for six selected time periods, after temporal homogeneization of geodetic mass balance by shifting, typically one to two years to a common date for intercomparison. The size of the dots indicates the area changes relative to 1960. *Temporal homogeneization was no applied in Öræfajökull in 2010–2015 due to limited limate data to perform such correction.*

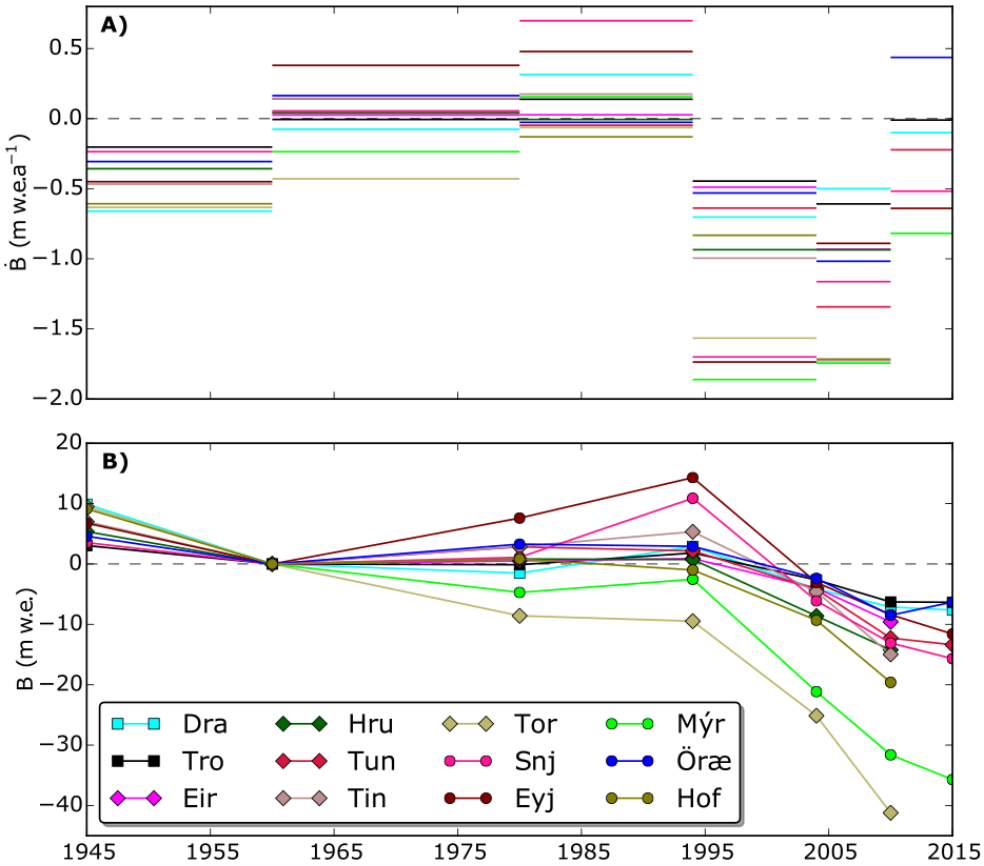

Fig. 5.2 A) The annual average rate of mass balance in 1945–2015. B) The cummulative mass balance, centered in 1960 when DEMs were available at all locations. Squares indicate glaciers located at the north and northwest of Iceland. Diamonds show glaciers located inland, and circles indicate glaciers located at the south and west coasts.

6 Outlook

Optical-based, modern satellite stereo images, such as Pléiades and WorldView are currently one of the best tools to monitor and measure glacier change and glacier mass balance. The data availability is rapidly increasing and becoming accessible to all the research community. This has direct implications for:

- Computation of seasonal mass balance in areas with complex topography and difficult access. This was proven successfully on Drangajökull (NW-Iceland). The main requirements to apply this technique are (1) measurements or good knowledge of snow density and (2) a sufficiently thick winter snow layer, which relates to a large seasonal mass balance (at least 1 m.w.e) for a reasonably large signal-to-noise ratio. This is particularly useful as a constrain for winter precipitation in inaccessible regions and areas of complex accumulation.

- Multiannual mass balance measurements. This data serves to update the state of glaciers to the present. In Iceland, the lidar surveys were carried out up to ten years ago. Even large size ice caps, such as Vatnajökull (~10,000 km²) can now be surveyed within a few satellite acquisitions with sensors like SPOT6/7, which have a good compromise between pixel size (1.5×1.5 m) and image footprint (60×300 km in stereo, Table 1).

- Improving the understanding of numerous glacier processes in a detail previously difficult to achieve. Fig. 6.1 shows an example of the complex systems affecting an Icelandic ice cap, Öræfajökull, revealed by a comparison of lidar with Pléiades data. These phenomena are mass balance-ice dynamics interaction, debris-coverage from a landslide event, ice lowering from a landslide, calving and ceasing of geothermal activity beneath an ice cauldron.

- Monitoring of natural hazards. Pléiades and SPOT6 stereo images were an important tool to monitor the subsidence of Bárðarbunga (W-Vatnajokull) in 2014 during the Bárðarbunga-Holuhraun volcanic eruption (Guðmundsson et al., 2016). Pléiades and WorldView stereo images are also utilized to monitor changes in geothermal systems beneath Mýrdalsjökull, Öræfajökull and Western Vatnajökull, which often cause glacier outbursts (jökulhaups). Additionally, these sensors have the potential to be used to study glacier surges.

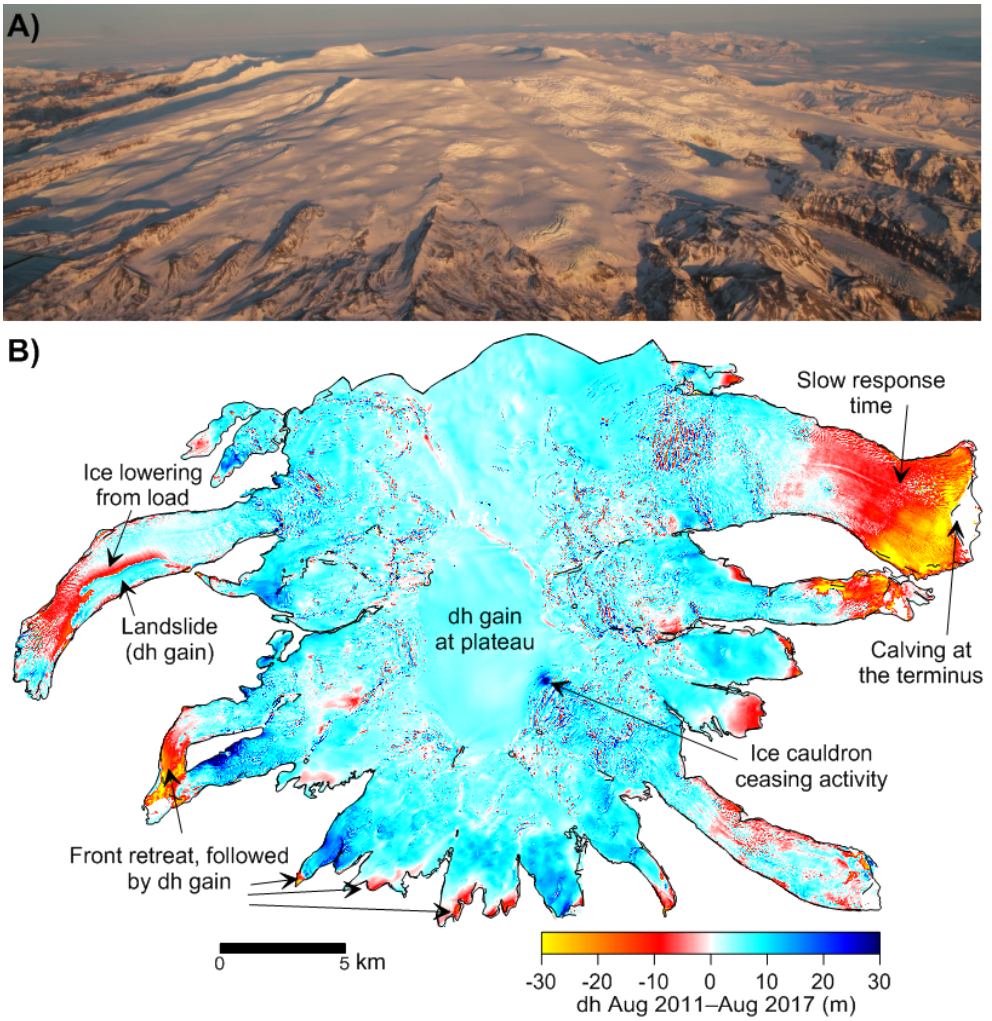

Fig. 6.1 A) Öræfajökull (S-Vatnajökull) in January 2018 from a monitoring flight. B) Elevation changes on Öræfajökull from August 2011 (lidar) to August 2017 (Pléiades). Red colors indicate lowering, and blue elevation gain. Note the front retreat in all the catchments, while the ice cap has had positive mass balance, showing the time delay of the glacier to adjust its geometry to a new climate. The thickening close to the margin indicates that front advances should likely occur after the date of acquisition of the Pléiades dataset.

Furthermore, strategies for DEM processing have significantly improved, revealing further potential in exploiting historical stereo images, which can be compared to modern data (lidar or satellite sub-meter stereo images) and yield maps of elevation changes with high resolution and accuracy, observing formerly unseen glacier processes and glacier evolution. The processing of historical photographs is still far from being fully automated, but there are ongoing, major efforts to facilitate their exploitation. In this thesis about 1000

images were used, less than 1% of the entire archive of aerial photographs in Iceland between 1937–2000.

The methods used in this thesis are also applicable to the three largest ice caps of Iceland, in particular due to available stereo images with a large footprint from spy satellites in 1980 and from high altitude photogrammetric surveys in 1960. Similarly, they are relevant elsewhere outside of Iceland, due to the vast archives of historical stereo images (airborne and spaceborne) available worldwide (e.g. data available from the U.S. Geological Survey http://earthexplorer.usgs.gov/).

Other applications in geosciences have been carried out in parallel to the presented work. The processing of historical aerial photographs of the last 70 years with similar methods as described here greatly enriched the knowledge of the history of volcanic eruptions in Hekla (S-Iceland). DEMs were created before and after each of the last five eruptions: 1947–1948, 1970, 1980–1981, 1991 and 2000, and were used to calculate accurate lava volumes and maps of lava thickness (Pedersen et al., 2018). In addition, these datasets revealed the development of a tephra-covered glacier emplaced on the western flank of Hekla, which has been repeatedly affected by eruptions in Hekla.

This work opens up an immense database, yielding 70-years of changes to Icelandic glaciers. It especially shows the behavior of the Icelandic glaciers prior to the warming in the 1990s. This provides a necessary constraint for modelling the past, present and future state of the glaciers in a varying climate and is useful for regional and global climate models (Marzeion et al., 2012, 2014; Huss and Hock, 2015). The regional trends of mass balance over six time periods during the last 70 years is an unique result, especially as most regional mass balance studies are focused on a few decades of data (e.g. Fischer et al., 2015; Brun et al., 2017), or over significantly smaller glacierized areas (Bauder et al., 2007; Soruco et al., 2009)

In addition, the results have important implications for GIA studies, which use glacier mass loss estimates from mass balance measurements as constraints in modelling. Ice caps like Mýrdalsjökull cause a significant GIA signal (Árnadóttir et al., 2009), and the obtained datasets deliver valuable data to improve the GIA modelling in Iceland. Moreover, a better constrain on GIA has a feedback into better usability of gravimetric methods to retrieve glacier mass balance (e.g. Sørensen et al., 2017).

The glacier mass balance is, in some cases, well explained by a simple linear fit with summer temperature and winter precipitation. However, the poor fits and unrealistic sensitivities retrieved for the assumed linear relationships at some glaciers are motivating for further research, as it is shown that the system affecting glacier changes can be far more complex than a simple climate model based on temperature and precipitation.

Some keys for better understanding the observed processes are the study of the full energy balance, including other climatic components, such as albedo and snow drift, the coupling of mass balance with ice dynamics, and further study of additional processes, e.g. the effect of volcanoes, debris, or dust events. The large dataset of mass balances and accurate maps of elevation changes obtained creates possibilities of additional research in these directions.

References

Aðalgeirsdóttir, G., Guðmundsson, S., Björnsson, H., Pálsson, F., Jóhannesson, T., Hannesdóttir, H., Sigurðsson, S. Þ. and Berthier, E.: Modelling the 20th and 21st century evolution of Hoffellsjökull glacier, SE-Vatnajökull, Iceland, The Cryosphere, 5(4), 961–975, doi:10.5194/tc-5-961-2011, 2011.

Ágústsson, H., Hannesdóttir, H., Thorsteinsson, T., Pálsson, F. and Oddsson, B.: Mass balance of Mýrdalsjökull ice cap accumulation area and comparison of observed winter balance with simulated precipitation, Jokull, 63, 91–104, 2013.

Andreassen, L. M., Elvehøy, H., Kjøllmoen, B. and Engeset, R. V.: Reanalysis of long-term series of glaciological and geodetic mass balance for 10 Norwegian glaciers, The Cryosphere, 10(2), 535–552, doi:10.5194/tc-10-535-2016, 2016.

Árnadóttir, T., Lund, B., Jiang, W., Geirsson, H., Björnsson, H., Einarsson, P. and Sigurdsson, T.: Glacial rebound and plate spreading: Results from the first countrywide GPS observations in Iceland, Geophys J Int, 177(2), 691–716, doi:10.1111/j.1365-246X.2008.04059.x, 2009.

Bader, H.: Sorge's law of densification of snow on high polar glaciers, Journal of Glaciology, 2(15), 319–323, 1954.

Bamber, J. L., Krabill, W., Raper, V., Dowdeswell, J. A. and Oerlemans, J.: Elevation changes measured on Svalbard glaciers and ice caps from airborne laser data, Annals of Glaciology, Vol 42, 2005, 42, 202–208, 2005.

Bauder, A., Funk, M. and Huss, M.: Ice-volume changes of selected glaciers in the Swiss Alps since the end of the 19th century, Annals of Glaciology, 46, 145–149, 2007.

Berthier, E., Arnaud, Y., Kumar, R., Ahmad, S., Wagnon, P. and Chevallier, P.: Remote sensing estimates of glacier mass balances in the Himachal Pradesh (Western Himalaya, India), Remote Sens Environ, 108(3), 327–338, doi:10.1016/j.rse.2006.11.017, 2007.

Bindschadler, R. and Vornberger, P.: Changes in the West Antarctic ice sheet since 1963 from declassified satellite photography, Science, 279(5351), 689–692, 1998.

Björnsson, H.: Subglacial lakes and jokulhlaups in Iceland, Global and Planetary Change, 35(3–4), 255–271, 2003.

Björnsson, H. and Pálsson, F.: Icelandic glaciers, Jökull, 58, 365–386, 2008.

Björnsson, H., Pálsson, F., Guðmundsson, S., Magnússon, E., Aðalgeirsdóttir, G., Jóhannesson, T., Berthier, E., Sigurðsson, O. and Thorsteinsson, T.: Contribution of Icelandic ice caps to sea level rise: trends and variability since the Little Ice Age, Geophys. Res. Lett., 40, 1–5, doi:10.1002/grl.50278, 2013.

Bojinski, S., Verstraete, M., Peterson, T. C., Richter, C., Simmons, A. and Zemp, M.: The Concept of Essential Climate Variables in Support of Climate Research, Applications, and Policy, Bull. Amer. Meteor. Soc., 95(9), 1431–1443, doi:10.1175/BAMS-D-13-00047.1, 2014.

Bolch, T., Sandberg Sørensen, L., Simonsen, S. B., Mölg, N., Machguth, H., Rastner, P. and Paul, F.: Mass loss of Greenland's glaciers and ice caps 2003–2008 revealed from ICESat laser altimetry data, Geophysical Research Letters, 40, 1–7, doi:10.1002/grl.50270, 2013.

Braithwaite, R. J. and Olesen, O. B.: Calculation of Glacier Ablation from Air Temperature, West Greenland, in Glacier Fluctuations and Climatic Change, edited by J. Oerlemans, pp. 219–233, Springer Netherlands., 1989.

Braithwaite, R. J. and Zhang, Y.: Sensitivity of mass balance of five Swiss glaciers to temperature changes assessed by tuning a degree-day model, Journal of Glaciology, 46(152), 7–14, 2000.

Brun, F., Berthier, E., Wagnon, P., Kääb, A. and Treichler, D.: A spatially resolved estimate of High Mountain Asia glacier mass balances from 2000 to 2016, Nature Geoscience, 10(9), 668, doi:10.1038/ngeo2999, 2017.

Cogley, J. G., Hock, R., Rasmussen, L. A., Arendt, A. A., Bauder, A., Braithwaite, R. J., Jansson, P., Kaser, G., Möller, M., Nicholson, L. and Zemp, M.: Glossary of glacier mass balance and related terms, IHP-VII Technical Documents in Hydrology No. 86, IACS Contribution No. 2, UNESCO-IHP, Paris, , 114, 2011.

Crochet, P. and Jóhannesson, T.: A dataset of daily temperature in Iceland for the period 1949–2010, Jökull, 61, 1–17, 2011.

Crochet, P., Jóhannesson, T., Jonsson, T., Sigurðsson, O., Björnsson, H., Pálsson, F. and Barstad, I.: Estimating the spatial distribution of precipitation in Iceland using a linear model of orographic precipitation, Journal of Hydrometeorology, 8(6), 1285–1306, 2007.

Csatho, B., Schenk, T., Van der Veen, C. J. and Krabill, W.: Intermittent thinning of Jakobshavn Isbræ, West Greenland, since the Little Ice Age, Journal of Glaciology, 54(184), 131–144, 2008.

Cuffey, K. M. and Paterson, W. S. B.: The physics of glaciers, Academic Press Inc, Amsterdam., 2010.

De Woul, M. and Hock, R.: Static mass-balance sensitivity of Arctic glaciers and ice caps using a degree-day approach, Annals of Glaciology, Vol 42, 2005, 42, 217–224, 2005.

Dee, D. P., Uppala, S. M., Simmons, A. J., Berrisford, P., Poli, P., Kobayashi, S., Andrae, U., Balmaseda, M. A., Balsamo, G., Bauer, P., Bechtold, P., Beljaars, A. C. M., van de Berg, L., Bidlot, J., Bormann, N., Delsol, C., Dragani, R., Fuentes, M., Geer, A. J., Haimberger, L., Healy, S. B., Hersbach, H., Hólm, E. V., Isaksen, L., Kållberg, P., Köhler, M., Matricardi, M., McNally, A. P., Monge-Sanz, B. M., Morcrette, J.-J., Park, B.-K., Peubey, C., de Rosnay, P., Tavolato, C., Thépaut, J.-N. and Vitart, F.: The ERA-Interim reanalysis: configuration and performance of the data assimilation system, Quarterly

Journal of the Royal Meteorological Society, 137(656), 553–597, doi:10.1002/qj.828, 2011.

Dehecq, A., Millan, R., Berthier, E., Gourmelen, N., Trouvé, E. and Vionnet, V.: Elevation Changes Inferred From TanDEM-X Data Over the Mont-Blanc Area: Impact of the X-Band Interferometric Bias, IEEE Journal of Selected Topics in Applied Earth Observations and Remote Sensing, 9(8), 3870–3882, doi:10.1109/JSTARS.2016.2581482, 2016.

DeWitt, B. A. and Wolf, P. R.: Elements of Photogrammetry(with Applications in GIS), McGraw-Hill Higher Education., 2000.

Elsberg, D. H., Harrison, W. D., Echelmeyer, K. A. and Krimmel, R. M.: Quantifying the effects of climate and surface change on glacier mass balance, Journal of Glaciology, 47(159), 649–658, 2001.

Farrell, S. L., Kurtz, N., Connor, L. N., Elder, B. C., Leuschen, C., Markus, T., McAdoo, D. C., Panzer, B., Richter-Menge, J. and Sonntag, J. G.: A First Assessment of IceBridge Snow and Ice Thickness Data Over Arctic Sea Ice, IEEE Transactions on Geoscience and Remote Sensing, 50(6), 2098–2111, doi:10.1109/TGRS.2011.2170843, 2012.

Fischer, M., Huss, M. and Hoelzle, M.: Surface elevation and mass changes of all Swiss glaciers 1980–2010, The Cryosphere, 9(2), 525–540, doi:10.5194/tc-9-525-2015, 2015.

Fischer, M., Huss, M., Kummert, M. and Hoelzle, M.: Application and validation of long-range terrestrial laser scanning to monitor the mass balance of very small glaciers in the Swiss Alps, The Cryosphere, 10(3), 1279–1295, doi:10.5194/tc-10-1279-2016, 2016.

Foresta, L., Gourmelen, N., Pálsson, F., Nienow, P., Björnsson, H. and Shepherd, A.: Surface elevation change and mass balance of Icelandic ice caps derived from swath mode CryoSat-2 altimetry, Geophysical Research Letters, 43(23), 12,138-12,145, doi:10.1002/2016GL071485, 2016.

Fountain, A. G. and Vecchia, A.: How many stakes are required to measure the mass balance of a glacier?, Geografiska Annaler Series a-Physical Geography, 81A(4), 563–573, 1999.

Gardner, A. S., Moholdt, G., Cogley, J. G., Wouters, B., Arendt, A. A., Wahr, J., Berthier, E., Hock, R., Pfeffer, W. T., Kaser, G., Ligtenberg, S. R. M., Bolch, T., Sharp, M. J., Hagen, J. O., van den Broeke, M. R. and Paul, F.: A Reconciled Estimate of Glacier Contributions to Sea Level Rise: 2003 to 2009, Science, 340(6134), 852–857, doi:10.1126/science.1234532, 2013.

Gourmelen, N., Escorihuela, M. J., Shepherd, A., Foresta, L., Muir, A., Garcia-Mondéjar, A., Roca, M., Baker, S. G. and Drinkwater, M. R.: CryoSat-2 swath interferometric altimetry for mapping ice elevation and elevation change, Advances in Space Research, 62(6), 1226–1242, doi:https://doi.org/10.1016/j.asr.2017.11.014, 2018.

Guðmundsson, M. T., Jónsdóttir, K., Hooper, A., Holohan, E. P., Halldórsson, S. A., Ófeigsson, B. G., Cesca, S., Vogfjörd, K. S., Sigmundsson, F., Högnadóttir, T., Einarsson, P., Sigmarsson, O., Jarosch, A. H., Jónasson, K., Magnússon, E., Hreinsdóttir, S., Bagnardi, M., Parks, M. M., Hjörleifsdóttir, V., Pálsson, F., Walter, T. R., Schöpfer, M. P.

J., Heimann, S., Reynolds, H. I., Dumont, S., Bali, E., Guðfinnsson, G. H., Dahm, T., Roberts, M. J., Hensch, M., Belart, J. M. C., Spaans, K., Jakobsson, S., Guðmundsson, G. B., Fridriksdóttir, H. M., Drouin, V., Dürig, T., Aðalgeirsdóttir, G., Riishuus, M. S., Pedersen, G. B. M., Boeckel, T. van, Oddsson, B., Pfeffer, M. A., Barsotti, S., Bergsson, B., Donovan, A., Burton, M. R. and Aiuppa, A.: Gradual caldera collapse at Bárdarbunga volcano, Iceland, regulated by lateral magma outflow, Science, 353(6296), aaf8988, doi:10.1126/science.aaf8988, 2016.

Guðmundsson, S., Björnsson, H., Magnússon, E., Berthier, E., Pálsson, F., Guðmundsson, M. T., Högnadóttir, T. and Dall, J.: Response of Eyjafjallajökull, Torfajökull and Tindfjallajökull ice caps in Iceland to regional warming, deduced by remote sensing, Polar Research, 30(7282), doi:10.3402/polar.v30i0.7282, 2011.

Harrison, W. D., Elsberg, D. H., Echelmeyer, K. A. and Krimmel, R. M.: On the characterization of glacier response by a single time-scale, Journal of Glaciology, 47(159), 659–664, 2001.

Hirschmuller, H.: Stereo Processing by Semiglobal Matching and Mutual Information, IEEE Transactions on Pattern Analysis and Machine Intelligence, 30(2), 328–341, doi:10.1109/TPAMI.2007.1166, 2008.

Hock, R.: Temperature index melt modelling in mountain areas, Journal of Hydrology, 282, 104–115, 2003.

Hock, R. and Holmgren, B.: A distributed surface energy-balance model for complex topography and its application to Storglaciaren, Sweden, Journal of Glaciology, 51(172), 25–36, 2005.

Hock, R., de Woul, M., Radic, V. and Dyurgerov, M.: Mountain glaciers and ice caps around Antarctica make a large sea-level rise contribution, Geophys Res Lett, 36, 2009.

Huss, M.: Density assumptions for converting geodetic glacier volume change to mass change, The Cryosphere, 7(3), 877–887, doi:10.5194/tc-7-877-2013, 2013.

Huss, M. and Hock, R.: A new model for global glacier change and sea-level rise, Frontiers in Earth Science, 3, doi:10.3389/feart.2015.00054, 2015.

Huss, M., Hock, R., Bauder, A. and Funk, M.: Conventional versus reference-surface mass balance, Journal of Glaciology, 58(208), 278–286, doi:10.3189/2012JoG11J216, 2012.

James, T. D., Murray, T., Barrand, N. E. and Barr, S. L.: Extracting photogrammetric ground control from lidar DEMs for change detection, Photogrammetric Record, 21(116), 312–328, 2006.

Jarosch, A. H.: Icetools: A full Stokes finite element model for glaciers, Comput. Geosci., 34(8), 1005–1014, doi:10.1016/j.cageo.2007.06.012, 2008.

Jóhannesson, T., Raymond, C. and Waddington, E. D.: Time-scale for adjustment of glaciers to changes in mass balance, Journal of Glaciology, 35(121), 355–369, 1989.

Jóhannesson, T., Sigurðsson, O., Laumann, T. and Kennett, M.: Degree-day glacier mass-balance modelling with applications to glaciers in Iceland, Norway and Greenland, Journal of Glaciology, 41(138), 345–358, doi:10.3189/S0022143000016221, 1995.

Jóhannesson, T., Björnsson, H., Magnússon, E., Guðmundsson, S., Pálsson, F., Sigurðsson, O., Thorsteinsson, T. and Berthier, E.: Ice-volume changes, bias estimation of mass-balance measurements and changes in subglacial lakes derived by lidar mapping of the surface of Icelandic glaciers, Annals of Glaciology, 54(63), 63–74, doi:10.3189/2013AoG63A422, 2013.

Kaser, G., Großhauser, M. and Marzeion, B.: Contribution potential of glaciers to water availability in different climate regimes, Proc Natl Acad Sci, 107(47), 20223–20227, doi:10.1073/pnas.1008162107, 2010.

Klok, E. J. and Oerlemans, J.: Model study of the spatial distribution of the energy and mass balance of Morteratschgletscher, Switzerland, Journal of Glaciology, 48(163), 505–518, 2002.

Kraus, K.: Photogrammetry, Geometry from Images and Laser Scans, 2nd. ed., De Gruyter, Berlin, Boston., 2011.

Krieger, G., Moreira, A., Fiedler, H., Hajnsek, I., Werner, M., Younis, M. and Zink, M.: TanDEM-X: A satellite formation for high-resolution SAR interferometry, Ieee Transactions on Geoscience and Remote Sensing, 45(11), 3317–3341, 2007.

Leclercq, P. W. and Oerlemans, J.: Global and hemispheric temperature reconstruction from glacier length fluctuations, Climate Dynamics, 38(5–6), 1065–1079, 2012.

Ligtenberg, S. R. M., Helsen, M. M. and van den Broeke, M. R.: An improved semi-empirical model for the densification of Antarctic firn, The Cryosphere, 5(4), 809–819, doi:10.5194/tc-5-809-2011, 2011.

Livingston, R. G.: A history of military mapping camera development, USAF Liaison Office, U.S. Army Engineer, Geodesy, Intelligence and Mapping R. & D. Agency, 79–110, 1963.

López-Moreno, J. I., Revuelto, J., Rico, I., Chueca-Cía, J., Julián, A., Serreta, A., Serrano, E., Vicente-Serrano, S. M., Azorin-Molina, C., Alonso-González, E. and García-Ruiz, J. M.: Thinning of the Monte Perdido Glacier in the Spanish Pyrenees since 1981, The Cryosphere, 10(2), 681–694, doi:10.5194/tc-10-681-2016, 2016.

Magnússon, E., Björnsson, H., Dall, J. and Pálsson, F.: Volume changes of Vatnajökull ice cap, Iceland, due to surface mass balance, ice flow, and subglacial melting at geothermal areas, Geophysical Research Letters, 32(5) [online] Available from: ://000227640800003, 2005.

Magnússon, E., Belart, J. M. C., Pálsson, F., Ágústsson, H. and Crochet, P.: Geodetic mass balance record with rigorous uncertainty estimates deduced from aerial photographs and lidar data – Case study from Drangajökull ice cap, NW Iceland, The Cryosphere, 10(1), 159–177, doi:10.5194/tc-10-159-2016, 2016.

Markus, T., Neumann, T., Martino, A., Abdalati, W., Brunt, K., Csatho, B., Farrell, S., Fricker, H., Gardner, A., Harding, D., Jasinski, M., Kwok, R., Magruder, L., Lubin, D., Luthcke, S., Morison, J., Nelson, R., Neuenschwander, A., Palm, S., Popescu, S., Shum, C. K., Schutz, B. E., Smith, B., Yang, Y. and Zwally, J.: The Ice, Cloud, and land Elevation Satellite-2 (ICESat-2): Science requirements, concept, and implementation, Remote Sensing of Environment, 190, 260–273, doi:https://doi.org/10.1016/j.rse.2016.12.029, 2017.

Marti, R., Gascoin, S., Houet, T., Ribière, O., Laffly, D., Condom, T., Monnier, S., Schmutz, M., Camerlynck, C., Tihay, J. P., Soubeyroux, J. M. and René, P.: Evolution of Ossoue Glacier (French Pyrenees) since the end of the Little Ice Age, The Cryosphere, 9(5), 1773–1795, doi:10.5194/tc-9-1773-2015, 2015.

Marzeion, B., Jarosch, A. H. and Hofer, M.: Past and future sea-level change from the surface mass balance of glaciers, The Cryosphere, 6(6), 1295–1322, doi:10.5194/tc-6-1295-2012, 2012.

Marzeion, B., Cogley, J. G., Richter, K. and Parkes, D.: Attribution of global glacier mass loss to anthropogenic and natural causes, Science, 345(6199), 919–921, 2014.

Nawri, N., Pálmason, B., Petersen, G. N., Björnsson, H. and Þorsteinsson, Á. Þ.: The ICRA atmospheric reanalysis project for Iceland, Icelandic Meteorological Office, VÍ 2017-005, 1–39, 2017.

Nilsson, J., Sandberg Sørensen, L., Barletta, V. R. and Forsberg, R.: Mass changes in Arctic ice caps and glaciers: implications of regionalizing elevation changes, The Cryosphere, 9(1), 139–150, doi:10.5194/tc-9-139-2015, 2015.

Noh, M.-J. and Howat, I. M.: Automated Coregistration of Repeat Digital Elevation Models for Surface Elevation Change Measurement Using Geometric Constraints, Geoscience and Remote Sensing, IEEE Transactions on, 52(4), 2247–2260, doi:10.1109/TGRS.2013.2258928, 2014.

Noh, M.-J. and Howat, I. M.: Automated stereo-photogrammetric DEM generation at high latitudes: Surface Extraction with TIN-based Search-space Minimization (SETSM) validation and demonstration over glaciated regions, GIScience & Remote Sensing, 52(2), 198–217, doi:10.1080/15481603.2015.1008621, 2015.

Nuth, C. and Kääb, A.: Co-registration and bias corrections of satellite elevation data sets for quantifying glacier thickness change, The Cryosphere, 5(1), 271–290, doi:10.5194/tcd-4-2013-2010, 2011.

Nye, J. F.: The response of glaciers and ice-sheets to seasonal and climatic changes, Proc R Soc Lond A Math Phys Sci, 256(1287), 559, doi:10.1098/rspa.1960.0127, 1960.

Oerlemans, J. and Reichert, B. K.: Relating glacier mass balance to meteorological data by using a seasonal sensitivity characteristic, Journal of Glaciology, 46(152), 1–6, 2000.

Ohmura, A.: Physical Basis for the Temperature-Based Melt-Index Method, J. Appl. Meteor., 40(4), 753–761, doi:10.1175/1520-0450(2001)040<0753:PBFTTB>2.0.CO;2, 2001.

Ohmura, A. and Boettcher, M.: Climate on the equilibrium line altitudes of glaciers: theoretical background behind Ahlmann's P/T diagram, Journal of Glaciology, 64(245), 489–505, doi:10.1017/jog.2018.41, 2018.

Otero, J., Navarro, F. J., Lapazaran, J. J., Welty, E., Puczko, D. and Finkelnburg, R.: Modeling the Controls on the Front Position of a Tidewater Glacier in Svalbard, Front. Earth Sci., 5, doi:10.3389/feart.2017.00029, 2017.

Pálsson, F., Guðmundsson, S., Björnsson, H., Berthier, E., Magnússon, E., Guðmundsson, S. and Haraldsson, H.: Mass and volume changes of Langjökull ice cap, Iceland, ~1890 to 2009, deduced from old maps, satellite images and in situ mass balance measurements, Jökull, 62, 81–96, 2012.

Pálsson, F., Gunnarsson, A., Pálsson, H. S., Steinþórsson, S. and Jónsson, Þ.: Vatnajökull: mass balance, meltwater drainage and surface velocity of the glacial year 2015-16, Institute of Earth Sciences University of Iceland and National Power Company, Report RH-14-2016, LV-2016-129, 2–53, 2016.

Paul, F., Bolch, T., Kääb, A., Nagler, T., Nuth, C., Scharrer, K., Shepherd, A., Strozzi, T., Ticconi, F., Bhambri, R., Berthier, E., Bevan, S., Gourmelen, N., Heid, T., Jeong, S., Kunz, M., Lauknes, T. R., Luckman, A., Merryman Boncori, J. P., Moholdt, G., Muir, A., Neelmeijer, J., Rankl, M., VanLooy, J. and Van Niel, T.: The glaciers climate change initiative: Methods for creating glacier area, elevation change and velocity products, Remote Sensing of Environment, 162, 408–426, doi:10.1016/j.rse.2013.07.043, 2015.

Pedersen G. B. M., Belart J. M. C., Magnússon E., Vilmundardóttir O. K., Kizel F., Sigurmundsson F. S., Gísladóttir G. and Benediktsson J. A.: Hekla Volcano, Iceland, in the 20th Century: Lava Volumes, Production Rates, and Effusion Rates, Geophysical Research Letters, 45(4), 1805–1813, doi:10.1002/2017GL076887, 2018.

Pierrot Deseilligny, M. and Clery, I.: Apero, AN Open Source Bundle Adjusment Software for Automatic Calibration and Orientation of Set of Images, ISPRS - International Archives of the Photogrammetry, Remote Sensing and Spatial Information Sciences, 3816, 269–276, doi:10.5194/isprsarchives-XXXVIII-5-W16-269-2011, 2011.

PROJ contributors: PROJ coordinate transformation software library, Open Source Geospatial Foundation. [online] Available from: https://proj4.org/, 2018.

Radic, V., Hock, R. and Oerlemans, J.: Volume-area scaling vs flowline modelling in glacier volume projections, Annals of Glaciology, Vol 46, 2007, 46, 234–240, 2007.

Raup, B., Racoviteanu, A., Khalsa, S. J. S., Helm, C., Armstrong, R. and Arnaud, Y.: The GLIMS geospatial glacier database: A new tool for studying glacier change, Global and Planetary Change, 56(1–2), 101–110, 2007.

Rolstad, C., Haug, T. and Denby, B.: Spatially integrated geodetic glacier mass balance and its uncertainty based on geostatistical analysis: application to the western Svartisen ice cap, Norway, J Glaciol, 55(192), 666–680, 2009.

Rupnik, E., Daakir, M. and Pierrot Deseilligny, M.: MicMac – a free, open-source solution for photogrammetry, Open Geospatial Data, Software and Standards, 2, 14, doi:10.1186/s40965-017-0027-2, 2017.

Sapiano, J. J., Harrison, W. D. and Echelmeyer, K. A.: Elevation, volume and terminus changes of nine glaciers in North America, Journal of Glaciology, 44(146), 119–135, 1998.

Schenk, T., Csatho, B., van der Veen, C. and McCormick, D.: Fusion of multi-sensor surface elevation data for improved characterization of rapidly changing outlet glaciers in Greenland, Remote Sensing of Environment, 149, 239–251, doi:10.1016/j.rse.2014.04.005, 2014.

Shean, D. E., Alexandrov, O., Moratto, Z. M., Smith, B. E., Joughin, I. R., Porter, C. and Morin, P.: An automated, open-source pipeline for mass production of digital elevation models (DEMs) from very-high-resolution commercial stereo satellite imagery, ISPRS Journal of Photogrammetry and Remote Sensing, 116, 101–117, doi:10.1016/j.isprsjprs.2016.03.012, 2016.

Sigurðsson, O.: Glacier variations in Iceland 1930–1995 – From the database of the Iceland Glaciological Society, Jökull, 45, 3–25, 1998.

Sold, L., Huss, M., Hoelzle, M., Andereggen, H., Joerg, P. C. and Zemp, M.: Methodological approaches to infer end-of-winter snow distribution on alpine glaciers, J. Glaciol., 59(218), 1047–1059, doi:10.3189/2013JoG13J015, 2013.

Sørensen, L. S., Jarosch, A. H., Aðalgeirsdóttir, G., Barletta, V. R., Forsberg, R., Pálsson, F., Björnsson, H. and Jóhannesson, T.: The effect of signal leakage and glacial isostatic rebound on GRACE-derived ice mass changes in Iceland, Geophys J Int, 209(1), 226–233, doi:10.1093/gji/ggx008, 2017.

Soruco, A., Vincent, C., Francou, B. and Gonzalez, J. F.: Glacier decline between 1963 and 2006 in the Cordillera Real, Bolivia, Geophysical Research Letters, 36, 2009.

Spriggs, R. M.: The calibration of Military Cartographic Cameras, Technical Note, Wright-Patterson Air Force Base, Ohio, USA, 1966.

Surazakov, A. B. and Aizen, V. B.: Positional accuracy evaluation of declassified Hexagon KH-9 mapping camera imagery, Photogrammetric Engineering & Remote Sensing, 76(5), 603–608, 2010.

Thorsteinsson, T., Sigurðsson, O., Jóhannesson, T., Larsen, G. and Wilhelms, F.: Ice core drilling on the Hofsjökull ice cap, Jökull, 51, 25–41, 2002.

Vaughan, D. G., Comiso, J. C., Allison, J., Carrasco, J., Kaser, R., Kwok, R., Mote, P., Murray, T., Paul, F., Ren, J., Rignot, E., Solomina, O., Steffen, K. and Zhang, T.: Observations: Cryosphere, in Climate Change 2013: The Physical Science Basis. Contribution of Working Group I to the Fifth Assessment Report of the Intergovernmental Panel on Climate Change, Cambridge University Press, Cambridge, United Kingdom and New York, NY, USA., 2013.

WGMS: Global Glacier Change Bulletin No. 2 (2014-2015), World Glacier Monitoring Service (WGMS), 244 pp, doi:10.5904/wgms-fog-2017-10, 2017.

Zemp, M., Thibert, E., Huss, M., Stumm, D., Rolstad Denby, C., Nuth, C., Nussbaumer, S. U., Moholdt, G., Mercer, A., Mayer, C., Joerg, P. C., Jansson, P., Hynek, B., Fischer, A., Escher-Vetter, H., Elvehøy, H. and Andreassen, L. M.: Reanalysing glacier mass balance measurement series, The Cryosphere, 7(4), 1227–1245, doi:10.5194/tc-7-1227-2013, 2013.

Zemp, M., Frey, H., Gärtner-Roer, I., Nussbaumer, S. U., Hoelzle, M., Paul, F., Haeberli, W., Denzinger, F., Ahlstrøm, A. P., Anderson, B., Bajracharya, S., Baroni, C., Braun, L. N., Cáceres, B. E., Casassa, G., Cobos, G., Dávila, L. R., Delgado Granados, H., Demuth, M. N., Espizua, L., Fischer, A., Fujita, K., Gadek, B., Ghazanfar, A., Hagen, J. O., Holmlund, P., Karimi, N., Li, Z., Pelto, M., Pitte, P., Popovnin, V. V., Portocarrero, C. A., Prinz, R., Sangewar, C. V., Severskiy, I., Sigurðsson, O., Soruco, A., Usubaliev, R. and Vincent, C.: Historically unprecedented global glacier decline in the early 21st century, Journal of Glaciology, 61(228), 745–762, doi:10.3189/2015JoG15J017, 2015.

Paper I

Winter mass balance of Drangajökull ice cap (NW Iceland) derived from satellite sub-meter stereo images

Joaquín M. C. Belart, Etienne Berthier, Eyjólfur Magnússon, Leif S. Anderson, Finnur Pálsson, Thorsteinn Thorsteinsson, Ian M. Howat, Guðfinna Aðalgeirsdóttir, Tómas Jóhannesson, and Alexander H. Jarosch.

The Cryosphere, 11, 1501-1517, 2017. https://doi.org/10.5194/tc-11-1501-2017

The Cryosphere, 11, 1501–1517, 2017
https://doi.org/10.5194/tc-11-1501-2017

The Cryosphere Open Access EGU

Winter mass balance of Drangajökull ice cap (NW Iceland) derived from satellite sub-meter stereo images

Joaquín M. C. Belart[1,2], Etienne Berthier[2], Eyjólfur Magnússon[1], Leif S. Anderson[1], Finnur Pálsson[1], Thorsteinn Thorsteinsson[3], Ian M. Howat[4], Guðfinna Aðalgeirsdóttir[1], Tómas Jóhannesson[3], and Alexander H. Jarosch[1]

[1]Institute of Earth Sciences, University of Iceland, Askja, Reykjavík, Iceland
[2]Laboratoire d'Etudes en Géophysique et Océanographie Spatiales, Centre National de la Recherche Scientifique (LEGOS–CNRS), Université de Toulouse, Toulouse, France
[3]Icelandic Meteorological Office, Reykjavík, Iceland
[4]School of Earth Sciences and Byrd Polar and Climate Research Center, Ohio State University, Columbus, USA

Correspondence to: Joaquín M. C. Belart (jmm11@hi.is)

Received: 18 October 2016 – Discussion started: 14 November 2016
Revised: 21 May 2017 – Accepted: 26 May 2017 – Published: 30 June 2017

Abstract. Sub-meter resolution, stereoscopic satellite images allow for the generation of accurate and high-resolution digital elevation models (DEMs) over glaciers and ice caps. Here, repeated stereo images of Drangajökull ice cap (NW Iceland) from Pléiades and WorldView2 (WV2) are combined with in situ estimates of snow density and densification of firn and fresh snow to provide the first estimates of the glacier-wide geodetic winter mass balance obtained from satellite imagery. Statistics in snow- and ice-free areas reveal similar vertical relative accuracy (< 0.5 m) with and without ground control points (GCPs), demonstrating the capability for measuring seasonal snow accumulation. The calculated winter (14 October 2014 to 22 May 2015) mass balance of Drangajökull was 3.33 ± 0.23 m w.e. (meter water equivalent), with ~ 60 % of the accumulation occurring by February, which is in good agreement with nearby ground observations. On average, the repeated DEMs yield 22 % less elevation change than the length of eight winter snow cores due to (1) the time difference between in situ and satellite observations, (2) firn densification and (3) elevation changes due to ice dynamics. The contributions of these three factors were of similar magnitude. This study demonstrates that seasonal geodetic mass balance can, in many areas, be estimated from sub-meter resolution satellite stereo images.

1 Introduction

Monitoring glacier changes improves understanding of the close connection between glacier mass balance and climate (Vaughan et al., 2013). Glacier monitoring is based on in situ and remote sensing measurements and has confirmed the strong sensitivity of glaciers to climate change. Monitoring has provided evidence for the continuous retreat and mass loss currently taking place in most glaciated regions on Earth (Vaughan et al., 2013; Zemp et al., 2015).

Observations of mass balance provide a valuable short-term overview of the glacier's mass budget and its implications for water storage, runoff and regional climate (e.g., Huss et al., 2008; Radić and Hock, 2014). In addition, these observations can reveal trends and patterns in glacier mass evolution and are commonly used in glacier modeling (e.g., Huss et al., 2008; Aðalgeirsdóttir et al., 2011). Seasonal records of glacier mass changes, however, are sparse, and many glaciated areas in the world are not currently monitored due to high cost and logistical challenges (Ohmura, 2011).

The most widely used method for measuring winter mass balance is the glaciological method (i.e., snow probing, snow pits and/or shallow cores). With adequate spatial sampling, this method can be used to estimate glacier-wide mass balance with errors of 0.1 to 0.3 m water equivalent (m w.e.; Fountain and Vecchia, 1999; Ohmura, 2011). Remote-sensing-based methods, such as repeated airborne

surveys (Machguth et al., 2006; Sold et al., 2013; Helfricht et al., 2014) or unmanned aerial vehicles surveys (Bühler et al., 2016; De Michele et al., 2016), are occasionally used for measuring snow accumulation. These methods allow for the creation of highly accurate and detailed digital elevation models (DEMs) that are compared when measuring changes in elevation and volume due to snow accumulation.

Satellite stereo images with sub-meter resolution (e.g., from WorldView or Pléiades with nearly global coverage) are available for the creation of accurate and detailed DEMs. The high spatial and radiometric resolutions of these images allow for the statistical correlation of features on low-contrast surfaces, including ice, snow and shadowed terrain (e.g., Berthier et al., 2014; Holzer et al., 2015; Willis et al., 2015; Shean et al., 2016). The DEMs obtained from these sensors have been tested and assessed in numerous studies, reporting relative DEM accuracy ranging from 0.2 to 1 m (Berthier et al., 2014; Lacroix et al., 2015; Noh and Howat, 2015; Willis et al., 2015; Shean et al., 2016). This accuracy indicates high potential for the usage of these sensors in measuring changes over short time intervals for glaciers with relatively high mass balance amplitude (half of the difference between winter and summer mass balance, Cogley et al., 2011). For example, sequential Pléiades DEMs have recently been successfully used for measuring snow thickness in mountainous areas (Marti et al., 2016).

In this paper, we evaluate the capabilities of Pléiades and WorldView2 (WV2) DEMs for measuring winter mass balance over an Icelandic ice cap. A processing chain is developed for constructing co-registered DEMs from sub-meter resolution optical stereo images. Co-registration is performed without external reference data, enabling application to remote glaciated areas where such data is lacking. Calculation of geodetic winter mass balance is constrained with in situ density measurements as well as simple firn and snow densification models. Finally, we validate our remote sensing results with in situ measurements of snow thickness.

2 Study site and data

2.1 Drangajökull ice cap

Approximately 11 000 km^2 of Iceland is covered by glaciers (Björnsson and Pálsson, 2008). Glaciological mass balance studies have been conducted on the three largest ice caps: Vatnajökull (since 1991, Björnsson et al., 2013), Langjökull (since 1997, Pálsson et al., 2012) and Hofsjökull (since 1988, Jóhannesson et al., 2013) (Fig. 1). Field campaigns are carried out twice per year to record the winter and summer mass balance at selected survey sites (Björnsson and Pálsson, 2008; Björnsson et al., 2013), and the measurements reveal typical mass balance amplitude of $\sim$ 1.5–3 m w.e. (Aðalgeirsdóttir et al., 2011; Pálsson et al., 2012; Björnsson et al., 2013) and even higher in some other glaciated areas such as Mýrdalsjökull and Öræfajökull ice caps (south Iceland) where limited mass balance surveys in the accumulation area have shown winter accumulation of 5–7 m w.e. (Guðmundsson, 2000; Ágústsson et al., 2013). These measurements have improved understanding of the impacts of climate change on glacier mass balance in the North Atlantic and have provided glacial runoff estimates, which are important for water resource management in Iceland.

The study area, Drangajökull ice cap, is located in NW Iceland (Fig. 1) between $\sim$ 60 and $\sim$ 900 m a.s.l. and has a total area of 143 km^2 (in 2014). Due to its distance from the Irminger Current, its climate is substantially different from other Icelandic glaciers near the south coast or in the central part of the island (Jóhannesson et al., 2013; Harning et al., 2016a, b). Geodetic observations have revealed that the average glacier-wide mass balance of Drangajökull during the period 1946–2011 was moderately negative (-0.26 ± 0.04 m w.e. a^{-1}; Magnússon et al., 2016a). The same observations revealed a striking difference in the mass balance between the western and eastern sides of the ice cap during this period, -0.16 ± 0.05 and -0.41 ± 0.04 m w.e. a^{-1}, respectively. The spatial distribution of the winter snow accumulation is a likely cause of this difference.

Relatively recent records of in situ mass balance measurements on this ice cap, together with the several meters of expected amount of snow accumulation during the winter, make Drangajökull an appropriate site for developing the described remote sensing methods. Additionally, Drangajökull's relatively small area makes it suitable for testing Pléiades and WV products (DEMs and orthoimages) because the ice cap is covered entirely or nearly entirely within a single stereo pair, eliminating the need for mosaicking and alignment of multiple DEMs from different dates, which would introduce additional complications and errors.

2.2 Satellite stereo images

Two pairs of Pléiades (French Space Agency, CNES) stereo images were acquired over Drangajökull: the first on 14 October 2014 (beginning of the winter) and the second on 22 May 2015 (end of the winter; Table 1 and Fig. 2). An additional dataset of stereo images was acquired from WV2 (DigitalGlobe Inc via the US National Geospatial Intelligence Agency) on 13 February 2015, covering $\sim$ 92 % of the ice cap (Table 1 and Fig. 2).

Pléiades and WV2 images have a spatial resolution of 0.7 and 0.5 m at nadir, respectively. The images are encoded in 12 bits (Pléiades) and 11 bits (WV2). The base to height (B / H) ratio from the stereo pairs ranges between 0.4 and 0.5 (Table 1), providing excellent stereo geometry while minimizing occlusions due to steep topography.

The October 2014 Pléiades images were acquired 1 day after the second significant snowfall of the winter (Fig. 2), showing fresh snow covering most of the imaged area. Fine

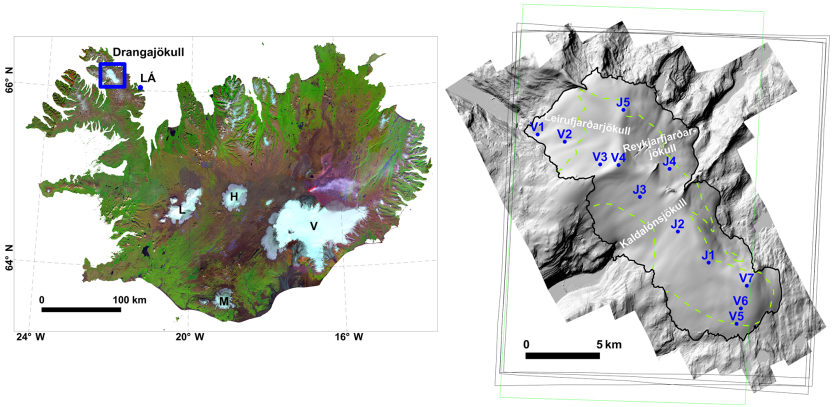

Figure 1. Area of study and data collected. (Left) Mosaic of Iceland from Landsat 8 images, mosaicked by the National Land Survey of Iceland. The blue rectangle locates the Drangajökull ice cap, and a blue dot indicates the location of the meteorological station "Litla Ávík" (LÁ). L, M, V and H represent the locations of Langjökull, Mýrdalsjökull, Vatnajökull and Hofsjökull ice caps, respectively. (Right) A shaded relief representation of a lidar DEM covering Drangajökull and vicinity in the summer 2011 (Jóhannesson et al., 2013). Margins of the ice cap are shown as a black polygon, and the equilibrium line altitude (ELA) obtained from the mass balance measurements over 2013–2014 is shown with a green dashed line. Blue dots indicate location of the in situ measurements. Locations labeled V1–7 have been measured since 2005, whereas locations labeled J1–5 were only measured in 2014 except J2, which was also measured in 2015. Black rectangles show the footprints of the Pléiades images, and a green rectangle shows the footprint of the WV2 DEM.

Table 1. Dates, type of data (split between remote sensing and in situ data), sampling and specifications of datasets used in this study.

	Date	Data type	Spatial resolution	Comments
Remote sensing	20 Jul 2011	Lidar DEM	2×2 m cell size	
	14 Oct 2014	Pléiades stereo	0.70 m pixel size	B / H 0.48
	13 Feb 2015	WV2 SETSM DEM & orthoimage	2×2 m cell size	B / H 0.45
	22 May 2015	Pléiades stereo	0.70 m pixel size	B / H 0.41
In situ	Springs 2005–2015	Snow density	6 to 12 points	Spring 2013 missing due to bad weather
	1 Jan 2014–31 Dec 2015	Daily precipitation & temperature		Litla Ávík
	30–31 Mar 2014 & 20 Sep 2014	net mass balance	12 points + interpolated net balance map	Spring 2014: shallow cores & GPR profiles. Autumn 2014: ablation stakes.
	19 Jun 2015	Winter mass balance	8 points	

details of the bare terrain, such as boulders (~ 2 m across), can, however, be clearly recognized in the images.

Due to the low solar illumination angle, the October 2014 and February 2015 images contain large shadows north of cliffs and nunataks, causing lack of contrast in these areas. The images of May 2015 contain areas with clouds at the southern border of Drangajökull, mostly located off-glacier (Fig. 2), and a few thin clouds over the ice cap, though the glacier surface remains visible. The February 2015 orthoimage reveals a similar off-glacier snow extent as the images of May 2015 (Fig. 2).

2.3 Lidar

A lidar DEM was produced from an airborne survey in July 2011 (Fig. 1) as part of larger effort to survey all Icelandic glaciers and ice caps from 2008–2012 (Jóhannesson et al., 2013). For Drangajökull, this survey covered an extensive ice-free area outside of the ice cap, up to ~ 10 km from the ice margin at some locations. The survey was carried out with an Optech ALTM 3100 lidar, with a typical point cloud density of 0.33 pts m^{-2}. A DEM with 2 m posting was produced from the point cloud (Magnússon et al., 2016a). An

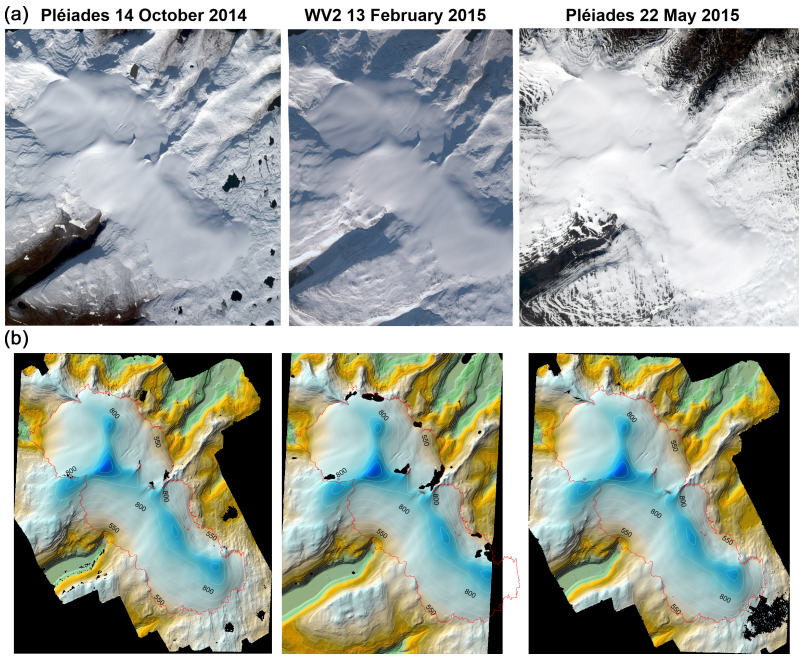

Figure 2. **(a)** Quickview (left image from each stereo pair) of the satellite images used. ©CNES 2014 and 2015, Airbus D&S, all copyrights reserved (Pléiades), and ©DigitalGlobe (WV2). Quickviews downloadable at http://www.intelligence-airbusds.com/en/4871-browse-and-order (Pléiades) and https://browse.digitalglobe.com (WV2). **(b)** The DEMs produced from each stereo pair, processed using scheme B, represented as a color hillshade with 50 m contours overlaid (elevation in meters above ellipsoid WGS84). A red polygon delineates the ice cap. Black colors indicate no data in the DEM.

uncertainty assessment performed on another lidar dataset from the same sensor acquired in similar conditions revealed an absolute vertical accuracy well within 0.5 m (Jóhannesson et al., 2011).

2.4 In situ and meteorological measurements

In situ mass balance measurements have been carried out by the Icelandic Meteorological Office (IMO) and the National Energy Authority on Drangajökull annually since 2005, typically at the end of May (winter mass balance) and again at the end of September (summer mass balance). Snow cores are drilled at six to eight locations at the end of each winter, except for the 2013 campaign (no measurements collected due to bad weather) and the extensive 2014 campaign, where 12 survey sites were measured (Fig. 1). For winter mass balance, the length, volume and weight of each segment of the core drilled were measured, allowing retrieving bulk snow density, snow thickness and the winter mass balance at each location (Fig. 1). Similar procedures for drilling are described in many previous studies (e.g. Guðmundsson, 2000; Thorsteinsson et al., 2002; Ágústsson et al., 2013). The position was measured using a handheld GPS at each core location.

We used the in situ data collected at eight of these locations in spring 2015 for data calibration and validation. These measurements were carried on 19 June 2015, which is 1 month later than usual due to an unusually cold spring. All available in situ records of snow density from 2005–2014 were also included in this study.

Additionally, a manually interpolated map of in situ net mass balance for the glaciological year 2013–2014 was obtained using measurements at the 12 mass balance survey sites and a 110 km profile of snow depth from ground penetrating radar (GPR) traversing through all the survey sites (unpublished data, IMO and IES). The locations of survey sites and the GPR profiles were chosen to represent the spatial variation and elevation dependence of the snow cover. The interpolation method is described for a similar dataset by Pálsson et al. (2012). A map of the Drangajökull bedrock topography (Magnússon et al., 2016b) was also used in this study, and daily precipitation and temperature measurements for 2014–2015 from the meteorological station Litla Ávík (LÁ, station #293, 40 km SE of Drangajökull, 15 m a.s.l., Fig. 1) were obtained from IMO (public data, www.vedur.is).

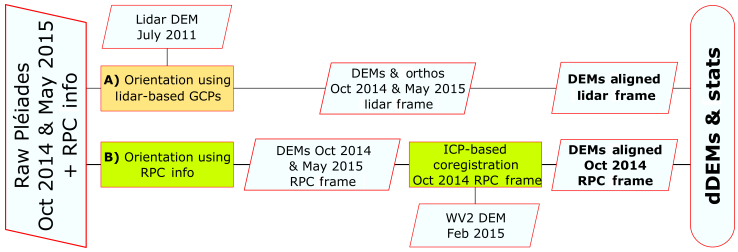

Figure 3. Flowchart of the different schemes studied for obtaining unbiased DEMs. Rectangles indicate processing steps and parallelograms indicate products. Orange squares indicate processing with ERDAS software, and green squares indicate processing with ASP software.

3 Methods

This section is organized as follows: in Sect. 3.1 we describe the processing of remote sensing data to obtain co-registered DEMs, in Sect. 3.2 we explain how we derive glacier-wide geodetic winter mass balance from the remote sensing observations and in situ calibration data, and in Sect. 3.3 we evaluate the results obtained from remote sensing by comparing them with in situ snow thickness measurements.

3.1 Processing of satellite data

Two different schemes (Fig. 3) were used to obtain the DEMs and the difference of DEMs (dDEM), spatially co-registered (e.g., Nuth and Kääb, 2011). Spatial calculations are done in the conformal conic Lambert projection, ISN93 (details at www.lmi.is). Scheme A involves lidar-derived ground control points (GCPs) as a reference, whereas scheme B involves common snow- and ice-free areas in the datasets. From each scheme, statistics of elevation difference in snow- and ice-free areas were calculated to verify that the dDEM is unbiased and to quantify its relative accuracy.

3.1.1 Scheme A: processing of Pléiades images using lidar-derived GCPs

The shaded relief lidar DEM was used as a reference for extracting GCPs (Berthier et al., 2014). The GCPs were typically large boulders surrounding the ice cap and on two of the nunataks exposed within the ice cap. These boulders were chosen as GCPs because they are easily recognized in both the lidar hillshade and the stereo images and because they adequately spread horizontally and vertically throughout the study area (e.g., Nuth and Kääb, 2011). Each pair of Pléiades stereo images was processed separately using the ERDAS Imagine (©Intergraph) software as follows: 40 tie points (TPs) were automatically measured on each stereo pair, and an additional 10 GCPs were manually digitized, five of which were common in the October 2014 and May 2015 Pléiades images. The original image's rational polynomial coefficients (RPCs) were thus refined by including the GCPs and TPs in the bundle adjustment.

After RPC refinement, a DEM was produced from each stereo pair by pixel-based stereo-matching with the routine enhanced automatic terrain extraction (eATE). Images were resampled to twice the native pixel size (i.e., to ~ 1.4 m), which balances the speed of processing and DEM quality. A triangulated irregular network (TIN) was produced from the point cloud and used for sampling a DEM in regular grid spacing of 4×4 m. An orthoimage (0.5×0.5 m pixel size) was also produced from the image closest to nadir of each pair.

Lidar-derived GCPs from ice-free areas have often been used in photogrammetric studies on glaciers (e.g., James et al., 2006; Berthier et al., 2014; Magnússon et al., 2016a). In the case of Pléiades and WorldView, a few GCPs are sufficient to remove most of the horizontal and vertical biases in the resulting DEMs (Berthier et al., 2014; Shean et al., 2016).

3.1.2 Scheme B: processing of Pléiades images with DEM co-registration

In this approach, the DEMs were produced from the pair of stereo images with the original RPCs. This work was carried out with the open source software Ames Stereo Pipeline (ASP, version 2.5.3) developed by NASA (Shean et al., 2016). The processing chain uses the routine *stereo*, producing a point cloud from each pair of stereo images, followed by the routine *point2dem*, which produces a gridded DEM (4×4 m grid size) and an orthoimage (0.5×0.5 m pixel size) for each pair of stereo images.

Areas with thin semitransparent clouds covering the ice cap in the May 2015 Pléiades images (Fig. 2) produced data gaps in the DEM. These image fragments were processed separately and then mosaicked and superimposed over the initial May 2015 Pléiades DEM and orthoimage. The correlation performed in these areas was based directly on the full-resolution images, instead of a pyramidal correlation from subsample images. This improved the correlation (Shean et al., 2016), resulting in full coverage of these areas (Fig. 2).

The snow- and ice-free areas were delineated from the May 2015 Pléiades orthoimage using a binary mask obtained by setting up a cutoff value of < 0.2 for the top of atmo-

sphere absolute reflectance. These images show clear contrast between snow and bare ground (Fig. 2), making image segmentation an efficient approach for the identification of bare ground.

The DEMs were co-registered using the routine *pc_align* in ASP software, based on the iterative closest point (ICP) algorithm for co-registration of two point clouds (Shean et al., 2016). The ICP was performed in two steps: (1) the snow- and ice-free areas of the May 2015 Pléiades DEM were used as a slave DEM, and the entire October 2014 Pléiades DEM was used as a master DEM. A transformation matrix with six parameters (three translations and three rotations) was calculated between the master and slave DEMs. (2) The transformation matrix was applied to the entire May 2015 Pléiades DEM. The applied transformation is quantified by the vector joining the centroids of the May 2015 Pléiades DEM before and after co-registration; this vector has a north component of 8.28 m, a west component of 7.57 m and a vertical component of 12.85 m. A slight planar tilt of 0.002° was corrected between the DEMs.

3.1.3 February 2015 WV2 DEM

The WV2 data was collected and processed as part of the ongoing US National Science Foundation ArcticDEM project. A gridded DEM with 2×2 m grid size was produced with the Surface Extraction with TIN-based Search-space Minimization (SETSM) software (Noh and Howat, 2015), using the RPC sensor model and no GCPs. The 13 February 2015 orthoimage acquired from WV2 was also provided in 2 m pixel size. Since the raw WV2 images were not available in this study, the February 2015 WV2 DEM was co-registered to the October 2014 Pléiades DEM using the ICP algorithm as described in the previous section (scheme B). First, the WV2 DEM, originally in polar stereographic projection, was reprojected and bilinearly resampled to 4×4 m. Then, the ICP algorithm was applied to the ice-free areas from the May 2015 Pléiades orthoimage after manually aligning it to the February 2015 WV2 orthoimage and verifying a similar distribution of snow-free areas between the orthoimages of February and May 2015. The vector joining the centroids of the WV2 DEM before and after co-registration has components 10.32 m to the north, 4.63 m to the east and an 8.81 m shift in the vertical. A slight planar tilt of 0.002° was corrected between the DEMs.

3.1.4 Statistics of elevation differences in snow- and ice-free areas

Statistical indicators of bias and data dispersion were calculated from the dDEM in snow- and ice-free areas using the October 2014 Pléiades DEM as a reference. This included number of cells, median, mean, standard deviation (SD) and normalized median absolute deviation (NMAD, Höhle and Höhle, 2009) over snow- and ice-free terrain. The bare ground areas in the May 2015 images (Fig. 2) were selected for the uncertainty analysis of the dDEM. In the October 2014 Pléiades images, off-glacier snow was on average less than 20 cm thick and therefore negligible in the error analysis (further described in Sect. 4.1).

Since the terrain of the ice cap is substantially different (i.e., much smoother) than its ice-free surroundings, statistics were also calculated after filtering snow- and ice-free areas based on (1) a high slope exclusion filter in which snow- and ice-free areas with slopes $> 20°$ were masked out, as performed in previous similar studies (Magnússon et al., 2016a) acknowledging that only 1 % of the ice cap area exhibits slopes larger than 20°; and (2) a shadow filter in which shadows were masked out from analytical hillshading (Tarini et al., 2006) using the sun position at the time of acquisition for the respective images. Shadows of the October 2014 Pléiades DEM and February 2015 WV2 DEM revealed much higher levels of noise than sun-exposed areas, and were mostly localized on snow- and ice-free areas, covering < 4 % of the ice cap in the February 2015 WV2 DEM.

DEM uncertainty based on SD or NMAD conservatively assumes totally correlated errors in the dDEM (Rolstad et al., 2009). However, the spatial autocorrelation inherent in the DEM may produce substantially lower uncertainty estimates than calculated by simple statistics (Rolstad et al., 2009; Magnússon et al., 2016a). A sequential Gaussian simulation (SGSim) was performed over the masked snow- and ice-free areas (Magnússon et al., 2016a) in order to calculate a likely bias-corrected mean elevation difference on the ice cap.

3.2 Computation of glacier-wide mass balance

Three dDEMs were produced from the different combinations: dDEM_{t1}^{t2}, dDEM_{t2}^{t3} and dDEM_{t1}^{t3}, where $t_1 = 14$ October 2014, $t_2 = 13$ February 2015 and $t_3 = 22$ May 2015 (Fig. 4). The glacier-wide geodetic winter mass balance was calculated as

$$\mathrm{Bw}_{t_1}^{t_f} = \rho_{\mathrm{Snow}t_f} \left(\overline{h}_{\mathrm{dDEM}_{t_1}^{t_f}} + \overline{C_{t_1}^{t_f}} \{h_{\mathrm{Firn}}\} + \overline{C_{t_1}^{t_f}} \{\overline{h}_{\mathrm{Snow}t_1}\} \right), \quad (1)$$

where t_f denotes the date of the last DEMs used and $\overline{h}_{\mathrm{dDEM}}$ is the average elevation change over the ice cap observed from the remote sensing data (dDEMs). The term $\rho_{\mathrm{Snow}t_f}$ is the bulk snow density at the time of the latter DEM, and $\overline{C_{t_1}^{t_f}}$ represents the spatially averaged densification of the firn layer, h_{Firn}, and the fresh snow, $\overline{h}_{\mathrm{Snow}t_1}$, existing on the glacier surface at t_1. The density and firn densification terms are quantified from field measurements (Sect. 3.2.2, 3.2.3 and 3.2.4). The mass balance $\mathrm{Bw}_{t_2}^{t_3}$ is calculated as the difference between $\mathrm{Bw}_{t_1}^{t_2}$ and $\mathrm{Bw}_{t_1}^{t_3}$.

Alternatively, the glacier-wide geodetic winter mass balance can be obtained relative to the summer surface, covered by fresh snow at t_1, assuming that firn or ice does not reap-

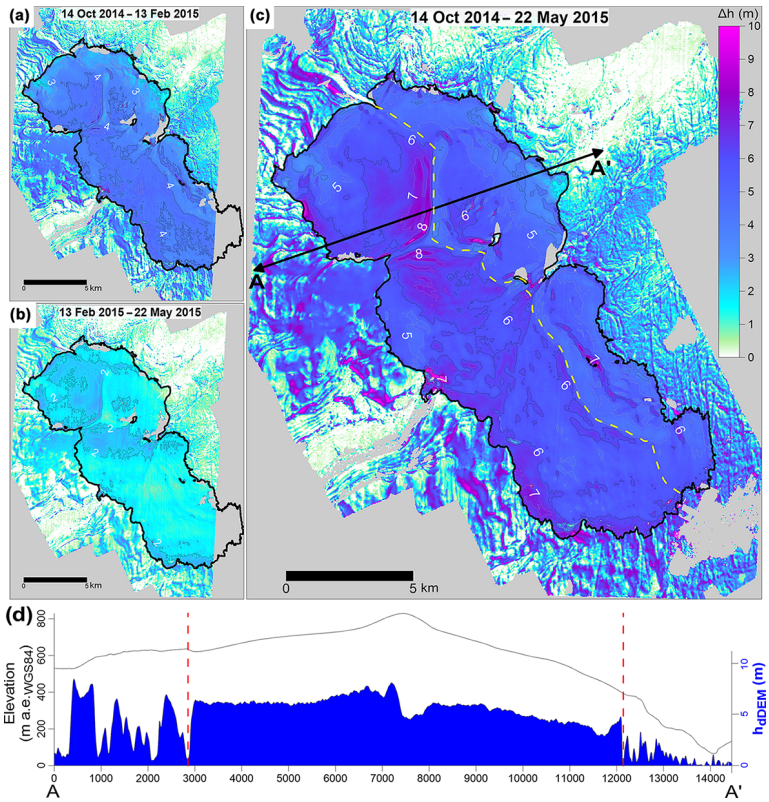

Figure 4. Elevation difference based on Pléiades and WV2 data. **(a)** Elevation difference from October 2014 Pléiades DEM to February 2015 WV2 DEM. **(b)** Elevation difference from February 2015 WV2 DEM to May 2015 Pléiades DEM. **(c)** Elevation difference from October 2014 Pléiades DEM to May 2015 Pléiades DEM. A black polygon indicates the glacier margin in October 2014. The yellow dashed line shows the boundary between the eastern and western halves of the ice cap. Contours on the ice cap were smoothed with a Gaussian filter of 9×9 window size. **(d)** Longitudinal profile A–A′ with surface elevation (black line, in meters above ellipsoid, m a.e.) and snow thickness (blue) over the glacier and ice-free areas. The red dashed lines indicate the location of the glacier margins.

pear on the glacier surface after t_1. This approach results in

$$\mathrm{Bw}^{t_f}_{\mathrm{Summer}} = \rho_{\mathrm{Snow}t_f}\left(\overline{h}_{\mathrm{dDEM}^{t_f}_{t_1}} + \overline{C^{t_f}_{t_1}\{h_{\mathrm{Firn}}\}} + \overline{h}_{\mathrm{Snow}t_1}\right). \quad (2)$$

In this case the date of the summer surface is not fixed, and it can vary over the ice cap (Cogley et al., 2011). This surface is, however, typically used as the reference when obtaining the winter balance from in situ mass balance measurements.

3.2.1 Average elevation change

The average elevation change over the ice cap, $\overline{h}_{\mathrm{dDEM}}$, is extracted from the dDEMs. The extent of the ice cap was digitized from the October 2014 Pléiades orthoimage, following the criteria defined in previous studies (Jóhannesson et al., 2013; Magnússon et al., 2016a) for glacier digitation, which excludes snowfields located at the western and southern sides of the ice cap. We assume that uncertainties in geodetic mass balance caused by digitization of the ice cap outlines are negligible due to the high image resolution.

The data gaps in the dDEMs within the ice cap occur in large shadows north of nunataks in October 2014 and February 2015 and in the south-easternmost part of the ice cap in February 2015 (Fig. 2). These shadows led to $< 1\,\%$ data gaps for $\mathrm{dDEM}^{t_3}_{t_1}$ and $\sim 8\,\%$ gaps for $\mathrm{dDEM}^{t_2}_{t_1}$ and $\mathrm{dDEM}^{t_3}_{t_2}$. The gaps in $\mathrm{dDEM}^{t_3}_{t_1}$ were filled by interpolation of the average elevation difference at 1 pixel surrounding boundary. $\overline{h}_{\mathrm{dDEM}^{t_3}_{t_1}}$ is virtually identical with and without gaps. The $\overline{h}_{\mathrm{dDEM}^{t_2}_{t_1}}$ was extrapolated into $100\,\%$ coverage of the ice cap assuming a linear relation between the average elevation change $\overline{h}_{\mathrm{dDEM}^{t_3}_{t_1}}$ and $\overline{h}_{\mathrm{dDEM}^{t_2}_{t_1}}$ in the overlapping areas

($\sim 92\,\%$ of total area) and in the total ice cap extent, known for $\overline{h}_{\mathrm{dDEM}_{t_1}^{t_3}}$.

3.2.2 Bulk snow density

The average bulk snow density on Drangajökull at the end of the winter 2014–2015 was $\rho_{\mathrm{Snow}t_3} = 554\,\mathrm{kg\,m^{-3}}$ ($\mathrm{SD} = 14\,\mathrm{kg\,m^{-3}}$), as deduced from eight snow cores at elevations ranging from 300 to 920 m a.s.l. This density value is used for conversion of volume to water equivalent for the geodetic winter mass balance calculations based on $\mathrm{dDEM}_{t_1}^{t_3}$. The estimated uncertainty in bulk snow density is $\pm 27\,\mathrm{kg\,m^{-3}}$, obtained from the SD from all available bulk snow density measurements in Drangajökull since the first field campaign in 2005. This error includes the uncertainty in density caused by (1) errors in measurements and (2) likely snow densification between the May 2015 Pléiades images and the June 2015 field campaign.

The midwinter (i.e., 13 February) density of snow is expected to be lower than the bulk snow density measured at the end of the winter. The value $\rho_{\mathrm{Snow}t_2} = 500 \pm 50\,\mathrm{kg\,m^{-3}}$ was adopted for the mass balance calculations based on $\mathrm{dDEM}_{t_1}^{t_2}$. This lower value of the snow density was observed in a few occasions on Drangajökull during early spring measurements (i.e., 2014 field campaign at the end of March, Fig. 7), and its uncertainty is accordingly large due to the lack of measurements.

The bulk density of snow accumulated for the period 3–14 October, $\rho_{\mathrm{Snow}t_1}$, is estimated as $400\,\mathrm{kg\,m^{-3}}$, which is typical for newly fallen snow on ice caps in Iceland (unpublished data, IES). The bulk density of snow fallen after the May Pléiades images is $\rho_{\mathrm{Snow}t_3-t_4} = 515\,\mathrm{kg\,m^{-3}}$, where $t_4 = 19$ June 2015 (date of the in situ measurements). This is estimated as an average value of snow density in the uppermost segment of each core measured in the field.

3.2.3 Firn densification

Densification of the firn layer leads to a continuous lowering of the bottom of the annual snow pack and an underestimate of snow volume changes estimated from the dDEM (Sold et al., 2013). The total area covered by firn at the end of the 2014 ablation season was $91\,\mathrm{km^2}$, or about 64 % of the ice cap, based on the extent of snow in a Landsat 8 image acquired on 16 September 2014 (data available from the US Geological Survey, http://earthexplorer.usgs.gov/). Similar spatial distribution of firn areas are inferred from the map of net annual mass balance of the year 2013–2014, showing 58 % of the ice cap with positive mass balance at the end of the summer.

The 2013–2014 net mass balance distribution was used to correct for firn densification, assuming this was a typical year of mass balance for Drangajökull. The net annual surface elevation change due to firn densification vertically integrated over the entire firn column should correspond to the average annual accumulation layer transformed from end-of-the-year snow density to ice (Sold et al., 2013), as

$$\overline{C_{\mathrm{ann}}}\{h_{\mathrm{Firn}}\} = \frac{b_{n+}}{\rho_{\mathrm{Firn_u}}} - \frac{b_{n+}}{\rho_{\mathrm{Firn_l}}}, \tag{3}$$

where b_{n+} is the mass balance of 2013–2014 (in units of $\mathrm{kg\,m^{-2}}$) over the accumulation area (positive, by definition), and $\rho_{\mathrm{Firn_u}}$ and $\rho_{\mathrm{Firn_l}}$ are the upper and lower values of density of the firn profile, estimated as $\rho_{\mathrm{Firn_u}} = 600\,\mathrm{kg\,m^{-3}}$ and $\rho_{\mathrm{Firn_l}} = 900\,\mathrm{kg\,m^{-3}}$. These values of density in the firn layer are consistent with the literature (Cuffey and Paterson, 2010) and with a measured deep density profile obtained on Hofsjökull ice cap in central Iceland (Thorsteinsson et al., 2002). For simplicity, the firn densification was distributed linearly over the time span covered (0.603 year for t_1^3 and 0.334 year for t_1^2), under the assumption that the firn densification does not vary seasonally. Slight variations can occur in the firn densification process through time, due to accumulation variability and rain – and meltwater percolation (Ligtenberg et al., 2011). The mean values of the firn densification maps, 0.41 and 0.23 m for t_1^3 and t_1^2 respectively, were scaled by the firn area within the ice cap in order to calculate the glacier-wide $\overline{C_{t_1}^{t_f}}\{h_{\mathrm{Firn}}\}$.

The above quantification of the firn densification is based on the mass balance measured extensively during a single year (2013–2014) and assumes equal net accumulation between years as well as a constant densification rate within the glaciological year. An uncertainty of 50 % in the firn correction was used for the error budget of the mass balance (Table 3), due to the assumptions and approximations involved in this method.

3.2.4 Fresh snow densification in the reference DEM

The October 2014 Pléiades DEM, used as a reference for the winter mass balance calculations, contains the first two snowfalls of the winter (Fig. 2), starting on 3 October. This thin snow layer densifies over time from settling, rainfall and compression (e.g., Ligtenberg et al., 2011), causing a lowering of the reference surface and leading to an underestimation of the total winter snow. The snow densification correction was calculated as

$$\overline{C_{t_1}^{t_f}}\left\{\overline{h}_{\mathrm{Snow}\,t_1}\right\} = \frac{W_{t_1}}{\rho_{t_1}} - \frac{W_{t_1}}{\rho_c}, \tag{4}$$

where W_{t_1} is the average thickness of the fresh snow (in m w.e.) at t_1 and ρ_c is the bulk density of same snow layer at time t_f, assuming that the entire fresh snow layer at $\mathrm{t_1}$ is preserved during the period t_1 to t_f. ρ_c is estimated as $600\,\mathrm{kg\,m^{-3}}$ for both $\mathrm{Bw}_{t_1}^{t_2}$ and $\mathrm{Bw}_{t_1}^{t_3}$. The first term on the right hand side of Eq. (4) corresponds to the $\overline{h}_{\mathrm{Snow}t_1}$, which is spatially averaged in Eq. (2). The value of W_{t_1} at a given

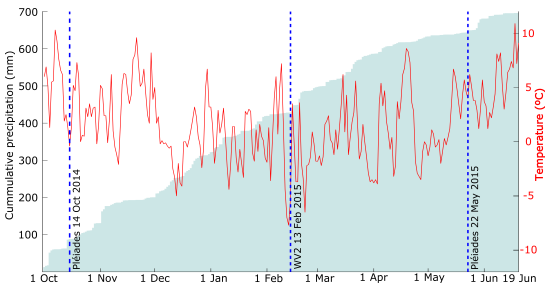

Figure 5. Cumulative precipitation (clear blue) and temperature (red line) for the winter 2014–2015 (1 October 2014 to 19 June 2015) from the station Litla Ávík. Blue dashed lines show the time of acquisition of satellite stereo images.

location was estimated as

$$W_{t_1} = \sum_{t=t_{\text{firstsnow}}}^{t_1} \left(\alpha\left(t\right) P\left(t\right) - \beta\left(t\right) \text{ddf} T_+(t)\right), \quad (5)$$

where P is daily precipitation (in m) and T_+ is average daily temperature for days when it is above 0 °C, but otherwise $T_+ = 0$ °C. α is a snow fall switch, taking the value 1 only if average daily temperature is below 1 °C, otherwise it is 0. $\beta\left(t^*\right)$ takes the value 1 if W_{t^*-1} is positive but is 0 otherwise to avoid accumulation of negative new snow. ddf is a simple degree-day melt factor for snow assumed to be 0.0055 m w.e. °C^{-1}, as obtained for snow on Langjökull ice cap, central Iceland (Guðmundsson et al., 2009).

The daily precipitation values P were obtained by scaling the daily precipitation values from LÁ for each in situ location by comparison of the net precipitation at LÁ through the entire winter ($P_{\text{LÁ}} = 0.684$ m, Fig. 5) and the measured accumulation at each in situ location, resulting in a scaling factor between ∼ 2 (V1, $\text{bw}_{2014\text{–}2015} = 1.54$ m w.e.) and ∼ 7 (V6, $\text{bw}_{2014\text{–}2015} = 4.93$ m w.e.). This assumes that all precipitation that falls on the ice cap through the winter remains in the snowpack, including rain, which is assumed to percolate into the cold snow pack where it refreezes as internal ice layers. The daily temperature values, T, were obtained for each in situ location by projecting temperature records from LÁ, using an elevation lapse rate of −0.006 °C m^{-1}, as has been measured for Langjökull ice cap (Guðmundsson et al., 2009).

The values of W_{t_1} and consequently $h_{\text{Snow}t_1}$ were obtained at each in situ site and averaged to obtain the glacier-wide $\overline{C_{t_1}^{t_f}}\,\overline{h}_{\text{Snow}t_1}$ and $\overline{h}_{\text{Snow}t_1}$ for Eqs. (1) and (2) respectively. The in situ locations are fairly evenly distributed over the elevation range of the ice cap and are therefore considered to be representative of the glacier-wide calculations. Based on the observed temporal and spatial variability, we conservatively estimate the uncertainties of $\overline{h}_{\text{Snow}t_1}$ and $\overline{C_{t_1}^{t_f}}\,\overline{h}_{\text{Snow}t_1}$ to be 50 and 75 %, respectively.

3.2.5 Error propagation

Assuming that the variables in Eq. (1) are not correlated to one another, the error in the mass balance calculation is obtained by

$$\Delta\text{Bw} = \sqrt{\left(\frac{\partial\text{Bw}}{\partial\rho_{\text{Snow}}}\Delta\rho_{\text{Snow}}\right)^2 + \left(\frac{\partial\text{Bw}}{\partial\overline{h}_{\text{dDEM}}}\Delta\overline{h}_{\text{dDEM}}\right)^2 + \left(\frac{\partial\text{Bw}}{\partial\overline{C}\,\Delta h_{\text{Firn}}}\Delta\overline{C}\left\{h_{\text{Firn}}\right\}\right)^2 + \left(\frac{\partial\text{Bw}}{\partial\overline{C}\,\overline{h}_{\text{Snow}t_1}}\Delta\overline{C}\left\{\overline{h}_{\text{Snow}t_1}\right\}\right)^2}, \quad (6)$$

where $\Delta\rho_{\text{Snow}}$ is the uncertainty in bulk snow density, $\Delta\overline{h}_{\text{dDEM}}$ is the uncertainty in average elevation change obtained from dDEM, $\Delta\overline{C}\left\{h_{\text{Firn}}\right\}$ is the uncertainty in firn correction and $\Delta\overline{C}\left\{\overline{h}_{\text{Snow}t_1}\right\}$ is the uncertainty in snow correction for the reference DEM. Table 2 summarizes the values and uncertainties of each variable affecting the calculation of the geodetic winter mass balance. The uncertainty of $\text{Bw}_{t_2}^{t_3}$ is calculated as the quadratic sum of uncertainties of $\text{Bw}_{t_1}^{t_2}$ and $\text{Bw}_{t_1}^{t_3}$. The error equation for Eq. (2) is analogous to Eq. (5), replacing the term $\Delta\overline{C}\left\{\overline{h}_{\text{Snow}t_1}\right\}$ by $\Delta\overline{h}_{\text{Snow}t_1}$.

3.3 Comparison of Pléiades-based elevation changes and in situ measurements

For validation of results, the elevation difference at the in situ locations was extracted using bilinear interpolation from dDEM_{t1}^{t3} from scheme A, since this scheme is fixed to the same reference frame as the in situ GPS coordinates (lidar frame, Fig. 3). The resulting elevation difference, $h_{\text{dDEM}_{t1}^{t3}}$ was compared with the snow thickness, $h_{\text{Snow in situ}}$, measured at the in situ locations in the 2015 campaign.

Three main factors cause differences in results between the remote sensing and the glaciological method (Sold et al., 2013): (1) the time difference between the DEMs and in situ surveys, (2) firn densification and (3) surface emergence or submergence due to ice dynamics. The corrected satellite-based elevation difference cdDEM_{t1}^{t3} for comparison to in situ data is

$$\text{cdDEM}_{t_1}^{t_3} = h_{\text{dDEM}_{t_1}^{t_3}} + C\left\{h_{\text{Firn}}\right\} + h_{\text{Snow}t_1} + h_{\text{Snow}t_3-t_4} + \text{d}h_{\text{dyn}}, \quad (7)$$

where $C\left\{h_{\text{Firn}}\right\}$ is the correction due to firn densification (Sect. 3.2.3) and $h_{\text{Snow}_{t_1}}$ is the correction due to snow accumulated before t_1 (Sect. 3.2.4). $h_{\text{Snow}t_3-t_4}$ is the correction for snow accumulation and ablation between t_3 (the 22 May Pléiades DEM) and the in situ snow thickness measurements, calculated in the same way as $h_{\text{Snow}t_1}$, using $\rho_{\text{Snow}t_3-t_4}$ and allowing for net negative values (i.e., the switch β in Eq. 5 is omitted). $\text{d}h_{\text{dyn}}$ is the surface emergence and submergence due to ice dynamics (Sect. 3.3.1). The magnitude/sign of these corrections differ between the accumulation and ablation areas (Fig. 6).

Table 2. Statistical analysis of the dDEMs in snow- and ice-free areas, and mean elevation difference on the ice cap, $\overline{h}_{\mathrm{dDEM}}$. N represents number of data points. The three bottom rows indicate the statistics after masking slopes $> 20°$ and shadows. Bias-corrected SGSim represents the mean elevation bias from 1000 simulations and the standard deviation of the simulations (details in Magnússon et al., 2016a).

	Scheme	N ($\times 10^6$)	Gaps ice cap (%)	Mean (m)	Median (m)	SD (m)	NMAD (m)	$\overline{h}_{\mathrm{dDEM}}$ (m)	Bias-corrected $\overline{h}_{\mathrm{dDEM}}$SGSim (m)
Raw snow–ice-free	A – lidar GCPs (Oct 2014 Pléiades minus May 2015 Pléiades DEM)	2.2	3.9 %	−0.16	−0.10	1.12	0.48	5.40	–
	B – ICP (Oct 2014 Pléiades minus May 2015 Pléiades DEM)	2.6	0.8 %	−0.06	−0.02	1.27	0.33	5.58	–
	WV2 ICP (Oct 2014 Pléiades minus Feb 2015 WV2 DEM)	2.4	8.2 %	0.14	0.05	1.17	0.47	3.84	–
Slopes & shadows mask	A – lidar GCPs (Oct 2014 Pléiades minus May 2015 Pléiades DEM)	1.4	6.2 %	−0.08	−0.05	0.49	0.35	5.36	5.61 ± 0.09
	B – ICP (Oct 2014 Pléiades minus May 2015 Pléiades DEM)	1.6	2.4 %	−0.07	−0.02	0.66	0.23	5.59	5.71 ± 0.10
	WV2 ICP (Oct 2014 Pléiades minus Feb 2015 WV2 DEM)	1.0	10.4 %	0.08	0.01	0.54	0.35	3.84	–

3.3.1 Ice dynamics

We compare two methods for estimating the effect of ice dynamics on local surface elevation change, $\mathrm{d}h_{\mathrm{dyn}}$, during the study period (e.g., Jarosch, 2008; Sold et al., 2013):

The emergence and submergence velocities $\mathrm{d}h_{\mathrm{dyn\ icetools}}$ were calculated using a full-Stokes ice flow model with the icetools library (Jarosch, 2008) and the finite element package, Fenics. The model calculates a 3-D velocity field resulting from the ice deformation, given the glacier geometry. The bedrock DEM (Magnússon et al., 2016b) and the October 2014 Pléiades DEM were used as inputs. The 2-D horizontal velocities measured with GPS in the 2013–2014 field campaigns were used to calibrate the ice flow rate factor, A. The annual emergence and submergence velocities across the ice cap were computed on a 200 m regular grid and scaled by 0.603, a factor to represent the time span $t_1 - t_3$ (14 October to 22 May), assuming constant velocities through the glaciological year.

Assuming that the glacier is in a steady state, the long-term average surface net balance (divided by the density of ice) equals in magnitude to the emergence and submergence velocities across the glacier (Sold et al., 2013). Acknowledging that there is significant year-to-year variability in surface net mass balance, the net mass balance measurements from the year 2013–2014, scaled by the water ($1000\,\mathrm{kg\,m^{-3}}$) to ice ($900\,\mathrm{kg\,m^{-3}}$) conversion factor, were assumed to be representative of local annual emergence and submergence velocities. The obtained values at the in situ locations were then scaled to represent $\mathrm{d}h_{\mathrm{dyn\ bn2013–2014}}$ over the time span $t_1 - t_3$.

4 Results

4.1 Uncertainty on elevation difference derived from satellite data

The statistics obtained from the dDEMs in snow- and ice-free areas (Table 2) allow for a quantitative comparison of the different methods and datasets used in the study. The statistics show smaller SDs and NMADs outside of the areas of high slopes and shadows due to the dependency of the DEM accuracy on the steepness of the terrain (Toutin, 2002; Müller et al., 2014; Lacroix, 2016; Shean et al., 2016) and the presence of shadows (Shean et al., 2016; Table 2). The vertical bias obtained after DEM co-registration ranges from 0 to 0.1 m based on the median, and the NMAD reveals random errors < 0.5 m in both schemes A and B as well as in the co-registered WV2 DEM. Both schemes yield a similar result for elevation difference, $\overline{h}_{\mathrm{dDEM}}$, on the ice cap. Details on the distribution of errors in the snow- and ice-free areas, as well as histograms of the distribution, are presented in the Supplement.

The thin layer of snow in the October 2014 Pléiades images (Fig. 2) could slightly skew the statistics. The snow thickness is expected to be less than 20 cm outside the ice cap based on snowfall observations on 13 October at locations V1, V2 and V5 (the closest in situ locations to the ice-free areas, Fig. 1), ranging from 0.13 m at V1 (291 m a.s.l.) to 0.27 m at V2 (668 m a.s.l.). The snow line was observed at an elevation of ~ 50 m a.s.l. in the October 2014 Pléiades images, and the majority (> 60 %) of the cells used for the statistics are at a lower elevation than V1.

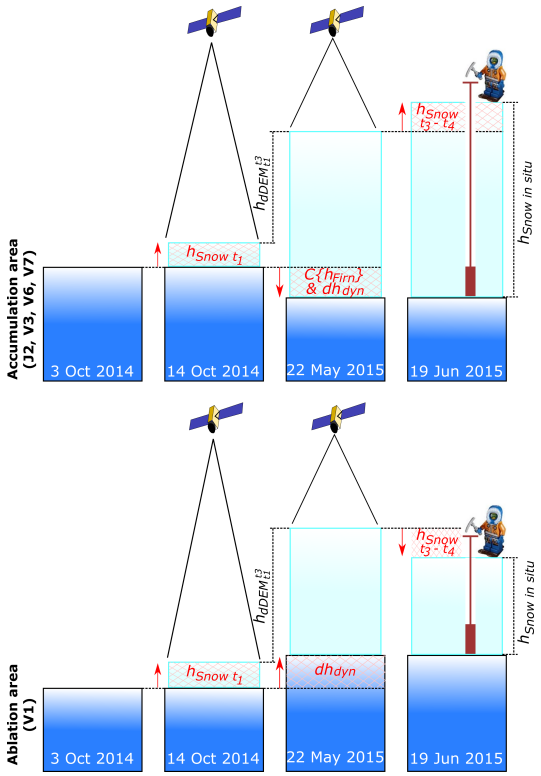

Figure 6. Sketch of the different factors, marked in red and indicated with red arrows, affecting the comparison between the glaciological (3 October 2014–19 June 2015) and geodetic (14 October 2014–22 May 2015) methods. Light blue represents snow fallen in winter, and dark blue represents preexisting ice and firn.

The results obtained from SGSim provide an uncertainty estimate of 95 % for the dDEM on the ice cap. The SGSim results from both schemes agree well and are within the uncertainty obtained from NMAD in the snow- and ice-free areas, which further supports the robustness of the two methods of DEM processing. All proxies used show almost no bias in the dDEMs (Table 2). The NMAD was kept as a conservative metric for dDEM uncertainty, since the presence of snow in the October 2014 Pléiades images may have affected the results from the SGSim in presumed snow- and ice-free areas, especially in close vicinity of the ice cap, leading to an erroneous bias estimate on the ice cap.

4.2 Maps of elevation differences and glacier-wide mass balance

Schemes A and B lead to similar elevation differences and uncertainty based on statistical analyses (Table 2). Since it contains fewer data gaps, scheme B was preferred for producing elevation difference maps (Fig. 4) and for the study of volume changes and the geodetic mass balance. The firn and fresh snow densification lead to a minor addition (~ 8 %) to the elevation difference, $\overline{h}_{\mathrm{dDEM}}$ (Table 3). Hence, the maps of dDEMs themselves reveal useful and realistic information about the pattern of snow accumulated in Drangajökull and surroundings (Fig. 4). The western half of the ice cap received more snow than the eastern half, with an average elevation difference $\overline{h}_{\mathrm{dDEM}} = 5.91$ m between October 2014 and May 2015, in comparison with the eastern half, $\overline{h}_{\mathrm{dDEM}} = 5.03$ m, during the same period, as suggested in Magnússon et al. (2016a). Significant snow accumulation was also observed in several snowfields outside the ice cap between October 2014 and May 2015.

The glacier-wide geodetic winter mass balance is $\mathrm{Bw} = 3.33 \pm 0.23$ m w.e. for the period 14 October 2014–22 May 2015, calculated from Eqs. (1) and (5). The mass balances obtained for the two periods of the same winter are $\mathrm{Bw} = 2.08 \pm 0.28$ m w.e. (14 October 2014 to 13 February 2015) and $\mathrm{Bw} = 1.26 \pm 0.37$ m w.e. (13 February to 22 May 2015). The glacier-wide geodetic winter mass balances from the start of the glaciological year, obtained from Eqs. (2) and (5), are $\mathrm{Bw} = 3.55 \pm 0.27$ m w.e. for the period 3 October 2014–22 May 2015, and $\mathrm{Bw} = 2.27 \pm 0.31$ m w.e. was calculated from 3 October 2014 to 13 February 2015. We quantify the error of each calculated mass balance and determine the weight of each variable from Eq. (5) in the total error budget (Table 3).

4.3 Pléiades vs. in situ data

As expected, the in situ measurements of snow thickness yield substantially higher values than the uncorrected difference in elevation measured from $\mathrm{dDEM}_{t_1}^{t_3}$ (May 2015 Pléiades DEM minus October 2014 Pléiades DEM) in the accumulation area (Fig. 6), with an average difference of 2.56 m for points V3, V6, V7 and J2. Conversely, at Point V1 in the ablation area, the in situ measurements of snow thickness are lower (difference of -0.98 m) than the difference in elevation from $\mathrm{dDEM}_{t_1}^{t_3}$. The areas closer to the ELA (points V2, V4 and V5, Fig. 1) show better agreement between glaciological and remote sensing methods before applying corrections (Table 4).

The estimated corrections applied for calculating $\Delta\mathrm{dDEM}_{t_1}^{t_3}$ are summarized in Table 4. Each correction has a different impact on the overall comparison, depending on the location of the in situ measurement. The highest corrections were estimated from ice dynamics deduced from the records of mass balance, $dh_{\mathrm{dyn\ bn}}$, reaching up to 1.69 m of emergence at location V1 in the lower part of the ablation area. Corrections typically span from 0 to 1 m (Table 4).

The estimated correction for the snowfall and ablation in the time difference between the beginning of winter (3 October) and the first satellite acquisition (14 October), $h_{\mathrm{Snow}t_1}$, assumes the start of winter with the first snowfall, on 3 Oc-

Table 3. Glacier-wide geodetic winter mass balance and associated error, calculated from Eq. (1). The elevation difference, $\overline{h}_{\mathrm{dDEM}}$, is observed from remote sensing data, while the bulk snow density (ρ_{Snow}) and densification of firn ($\overline{C}\{h_{\mathrm{Firn}}\}$) and fresh snow ($\overline{C}\{\overline{h}_{\mathrm{Snow}t_1}\}$) are inferred values from field measurements. For each variable its value and the associated error are shown, and in the row below its conversion into mass balance is shown. $\Delta\mathrm{Bw}_{\rho_{\mathrm{Snow}}}$ shows the contribution of the bulk snow density into the uncertainty in the mass balance. The total uncertainty of Bw is computed as the quadratic sum of the uncertainty (in m w.e.) of the elevation difference, firn and fresh snow densification, and bulk snow density.

Time period	ρ_{Snow} (kg m^{-3})	$\overline{h}_{\mathrm{dDEM}}$	$\overline{C}\{h_{\mathrm{Firn}}\}$	$\overline{C}\{\overline{h}_{\mathrm{Snow}\,t_1}\}$	$\Delta\mathrm{Bw}_{\rho_{\mathrm{Snow}}}$ (m w.e.)	Bw (m w.e.)
t_1^3 (14 Oct 2014–22 May 2015)	554 ± 27	5.58 ± 0.23 m 3.09 ± 0.13 m w.e.	0.24 ± 0.12 m 0.13 ± 0.07 m w.e.	0.20 ± 0.15 m 0.11 ± 0.08 m w.e.	0.16	3.33 ± 0.23
t_1^2 (14 Oct 2014–13 Feb 2015)	500 ± 50	3.82 ± 0.35 m 1.91 ± 0.18 m w.e.	0.13 ± 0.07 m 0.07 ± 0.03 m w.e.	0.20 ± 0.15 m 0.10 ± 0.07 m w.e.	0.21	2.08 ± 0.28

tober 2014. However, imagery from Landsat and MODIS reveal ice on the low glacier areas in the days before the snowfall on 13 October 2014. At this location it was therefore assumed that the later snowfall marked the beginning of the winter (Table 4).

The mean difference between the in situ measurements and the difference in elevation from $\mathrm{dDEM}_{t_1}^{t_3}$ is 1.34 m (SD = 1.43, $N = 8$). The mean difference and its standard deviation are significantly reduced after applying the corrections, obtaining a mean difference of 0.52 m (SD = 0.46) when calculating $\Delta\mathrm{dDEM}_{t_1}^{t_3}$ using $\mathrm{d}h_{\mathrm{dyn\ icetools}}$ and a mean of 0.34 m (SD = 0.64) when calculating $\Delta\mathrm{dDEM}_{t_1}^{t_3}$ using $\mathrm{d}h_{\mathrm{dyn\ bn2013–2014}}$.

5 Discussion

5.1 Pléiades and WorldView DEMs for measuring snow accumulation

We measure the glacier-wide geodetic mass balance during the winter of 2014–2015, as well as two sub-periods of the same winter, by differencing DEMs obtained from satellite data. In our calculations, we incorporate corrections for snow density and densification of firn and fresh snow, based on in situ measurements. This technique can be applied in small and medium size glaciers (typically $\sim 1000\,\mathrm{km}^2$ can be stereoscopically covered at once based on the capabilities of Pléiades and WorldView), with sufficiently high mass balance amplitude (~ 0.5–1 m w.e. or higher). The main advantages of using stereoscopic satellite images are repeatability and coverage of remote glaciated areas. The use of external reference data for bundle adjustment prior to stereo correlation, such as lidar-based or GPS-based GCPs, does not improve the relative accuracy of the Pléiades and WorldView DEMs used here (Table 2).

Combining data from Pléiades and WorldView allows for high spatial resolution within a short (3–4 month) interval. The availability of these data and the presented processing strategy allow, to our knowledge, for the first optical satellite-based measurement of winter accumulation on a glacier. Both sensors result in a similar level of accuracy (Table 2) and their combination enables more detailed studies of glacier changes. The ArcticDEM project (data available at http://arcticdemapp.s3-website-us-west-2.amazonaws.com/explorer/) freely offers multi-temporal DEMs of the Arctic region collected since ~ 2010 with dense temporal repetition (more than 30 DEMs during the last 6 years in certain regions of Greenland, e.g., Willis et al., 2015), therefore providing a high potential for similar studies of geodetic mass balance on seasonal timescales.

The two DEM processing schemes have advantages and disadvantages. Scheme A provides DEMs, orthoimages and dDEMs in an absolute reference system, based on a geodetic network where the lidar DEM is fixed (or similar if GPS-based GCPs are used). This scheme is appropriate when limited unchanged areas are available or if there are identifiable features for extraction of GCPs. This approach, however, requires external spatial information and tedious manual GCP selection. Scheme B uses a highly automated workflow and is independent of spatial information other than the satellite images and camera model information. Co-registration based on scheme B, while ideally requiring well-distributed static control surface, can be applied with an adequate distribution of slope and aspect over limited control surfaces (Shean et al., 2016). The three different processing software (ERDAS Imagine, ASP and SETSM) provided satisfactory results for obtained dDEMs.

5.2 Correction of physical glacier phenomena for calculating geodetic winter mass balance

In addition to the remote sensing data, the in situ measurements of the bulk snow density and the densification of the firn layer and fresh snow are needed to retrieve the glacier-wide geodetic winter mass balance (Eqs. 1 and 2). Ice dynamics do not affect the glacier-wide geodetic winter mass balance due to mass conservation (Cuffey and Paterson, 2010).

Table 4. Comparison of values of snow thickness, $h_{\text{snow insitu}}$, measured in the field, and elevation difference obtained from Pléiades DEMs, $h_{\text{dDEM}_{t_1}^{t_3}}$. The table lists all corrections applied pointwise to the Pléiades elevation differences $\text{dDEM}_{t_1}^{t_3}$ to make them comparable to the in situ measurements (see text for details). The table also compares two approaches carried out for correction of surface emergence and submergence velocities: (1) $\text{d}h_{\text{dyn icetools}}$ using a glacier ice flow model (Jarosch, 2008) and (2) $\text{d}h_{\text{dyn bn2013–2014}}$ using records of mass balance (Sold et al., 2013). $c_1\text{dDEM}_{t_1}^{t_3}$ and $c_2\text{dDEM}_{t_1}^{t_3}$ show the corrected $\text{dDEM}_{t_1}^{t_3}$, using the two different approaches, and Res_1 and Res_2 are the residuals between the glaciological and geodetic methods after applying the corrections.

	h_{Snow} in situ (m)	$h_{\text{dDEM}_{t_1}^{t_3}}$ (m)	$C\{h_{\text{Firn}}\}$ (m)	h_{Snow} t_1 (m)	h_{Snow} $t_3 - t_4$ (m)	$\text{d}h_{\text{dyn}}$ icetools (m)	$c_1\text{dDEM}_{t_1}^{t_3}$ (m)	Res_1 (m)	$\text{d}h_{\text{dyn}}$ bn2013–2014 (m)	$c_2\text{dDEM}_{t_1}^{t_3}$ (m)	Res_2 (m)
V1	2.90	3.88	0.00	0.13	−0.95	−0.51	2.55	0.35	−1.69	1.37	1.53
V2	5.63	5.34	0.00	0.28	−0.25	−0.50	4.87	0.76	−0.88	4.49	1.14
V3	8.38	5.86	0.58	0.84	0.21	0.10	7.58	0.80	1.16	8.64	−0.26
V4	4.95	4.18	0.13	0.62	0.13	0.21	5.26	−0.31	0.25	5.31	−0.36
V5	5.68	5.32	0.00	0.35	−0.08	−0.09	5.50	0.18	−0.07	5.52	0.16
V6	8.60	5.67	0.50	0.80	0.24	0.02	7.23	1.37	1.00	8.20	0.40
V7	8.09	5.21	0.44	0.91	0.29	0.70	7.55	0.54	0.88	7.73	0.36
J2	7.60	5.67	0.41	0.77	0.17	0.12	7.14	0.46	0.81	7.83	−0.23
Abs mean			0.26	0.59	0.29	0.28			0.84		

The sensitivity of the mass balance calculation was tested with different snow densities measured during the 2005–2014 field campaigns in Drangajökull (Fig. 7). The glacier-wide geodetic winter mass balance is reduced by 1 % when the average of all previous density records is used instead of the mean 2015 bulk snow density. The minimum average bulk snow density recorded (511 kg m^{-3} in 2011) results in 8 % lower mass balance, and the maximum average bulk snow density recorded (583 kg m^{-3} in 2008) results in a 5 % higher mass balance. We obtained similar discrepancies by using snow density records from other Icelandic ice caps. Bulk snow density measured on Mýrdalsjökull ice cap in 2010 (Ágústsson et al., 2013) and on Langjökull ice cap in 2015 produced a 3 and 10 % overestimation and underestimation of mass balance, respectively.

Bulk snow density can vary substantially between different glaciers or between different years in the same area. Individual years, however, show relatively low scatter of bulk snow density distribution over the different in situ locations on Drangajökull (Fig. 7). The low scatter indicates that bulk snow density measurements taken at one or many points on a date close to that of the satellite acquisitions, if adequately selected for the whole ice cap, should give reasonable results for glacier-wide geodetic winter mass balance calculations.

The firn densification model assumes a temporally constant annual mass balance in the accumulation area, which is a significant source of uncertainty due to high inter-annual climate variability. Other methods can be used for a more accurate correction for firn densification, such as deep core drilling (Thorsteinsson et al., 2002), or robust firn layer observations and modeling (e.g., Sold et al., 2015). For large areas, such as catchments of the Greenland Ice Sheet, a firn densification model such as IMAU-FDM (Ligtenberg et al., 2011), forced by a surface mass balance model such as the RACMO2.3 (Noël et al., 2015) can also be applied. However, the resolution (typically 11 km) of these models may be too coarse to resolve a relatively small Icelandic ice cap such as Drangajökull.

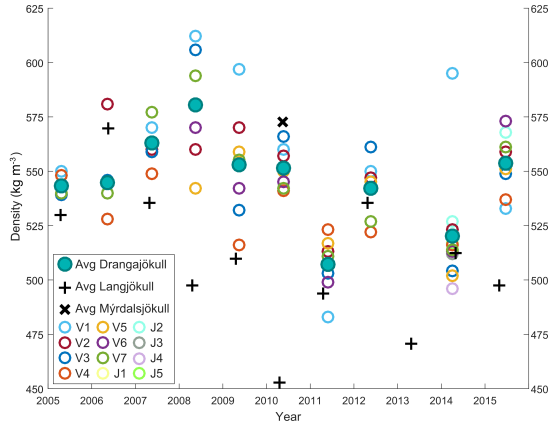

Figure 7. The density values obtained at each in situ location for field campaigns 2005–2015. Each circle represents the average density of the shallow core at each in situ location. Blue filled circles show the average density measurements. Black "+" shows the averaged density measured on Langjökull, and black "×" shows the averaged density measured on Mýrdalsjökull ice cap in year 2010 (Ágústsson et al., 2013). The 2013 campaign was not carried out due to bad weather conditions.

The densification caused by fresh snow potentially present at the time of acquisitions of the reference (initial) DEM needs to be studied differently for each case and will depend

on the amount of snow falling between the beginning of the glaciological winter and the satellite acquisition. If satellite images are acquired prior to the start of the winter, this effect disappears, and a correction due to surface melt should be assessed (e.g., by using a degree-day model as in Eq. 5). Densification of fresh snow corrected by Eq. (1) leads to smaller uncertainty than shifting the mass balance to the beginning of the season using Eq. (2), and the uncertainty associated with Eq. (2) will increase with the length of the time period from the start of the winter to t_1.

Firn and fresh snow densification have little effect on the geodetic winter mass balance, increasing it by 8 % (Table 3), indicating that even if these variables remain unknown (i.e., in remote areas), adequate calculations of geodetic mass balance can be performed with moderately increased uncertainties, ranging between 5 and 10 % for glaciers with mass balance amplitude similar to Drangajökull. The error in geodetic mass balance is primary controlled by our knowledge of physical glacier phenomena (bulk snow density and densification of firn and fresh snow) and, to a lesser degree, by the accuracy of the derived maps of elevation differences from the satellite data (Table 3).

5.3 Validation of results: remote sensing vs. in situ

The glacier-wide geodetic mass balances suggest that ∼ 60 % of the winter accumulation occurred during the first 4 months of the winter (14 October 2014–13 February 2015, Table 3). Precipitation records at a weather station ∼ 40 km from the ice cap indicate the same ratio of accumulation for the two time periods: 342 mm (62 % of total) between 14 October 2014 and 13 February 2015 and 218 mm (38 % of total) between 13 February and 22 May 2015 (Fig. 5). The consistency of the ratio of accumulation in the two sub-periods observed at the weather station and calculated from the satellite images is encouraging and also supports the applicability of the corrections applied due to differences in time between in situ and geodetic mass balance observations.

The temporal offset between the glaciological and the geodetic measurements results in some ambiguity in the definition of the beginning and end of the mass balance season. Glaciological measurements generally use the previous summer layer as reference, which ensures a well-defined starting point of the mass balance year, despite the fact that the date chosen for the spring campaign (i.e., the winter balance end date) is not objectively defined. For example, two snow events occurred in late May and early June, which can either be considered part of the winter or summer balance seasons. The timing of remote sensing surveys are further dependent on sensor tasking and favorable weather (cloud-free) conditions, and, as a consequence, a temporal offset between glaciological and geodetic observations is likely to occur.

The points V1–V4 are located at Leirufjarðarjökull (Fig. 1), a surge-type glacier (Björnsson et al., 2003; Brynjólfsson et al., 2016). The dynamics of this glacier outlet are, by nature, not in balance with the rate of accumulation or ablation, and thus the calculation of emergence and submergence velocities from the net annual mass balance is inappropriate at these locations. On the other hand, an underestimation of submergence velocities is observed over the southern areas using the full-Stokes ice flow model, possibly explained by the lack of basal sliding in the ice flow model. Only minor elevation changes were detected in this part of the glacier in the past decades (Magnússon et al., 2016a), and it is not known to surge; hence, the net annual mass balance approach may be more suitable in this area.

6 Conclusions

This study shows the capabilities of sub-meter satellite stereo images for measuring winter mass balance. The DEMs created from Pléiades and WV2 satellite stereo images reveal relative accuracy of 0.2–0.3 m (for slopes $< 20°$), which allows measuring the evolution of snow accumulation in two periods of the winter on Drangajökull ice cap. Two methodologies used for the processing of DEMs yield similar accuracy and elevation changes with and without using GCPs, showing that the processing of modern sub-meter satellite stereo images for measuring glacier elevation change can be performed without external reference data, such as lidar or GPS data, as long as areas of stable (snow- and ice-free) terrain are present in the imagery to serve as relative control.

The glacier-wide geodetic winter mass balance was 3.33 ± 0.23 m w.e. for 14 October 2014–22 May 2015, with ∼ 60 % of the accumulation occurring between 14 October 2014 and 13 February 2015. Besides the remote sensing observations, the glacier-wide geodetic winter mass balance calculation requires knowledge of the bulk snow density for volume to water equivalent conversion and a correction for firn and fresh snow densification, which are estimated in this study from in situ measurements. The uncertainty in the bulk snow density is the largest contributor to the uncertainty in glacier-wide geodetic winter mass balance and is significantly larger than the uncertainty in the average elevation change and the firn and fresh snow densification.

Densification of firn and fresh snow produces a systematic but minor (8 %) increase to the mass balance obtained from the geodetic method. This contribution may vary for individual cases depending on the climatic conditions and the timing of snowfall events relative to reference (i.e., start of winter) image acquisition. Uncertainties in geodetic winter mass balance can be minimized with records of bulk snow density and previous years' mass balance. Extrapolation of snow density from other glaciers with different characteristics can, however, lead to slightly larger errors (up to 10 %).

The satellite-derived map of elevation change and eight in situ measurements of snow thickness are in agreement after correcting for three phenomena of sub-meter to meter-level elevation change: (1) the difference in time between

in situ campaigns and satellite acquisitions, (2) the effect of firn densification in the accumulation area and (3) the vertical component of the ice flow motion. While glacier winter mass balance measurements have been sparse due to the difficulty in obtaining field measurements and the low contrast of snow-covered terrain preventing photogrammetric surveying, we demonstrate that sub-meter satellite imagery may offer a powerful new tool for glacier mass balance monitoring on sub-annual timescale. The potential for this approach is enhanced by the rapid increase and availability of optical satellites collecting stereo images in glaciated regions with dense temporal resolution. Due to the relative accuracy of the DEMs and uncertainties in snow density and firn and fresh snow densification, repeated DEMs are capable of obtaining useful estimates of the glacier-wide seasonal mass balance in areas where expected mean thickness of winter snow exceeds 1 m. The accuracy is improved significantly when satellite data and in situ information are combined.

Data availability. The WV2 DEM is available at http://arcticdemapp.s3-website-us-west-2.amazonaws.com/explorer/ (Noh and Howat., 2015). The lidar data are available upon request to the authors (Jóhannesson et al., 2013), and the meteorological data are available upon request at www.vedur.is. The Pléiades data and in situ measurements have data access restrictions.

The Supplement related to this article is available online at https://doi.org/10.5194/tc-11-1501-2017-supplement.

Competing interests. The authors declare that they have no conflict of interest.

Acknowledgements. We thank the editor Valentina Radić and the reviewers David Shean and Ruzica Dadic for their valuable comments, which greatly improved the quality of the initial manuscript. We also thank Sydney Gunnarson for proof reading the revised manuscript. This study was funded by the University of Iceland (UI) Research Fund. Pléiades images were acquired at research price thanks to the CNES ISIS program (http://www.isis-cnes.fr). The WV2 DEM was obtained through the ArcticDEM project. This work is a contribution to the Rannís grant of excellence project, ANATILS. Collaboration and travels between IES and LEGOS were funded by the Jules Verne research fund and the TOSCA program from the French Space Agency, CNES. This study used the recent lidar mapping of the glaciers in Iceland that was funded by the Icelandic Research Fund, the Landsvirkjun research fund, the Icelandic Road Administration, the Reykjavík Energy Environmental and Energy Research Fund, the Klima-og Luftgruppen (KoL) research fund of the Nordic Council of Ministers, the Vatnajökull National Park, the organization Friends of Vatnajökull, the National Land Survey of Iceland, the Icelandic Meteorological Office and the UI research fund. The ground-based mass balance measurements on Drangajökull have been jointly funded by Orkubú Vestfjarða (Westfjord Power Company), the National Energy Authority (2004–2009) and the Icelandic Meteorological Office (2009–2015).

Edited by: Valentina Radic
Reviewed by: David Shean and Ruzica Dadic

References

Aðalgeirsdóttir, G., Guðmundsson, S., Björnsson, H., Pálsson, F., Jóhannesson, T., Hannesdóttir, H., Sigurðsson, S. Þ., and Berthier, E.: Modelling the 20th and 21st century evolution of Hoffellsjökull glacier, SE-Vatnajökull, Iceland, The Cryosphere, 5, 961–975, https://doi.org/10.5194/tc-5-961-2011, 2011.

Ágústsson, H., Hannesdóttir, H., Thorsteinsson, T., Pálsson, F., and Oddsson, B.: Mass balance of Mýrdalsjokull ice cap accumulation area and comparison of observed winter balance with simulated precipitation, Jökull, 63, 91–104, 2013.

Berthier, E., Vincent, C., Magnússon, E., Gunnlaugsson, Á. Þ., Pitte, P., Le Meur, E., Masiokas, M., Ruiz, L., Pálsson, F., Belart, J. M. C., and Wagnon, P.: Glacier topography and elevation changes derived from Pléiades sub-meter stereo images, The Cryosphere, 8, 2275–2291, https://doi.org/10.5194/tc-8-2275-2014, 2014.

Björnsson, H. and Pálsson, F.: Icelandic glaciers, Jökull, 58, 365–386, 2008.

Björnsson, H., Pálsson, F., Sigurdsson, O., and Flowers, G. E.: Surges of glaciers in Iceland, Ann. Glaciol., 36, 82–90, 2003.

Björnsson, H., Pálsson, F., Guðmundsson, S., Magnússon, E., Aðalgeirsdóttir, G., Jóhannesson, T., Berthier, E., Sigurðsson, O., and Thorsteinsson, T.: Contribution of Icelandic ice caps to sea level rise: trends and variability since the Little Ice Age, Geophys. Res. Lett., 40, 1–5, https://doi.org/10.1002/grl.50278, 2013.

Brynjólfsson, S., Schomacker, A., Korsgaard, N. J., and Ingólfsson, Ó.: Surges of outlet glaciers from the Drangajökull ice cap, northwest Iceland, Earth Planet. Sc. Lett., 450, 140–151, https://doi.org/10.1016/j.epsl.2016.06.039, 2016.

Bühler, Y., Adams, M. S., Bösch, R., and Stoffel, A.: Mapping snow depth in alpine terrain with unmanned aerial systems (UASs): potential and limitations, The Cryosphere, 10, 1075–1088, https://doi.org/10.5194/tc-10-1075-2016, 2016.

Cogley, J. G., Hock, R., Rasmussen, L. A., Arendt, A. A., Bauder, A., Braithwaite, R. J., Jansson, P., Kaser, G., Möller, M., Nicholson, L., and Zemp, M.: Glossary of glacier mass balance and related terms, IHP-VII Technical Documents in Hydrology No. 86, IACS Contribution No. 2, UNESCO-IHP, Paris, 114, 2011.

Cuffey, K. M. and Paterson, W. S. B.: The physics of glaciers, Academic Press Inc., Amsterdam, 2010.

De Michele, C., Avanzi, F., Passoni, D., Barzaghi, R., Pinto, L., Dosso, P., Ghezzi, A., Gianatti, R., and Della Vedova, G.: Using a fixed-wing UAS to map snow depth distribution: an evaluation at peak accumulation, The Cryosphere, 10, 511–522, https://doi.org/10.5194/tc-10-511-2016, 2016.

Fountain, A. G. and Vecchia, A.: How many stakes are required to measure the mass balance of a glacier?, Geogr. Ann. A, 81, 563–573, 1999.

Guðmundsson, M. T.: Mass balance and precipitation on the summit plateau of Oraefajokull, SE-Iceland, 48, 49–54, 2000.

Guðmundsson, S., Björnsson, H., Pálsson, F., and Haraldsson, H. H.: Comparison of energy balance and degree-day models of summer ablation on the Langjokull ice cap, SW-Iceland, Jökull, 59, 1–18, 2009.

Harning, D. J., Geirsdóttir, Á., Miller, G. H., and Zalzal, K.: Early Holocene deglaciation of Drangajökull, Vestfirðir, Iceland, Quaternary Sci. Rev., 153, 192–198, https://doi.org/10.1016/j.quascirev.2016.09.030, 2016a.

Harning, D. J., Geirsdóttir, Á., Miller, G. H., and Anderson, L.: Episodic expansion of Drangajökull, Vestfirðir, Iceland, over the last 3 ka culminating in its maximum dimension during the Little Ice Age, Quaternary Sci. Rev., 152, 118–131, https://doi.org/10.1016/j.quascirev.2016.10.001, 2016b.

Helfricht, K., Kuhn, M., Keuschnig, M., and Heilig, A.: Lidar snow cover studies on glaciers in the Ötztal Alps (Austria): comparison with snow depths calculated from GPR measurements, The Cryosphere, 8, 41–57, https://doi.org/10.5194/tc-8-41-2014, 2014.

Höhle, J. and Höhle, M.: Accuracy assessment of digital elevation models by means of robust statistical methods, ISPRS J. Photogramm. Remote Sens., 64, 398–406, https://doi.org/10.1016/j.isprsjprs.2009.02.003, 2009.

Holzer, N., Vijay, S., Yao, T., Xu, B., Buchroithner, M., and Bolch, T.: Four decades of glacier variations at Muztagh Ata (eastern Pamir): a multi-sensor study including Hexagon KH-9 and Pléiades data, The Cryosphere, 9, 2071–2088, https://doi.org/10.5194/tc-9-2071-2015, 2015.

Huss, M., Bauder, A., Funk, M., and Hock, R.: Determination of the seasonal mass balance of four Alpine glaciers since 1865, J. Geophys. Res.-Earth, 113, F01015, https://doi.org/10.1029/2007JF000803, 2008.

James, T. D., Murray, T., Barrand, N. E., and Barr, S. L.: Extracting photogrammetric ground control from lidar DEMs for change detection, Photogramm. Rec., 21, 312–328, 2006.

Jarosch, A. H.: Icetools: A full Stokes finite element model for glaciers, Comput. Geosci., 34, 1005–1014, https://doi.org/10.1016/j.cageo.2007.06.012, 2008.

Jóhannesson, T., Björnsson, H., Pálsson, F., Sigurðsson, O., and Þorsteinsson, Þ.: LiDAR mapping of the Snæfellsjökull ice cap, western Iceland, Jökull, 61, 19–32, 2011.

Jóhannesson, T., Björnsson, H., Magnússon, E., Guðmundsson, S., Pálsson, F., Sigurðsson, O., Thorsteinsson, T., and Berthier, E.: Ice-volume changes, bias estimation of mass-balance measurements and changes in subglacial lakes derived by lidar mapping of the surface of Icelandic glaciers, Ann. Glaciol., 54, 63–74, https://doi.org/10.3189/2013AoG63A422, 2013.

Lacroix, P.: Landslides triggered by the Gorkha earthquake in the Langtang valley, volumes and initiation processes, Earth Planets Space, 68, 46, https://doi.org/10.1186/s40623-016-0423-3, 2016.

Lacroix, P., Berthier, E., and Maquerhua, E. T.: Earthquake-driven acceleration of slow-moving landslides in the Colca valley, Peru, detected from Pléiades images, Remote Sens. Environ., 165, 148–158, https://doi.org/10.1016/j.rse.2015.05.010, 2015.

Ligtenberg, S. R. M., Helsen, M. M., and van den Broeke, M. R.: An improved semi-empirical model for the densification of Antarctic firn, The Cryosphere, 5, 809–819, https://doi.org/10.5194/tc-5-809-2011, 2011.

Machguth, H., Eisen, O., Paul, F., and Hoelzle, M.: Strong spatial variability of snow accumulation observed with helicopter-borne GPR on two adjacent Alpine glaciers, Geophys. Res. Lett., 33, L13503, https://doi.org/10.1029/2006GL026576, 2006.

Magnússon, E., Muñoz-Cobo Belart, J., Pálsson, F., Ágústsson, H., and Crochet, P.: Geodetic mass balance record with rigorous uncertainty estimates deduced from aerial photographs and lidar data – Case study from Drangajökull ice cap, NW Iceland, The Cryosphere, 10, 159–177, https://doi.org/10.5194/tc-10-159-2016, 2016a.

Magnússon, E., Belart, J. M. C., Pálsson, F., Anderson, L., Gunnlaugsson, Á. Þ., Berthier, E., Ágústsson, H., and Geirsdottir, A.: The subglacial topography of Drangajökull ice cap, NW-Iceland, deduced from dense RES-profiling, Jökull, 66, 1–26, 2016b.

Marti, R., Gascoin, S., Berthier, E., de Pinel, M., Houet, T., and Laffly, D.: Mapping snow depth in open alpine terrain from stereo satellite imagery, The Cryosphere, 10, 1361–1380, https://doi.org/10.5194/tc-10-1361-2016, 2016.

Müller, J., Gärtner-Roer, I., Thee, P., and Ginzler, C.: Accuracy assessment of airborne photogrammetrically derived high-resolution digital elevation models in a high mountain environment, ISPRS J. Photogramm. Remote Sens., 98, 58–69, https://doi.org/10.1016/j.isprsjprs.2014.09.015, 2014.

Noël, B., van de Berg, W. J., van Meijgaard, E., Kuipers Munneke, P., van de Wal, R. S. W., and van den Broeke, M. R.: Evaluation of the updated regional climate model RACMO2.3: summer snowfall impact on the Greenland Ice Sheet, The Cryosphere, 9, 1831–1844, https://doi.org/10.5194/tc-9-1831-2015, 2015.

Noh, M.-J. and Howat, I. M.: Automated stereo-photogrammetric DEM generation at high latitudes: Surface Extraction with TIN-based Search-space Minimization (SETSM) validation and demonstration over glaciated regions, GIScience Remote Sens., 52, 198–217, https://doi.org/10.1080/15481603.2015.1008621, 2015.

Nuth, C. and Kääb, A.: Co-registration and bias corrections of satellite elevation data sets for quantifying glacier thickness change, The Cryosphere, 5, 271–290, https://doi.org/10.5194/tc-5-271-2011, 2011.

Ohmura, A.: Observed Mass Balance of Mountain Glaciers and Greenland Ice Sheet in the 20th Century and the Present Trends, Surv. Geophys., 32, 537–554, 2011.

Pálsson, F., Guðmundsson, S., Björnsson, H., Berthier, E., Magnússon, E., Guðmundsson, S., and Haraldsson, H.: Mass and volume changes of Langjökull ice cap, Iceland, ∼ 1890 to 2009, deduced from old maps, satellite images and in situ mass balance measurements, Jökull, 62, 81–96, 2012.

Radić, V. and Hock, R.: Glaciers in the Earth's Hydrological Cycle: Assessments of Glacier Mass and Runoff Changes on Global and Regional Scales, Surv. Geophys., 35, 813–837, https://doi.org/10.1007/s10712-013-9262-y, 2014.

Rolstad, C., Haug, T., and Denby, B.: Spatially integrated geodetic glacier mass balance and its uncertainty based on geostatistical analysis: application to the western Svartisen ice cap, Norway, J. Glaciol., 55, 666–680, 2009.

Shean, D. E., Alexandrov, O., Moratto, Z. M., Smith, B. E., Joughin, I. R., Porter, C., and Morin, P.: An automated, open-source pipeline for mass production of digital elevation models (DEMs) from very-high-resolution commercial stereo satellite

imagery, ISPRS J. Photogramm. Remote Sens., 116, 101–117, https://doi.org/10.1016/j.isprsjprs.2016.03.012, 2016.

Sold, L., Huss, M., Hoelzle, M., Andereggen, H., Joerg, P. C., and Zemp, M.: Methodological approaches to infer end-of-winter snow distribution on alpine glaciers, J. Glaciol., 59, 1047–1059, https://doi.org/10.3189/2013JoG13J015, 2013.

Sold, L., Huss, M., Eichler, A., Schwikowski, M., and Hoelzle, M.: Unlocking annual firn layer water equivalents from ground-penetrating radar data on an Alpine glacier, The Cryosphere, 9, 1075–1087, https://doi.org/10.5194/tc-9-1075-2015, 2015.

Tarini, M., Cignoni, P., and Montani, C.: Ambient Occlusion and Edge Cueing for Enhancing Real Time Molecular Visualization, IEEE T. Vis. Comput. Gr., 12, 1237–1244, https://doi.org/10.1109/TVCG.2006.115, 2006.

Thorsteinsson, T., Sigurðsson, O., Jóhannesson, T., Larsen, G., and Wilhelms, F.: Ice core drilling on the Hofsjökull ice cap, Jökull, 51, 25–41, 2002.

Toutin, T.: Three-dimensional topographic mapping with ASTER stereo data in rugged topography, IEEE T. Geosci. Remote Sens., 40, 2241–2247, https://doi.org/10.1109/TGRS.2002.802878, 2002.

Vaughan, D. G., Comiso, J. C., Allison, J., Carrasco, J., Kaser, R., Kwok, R., Mote, P., Murray, T., Paul, F., Ren, J., Rignot, E., Solomina, O., Steffen, K., and Zhang, T.: Observations: Cryosphere, in Climate Change 2013: The Physical Science Basis. Contribution of Working Group I to the Fifth Assessment Report of the Intergovernmental Panel on Climate Change, Cambridge University Press, Cambridge, UK and New York, NY, USA, 2013.

Willis, M. J., Herried, B. G., Bevis, M. G., and Bell, R. E.: Recharge of a subglacial lake by surface meltwater in northeast Greenland, Nature, 518, 223–227, 2015.

Zemp, M., Frey, H., Gärtner-Roer, I., Nussbaumer, S. U., Hoelzle, M., Paul, F., Haeberli, W., Denzinger, F., Ahlstrøm, A. P., Anderson, B., Bajracharya, S., Baroni, C., Braun, L. N., Cáceres, B. E., Casassa, G., Cobos, G., Dávila, L. R., Delgado Granados, H., Demuth, M. N., Espizua, L., Fischer, A., Fujita, K., Gadek, B., Ghazanfar, A., Hagen, J. O., Holmlund, P., Karimi, N., Li, Z., Pelto, M., Pitte, P., Popovnin, V. V., Portocarrero, C. A., Prinz, R., Sangewar, C. V., Severskiy, I., Sigurðsson, O., Soruco, A., Usubaliev, R., and Vincent, C.: Historically unprecedented global glacier decline in the early 21st century, J. Glaciol., 61, 745–762, https://doi.org/10.3189/2015JoG15J017, 2015.

Suplementary information: Winter mass balance of Drangajökull ice cap (NW Iceland) derived from satellite sub-meter stereo images

Elevation differences on the snow- and ice-free areas, statistics and histograms

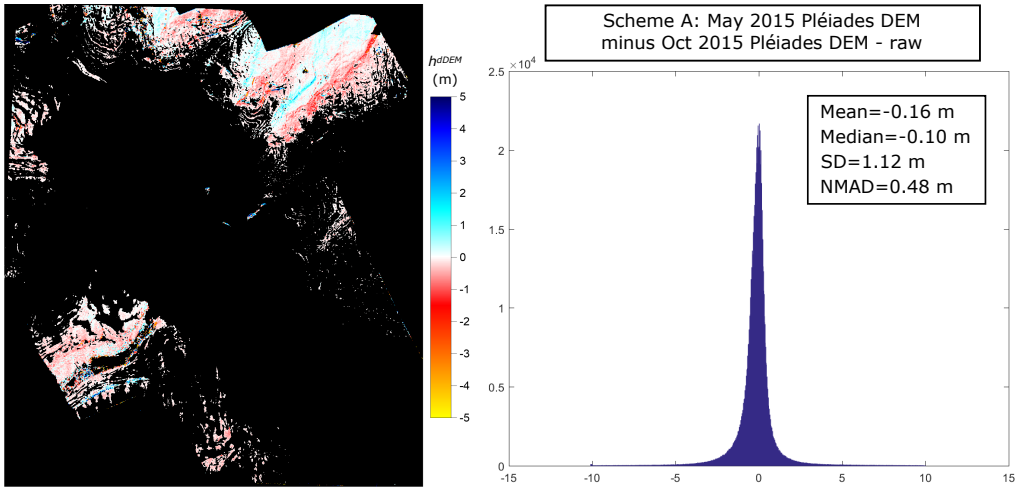

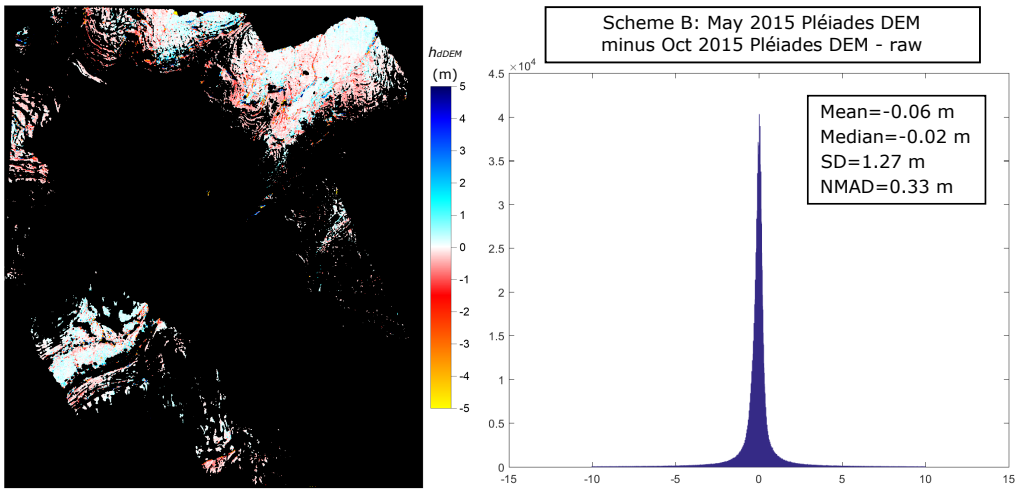

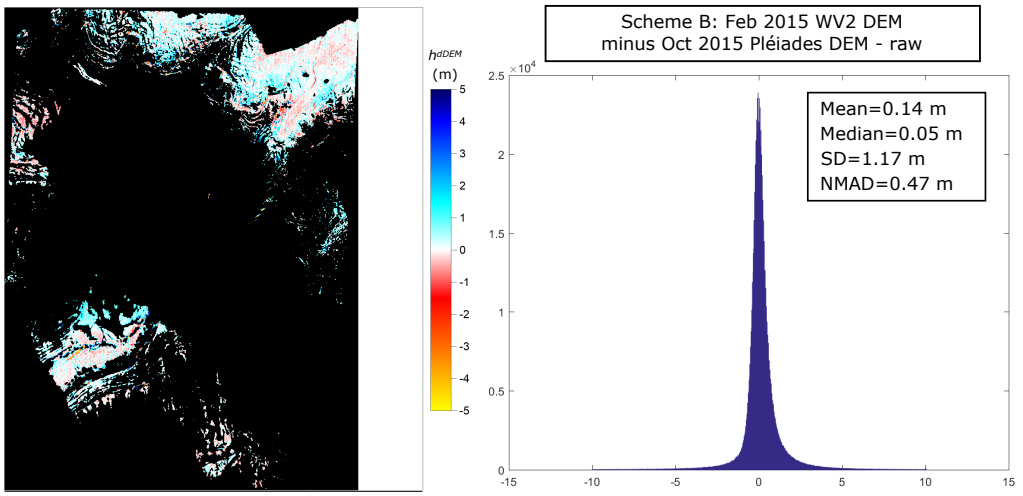

Elevation differences on the snow- and ice-free areas, statistics and histograms (continuation)

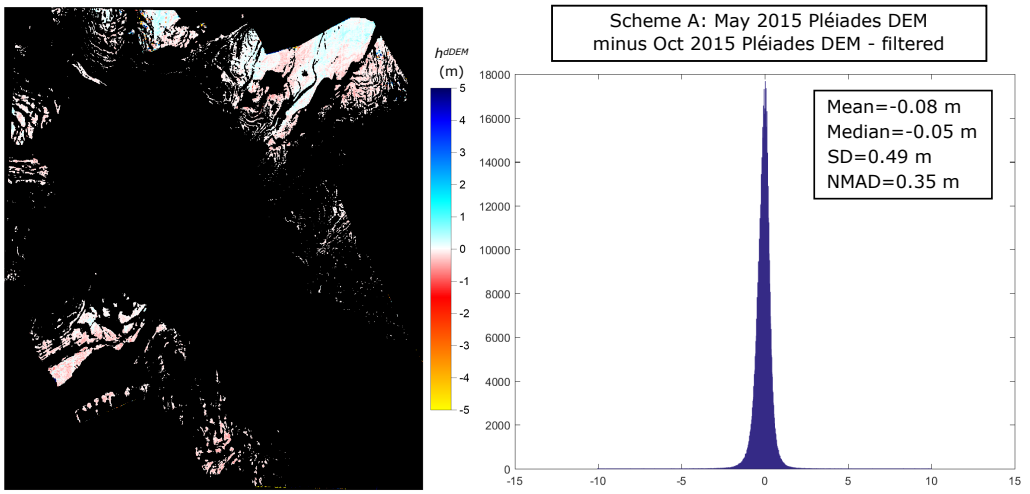

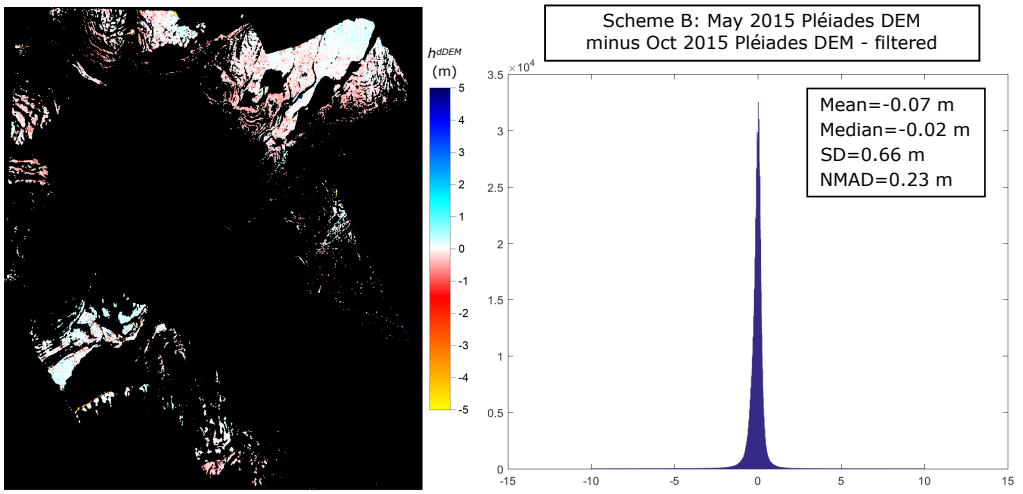

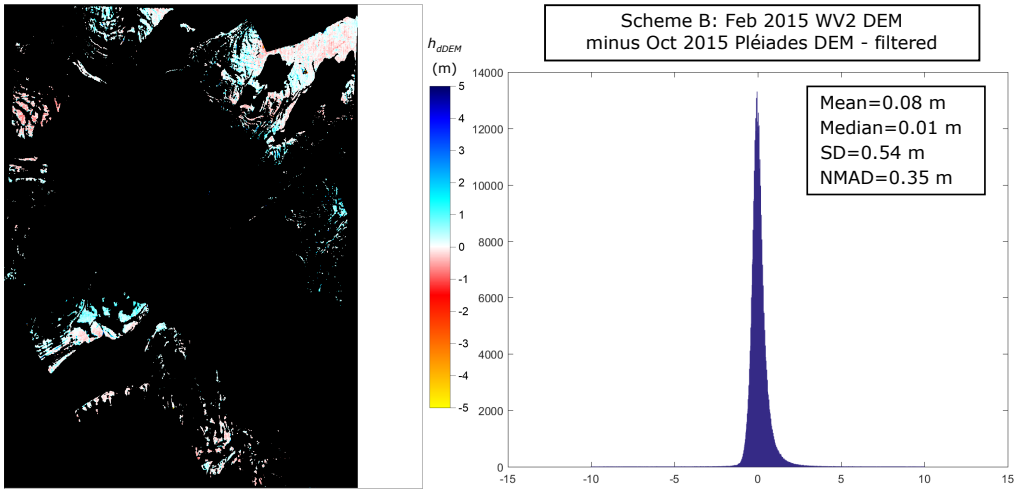

Paper II

The geodetic mass balance of Eyjafjallajökull ice cap for 1945–2014: processing guidelines and relation to climate

Joaquín M.C. Belart, Eyjólfur Magnússon, Etienne Berthier, Finnur Pálsson, Guðfinna Aðalgeirsdóttir, Tómas Jóhannesson.

Manuscript in revision in Journal of Glaciology

The geodetic mass balance of Eyjafjallajökull ice cap for 1945–2014: processing guidelines and relation to climate

Joaquín M. C. Belart,[12*] Eyjólfur Magnússon,[1] Etienne Berthier,[2] Finnur Pálsson,[1] Guðfinna Aðalgeirsdóttir,[1] Tómas Jóhannesson[3]

[1]Institute of Earth Sciences, University of Iceland (IES), Askja, Reykjavík, Iceland
[2]Laboratoire d'Etudes en Géophysique et Océanographie Spatiales (LEGOS), Université de Toulouse, CNES, CNRS, IRD, UPS, F-31400 Toulouse, France
[3]Icelandic Meteorological Office (IMO), Reykjavík, Iceland

ABSTRACT. Mass balance measurements of Icelandic glaciers are sparse through the 20th century. However, the large archive of stereo images available allows estimates of glacier-wide mass balance ($\dot{B}$) in decadal time steps since 1945. Combined with climate records, they provide further insight into glacier-climate relationship. This study presents a workflow to process aerial photographs (1945–1995), spy satellite imagery (1977–1980) and modern satellite stereo images (since 2000) using photogrammetric techniques and robust statistics in a highly automated, open-source pipeline to retrieve seasonally corrected, decadal glacier-wide geodetic mass balances. In our test area, Eyjafjallajökull (S-Iceland, ~70 km²), we obtain a mass balance of $\dot{B}_{1945}^{2014} = -0.27 \pm 0.03$ m w.e. a^{-1}, with maximum and minimum of $\dot{B}_{1984}^{1989} = 0.77 \pm 0.19$ m w.e. a^{-1} and $\dot{B}_{1994}^{1998} = -1.94 \pm 0.34$ m w.e. a^{-1} respectively, attributed to climatic forcing, and $\dot{B}_{2009}^{2010} = -3.39 \pm 0.43$ m w.e. a^{-1}, mostly caused by the April 2010 eruption. The reference-surface mass balances correlate with summer temperature and winter precipitation, and a linear model replicates 80% of the mass balance variability, yielding a static sensitivity of mass balance to summer temperature and winter precipitation of -2.1 ± 0.4 m w.e. a^{-1} K^{-1} and 0.5 ± 0.3 m w.e. a^{-1} (10%)$^{-1}$, respectively. This study serves as a template that can be used to estimate of mass-balance changes and glaciers' response to climate.

Keywords: remote sensing, geodetic mass balance, glacier–climate relationship

1 Introduction

Most glacierized regions in the world have experienced glaciers' recession since the end of the Little Ice Age due to warming climate (Vaughan and others, 2013; Zemp and others, 2015), among them all Icelandic glaciers (Björnsson and others, 2013). These changes have, however, been far from uniform. Glaciers have shown retreats and advances in decadal time spans (e.g. Huss and others, 2010; Björnsson and others, 2013). Measuring and monitoring these changes has enabled better understanding of the relation between glaciers and climate (e.g. Aðalgeirsdóttir and others, 2011; Ohmura, 2011). This is useful in three ways: (1) for understanding how glaciers respond to changes in climate, such as increasing temperature or precipitation (De Woul and Hock, 2005; Marzeion and others, 2014; Sakai and Fujita, 2017), (2) for improving climate records inferred from observed glacier changes (e.g. Leclercq and Oerlemans, 2012) and (3) for improving projection of glacier change (e.g. Huss and Hock, 2018).

For a broad range of ice masses there are abundant archives of stereo photographs, often extending further back in time and covering larger areas than the field mass balance measurements. These are to a large extent the result of the exhaustive work of US photogrammetric campaigns, which started worldwide after World War II (Spriggs, 1966) and continued with spaceborne cameras with the first optical spy satellites in 1960 (e.g. Bindschadler and Vornberger, 1998).

In Iceland, two direct methods have commonly been used in recent decades (>20 year records) to observe glacier mass changes: (1) in situ measurements of accumulation and ablation on the main ice caps (Björnsson and others, 1998; Pálsson and others, 2012; Björnsson and others, 2013; Jóhannesson and others, 2013) and (2) comparison of digital elevation models (DEMs) from different time periods obtained from multiple sources including contour maps, stereo imagery or airborne radar (e.g. Guðmundsson and others, 2011; Magnússon and others, 2016). While the in situ measurements of mass balance only span the last ~25 years (Björnsson and others, 2013), geodetic records span ~70 years (e.g. Magnússon and others, 2016) and up to ~80 years (e.g. Pálsson and others, 2012). Combined with long records of climatic data, these have provided estimates of glacier mass balance sensitivity to changes in temperature (Guðmundsson and others, 2011; Pálsson and others, 2012).

There is a large archive of stereo photographs acquired in Iceland between 1945 and 1995 with a temporal frequency of 5 to 20 years, containing valuable glaciological information (Magnússon and others, 2016). Satellite stereo imagery from the last two decades extends the records up to the present (Guðmundsson and others, 2011; Berthier and others, 2014). This opens the possibility of creating unique time series of elevation changes of the Icelandic glaciers, thereby expanding knowledge of the last century of glacier variations and allowing further studies of glacier response to climate forcing.

The processing of optical stereo imagery has improved during recent years due to advances in computer vision and image processing. New tools and algorithms are available to solve for the image orientation, such as structure from motion (SfM, e.g. Pierrot Deseilligny and Clery, 2011). Image correlation can be performed with high precision and detail using semi-global matching (Hirschmuller, 2008). These tools are accessible to the community with open-source software such as MicMac (IGN, France; Pierrot Deseilligny and Clery, 2011; Rupnik and others, 2017) and the NASA Ames Stereo Pipeline (ASP) (Shean and others, 2016).

Moreover, publicly accessible archives of high-resolution DEMs with sub-meter uncertainties have become available in recent years. The main glacierized regions in Iceland were surveyed with airborne lidar between 2008 and 2012, an initiative during the 2008 International Polar Year (IPY) (Jóhannesson and others, 2013). In addition, the current state of the glaciers and ice caps is being monitored by satellite sub-meter stereo imagery, such as Pléiades and WorldView (Berthier and others, 2014; Noh and Howat, 2015; Willis and others, 2015; Shean and others, 2016; Belart and others, 2017). The high-resolution DEMs are not only useful for updating the glacier's topography, but also provide valuable data to generate improved DEMs from the archives of stereo imagery. This is achieved by using co-registration techniques in overlapping off-glacier areas between the historical datasets and the modern DEMs (Barrand and others, 2009; Papasodoro and others, 2015, Fieber and others, 2018). Finally, different techniques of bias corrections are now commonly applied (Nuth and Kääb, 2011), uncertainty assessment is carried out with geostatistics (Rolstad and others, 2009;

Magnússon and others, 2016) and seasonal signals are modeled to interpret the glaciological results properly (e.g. Magnússon and others, 2016).

The goal of this study is to take advantage of these recent developments in data availability and processing in order to unlock the archive of stereo images available in Iceland. Here, we present a pipeline, based on open-source software, to exploit the archive and infer glacier-wide mass balances ($\dot{B}$) for multiple time periods since 1945. The obtained records of $\dot{B}$ are corrected from seasonal effects using records of temperature and precipitation. The seasonally corrected record of $\dot{B}$ is compared with the climate data in order to infer static mass-balance sensitivity to temperature and precipitation (Oerlemans and Reichert, 2000; De Woul and Hock, 2005; Cogley and others, 2011). Eyjafjallajökull is selected as a test area because of the large amount of data available and its highly dynamic landscape, with rapid changes due to glacier–climate (Guðmundsson and others, 2011) and ice–volcano interactions (Sigmundsson and others, 2010), making this study area both challenging and interesting. The aim is also to develop sufficiently automated methods to facilitate their application to other glacierized areas in Iceland and elsewhere.

2 Study area

Eyjafjallajökull (Fig. 1) is located ~10 km from the south coast of Iceland, with a climate mainly controlled by the Irminger Current (Björnsson and others, 2013). Guðmundsson and others (2011) calculated the geodetic mass balance for 1984–2004 based on contour maps and remote sensing data, and estimated a higher sensitivity of mass balance to temperature than for other glaciers located further inland (e.g. De Woul and Hock, 2005; Pálsson and others, 2012). This is likely explained by the proximity of the ice cap to the coast, with more precipitation and mass turnover. The April 2010 eruption in Eyjafjallajökull opened a >100 m deep melt channel (Fig. 1), draining northwards and extending close to the glacier margin of the Gígjökull outlet glacier. The estimated ice melt by the eruption was 10–13·10^7 m^3 (Oddsson and others, 2016).

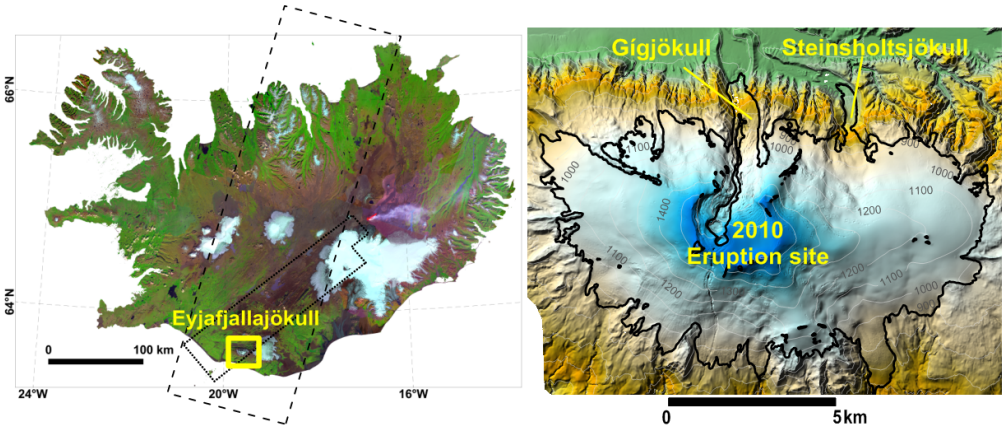

Fig. 1: Location map. Left: Mosaic of Landsat 8 images of Iceland. The dashed rectangle shows the footprints of the 1980 KH-9 images. The thin black dotted polygon shows the extent of the 1998 EMISAR DEM (Magnússon, 2003; Dall, 2003), and the thick yellow rectangle shows the location of Eyjafjallajökull. Right: Colored shaded relief from a lidar DEM surveyed in August 2010. The black line

shows the glacier extent in 2010. The lidar survey took place ~4 months after the 2010 eruption, revealing an open channel of melted ice at the eruption site and along the paths of lava flows extending to the north from the main crater.

3 Data

The data used in this study are organized into two categories: (1) DEM sources and (2) climate data. Point (1) encompasses three sub-categories: (1) frame stereo imagery, consisting of scanned analog imagery obtained from a camera, (2) pushbroom stereo imagery, i.e. imagery obtained from a pushbroom optical sensor and (3) non-stereo-based DEMs. The last group comprises the lidar DEM from 2010 (Jóhannesson and others, 2013) and an airborne Synthetic Aperture Radar DEM from 1998 (EMISAR; Dall, 2003; Magnússon, 2003), which are further described in Supplement S1.

3.1 DEM Sources

3.1.1 Frame stereo imagery

The frame imagery was subdivided into four groups:

(1) 1945–1946 – American Mapping Service (AMS): These surveys, part of the US photoreconnaissance program, consist of a full survey of Iceland in the summers of 1945 and 1946. This series consists on copies of the original films, stored at the National Land Survey of Iceland (Landmælingar Íslands, LMÍ). The cameras had a format of 23×23 cm and a focal length of 153 mm. The images from this series typically have a scale of 1:40000 (flight altitude of 6700 m a.s.l.).

(2) 1960–1961 – Defense Mapping Agency (DMA): As a continuation of the US photoreconnaissance missions, about 70% of Iceland was resurveyed in the summers of 1960 and 1961, except for the eastern part of the country. The data are also a copy of the original films, stored at LMÍ. The cameras used in this survey (format 23×23 cm) have basic calibration certificates, including focal length (153 mm) and radial distortion (Spriggs, 1966).

(3) 1950s–1990s – LMÍ: Photogrammetric campaigns organized by local institutions began to cover selected areas of Iceland in the 1950s, turning into systematic and country-wide surveys in the 1970s. The first campaigns were carried out with small-format images (18×18 cm, focal length 115 mm) and were replaced by standard aerial mapping cameras from the 1970s onwards (23×23 cm, focal length 153 mm). Original films are available at LMÍ.

(4) 1977–1980 – Hexagon KH-9 Mapping Camera images (KH-9): The declassified satellite photoreconnaissance missions consist of a total of nine satellite missions, spanning 1959–1984, for which most of the data became publicly available between 1992 and 2011 (e.g. Bindschadler and Vornberger, 1998; Surazakov and Aizen, 2010). In this study, we use six images from the Hexagon KH-9 mission # 1216, acquired in 1980, crossing Iceland from north to south, including, among other glacierized areas, a complete coverage of (from south to north) the Eyjafjallajökull, Mýrdalsjökull and Höfsjökull as well as the cluster of Tröllaskagi glaciers. The images have a format of 23×46 cm and a focal length of 305 mm (Surazakov and Aizen, 2010).

The AMS, DMA and LMÍ series were obtained from the National Land Survey of Iceland (http://www.lmi.is), which stores negatives and prints of the aerial surveys carried out from the 1930s to the 1990s. All the data are publicly available upon request, and scanning of the negative films was carried out with a photogrammetric scanner (further details in Supplement S2).The KH-9 satellite frame imagery was obtained from the United States Geological Survey (USGS, https://www.usgs.gov/).

3.1.2 Pushbroom stereo imagery

The pushbroom imagery used can be categorized into three groups:

(1) 2000–present – ASTER: The ASTER satellite has been in operation since 2000 with numerous acquisitions on glaciers thanks to the GLIMS program (Raup and others, 2007), and the data collected are publicly available at https://search.earthdata.nasa.gov/. A stereopair from ASTER, acquired in late summer 2009, was processed to analyze the glacier changes prior to the Eyjafjallajökull 2010 eruption.

(2) 2002–2015 – SPOT5 (©CNES & Airbus D&S): This satellite has been successfully used in numerous surveys of ice masses (e.g. Korona and others, 2009). We obtained a stereopair from SPOT5 acquired in October 2004 (Guðmundsson and others, 2011).

(3) 2011–present – Pléiades (©CNES & Airbus D&S): Pléiades stereo images offer the capabilities of creating highly accurate and detailed DEMs in glacierized areas thanks to their geometric and radiometric resolution (Berthier and others, 2014; Belart and others, 2017). We use a Pléiades stereopair acquired on 11 August 2014, with an almost complete coverage of the Eyjafjallajökull. Some clouds covered a small portion of the southwest margin of the ice cap.

Table 1. Dates, sources and basic information of the datasets. GSD: Ground Sampling Distance (m), approximated for the frame stereo imagery based on the sensor elevation above ground, focal length and scanning resolution.

Date	Series	GSD Ortho	GSD DEM	Number of images
29 Sept 1945	AMS	1	5	12
5 Aug 1960	DMA	0.5	5	36
5 & 13 Aug 1960	LMÍ	0.5	5	39
28 Jul 1980	LMÍ	1	5	16
22 Aug 1980	KH-9	5	20	6
4 Sept 1984	LMÍ	0.5	5	22
31 Jul 1989	LMÍ	0.5	5	18
6 Aug 1994	LMÍ	0.5	5	29
12 Aug 1998	EMISAR	N/A	5	N/A
5 Oct 2004	SPOT5	5	20	2
7 Oct 2009	ASTER	15	30	2
10–11 Aug, 16 Sept 2010	Lidar	1*	1	N/A
11 Aug 2014	Pléiades	0.5	4	2

*An intensity map was produced from the lidar pulses, providing an additional mode of visualization of the lidar data for mapping purposes.

3.2 Climate data

The gridded daily temperature of Iceland, produced by Crochet and Jóhannesson (2011), was used in this study. This dataset consists of 1×1 km gridded daily air temperature at 2 m above ground, spanning 1949–2016, deduced by interpolation of weather station observations reduced to sea level with a constant vertical temperature lapse rate of 6.5 °C km^{-1}, and adjusted back to the topography with a 1×1 km DEM and the same constant vertical lapse rate.

Gridded daily precipitation of Iceland was obtained from two sources: (1) the linear theory model of orographic precipitation (LT-Model, Crochet and others, 2007), available for the period 1958–2007 in 1×1 km resolution, and the HARMONIE numerical model (HM-Model, Bengtsson and others, 2017; Nawri and others, 2017), spanning 1980–2016 with 2.5×2.5 km resolution.

4 Methods

The methods section can be divided into three successive steps: (1) creating maps of elevation difference, (2) calculation of seasonally corrected mass balances and (3) joint analysis of mass balance and climatic data.

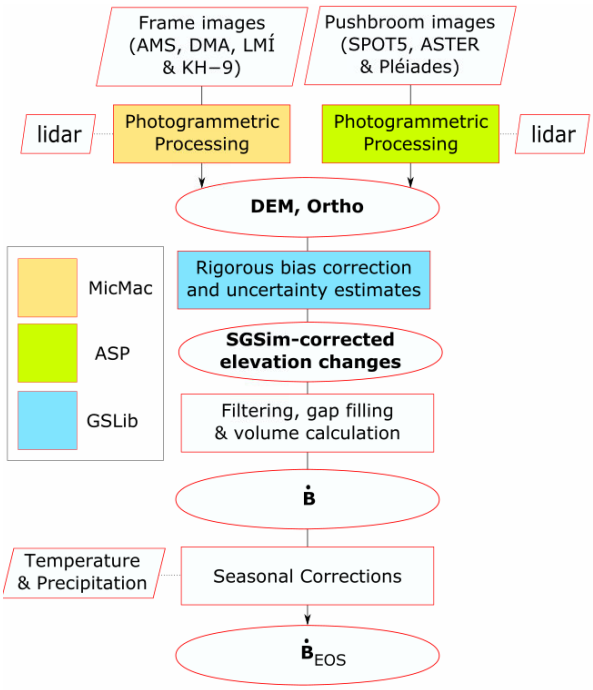

Fig. 2: Diagram of generic workflow followed. Trapezoids show input data, rectangles indicate processes and ovals indicate outputs. $\dot{B}_{EOS}$ is the glacier-wide mass balance at the end of summer.

4.1 Creating maps of elevation difference

4.1.1 Frame stereo imagery (MicMac)

The frame stereo imagery was processed using the open-source software, MicMac (© National Institute of Geographic and Forestry Information, IGN, France; Pierrot Deseilligny and Clery, 2011; Rupnik and others, 2017) to obtain DEMs and orthophoto.. The general workflow is explained in Rupnik and others (2017), and the routines utilized are further described in Supplement S2.

Our pipeline started with the scanned frame imagery as input, cropped by the fiducial marks, and 11–20 Ground Control Points (GCPs) manually digitized, extracted from the lidar DEM viewed as a hillshade (e.g. James and others, 2006; Barrand and others, 2009), with an adequate distribution horizontally and vertically outside the ice cap and at nunataks. We measured 65 GCPs for the KH-9 photographs distributed over their overlapping areas with the available lidar data.

The image orientation was solved in two steps: (1) calculating relative orientation from automatic measurement of tie points and SfM, and (2) solving for absolute orientation by robust bundle adjustment using GCPs, in which the camera parameters were also refined. Once the images were oriented, a point cloud was created using semi-global matching and linearly interpolated onto a regular 5×5 m grid. A mosaic of orthoimages was also generated (Fig. 2).

By using well-distributed GCPs, the likelihood of significant biases in the DEMs relative to the reference DEM was minimized (Magnússon and others, 2016). Yet, remaining residual errors in orientation need to be acknowledged, especially in areas far away from GCPs. These errors are spatially-variable, and due to the sensor's geometry, the residual errors can have a significant vertical component. Localized errors in horizontal position can also be expected, particularly in the oldest datasets. We do not attempt to correct horizontal errors, but we acknowledge that relative errors in horizontal positions can affect the obtained vertical errors, studied in the uncertainty analysis (section 4.1.3).

4.1.2 Pushbroom stereo imagery (ASP)

ASP is a robust, open-source and automated photogrammetric package commonly used for processing pushbroom satellite stereo images (NASA; Shean and others, 2016). The pipeline used the orbital information from the imagery, generally presented as Rational Polynomial Coefficients (RPCs), and no GCPs were used.

The processing of ASTER and SPOT5 DEMs was performed with an ASP setup slightly modified (Supplement S3) from that of Brun and others (2017), and inspired by Lacroix (2016). Pléiades imagery was processed as described in Belart and others (2017).

SPOT5, ASTER and Pléiades DEMs were co-registered to the lidar using the Iterative Closest Point (ICP) algorithm in ASP (Shean and others, 2016; Belart and others, 2017). The 3D transformation served to refine the orbital information and produce a co-registered orthoimage. Additional details of the processing are described in Supplement S3.

4.1.3 Correction and uncertainty assessment of the obtained mean elevation change

The difference of DEMs (dDEM) can be affected by spatially-variable errors due to residual errors in the sensor orientation (interior and exterior). This effect can be particularly enhanced in the oldest datasets, e.g. 1945 and 1960, where the camera geometry is not fully constrained (e.g. Magnússon and others, 2016).

To correct the spatially-variable errors in the dDEM, we used a modified version of the Sequential Gaussian Simulation (SGSim) described by Magnússon and others (2016). In this study, it is included in an automate pipeline using the command-line interface for the open-source software GSLib (Deutsch, 1998). The SGSim calculates 1000 realizations of simulated maps (2D grids) of spatially-variable errors for each dDEM within the ice cap, using as input the off-glacier areas of the dDEM and a modeled semivariogram, also constrained by the off-glacier areas of the dDEM.

Each realization simulates the error of the elevation change on each grid node within the ice cap. Averaged over the glacierized area, this results on the simulated error of the glacier-wide the mean elevation change (Table 2). From a probability distribution based on the histogram of the 1000 realization, we approximated the 95% confidence interval of the glacier-wide mean elevation change.

Unlike Magnússon and others (2016), in this study the dDEM are not bias corrected based on a single mean of the probability distribution. Instead, we subtracted the derived mean of the 1000 realizations for each individual grid node within the ice cap. This approach results in the same correction for the mean elevation change (Table 2) but also results in more realistic localized corrections for the obtained dDEMs for visualization (Fig. 4). Details of the SGSim methodology are described in Supplement S4.

This method takes into account the spatial autocorrelation of the dDEMs, producing a spatially-variable error correction. This results in significantly lower uncertainties in glacier-wide mean elevation change and volume change than proxies based on descriptive statistics (Rolstad and others, 2009, Magnússon and others, 2016), such as standard deviation or Normalized Median Absolute Deviation (NMAD, Höhle and Höhle, 2009) (Table 2). To verify the robustness of the SGSim, we used the two independent datasets at similar dates in 1960 and 1980, respectively (1960 DMA, 1960 LMÍ, 1980 LMÍ and 1980 KH-9; Table 1), for which we calculated the glacier-wide mean elevation changes compared to the 2010 lidar DEM (considered as a ground truth). We could thus confirm that the glacier-wide mean elevation difference during 1960–2010 and 1980–2010 corrected using SGSim agreed well within the uncertainty estimates using the different datasets and that the agreement is better than with other, more simple, bias-correction models. The results of these tests are further described in the Supplement (Table S1).

4.2 Calculation of seasonally corrected mass balance

The volume changes dV_{t1}^{t2} for the selected time intervals were calculated from SGSim-corrected maps of elevation change. Since they contained some data gaps (up to 15% of the ice cap area, in the worst case of the 1989 series), a gap interpolation and outlier filtering were also performed, as described in Supplement S5. The glacier-wide geodetic mass balance $\dot{B}$ was calculated with the following equation (Fischer and others, 2015; Magnússon and others, 2016):

$$\dot{B}_{t1}^{t2} = \frac{dV_{t1}^{t2}\, c}{\overline{A_{t1}^{t2}}\, dt} \quad (1)$$

where $\overline{A_{t1}^{t2}}$ is the average area for the two dates, dt is the time difference, in absolute years, and c is the conversion factor of volume to water equivalent, here chosen as 0.85 ± 0.06 (Huss, 2013). This value is recommended over time periods longer than 5 years (Huss, 2013), hence we assume twice as large uncertainty (± 0.12) for the conversion factor in time periods of 4 and 5 years (1980–1984; 1984–1989; 1989–1994; 1994–1998; 2004–2009; 2010–2014). For the period 2009–2010, a conversion factor of 0.90 ± 0.10 is chosen, assuming the elevation change is mostly due to ice melted by the April 2010 eruption.

The glacier-wide geodetic mass balance was then temporally adjusted to the end of the summer, $\dot{B}_{EOS}$, to facilitate comparison with traditional mass-balance measurements and climate fluctuations, thus avoiding the effect of seasonal signals that are particularly strong in a relative sense for short time periods. A volume correction was calculated between the date of each DEM dataset t1 and t2), and 1 October of the same year (Magnússon and others, 2016). For simplicity, the DEMs of 1945, 2004 and 2009 were not shifted seasonally as they were acquired at most 1 week apart from 1 October (Table 1). $\dot{B}_{EOS}$ was computed as

$$\dot{B}_{EOS}{}_{t1}^{t2} = \frac{dV_{t1}^{t2} - dV_{t1}^{1\,Oct} + dV_{t2}^{1\,Oct}}{\overline{A_{t1}^{t2}}\, dt} c \quad (2)$$

where $dV_{t1}^{1\,Oct}$ is the volume of the seasonal correction calculated between t1 and 1 October of the same year, and analogously for $dV_{t2}^{1\,Oct}$. Eq.2 neglects the correction of area to 1 October. The seasonal correction integrated over the ice cap was calculated from the climate model of temperature (T) and precipitation (P) as

$$dV_{tDEM}^{1\,Oct} = \sum_{tDEM}^{1\,Oct} \int^{glacier} \left\{ \alpha \frac{ddf_{f\&i}\, T_+}{c_{f\&i}} + \beta \frac{ddf_s\, T_+}{c_s} - \frac{P_{(T<1°C)}}{c_s} \right\} (t, x, y) dA \quad (3)$$

where $ddf_{f\&i}$ is a degree-day factor of firn and ice of 6.5 ± 0.5 mm w.e. °C^{-1} (Guðmundsson and others, 2009; Magnússon and others, 2016), ddf_s is a degree-day factor of snow of 5.5 ± 0.5 mm w.e. °C^{-1} (Guðmundsson and others, 2009; Belart and others, 2017), $c_{f\&i}$ is the conversion factor of firn and ice to water of 0.75 ± 0.1 and c_s is the conversion factor of snow to water of 0.5 ± 0.1. α and β are binary switches; $\alpha = 1$ and $\beta = 0$, meaning that the glacier surface at the location analyzed contains firn or ice, until $P_{(T<1°C)} < 0$, when they switch to $\alpha = 0$ and $\beta = 1$, meaning that new snow is present at the location, changing the *ddf* and conversion factor. If the new snow is completely melted, the switches turn back to $\alpha = 0$ and $\beta = 1$ as firn and ice reappear on the glacier surface (Fig. 3). The gridded temperature from Crochet and Jóhannesson (2011) was used to calculate the positive degree-days, T_+, and to set the 1°C threshold between rain and snow in precipitation (Jóhannesson and others, 1995). The HM-Model was utilized to infer *P* for the period 1980–2014 since the numerical model shows a realistic fit to precipitation records (Nawri and others, 2017a). The seasonal corrections of the 1960 datasets were computed with the LT-Model from Crochet and others (2007) after scaling it towards the HM model by linearly fitting summer precipitation in the overlapping time period (1980–2006). The gridded climate data were bilinearly resampled to 20 m grid to adequately crop the coarse model results to the glacier outline.

This methodology ignores changes in ice surface elevation caused by vertical ice motion, which is on the same order as the seasonal mass balance. This does not matter for glacier-wide calculations as the integral of the vertical ice surface velocity is zero over whole ice flow basins by continuity (e.g. Belart and others, 2017).

The seasonal correction from Eqn (3) was calculated by bootstrapping, performing 1000 realizations of the correction and adding random Gaussian errors on each iteration to the variables $ddf_{f\&i}$, ddf_s, $c_{f\&i}$, c_s, *T* and *P*. A summary of parameters and uncertainties is described in the Supplement S6. The errors added to *T* and *P* were applied as offsets, up to ±0.5 °C (T) and ±50 mm (P) to the entire climatic data on Eyjafjallajökull, as random errors at individual grid points would cancel each other out in the bootstrapping method and spatially widespread offsets are more likely to occur (Nawri and others, 2017a). From the histogram of the 1000 realizations we extracted the median value of $dV_{tDEM}^{1\,Oct}$ with 95% confidence interval for each date of survey (Fig. 3). Results of this correction are summarized in Table S3.

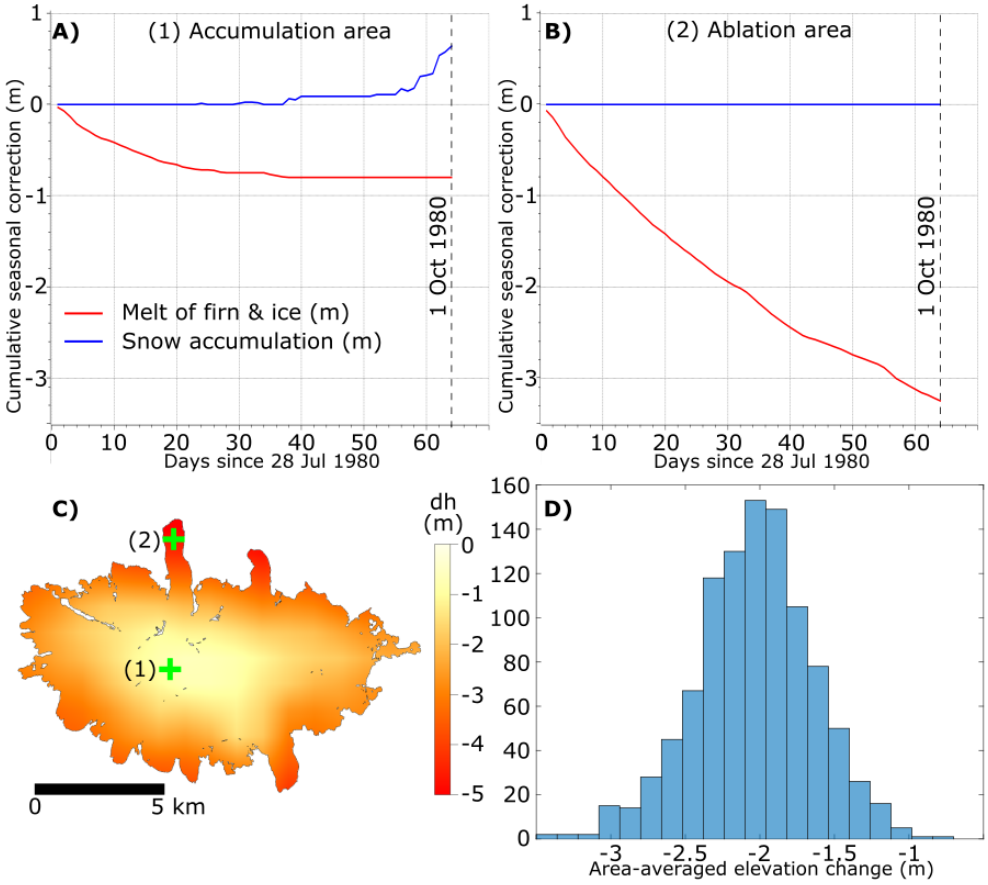

Fig. 3. (A, B) One iteration of calculated cumulative seasonal correction, at two grid locations (1) and (2), between 27 July 1980 and 1 October 1980 (the longest seasonal correction). (C) Total seasonal correction for the same iteration (cumulative melt minus cumulative snow accumulation). Green crosses indicate location of the profiles in (A) and (B). (D) A histogram of 1000 realizations of the seasonal correction (averaged over the whole ice cap) from bootstrapping.

The uncertainties of $\dot{B}$ and $\dot{B}_{EOS}$ were calculated by the addition *in quadrature* of the partial derivative of each variable multiplied by its uncertainty, assuming that the variables of Eqns (1) and (2) were uncorrelated and had uncertainties following normal distributions (Fischer and others, 2015; Magnússon and others, 2016). The glacierized areas were always digitized by the same operator and using the same criteria of definition of the ice cap boundaries. Uncertainties in the area were neglected: given the size of Eyjafjallajökull, the maximum area uncertainty was assumed of 5%, as digitized from the coarsest resolution (ASTER) dataset (Raup and others, 2014). This would only lead to <0.01 m w.e.a^{-1} increase of the uncertainty of the geodetic mass balance.

4.3 Joint analysis of mass balance and climatic records

The calculated $\dot{B}_{EOS}$ overlaps in time with the climatic records for the period 1960–2014. With this data we constrained a statistical model relating mass balance and climate forcing, which also allowed retrieving the static mass-balance sensitivity to changes in climatic variables (De Woul and Hock, 2005; Ohmura, 2011; Sakai and Fujita, 2017). The time span of our observations is long enough to be affected by dynamic adjustments of glacier geometry (Huss and others, 2012). We thus assume that the annual, reference-surface mass balance (Elsberg and others, 2001; Harrison and others, 2001) can be described linearly as a function of the summer temperature, Ts, and winter precipitation, Pw (e.g. Oerlemans and Reichert, 2000; De Woul and Hock, 2005; Schuler and others, 2005)

$$\dot{B}_{EOS} + b_g \Delta V + b_a \Delta A = \varphi Ts + \omega Pw + k \quad (4)$$

where b_g and b_a are the effective balance-rate gradient and balance rate at the terminus, respectively (Harrison and others, 2001), and ΔV and ΔA are the changes in volume and area between a reference date and the intermediate date of each time period, respectively.

The static sensitivity of mass balance to 1°C warming in summer temperature, $\partial \dot{B} / \partial Ts$, is represented by φ, and analogously, $\partial \dot{B} / \partial Pw = \omega$, which yields the sensitivity of mass balance to changes in winter precipitation. The parameter k represents a residual term due to any nonlinear effect of the above variables as well as contribution of other variables affecting the mass balance not accounted for (Oerlemans and Reichert, 2000); here we assume that the variability of this term is small and therefore set as constant. This is further considered in the Discussion.

With the gridded climatic records we calculated summer temperature and winter precipitation for each year at the Equilibrium Line Altitude (ELA, De Woul and Hock, 2005) of Eyjafjallajökull, and defining the glaciological year from 1 October to 30 September, with the beginning of summer on 20 May (Magnússon and others, 2016; Belart and others, 2017). The results were averaged to match the time periods of the geodetic mass balance from 1960 to 2014. We excluded the intervals 2009–2010 and 2010–2014 in the analysis, since they were strongly affected by the April 2010 volcanic eruption. The winter precipitation 1960–1980 was calculated from the LT Model after linearly adjusting it to the HM Model using winter precipitation in the overlapping years (1980–2006). For the periods 1960–1980 and 1980–1984 we selected the geodetic results extracted from the KH-9 DEM, as the required seasonal correction was smaller.

The precipitation was normalized (Oerlemans and Reichert, 2000), dividing it by the average winter precipitation during 1960–2014: 5220 mm. This value is similar to rates of winter accumulation

measured on the neighboring Mýrdalsjökull ice cap (Ágústsson and others, 2013). Sensitivity to a 10% winter precipitation increase was therefore calculated as 10% of ω (e.g. Oerlemans and Reichert, 2000; Schuler and others, 2005).

Altogether we obtained seven independent equations that were solved by weighted least-squares fit. We performed the adjustment based on two scenarios: (1) fixing $b_g = 0.01$ a^{-1} and $b_a = -5$ m a^{-1} as a first estimate based on literature (Harrison and others, 2001) and from the geodetic records of Eyjafjallajökull and solving for three unknowns (φ, ω, k); (2) considering that ΔV and ΔA are linearly dependent for the analyzed time periods (R^2=0.97, N=7), Eqn (4) can be simplified to

$$\dot{B}_{EOS} = \varphi Ts + \omega Pw + \gamma \Delta A + k \quad (5)$$

where γ includes both terms b_g and b_a and allows solving the least-square fit with four unknowns $(\varphi, \omega, \gamma, k)$. Both scenarios yielded highly similar results. We did not attempt to solve the terms b_g and b_a as additional unknowns in the least-square fit since the system may become unstable, due to limited amount of observations and high correlation between terms.

Finally, using Eqn (5) with the solved parameters we computed the annual mass balance from 1958 to 2014 using the annual winter precipitation, summer temperature and glacier area, assumed to change at the same annual rate between each two datasets.

5 Results

5.1 Elevation changes and uncertainties

The SGSim-correction yielded uncertainties of sub-meter to a meter (Table 2) in the glacier-wide elevation difference. Uncertainties are larger and biases are significantly different when using descriptive statistics off-glacier (Table 2 and Table S3), as observed by Magnússon and others (2016) and Rolstad and others (2009). Using the SGSim-correction for two datasets with close dates of survey, 1960 DMA and 1960 LMÍ series (Table 1), the glacier-wide mean elevation change during 1960–2010 is -13.83 ± 0.31 m and -13.38 ± 0.41 m respectively. The remaining difference is largely explained by -0.36 ± 0.14 m of melting between datasets, calculated from the seasonal correction described in Section 4.2. Similarly, the glacier-wide mean elevation change during 1980–2010 is -20.13 ± 0.41 m (LMÍ dataset) and -19.35 ± 0.99 m (KH-9 dataset). In this case, the seasonal effect is larger, -1.43 ± 0.44 m, also explaining most of the observed difference. Larger mismatch of glacier-wide mean elevation difference were found when the correction was based only on off-glacier areas, up to 3.4 m difference (both series of 1960–2010) and up to 3.5 m difference (both series 1980–2010), which further diverge when applying seasonal correction.

The time series of elevation changes reveal strong fluctuations in the volume of the ice cap through recent decades, showing overall mass loss in 1945–1960 and 1994–2014, and mass gain in 1960–1994 (Figs 4 and 5). The rates of elevation change in 1960–1994 (mass gain) and 1994–2014 (mass loss) show a mirrored pattern in the rate of elevation change as a function of altitude (Fig. 5). Glacier-wide mean cumulative elevation change is 14 m for 1960–1994 and –27 m for 1994–2014. The glacier catchments on the north side (Gígjökull and Steinsholtsjökull, Fig. 1) contain the fastest-

changing outlets, thickening up to 130 m in 1960–1994 and thinning up to 200 m in 1994–2014 near their respective termini.

The changes in the most recent periods, 2009–2010 and 2010–2014, are affected by the April 2010 Eyjafjallajökull eruption. A maximum thinning of 180 m is observed in 2009–2010, due to the subglacial melting along the lava paths of the 2010 eruption, and filling of the opened channel is observed in 2010–2014 as an effect of ice dynamics (Aðalgeirsdóttir and others, 2000), leading to maximum thickening of 100 m in 2010–2014 (Fig. 4).

The DEM and orthoimage created from the declassified KH-9 imagery cover approximately one-third of Iceland and about one-third of the glacierized areas (~3400 km^2) of the country (Fig. 6). From the comparison with the 2010 lidar, the SGSim-corrected glacier-wide elevation change has an uncertainty of 1 m at 95% confidence level (Table S1). The KH-9 DEM and EMISAR DEMs have a large overlap, allowing the comparison of the datasets and analysis of large-scale elevation changes. Results show a good fit between the KH-9 DEM and EMISAR, with a median elevation difference of 2.08 m and NMAD of 5.73 m in all unchanged areas, including areas far away (>50 km) from the GCPs (Fig. 6). These statistics are partially affected by the errors of the EMISAR DEM, which has a relative accuracy of 1–2 m (Magnússon, 2003; Guðmundsson and others, 2011) as well as errors related to the different resolution of the grids compared. This comparison also reveals clear signals of glacier changes during 1980–1998, specifically mass loss of Eyjafjallajökull and Mýrdalsjökull, and advance of the several surging outlet glaciers in west Vatnajökull (Björnsson and others, 2003).

Table 2. Statistics off- and on-glacier from the multiple dDEM combinations. Statistics (median ± NMAD elevation difference) off-glacier were calculated after excluding slope >30°

Series	**dDEM off-glacier**	**dDEM on-glacier**	
	Median ± NMAD (m)	Glacier-wide mean of SGSim-correction ± 95% uncertainty (m)	SGSim-corrected glacier-wide mean elevation change (m)
1945 AMS–1960 DMA	2.61 ± 5.54	–3.31 ± 1.96	–6.07 ± 1.81
1960 DMA–1980 LMÍ	–1.81 ± 3.73	2.22 ± 0.38	8.56 ± 0.40
1960 DMA–1980 KH-9	–5.43 ± 6.82	2.24 ± 1.19	7.49 ± 1.16
1980 LMÍ–1984 LMÍ	0.46 ± 2.43	–0.52 ± 0.49	–0.99 ± 0.48
1980 KH-9–1984 LMÍ	6.02 ± 4.61	–0.87 ± 1.21	0.47 ±1.12
1984 LMÍ–1989 LMÍ	–0.67 ± 2.03	3.00 ± 0.48	4.55 ± 0.46
1989 LMÍ–1994 LMÍ	0.93 ± 1.68	–2.19 ± 0.50	2.55 ± 0.48
1994 LMÍ–1998 EMISAR	0.13 ± 1.30	–0.41 ± 0.29	–8.66 ± 0.29
1998 EMISAR–2004 SPOT5	0.02 ± 2.56	0.12 ± 0.18	–11.94 ± 0.18
2004 SPOT5–2009 ASTER	–1.48 ± 5.21	–1.74 ± 0.24	–2.22 ± 0.24
2009 ASTER–2010 lidar	0.38 ± 3.25	0.72 ± 0.23	–3.56 ± 0.23
2010 lidar–2014 Pléiades	–0.02 ± 0.32	–0.35 ± 0.08	–1.59 ± 0.08
1960 DMA–1994 LMÍ	–1.74 ± 2.82	1.98 ± 0.30	13.90 ± 0.29
1994 LMÍ–2014 Pléiades	–0.24 ± 0.75	0.29 ± 0.22	–26.84 ± 0.21
1945 AMS–2014 Pléiades	–0.34 ± 4.69	–1.11 ± 2.24	–19.54 ± 2.24

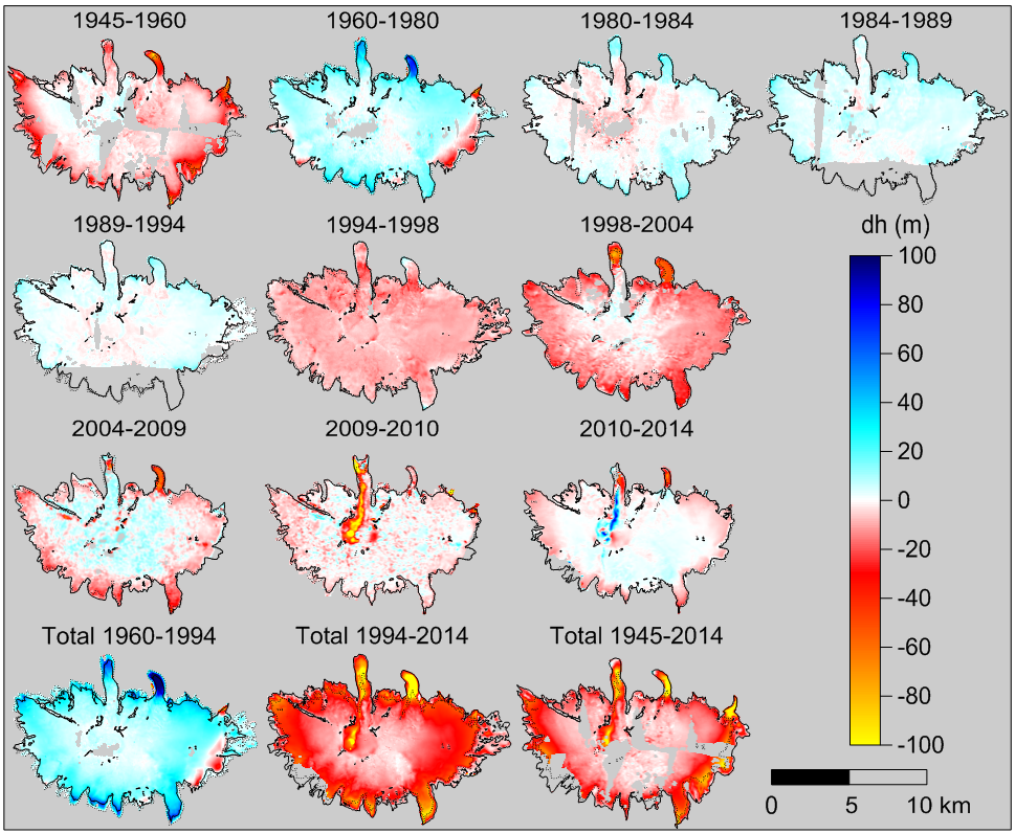

Fig. 4. Time series of elevation changes of Eyjafjallajökull. The dDEMs were plotted after applying the SGSim and seasonal correction, hence all dates are relative to 1 October. Red and yellow color indicates lowering, and cyan and blue indicate thickening. A continuous black polygon and a dashed black polygon indicate the ice cap extent and nunataks at the start and end of the analyzed time period, respectively. The three bottom images show the total elevation changes during multi-decadal time periods, 1960–1994 (mass gain), 1994–2014 (mass loss) and 1945–2014 (longest time interval).

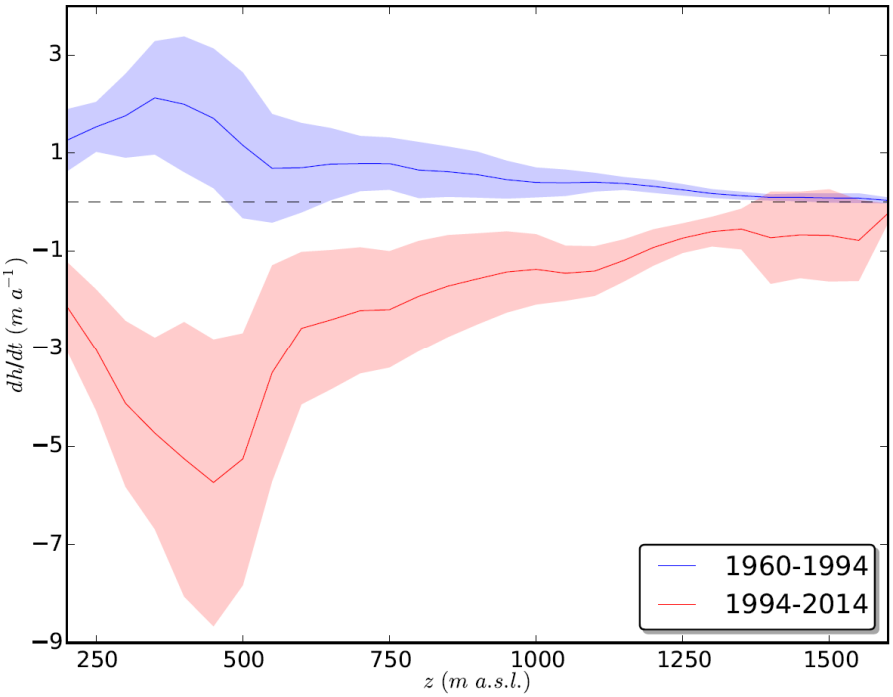

Fig. 5: Mean rate of elevation change extracted for 50 m elevation bands (solid lines) and the corresponding standard deviation (filled areas) for the two time periods with most extreme changes: 1960–94 (blue) and 1994–2014 (red).

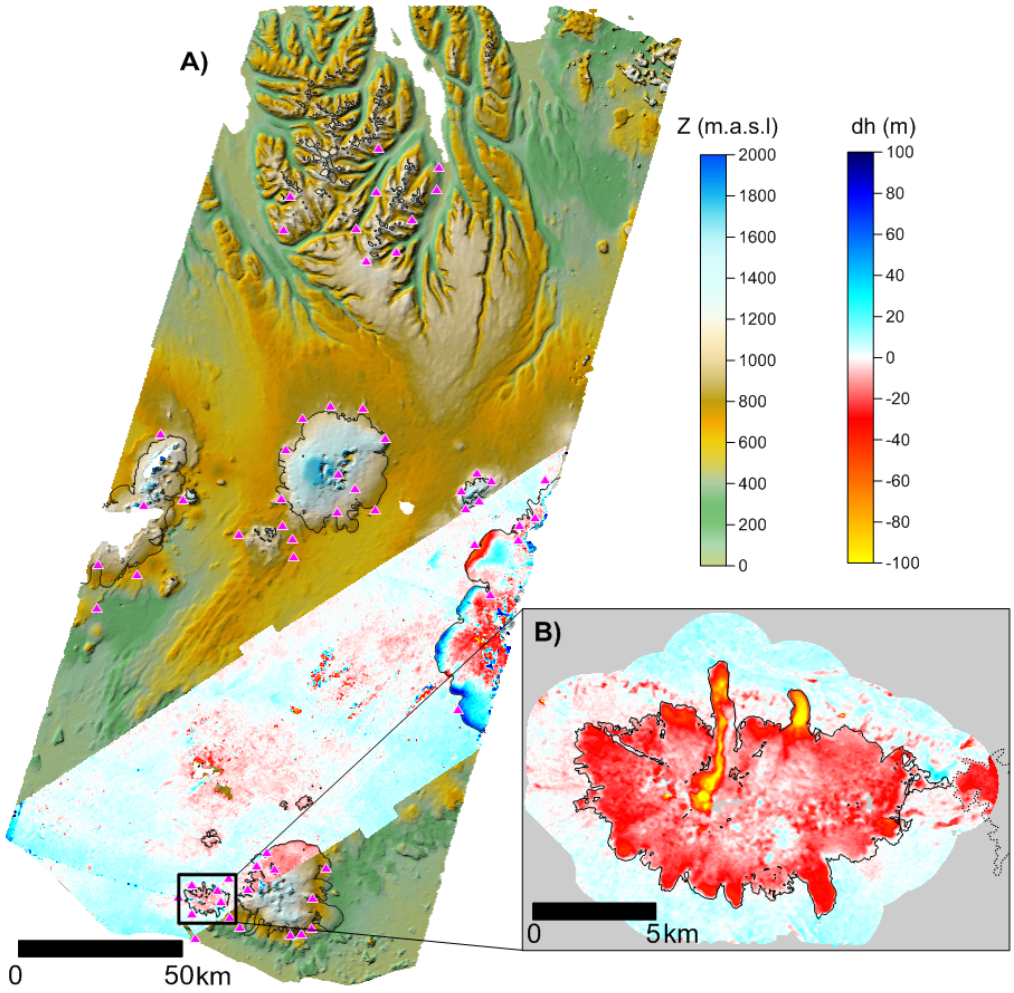

Fig. 6: Results from 1980 KH-9 processing. (a) KH-9 DEM from 22 August 1980 in a color hillshade, overlaid with the difference of elevation between the KH-9 DEM and the EMISAR DEM (1998). Red color indicates lowering, and blue color indicates increase in elevation. Triangles show the GCPs used for the processing of the KH-9 DEM, located where lidar data were available. The outlines of glacierized areas are shown with black lines, extracted from the GLIMS glacier database (Raup and others, 2007). Note thickening at the margin of the southwest outlets from Vatnajökull ice cap, which surged between 1992 and 1994 (Björnsson and others, 2003). (b) Difference in elevation between the KH-9 DEM (1980) and the lidar DEM (2010), together with elevation differences within a 2 km buffer from the glacier outline. The greatest lowering is due to the April 2010 Eyjafjallajökull eruption and the melting of Steinsholtsjökull (northwest). Dashed lines indicate the neighbor ice cap, Mýrdalsjökull.

5.2 Geodetic mass balance

The geodetic records yield a negative mass balance of $\dot{B}_{EOS}{}_{1945}^{2014} = -0.27 \pm 0.03$ m w.e. a^{-1} for the entire study period, reaching a maximum of $\dot{B}_{EOS}{}_{1984}^{1989} = 0.77 \pm 0.19$ m w.e. a^{-1} and a minimum of $\dot{B}_{EOS}{}_{1994}^{1998} = -1.94 \pm 0.34$ m w.e. a^{-1}. During the period 2009–2010, which includes the Eyjafjallajökull eruption, the mass loss was $\dot{B}_{2009}^{2010} = -3.39 \pm 0.43$ m w.e. a^{-1} (without seasonal correction, further described in the Discussion). Detailed results of the mass balance for each time interval are provided in Table 3.

There are differences up to 0.4 m w.e. a^{-1} between uncorrected and seasonally corrected geodetic mass balances for periods as short as 4–6 years, but the difference becomes negligible for long periods (≥20 years, Table 3). The seasonal correction is particularly high in geodetic calculations involving the LMÍ datasets from the 1980s due to seasonal variations in acquisition dates (Table 1). The largest seasonal correction was -1.98 ± 0.69 m (glacier-wide lowering) for the LMÍ DEM of 28 July 1980, since it was acquired 2 months before the end of the summer, whereas -0.56 ± 0.40 m was estimated between 22 August 1980 (KH-9) and 30 September 1980. The seasonal corrections for each date of survey are listed in Supplement S6 (Table S2).

Table 3. Glacier-wide geodetic mass balance of Eyjafjallajökull with and without seasonal correction

Time period	$\dot{B}$ (m w.e. a^{-1})	$\dot{B}_{EOS}$ (m w.e. a^{-1})
1945–60	–0.36 ± 0.11	–0.45 ± 0.12
1960–80 LMÍ	0.36 ± 0.03	0.35 ± 0.05
1960–80 KH-9	0.33 ± 0.06	0.38 ± 0.07
1980 LMÍ–1984	–0.23 ± 0.11	0.20 ± 0.21
1980 KH-9–1984	0.13 ± 0.26	0.25 ± 0.29
1984–89	0.91 ± 0.10	0.77 ± 0.19
1989–94	0.44 ± 0.09	0.37 ± 0.21
1994–98	–1.95 ± 0.28	–1.94 ± 0.34
1998–2004	–1.78 ± 0.13	–1.60 ± 0.14
2004–09	–0.39 ± 0.05	–0.39 ± 0.05
2009–10	–3.43 ± 0.43	–5.12 ± 0.90*
		–3.39 ± 0.43**
2010–14	–0.41 ± 0.06	–0.24 ± 0.22*
		–0.64 ± 0.17**
Cold 1960–94	0.38 ± 0.03	0.39 ± 0.04
Warm 1994–2014	–0.86 ± 0.06	–0.86 ± 0.07
Total 1945–2014	–0.26 ± 0.03	–0.27 ± 0.03

* $\dot{B}_{EOS}$ obtained after applying seasonal correction on the 2010 dataset (the insulation effect from the tephra is not taken into account).

** $\dot{B}_{EOS}$ calculated excluding the seasonal correction of the 2010 dataset (assuming the tephra layer insulated the ice cap during summer 2010).

5.3 Correlation between climatic variables and geodetic mass balance

The time series of summer temperature at the ELA (1200–1300 m a.s.l.) and its average over the time periods of the geodetic mass balance reveal a clear cooling during the early 1980s, reaching a minimum of $Ts_{1980}^{1984} = 1.9°C$, averaged. Temperatures gradually increased to $Ts_{1998}^{2004} = 3.3°C$, and remained high with little change until 2014 (Fig. 7).

On the other hand, the winter precipitation shows an increase reaching its maximum of $Pw_{1989}^{1994}/ref = 1.15$. This is followed by a drop and minimum of $Pw_{1994}^{1998}/ref = 0.85$. The last three time periods are close to average and have a high annual variability (Fig. 7).

Results from the linear fit of seasonally corrected, reference-surface geodetic mass balance and climate records yield a static mass-balance sensitivity to 1°C warming in summer temperature and 10% increase in winter precipitation of -2.08 ± 0.45 m w.e. a^{-1} K^{-1} and 0.51 ± 0.25 m w.e. a^{-1} $(10\%)^{-1}$, respectively. The observed versus modeled mass balance yields a coefficient of determination
$R^2 = 0.81$ (N=7). The mean absolute residual is 0.28 m w.e. a^{-1}, with highest residual of 1.30 m w.e. a^{-1} for the period 1980–84 (Fig. 7), thus indicating a rather poor fit in the least-squares adjustment for this specific time period. The modeled annual mass balance yields an interannual variability of (SD=1.57 m w.e. a^{-1}, N=56).

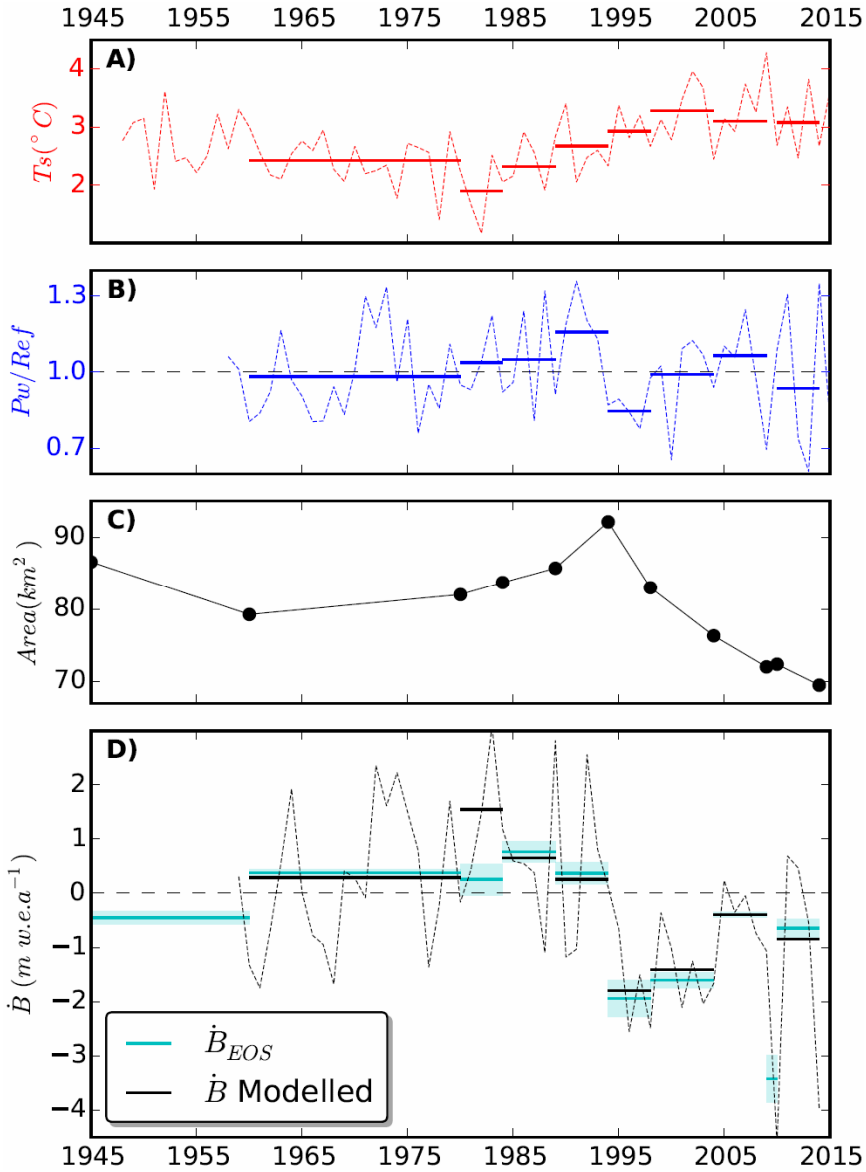

Fig. 7: (A) Inferred summer temperature at the ELA during 1948–2015 (dashed lines) and averages over the time periods of the geodetic mass balance (solid lines). (B) Normalized winter precipitation at ELA (winter precipitation divided by 1960–2014 average), both annual (dashed line) and averaged over the geodetic mass balance periods (solid lines). The period 1958–1979 was calculated from the scaled LT-Model (section 4.3), and the period 1980–2015 was extracted from the HM-Model. (C) Black points indicate area measured at each year of survey. (D) Comparison of observed $\dot{B}_{EOS}$ (cyan lines) and modeled mass balance from Eqn (5) (black lines). The plotted mass balance and area involving the 1980 dataset is calculated using the KH-9 series because it is closer to the end of the summer. All dates are fixed to the glaciological year starting on 1 October.

6 Discussion

6.1 Remote sensing and open-source alternatives: MicMac, ASP and GSLib

The pipeline of processing stereoscopic data (aerial, spaceborne, frame and pushbroom) and assessing uncertainties was carried out in a semi-automated workflow. Manual steps in the workflow are: (1) measurement of fiducial marks in the frame imagery, (2) measurements of GCPs, (3) digitization of glacier outlines, (4) manual mask of unfiltered artifacts and (5) fitting of a semivariogram model.

Many studies have used photogrammetry and SfM for DEM generation for glaciers with historical aerial photographs generally using commercial software (e.g. Barrand and others, 2009; Mölg and Bolch, 2017; Fieber and others, 2018). Here the entire processing was carried out using only open-source software (MicMac). The obtained uncertainties of elevation changes are similar to previous studies using commercial software, such as ERDAS Imagine for frame stereo imagery processing (e.g. Magnússon and others, 2016) or PCI Geomatica for pushbroom stereo imagery processing (Berthier and others, 2014). The use of semi-global matching in point cloud generation produces an excellent level of detail and limited gaps in DEMs, even in snow areas with low contrast. This illustrates that robust scientific research can be carried out using open-source alternatives. In addition, most input data for our study are open access (see Data availability section below). The semi-automated pipelines and open data provide important tools that can be used in future work, given the amount of historical aerial photographs available in Iceland and elsewhere.

This study further supports the need for robust geostatistics to assess uncertainties of volume changes deduced from DEM difference, as previously shown by Rolstad and others (2009) and Magnússon and others (2016). The tests using two surveys conducted close in time both in 1960 and 1980 (Table S1) show excellent agreement of glacier-wide mean elevation changes between each dataset and the 2010 lidar DEM using the SGSim-correction. The difference between glacier-wide elevation changes when utilizing different datasets is <1 m and <2 m for 1960–2010 and 1980–2010, respectively, which is to a large degree explained by the seasonal elevation change between the respective surveys.

The other methods tested for glacier-wide bias correction and uncertainty estimates, median and NMAD of the off-glacier areas, and median and NMAD of the off-glacier areas at 1 km buffer from the ice cap boundary, led to significantly higher discrepancies in the comparisons of the glacier-wide elevation change 1960–2010 using the twin datasets of 1960, and analogously for the twin comparisons of 1980–2010. While the three methods applied to obtain corrected the glacier-wide mean elevation change agreed within their error bars, the error bars of the SGSim were substantially smaller. This further supports that higher level of information can be extracted from geodetic records when applying SGSim (Magnússon and others, 2016).

Our work exploits Hexagon KH-9 Mapping Camera stereo imagery, generating a DEM of about one-third of Iceland and covering ~3400 km^2 of the following ice masses: Mýrdalsjökull, Hofsjökull, east Langjökull, west Vatnajökull, Kerlingafjöll, Tungnafellsjökull, Tindfjallajökull, Torfajökull and the Tröllaskagi cluster of glaciers. The comparison with lidar in ice- and snow-free areas yields NMAD = 4.07 m (proxy for DEM precision) on slopes <30°, and its uncertainty derived from the

SGSim-corrected glacier-wide elevation change compared with lidar was 1 m (95% confidence level, Table S1). This strengthens the potential of these datasets in geodetic mass balance studies.

A comparison with an independent DEM from the source of GCPs (EMISAR DEM) shows limited distortion of the DEM (NMAD=5.73 m), including areas far away from GCPs. It also reveals the changes in Eyjafjallakökull, Tindfjallajökull, Torfajökull and the western side of Vatnajökull between 1980 and 1998 (Fig. 6), in particular the advances of some outlets of west Vatnajökull due to their surges in the early 1990s (Björnsson and others, 2003). We did not run SGSim between KH-9 and EMISAR DEMs, since no further analysis of a particular area of interest was carried out based on this comparison. The KH-9 spy satellites imaged the entire country in 1977–1980, and previous spy satellite missions imaged large areas of the country since the 1960s (data not scanned, USGS, https://www.usgs.gov/), making these dataset useful for expanding knowledge of the state of Icelandic glaciers in a varying climate with lower temperatures and higher precipitation than at present (Fig. 7).

The time series of elevation differences were completed using spaceborne, pushbroom-based stereo imagery from the last two decades. ASTER offers high potential for producing a series of elevation differences from 2000-present (Nuimura and others, 2012; Willis and others, 2012; Berthier and others, 2016; Brun and others, 2017) and enabled constraining the signal of ice–volcano interaction to the period 2009–2010. SPOT5 provided a DEM observation in 2004, resulting on larger temporal resolution for 2000–2010. Both ASTER and SPOT5 DEMs were processed with open-source software, and the uncertainty obtained was comparable to or better than other studies using similar datasets (e.g. Korona and others, 2009; Berthier and others, 2016).

Our methodology relies on an accurate and high-resolution DEM as a source of GCPs for the frame imagery and for co-registration for the pushbroom imagery. Alternatively to the lidar DEM used here, other data sources could be used, such as a Pléiades-based data (Papasodoro and others, 2015) or WorldView-based data (Fieber and others, 2018). The relative precision of Pléiades- and WorldView-based DEMs is <0.5 m (Slopes <10°) and overall <1 m (e.g. Berthier and others, 2014; Shean and others, 2016; Belart and others, 2017), often close to the precision of lidar (e.g. Jóhannesson and others, 2011). The absolute accuracy of these DEMs is affected by uniform horizontal and vertical biases on the order of meters or a few meters and to some degree tilts leading to vertical biases on the same order, but these cancel out in the calculation of elevation changes if GCPs are based on the same Pléiades- and WorldView-based DEMs. Both data sources are of relatively easy access to the research community; for example WorldView data are freely available for latitudes >60°N via ArcticDEM (Porter and others, 2018).

6.2 Area, elevation and mass balance changes in Eyjafjallajökull

The ice cap retreated and thinned in 1945–1960, advanced and thickened in 1960–1994 and retreated and thinned again in 1994–2014. In situ observations of front variations from the Icelandic Glaciological Society (http://spordakost.jorfi.is/) indicate that the outlet Gígjökull started to advance between 1971 and 1979 (Sigurðsson, 1998). The northern outlets show much more rapid front changes than the southern outlets, suggesting higher ice motion in the northern ice catchments versus the southern catchments. This also explains why during 1960–1980 the northern outlets were advancing and thickening while the southeast and southwest margins were still retreating (Fig. 4).

There is a lag between the maximum geodetic mass balance in 1984–1989 and the area maximum, reached in 1994 (Fig. 7), which is due to the delayed response of the glacier to the climatic forcing (e.g. Bahr and others, 1998).

Our study underlines the importance of seasonal corrections in the interpretation of records of geodetic mass balance, in particular for glaciers with a maritime regime and high mass turnover (e.g. Magnússon and others, 2016; Belart and others, 2017). Without seasonal corrections, the geodetic mass balances can be misleading over short time periods, for instance in the 1980s when the surveys were conducted during various times in the season (Table 1). However, the seasonal corrections are negligible in long (≥20 years) time periods. Our approach to correct seasonal volume changes refined the degree-day model of Magnússon and others (2016) by accounting for snowfall and snow melt at high elevation, and used bootstrapping to infer the uncertainty, which is generally 30–50% of the correction (Fig. 3). The uncertainty increases with snow correction (generally in late summer) due to the uncertainty in the snow parameters, i.e. the temperature threshold between rain & snow, *ddf* and snow density.

The seasonal correction applied to the 2010 dataset was, however, significantly affected by the 2010 volcanic eruption. The *ddf* does not take into consideration the tephra deposited on the surface of the ice cap. The maps of tephra thickness indicate >2 cm of tephra around Eyjafjallajökull and up to 1 m at locations close to the crater (Guðmundsson and others, 2012). This likely enhanced the melt locally at the lowest elevations, but insulated the majority of the ice cap during summer 2010 (Dragosics and others, 2016). The seasonal correction presented for August–October 2010 would be likely too negative and an overestimation of the melting in this time period.

We do not account for elevation change and subsequent volume change of the summer snowfall due to firn and fresh snow densification in the seasonal corrections as this can only lead to a minor volume correction. If we assume similar rates of firn and fresh snow densification as calculated for Drangajökull ice cap, northwest Iceland (Belart and others, 2017), this would lead to a glacier-wide correction of ~0.07 m, or 3% of the calculated seasonal correction for the 1980 dataset (the largest seasonal correction), well within the uncertainty estimates.

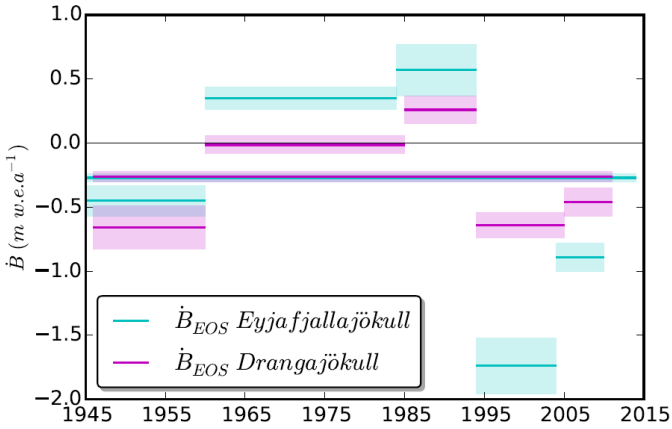

Fig. 8: Geodetic mass balance of Eyjafjallajökull and Drangajökull (Magnússon and others 2016) at selected time intervals. Averages over multiple geodetic mass balance periods are weighted with the number of years of each period.

The obtained geodetic mass balances agree within the error bars with the results from Guðmundsson and others (2011) for Eyjafjallajökull. In comparison to Drangajökull ice cap (northwest Iceland), the geodetic mass balance 1945–2014 is similar to that calculated for 1946–2011 by Magnússon and others (2016). Both ice caps present an overall trend of negative–positive–negative mass balance (Fig. 8), although for Drangajökull the decline was larger in the early years of the geodetic records. During 1960–1994, the mass balances of Eyjafjallajökull were significantly higher than for Drangajökull, and after 1994 Drangajökull shows less negative mass balance than Eyjafjallajökull. The larger mass turnover and higher mass balance variation of Eyjafjallajökull is consistent with its proximity to the persistent paths of the North Atlantic low pressure system, with high precipitation rates, and the warm seas surface temperatures from the Irminger ocean current that largely controls the temperatures over the ice cap, whereas Drangajökull is affected by the cold East Greenland current (Björnsson and others, 2013).

6.3 Relation between glacier and climate

The geodetic mass balance, summer temperature and winter precipitation are well correlated; mass balance increases with lower temperatures and higher precipitation, and vice versa (Fig. 7). Previous studies have analyzed mass balance sensitivity in relation to temperature (Guðmundsson and others, 2011; Pálsson and others, 2012), by using geodetic mass balance and records from nearby weather stations. These studies, however, show a high variability in the results depending on which weather station was used, use few time periods and do not include sensitivity to precipitation. The long-term records of gridded climate data (Crochet and others, 2007; Crochet and Jóhannesson, 2011; Nawri and others, 2017b) and geodetic mass balance allow more in-depth study of the ice cap's response to climate variations.

The link between climate and mass balance needs to account for glacier adjustment to different climates, especially if the mass-balance records span long time periods in comparison to the relatively short response time of the glacier. This is accounted for by calculating reference-surface mass balance (Elsberg and others, 2001; Harrison and others, 2001), which allows comparison of long-term mass balance and climatic variables (Huss and others, 2012). The shift to reference-surface is also needed due to the static definition of the sensitivities calculated in this study (De Woul and Hock, 2005). Other tests (not shown) yielded worse least-square fit if the reference-surface mass balance was not accounted for.

We observe that a simple linear equation relating reference-surface mass balance with summer temperature and winter precipitation can explain 80% of the observed mass balance, but yields a rather poor fit in one particular period. The misfit for 1980–1984 can be explained by a poorly constrained conversion of volume to water equivalent, due to the short time interval (4 years) in a near-balance time period (Huss, 2013), or by an oversimplified relation between mass balance and climate. The latter has nonlinear components (Oerlemans and Reichert, 2000), and additional variables not considered may cause significant variations in the mass balance. For example, strong albedo changes can take place as a consequence of summer snowfalls or from dust events. Alternative equations to estimate mass balance from climatic variables were tested but did not yield a better fit than the equation using summer temperature and winter precipitation: (1) using annual

temperature and precipitation (Guðmundsson and others, 2011; Pálsson and others, 2012) and (2) using the number of positive degree-days instead of temperature.

The obtained sensitivities for Eyjafjallajökull (–2.1 m w.e.a^{-1} K^{-1} and 0.5 m w.e. a^{-1} $(10\%)^{-1}$) are higher than the sensitivities at selected catchments of Hofsjökull and Vatnajökull (–0.8 to –2 m w.e.a^{-1} K^{-1} and 0.1 to 0.3 m w.e. a^{-1} $(10\%)^{-1}$), or other maritime glaciers in the world such as Wolverine, Alaska (–0.8 m w.e.a^{-1} K^{-1} and 0.2 m w.e. a^{-1} $(10\%)^{-1}$) (De Woul and Hock 2005). In particular the sensitivity to precipitation in Eyjafjallajökull is high due to the vast amount of precipitation in the area (the average winter precipitation 1960–2014 is 5220 mm), more than three times the amount of snow accumulation measured in situ at the Icelandic catchments analyzed by De Woul and Hock (2005). Climatic conditions and sensitivities of Eyjafjallajökull agree and are more similar to those of the maritime glacier Ålfotbreen, Norway (–1.7 m w.e.a^{-1} K^{-1} and 0.5 m w.e. a^{-1} $(10\%)^{-1}$), obtained by Engelhardt and others (2015).

Although cautious interpretation is needed in the modeled annual mass balance due to outliers in the least-square method (Fig. 7), it shows larger interannual variability (SD=1.57 m w.e. a^{-1}, N=56) than other Icelandic glacierized areas such as Langjökull (SD=0.82 m w.e. a^{-1}, N=14 (Pálsson and others, 2012)), Vatnajökull (SD=0.83 m w.e. a^{-1}, N=19 (Björnsson and others, 2013)) or Hofsjökull (SD=0.88 m w.e. a^{-1}, N=23 (Jóhannesson and others, 2013)). The high sensitivity to precipitation and high interannual variability can be explained by the more maritime regime of Eyjafjallajökull.

In a regional context, this simple approach to infer annual mass balance as function of climate variables presents a useful tool for a temporal homogenization of mass balances (Lambrecht and Kuhn, 2007; Fischer and others, 2015), as the regional surveys of ice masses often take place within a few years (e.g. Jóhannesson and others, 2013), which causes difficulties in mass balance intercomparisons.

7 Conclusions

This study has described a workflow to extract decadal geodetic mass balance for the last ~70 years based on records of airborne and satellite stereo images from frame and pushbroom sensors, thus producing a series of DEMs, orthoimages and dDEMs with robust uncertainty estimates. Seasonal differences between dates of survey were corrected using a simple degree-day model that considers possible snowfall in summer. All the processes were carried out with open-source software (e.g. MicMac, ASP and GSLib). Among the datasets, we processed six frames from the declassified Hexagon KH-9 Mapping Camera and obtained a DEM covering ~1/3 of Iceland from 1980, including ~3400 km^2 of ice masses. These tools are useful for in-depth regional studies of geodetic mass balance and glacier–climate relationship in Iceland and can be applied elsewhere.

Applied to our test area, Eyjafjallajökull, our pipeline provides a detailed time series of elevation changes and mass balance. The ~70 year average mass balance is $\dot{B}_{1945}^{2014} = -0.27 \pm 0.03$ m w.e. a^{-1}, and we observe high variability on decadal timescales, reaching a maximum of $\dot{B}_{1984}^{1989} = 0.77 \pm 0.19$ m w.e. a^{-1}, and minimums of $\dot{B}_{1994}^{1998} = -1.94 \pm 0.34$ m w.e. a^{-1} for climatic forcing and $\dot{B}_{2009}^{2010} = -3.39 \pm 0.49$ m w.e. a^{-1} mostly due to the subglacial melting during the April 2010 eruption.

Variations in the reference-surface mass balance correlate with changes in summer temperature and winter precipitation, and a simple linear model can explain most of the observed mass balance variations, except for the period 1980-84. The static sensitivity to 1°C warming and 10% precipitation increase is -2.08 ± 0.45 m w.e. a^{-1} K^{-1} and 0.51 ± 0.25 m w.e. a^{-1} $(10\%)^{-1}$, respectively. The sensitivity to precipitation is substantially higher than estimates at other locations in Iceland, probably due to the strong maritime regime of Eyjafjallajökull.

This study serves as a template, of particular relevance and applicability in a regional context, for extraction of long records of geodetic mass balances and the study of the glaciers' response to climate and other possible forcing.

Data availability

All the frame imagery used in the study is open access, upon request to Landmælingar Íslands (www.lmi.is), or downloadable from the US Geological Survey (www.earthexplorer.usgs.gov). The pushbroom images from SPOT5 and Pléiades, as well as the EMISAR DEM, have data access restriction. All the maps of elevation difference are available upon request. ASTER imagery can be downloaded at https://search.earthdata.nasa.gov/. The lidar data are available upon request to the authors (Jóhannesson and others, 2013). All meteorological data (daily temperature and precipitation, both LT-Model and HM-Model) are available upon request from www.vedur.is.

Acknowledgements

This study was funded by the University of Iceland (UI) Research Fund. Collaboration and travels between IES and LEGOS were funded by the Jules Verne research fund. We thank David Shean and an anonymous reviewer for their valuable comments, which greatly improved the manuscript. We thank Carsten Kristiansson at LMÍ for scanning the aerial photographs, Oleg Alexandrov for his helpful tips and advice on ASP, Luc Girod for his help in the MicMac forum and Deirdre Clark and Ken Moxham for the English-language editing of the manuscript. Pléiades images were acquired at research price thanks to the CNES ISIS program (http://www.isis-cnes.fr). This study uses the lidar mapping of the glaciers in Iceland, funded by the Icelandic Research Fund, the Landsvirkjun research fund, the Icelandic Road Administration, the Reykjavík Energy Environmental and Energy Research Fund, the Klima- og Luftgruppen research fund of the Nordic Council of Ministers, the Vatnajökull National Park, the organization Friends of Vatnajökull, LMÍ, IMO and the UI research fund. This study uses the GLIMS database of the outlines of Icelandic glaciers. E.B. acknowledges support from the French Space Agency (CNES) through the TOSCA program.

References

Aðalgeirsdóttir G, Guðmundsson GH and Björnsson H (2000) The response of a glacier to a surface disturbance: a case study on Vatnajökull ice cap, Iceland. *Ann. Glaciol.* **31**, 104–110

Aðalgeirsdóttir G, Guðmundsson S, Björnsson H, Pálsson F, Jóhannesson T, Hannesdóttir H, Sigurðsson SÞ and Berthier E (2011) Modelling the 20th and 21st century evolution of Hoffellsjökull glacier, SE-Vatnajökull, Iceland. *The Cryosphere* **5**(4), 961–975 (doi:10.5194/tc-5-961-2011)

Ágústsson H, Hannesdóttir H, Thorsteinsson T, Pálsson F and Oddsson B (2013) Mass balance of Mýrdalsjökull ice cap accumulation area and comparison of observed winter balance with simulated precipitation. *Jökull* **63**, 91–104

Bahr DB, Pfeffer WT, Sassolas C and Meier MF (1998) Response time of glaciers as a function of size and mass balance: 1. Theory. *J. Geophys. Res.-Solid Earth* **103**(B5), 9777–9782

Barrand NE, Murray T, James TD, Barr SL and Mills JP (2009) Optimizing photogrammetric DEMs for glacier volume change assessment using laser-scanning derived ground-control points. *J. Glaciol.* **55**(189), 106–116

Belart JMC, Berthier E, Magnússon E, Anderson LS, Pálsson F, Thorsteinsson T, Howat IM, Aðalgeirsdóttir G, Jóhannesson T and Jarosch AH (2017) Winter mass balance of Drangajökull ice cap (NW Iceland) derived from satellite sub-meter stereo images. *The Cryosphere* **11**(3), 1501–1517 (doi:10.5194/tc-11-1501-2017)

Bengtsson L, Andrae U, Aspelien T, Batrak Y, Calvo J, de Rooy W, Gleeson E, Hansen-Sass B, Homleid M, Hortal M, Ivarsson K-I, Lenderink G, Niemelä S, Nielsen KP, Onvlee J, Rontu L, Samuelsson P, Muñoz DS, Subias A, Tijm S, Toll V, Yang X and Køltzow MØ (2017) The HARMONIE–AROME Model Configuration in the ALADIN–HIRLAM NWP System. *Mon. Weather Rev.* **145**(5), 1919–1935 (doi:10.1175/MWR-D-16-0417.1)

Berthier E, Cabot V, Vincent C and Six D (2016) Decadal Region-Wide and Glacier-Wide Mass Balances Derived from Multi-Temporal ASTER Satellite Digital Elevation Models. Validation over the Mont-Blanc Area. *Front. Earth Sci.* **4** (doi:10.3389/feart.2016.00063)

Berthier E, Vincent C, Magnússon E, Gunnlaugsson ÁÞ, Pitte P, Le Meur E, Masiokas M, Ruiz L, Pálsson F, Belart JMC and Wagnon P (2014) Glacier topography and elevation changes derived from Pléiades sub-meter stereo images. *The Cryosphere* **8**(6), 2275–2291 (doi:10.5194/tc-8-2275-2014)

Bindschadler R and Vornberger P (1998) Changes in the West Antarctic ice sheet since 1963 from declassified satellite photography. *Science* **279**(5351), 689–692

Björnsson H, Pálsson F, Guðmundsson MT and Haraldsson HH (1998) Mass balance of western and northern Vatnajökull, Iceland, 1991-1995. *Jökull* **45**, 35–38

Björnsson H, Pálsson F, Guðmundsson S, Magnússon E, Aðalgeirsdóttir G, Jóhannesson T, Berthier E, Sigurðsson O and Thorsteinsson T (2013) Contribution of Icelandic ice caps to sea level rise: trends and variability since the Little Ice Age. *Geophys. Res. Lett.* **40**, 1–5 (doi:10.1002/grl.50278)

Björnsson H, Pálsson F, Sigurðsson O and Flowers GE (2003) Surges of glaciers in Iceland. *Ann. Glaciol. Vol 36*, 82–90

Brun F, Berthier E, Wagnon P, Kääb A and Treichler D (2017) A spatially resolved estimate of High Mountain Asia glacier mass balances from 2000 to 2016. *Nat. Geosci.* **10**(9), 668 (doi:10.1038/ngeo2999)

Cogley JG, Hock R, Rasmussen LA, Arendt AA, Bauder A, Braithwaite RJ, Jansson P, Kaser G, Möller M, Nicholson L and Zemp M (2011) Glossary of glacier mass balance and related terms, IHP-VII Technical Documents in Hydrology No. 86, IACS Contribution No. 2, UNESCO-IHP, Paris. , 114

Crochet P and Jóhannesson T (2011) A dataset of daily temperature in Iceland for the period 1949–2010. *Jökull* **61**, 1–17

Crochet P, Jóhannesson T, Jonsson T, Sigurðsson O, Björnsson H, Pálsson F and Barstad I (2007) Estimating the spatial distribution of precipitation in Iceland using a linear model of orographic precipitation. *J. Hydrometeorol.* **8**(6), 1285–1306

Dall J (2003) Cross-calibration of interferometric SAR data. *Sonar Navig. IEE Proc. - Radar* **150**(3), 177–183 (doi:10.1049/ip-rsn:20030448)

De Woul M and Hock R (2005) Static mass-balance sensitivity of Arctic glaciers and ice caps using a degree-day approach. *Ann. Glaciol. Vol 42 2005* **42**, 217–224

Deutsch CV (1998) GSLIB - Geostatistical Software Library and User"s Guide. https://infoscience.epfl.ch/record/51514

Dragosics M, Meinander O, Jónsdóttír T, Dürig T, Leeuw GD, Pálsson F, Dagsson-Waldhauserová P and Thorsteinsson T (2016) Insulation effects of Icelandic dust and volcanic ash on snow and ice. *Arab. J. Geosci.* **9**(2), 126 (doi:10.1007/s12517-015-2224-6)

Elsberg DH, Harrison WD, Echelmeyer KA and Krimmel RM (2001) Quantifying the effects of climate and surface change on glacier mass balance. *J. Glaciol.* **47**(159), 649–658

Engelhardt M, Schuler TV and Andreassen LM (2015) Sensitivities of glacier mass balance and runoff to climate perturbations in Norway. *Ann. Glaciol.* **56**(70), 79–88 (doi:10.3189/2015AoG70A004)

Fieber KD, Mills JP, Miller PE, Clarke L, Ireland L and Fox AJ (2018) Rigorous 3D change determination in Antarctic Peninsula glaciers from stereo WorldView-2 and archival aerial imagery. *Remote Sens. Environ.* **205**(Supplement C), 18–31 (doi:10.1016/j.rse.2017.10.042)

Fischer M, Huss M and Hoelzle M (2015) Surface elevation and mass changes of all Swiss glaciers 1980–2010. *The Cryosphere* **9**(2), 525–540 (doi:10.5194/tc-9-525-2015)

Guðmundsson S, Björnsson H, Magnússon E, Berthier E, Pálsson F, Guðmundsson MT, Högnadóttir T and Dall J (2011) Response of Eyjafjallajökull, Torfajökull and Tindfjallajökull ice caps in Iceland to regional warming, deduced by remote sensing. *Polar Res.* **30**(7282) (doi:10.3402/polar.v30i0.7282)

Guðmundsson S, Björnsson H, Pálsson F and Haraldsson HH (2009) Comparison of energy balance and degree-day models of summer ablation on the Langjökull ice cap, SW-Iceland. *Jökull* **59**, 1–18

Guðmundsson MT, Thordarson T, Höskuldsson Á, Larsen G, Björnsson H, Prata FJ, Oddsson B, Magnússon E, Högnadóttir T, Petersen GN, Hayward CL, Stevenson JA and Jónsdóttir I (2012) Ash generation and distribution from the April-May 2010 eruption of Eyjafjallajökull, Iceland. *Sci. Rep.* **2**, 572 (doi:10.1038/srep00572)

Harrison WD, Elsberg DH, Echelmeyer KA and Krimmel RM (2001) On the characterization of glacier response by a single time-scale. *J. Glaciol.* **47**(159), 659–664

Hirschmuller H (2008) Stereo Processing by Semiglobal Matching and Mutual Information. *IEEE Trans. Pattern Anal. Mach. Intell.* **30**(2), 328–341 (doi:10.1109/TPAMI.2007.1166)

Höhle J and Höhle M (2009) Accuracy assessment of digital elevation models by means of robust statistical methods. *ISPRS J. Photogramm. Remote Sens.* **64**(4), 398–406 (doi:10.1016/j.isprsjprs.2009.02.003)

Huss M (2013) Density assumptions for converting geodetic glacier volume change to mass change. *The Cryosphere* **7**(3), 877–887 (doi:10.5194/tc-7-877-2013)

Huss M and Hock R (2018) Global-scale hydrological response to future glacier mass loss. *Nat. Clim. Change* **8**(2), 135–140 (doi:10.1038/s41558-017-0049-x)

Huss M, Hock R, Bauder A and Funk M (2010) 100-year mass changes in the Swiss Alps linked to the Atlantic Multidecadal Oscillation. *Geophys. Res. Lett.* **37**

Huss M, Hock R, Bauder A and Funk M (2012) Conventional versus reference-surface mass balance. *J. Glaciol.* **58**(208), 278–286 (doi:10.3189/2012JoG11J216)

James TD, Murray T, Barrand NE and Barr SL (2006) Extracting photogrammetric ground control from lidar DEMs for change detection. *Photogramm. Rec.* **21**(116), 312–328

Jóhannesson T, Björnsson H, Magnússon E, Guðmundsson S, Pálsson F, Sigurðsson O, Thorsteinsson T and Berthier E (2013a) Ice-volume changes, bias estimation of mass-balance measurements and changes in subglacial lakes derived by lidar mapping of the surface of Icelandic glaciers. *Ann. Glaciol.* **54**(63), 63–74 (doi:10.3189/2013AoG63A422)

Jóhannesson T, Björnsson H, Magnússon E, Guðmundsson S, Pálsson F, Sigurðsson O, Thorsteinsson T and Berthier E (2013b) Ice-volume changes, bias estimation of mass-balance measurements and changes in subglacial lakes derived by lidar mapping of the surface of Icelandic glaciers. *Ann. Glaciol.* **54**(63), 63–74 (doi:10.3189/2013AoG63A422)

Jóhannesson T, Björnsson H, Pálsson F, Sigurðsson O and Þorsteinsson Þ (2011) LiDAR mapping of the Snæfellsjökull ice cap, western Iceland. *Jökull* **61**, 19–32

Jóhannesson T, Sigurðsson O, Laumann T and Kennett M (1995) Degree-day glacier mass-balance modelling with applications to glaciers in Iceland, Norway and Greenland. *J. Glaciol.* **41**(138), 345–358 (doi:10.3189/S0022143000016221)

Korona J, Berthier E, Bernard M, Remy F and Thouvenot E (2009) SPIRIT. SPOT 5 stereoscopic survey of Polar Ice: Reference Images and Topographies during the fourth International Polar Year (2007-2009). *ISPRS J. Photogramm. Remote Sens.* **64**, 204–212 (doi:10.1016/j.isprsjprs.2008.10.005)

Krimmel RM (1999) Analysis of difference between direct and geodetic mass balance measurements at South Cascade Glacier, Washington. *Geogr. Ann. Ser. -Phys. Geogr.* **81A**(4), 653–658

Lacroix P (2016) Landslides triggered by the Gorkha earthquake in the Langtang valley, volumes and initiation processes. *Earth Planets Space* **68**(1), 46 (doi:10.1186/s40623-016-0423-3)

Lambrecht A and Kuhn M (2007) Glacier changes in the Austrian Alps during the last three decades, derived from the new Austrian glacier inventory. *Ann. Glaciol.* **46**, 177–184

Leclercq PW and Oerlemans J (2012) Global and hemispheric temperature reconstruction from glacier length fluctuations. *Clim. Dyn.* **38**(5–6), 1065–1079

Magnússon E (2003) Airborne SAR data from S-Iceland: analyses, DEM improvements and glaciological application. *MSc Thesis Dep. Phys. Univ. Icel.*

Magnússon E, Belart JMC, Pálsson F, Ágústsson H and Crochet P (2016) Geodetic mass balance record with rigorous uncertainty estimates deduced from aerial photographs and lidar data – Case study from Drangajökull ice cap, NW Iceland. *The Cryosphere* **10**(1), 159–177 (doi:10.5194/tc-10-159-2016)

Marzeion B, Cogley JG, Richter K and Parkes D (2014) Attribution of global glacier mass loss to anthropogenic and natural causes. *Science* **345**(6199), 919–921

Mölg N and Bolch T (2017) Structure-from-Motion Using Historical Aerial Images to Analyse Changes in Glacier Surface Elevation. *Remote Sens.* **9**(10), 1021 (doi:10.3390/rs9101021)

Nawri N, Pálmason B, Petersen GN, Björnsson H and Þorsteinsson ÁÞ (2017a) The ICRA atmospheric reanalysis project for Iceland. *Icel. Meteorol. Off.* **VÍ 2017-005**, 1–39

Nawri N, Pálmason B, Petersen GN, Björnsson H and Þorsteinsson ÁÞ (2017b) The ICRA atmospheric reanalysis project for Iceland. *Icel. Meteorol. Off.* **VÍ 2017-005**, 1–39

Noh M-J and Howat IM (2015) Automated stereo-photogrammetric DEM generation at high latitudes: Surface Extraction with TIN-based Search-space Minimization (SETSM) validation and demonstration over glaciated regions. *GIScience Remote Sens.* **52**(2), 198–217 (doi:10.1080/15481603.2015.1008621)

Nuimura T, Fujita K, Yamaguchi S and Sharma RR (2012) Elevation changes of glaciers revealed by multitemporal digital elevation models calibrated by GPS survey in the Khumbu region, Nepal Himalaya, 1992–2008. *J. Glaciol.* **58**(210), 648–656 (doi:10.3189/2012JoG11J061)

Nuth C and Kääb A (2011) Co-registration and bias corrections of satellite elevation data sets for quantifying glacier thickness change. *The Cryosphere* **5**(1), 271–290 (doi:10.5194/tcd-4-2013-2010)

Oddsson B, Guðmundsson MT, Edwards BR, Thordarson T, Magnússon E and Sigurðsson G (2016) Subglacial lava propagation, ice melting and heat transfer during emplacement of an intermediate lava flow in the 2010 Eyjafjallajökull eruption. *Bull. Volcanol.* **78**(7), 48 (doi:10.1007/s00445-016-1041-4)

Oerlemans J and Reichert BK (2000) Relating glacier mass balance to meteorological data by using a seasonal sensitivity characteristic. *J. Glaciol.* **46**(152), 1–6

Ohmura A (2011) Observed Mass Balance of Mountain Glaciers and Greenland Ice Sheet in the 20th Century and the Present Trends. *Surv. Geophys.* **32**(4–5), 537–554

Pálsson F, Guðmundsson S, Björnsson H, Berthier E, Magnússon E, Guðmundsson S and Haraldsson H (2012) Mass and volume changes of Langjökull ice cap, Iceland, ~1890 to 2009, deduced from old maps, satellite images and in situ mass balance measurements. *Jökull* **62**, 81–96

Papasodoro C, Berthier E, Royer A, Zdanowicz C and Langlois A (2015) Area, elevation and mass changes of the two southernmost ice caps of the Canadian Arctic Archipelago between 1952 and 2014. *The Cryosphere* **9**(4), 1535–1550 (doi:10.5194/tc-9-1535-2015)

Pierrot Deseilligny M and Clery I (2011) Apero, AN Open Source Bundle Adjusment Software for Automatic Calibration and Orientation of Set of Images. *ISPRS - Int. Arch. Photogramm. Remote Sens. Spat. Inf. Sci.* **3816**, 269–276 (doi:10.5194/isprsarchives-XXXVIII-5-W16-269-2011)

Porter C, Morin P, Howat I, Noh M-J, Bates B, Peterman K, Keesey S, Schlenk M, Gardiner J, Tomko K, Willis M, Cloutier M, Husby E, Foga S, Nakamura H, Platson M, Wethington M Jr, Williamson C, Bauer G, Enos J, Arnold G, Kramer W, Becker P, Doshi A, D'Souza C, Cummens P, Laurier F and Bojesen M (2018) ArcticDEM. (doi:10.7910/DVN/OHHUKH)

Raup BH, Khalsa SJS, Armstrong RL, Sneed WA, Hamilton GS, Paul F, Cawkwell F, Beedle MJ, Menounos BP, Wheate RD, Rott H, Shiyin L, Xin L, Donghui S, Guodong C, Kargel JS, Larsen CF, Molnia BF, Kincaid JL, Klein A and Konovalov V (2014) Quality in the GLIMS Glacier Database. Kargel JS, Leonard GJ, Bishop MP, Kääb A, and Raup BH eds. *Global Land Ice Measurements from Space*. Springer Berlin Heidelberg, Berlin, Heidelberg, 163–182 (doi:10.1007/978-3-540-79818-7_7)

Raup B, Racoviteanu A, Khalsa SJS, Helm C, Armstrong R and Arnaud Y (2007) The GLIMS geospatial glacier database: A new tool for studying glacier change. *Glob. Planet. Change* **56**(1–2), 101–110

Rolstad C, Haug T and Denby B (2009) Spatially integrated geodetic glacier mass balance and its uncertainty based on geostatistical analysis: application to the western Svartisen ice cap, Norway. *J. Glaciol.* **55**(192), 666–680

Rupnik E, Daakir M and Pierrot Deseilligny M (2017) MicMac – a free, open-source solution for photogrammetry. *Open Geospatial Data Softw. Stand.* **2**, 14 (doi:10.1186/s40965-017-0027-2)

Sakai A and Fujita K (2017) Contrasting glacier responses to recent climate change in high-mountain Asia. *Sci. Rep.* **7**(1), 13717 (doi:10.1038/s41598-017-14256-5)

Schuler TV, Hock R, Jackson M, Elvehoy H, Braun M, Brown I and Hagen JO (2005) Distributed mass-balance and climate sensitivity modelling of Engabreen, Norway. *Ann. Glaciol. Vol 42 2005* **42**, 395–401

Shean DE, Alexandrov O, Moratto ZM, Smith BE, Joughin IR, Porter C and Morin P (2016) An automated, open-source pipeline for mass production of digital elevation models (DEMs) from very-high-resolution commercial stereo satellite imagery. *ISPRS J. Photogramm. Remote Sens.* **116**, 101–117 (doi:10.1016/j.isprsjprs.2016.03.012)

Sigmundsson F, Hreinsdóttir S, Hooper A, Árnadóttir T, Pedersen R, Roberts MJ, Óskarsson N, Auriac A, Decriem J, Einarsson P, Geirsson H, Hensch M, Ófeigsson BG, Sturkell E, Sveinbjörnsson H and Feigl KL (2010) Intrusion triggering of the 2010 Eyjafjallajökull explosive eruption. *Nature* **468**(7322), 426 (doi:10.1038/nature09558)

Sigurðsson O (1998) Glacier variations in Iceland 1930-1995 – from the database of the Iceland Glaciological Society. *Jökull* **45**, 3–25

Spriggs RM (1966) The calibration of Military Cartographic Cameras, Technical Note. *Wright-Patterson Air Force Base Ohio USA*

Surazakov AB and Aizen VB (2010) Positional accuracy evaluation of declassified Hexagon KH-9 mapping camera imagery. *Photogramm. Eng. Remote Sens.* **76**(5), 603–608

Vaughan DG, Comiso JC, Allison J, Carrasco J, Kaser R, Kwok R, Mote P, Murray T, Paul F, Ren J, Rignot E, Solomina O, Steffen K and Zhang T (2013) Observations: Cryosphere. *Climate Change 2013: The Physical Science Basis. Contribution of Working Group I to the Fifth Assessment Report of the Intergovernmental Panel on Climate Change*. Cambridge University Press, Cambridge, United Kingdom and New York, NY, USA

Willis MJ, Herried BG, Bevis MG and Bell RE (2015) Recharge of a subglacial lake by surface meltwater in northeast Greenland. *Nature* **518**(7538), 223–227

Willis MJ, Melkonian AK, Pritchard ME and Rivera A (2012) Ice loss from the Southern Patagonian Ice Field, South America, between 2000 and 2012. *Geophys. Res. Lett.* **39**(L17501), 1–6 (doi:10.1029/2012GL053136)

Zemp M, Frey H, Gärtner-Roer I, Nussbaumer SU, Hoelzle M, Paul F, Haeberli W, Denzinger F, Ahlstrøm AP, Anderson B, Bajracharya S, Baroni C, Braun LN, Cáceres BE, Casassa G, Cobos G, Dávila LR, Delgado Granados H, Demuth MN, Espizua L, Fischer A, Fujita K, Gadek B, Ghazanfar A, Hagen JO, Holmlund P, Karimi N, Li Z, Pelto M, Pitte P, Popovnin VV, Portocarrero CA, Prinz R, Sangewar CV, Severskiy I, Sigurðsson O, Soruco A, Usubaliev R and Vincent C (2015) Historically unprecedented global glacier decline in the early 21st century. *J. Glaciol.* **61**(228), 745–762 (doi:10.3189/2015JoG15J017)

Supplementary information: The geodetic mass balance of Eyjafjallajökull ice cap for 1945–2014: processing guidelines and relation to climate

This document includes:

Supplement on methods S1 to S6

Figs S1 to S5

Tables S1 to S3

References

Supplement on methods

S1. Preprocessing of lidar and EMISAR DEMs

The lidar surveys of the Icelandic glaciers carried out between 2008 and 2012 were used in this study, described in detail in Jóhannesson and others (2013). Eyjafjallajökull was surveyed with lidar on 10–11 August 2010 and additional proglacier areas on 16 September 2010. We also included lidar data from Mýrdalsjökull, Hofsjökull, west Vatnajökull, Tungnafellsjökull, Kerlingafjöll, Tröllaskagi and Langjökull, which overlap with the extent of the KH-9 images and are useful for Ground Control Point (GCP) extraction. The lidar survey of Langjökull was acquired by the Scott Polar Research Institute (SPRI), Cambridge, UK, in 2007 (Pope and others, 2013). The relative vertical accuracy of the lidar data is >0.3 m (Jóhannesson and others, 2011).

We linearly interpolated the first return of the lidar point cloud, creating gridded DEMs. For digitation of GCPs from the aerial photographs of Eyjafjallajökull, the DEMs were created in 1×1 m, similar to the Ground Sampling Distance (GSD) of the aerial photographs. All the lidar data were also interpolated in 5×5 m grid posting to match the GSD of the KH-9 images and to derive the maps of elevation changes. This was done with the routine *point2dem* in ASP software (© NASA). All the calculations were performed in ISN93 Lambert coordinates and datum (details at www.lmi.is).

A DEM was produced from airborne Synthetic Aperture Radar (SAR) in summer 1998, carried out by the Electromagnetic Institute of the Technical University of Denmark (Dall, 2003). This DEM was corrected based on comparison with an extensive set of GPS profiles by Magnússon (2003) and has been used in many studies of landscape changes in Iceland (e.g. Magnússon and others, 2005; Guðmundsson and others, 2011; Pedersen and others, 2018). The effects of snow penetration in snow areas are negligible due to the wavelength of the system and the presence of wet snow at the date of survey (Rott and Davis, 1993; Guðmundsson and others, 2011). The EMISAR DEM was co-registered to the lidar by applying the Iterative Closest Point (ICP) method using unchanged areas and applying the calculated transformation to the original EMISAR DEM using the routine *pc_align* in ASP software (Shean and others, 2016; Belart and others, 2017).

S2. Photogrammetric processes of frame imagery

The airborne frame stereo imagery was scanned with a photogrammetric scanner Vexcel Ultrascan 5000 at the National Land Survey of Iceland, at a resolution of 15 µm (images from 1980s and 1990s) and 20 µm (images older than 1980s). The KH-9 stereo imagery was scanned at 7 µm by the United

States Geological Survey. Information about the focal length was compiled from calibration certificates, handwritten information on the frames and from Surazakov and Aizen (2010).

The frame images contained either fiducial marks (the series of images from 1960 onwards, four marks in all the series with the exception of 1994, with eight marks), pseudofiducial marks (systematic marks existing at the same location over all the series of images, series of 1945) or a Réseau plate with systematic crosses over the entire image, e.g. 1058 crosses for the KH-9 imagery (Surazakov and Aizen, 2010). These marks served to establish a common frame where the camera lens distortions and the position of the principal point of autocollimation (PPA, e.g. DeWitt and Wolf, 2000) are systematically controlling the interior orientation together with the focal length. Fiducial coordinates were extracted from calibration certificates (LMI Series), were assumed with a 1×1 cm spacing in the Réseau plate (Surazakov and Aizen, 2010) and were measured and averaged over 5 images in the 1945 and 1960 series.

The frames were cropped based on the fiducials, using bilinear interpolation. This also served to crop the metadata at the border of the images that often cause difficulties in image correlation techniques, and recreating the scenario of a digital frame imagery. The transformation method for the airborne frame imagery was a 2D affine transformation and thin spline transformation for the KH-9 imagery.

The MicMac routine *tapioca* computed tie points between overlapping images, using the Scale-Invariant Feature Transform (SIFT) algorithm (Lowe, 2004). With the tie points and an initial camera geometry, MicMac solved the relative image orientation and improved the camera geometry with the routine *tapas.* Then, with the image and geographic coordinates of the GCPs as input, the routine *campari* performed a robust bundle block adjustment with compensation for heterogeneous observations and refinement of camera parameters. The uncertainties set to the GCPs were ±1 m (XYZ). The bundle adjustment was implemented in a Euclidean 3D system since MicMac does not support the bundle adjustment in spatial reference systems projected over an ellipsoid (Fig. S1).

With the images oriented in a ground spatial reference system, the routine *Malt* performed semi-global matching (Hirschmuller, 2008) to produce disparity maps, which were converted to point clouds with *nuage2ply*. The point cloud was transformed into ISN93 Lambert coordinates and linearly interpolated into a regular grid using *point2dem* in the ASP software. The routine *Tawny* enabled the creation of a continuous orthomosaic from the frame imagery, which was also resampled and projected onto the ISN93 spatial reference system (Fig. S1).

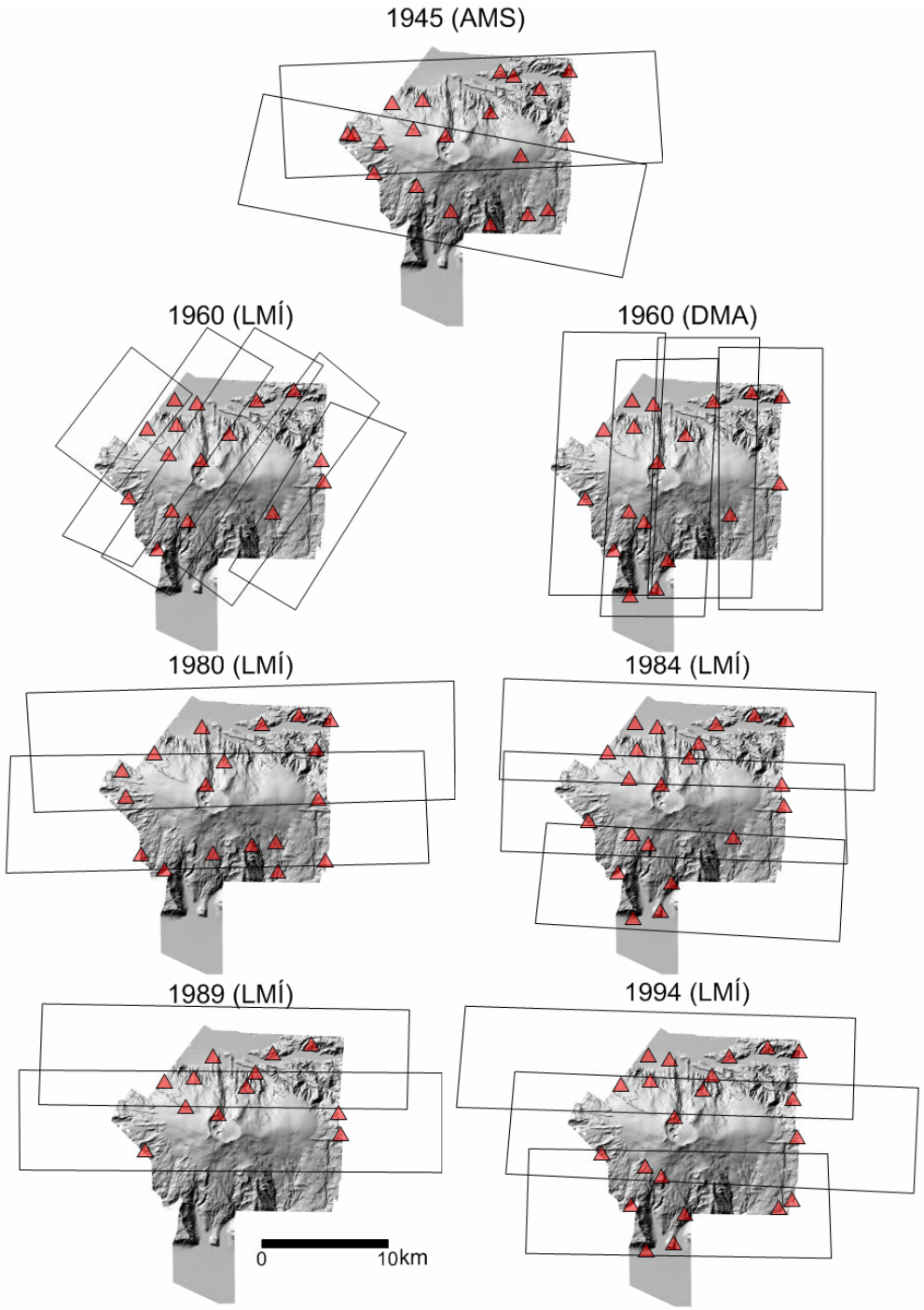

Fig. S1. Flight line (solid lines) and GCP distribution (red triangles) on each photogrammetric survey between 1945–1994. The lidar DEM of 2010 is displayed as reference, as a shaded relief.

S3. Processing of pushbroom images

The processing of pushbroom sensors in ASP used as input the pushbroom imagery with the Rational Polynomial Coefficients (RPC). The SPOT5-HRS imagery had a rigorous physical model of the pushbroom sensor, which was converted into RPC with the routine *add_spot_rpc.*

The ASTER dataset was processed in two runs: (1) a coarse-resolution DEM was produced with the routines *stereo* and *point2dem* and entered as input to create an orthoimage from each image of the stereopair, using the routine *mapproject*, and (2) the orthorectified stereopair, along with the coarse-resolution DEM, was used as input in a second run of the routines *stereo* and *point2dem*. The latter process has shown improvements in detail and accuracy of the resulting DEM (Lacroix, 2016; Brun and others, 2017).

The SPOT5 stereopair was first prepared with the routine *bundle_adjust*, which calculates homologous tie points between the stereopair and refines the RPC. Then, the routines *stereo* and *point2dem* were utilized to produce the DEM and orthoimage.

The processing of the Pléiades DEM and orthoimage was carried out with the routines *stereo* and *point2dem* (Marti and others, 2016; Belart and others, 2017). These routines were called twice, with slightly different setups of thresholds for matching, merging of the resulting DEMs and orthoimages from each run, and reducing the data gaps of the results (Belart and others, 2017).

The resulting DEMs from Pléiades, SPOT5 and ASTER were co-registered with the lidar using the routine *pc_align,* and solving for six transformation parameters: three translations and three rotations. The orthoimages were co-registered by applying translations to them based on the shifts previously calculated by the DEM co-registration.

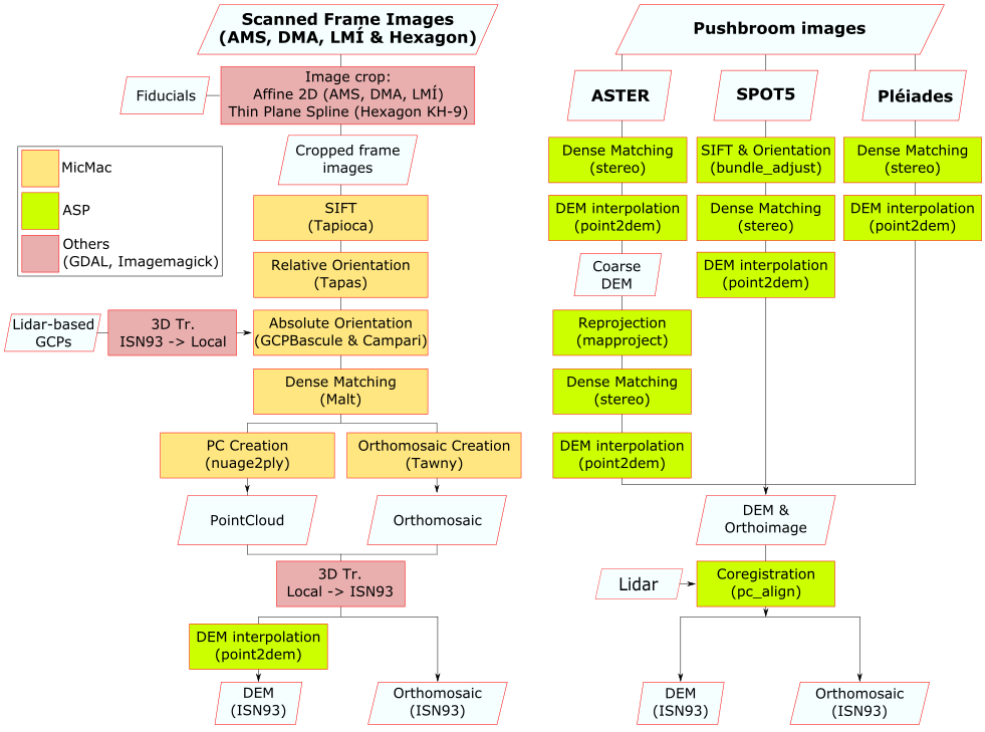

Fig. S2: Pipeline followed to process scanned frame images (left) and pushbroom images (right).

S4. Sequential Gaussian Simulation: pipeline and validation

The uncertainty estimates of the difference of DEMs (dDEM) were based on the work by Magnússon and others (2016). The main difference was the script-based, open-source workflow followed, with data preparation based on GDAL/OGR (GDAL/OGR contributors, 2018) and geostatistical analyses based on GSLib (Deutsch, 1998) (Fig. S2).

The data preparation consisted of producing a grid of the off-glacier areas from each dDEM. This only included areas where no elevation changes were expected during the time period analyzed, and served as a proxy to evaluate the dDEMs' uncertainties. These uncertainties were mostly due to residuals in the image orientation (both interior and exterior) of the two datasets used for the creation of a given dDEM (Fig. S3).

The preparation of the grid of the off-glacier areas was carried out in a semi-automatic workflow: (1) A slope mask excluding >30° slopes was applied over the dDEM, considered representative for the slopes on the ice cap. (2) A snow mask was applied to the result, obtained from setting a threshold on the orthomosaic containing the most snow between the two datasets. (3) The glaciated areas were masked out, as well as the areas with clear changes during the covered time period. This included landslides (Steinsholtsjökull; Kjartansson, 1967), erosion from jökuhlaups (e.g. Jökulsá river draining from Gígjökull; Oddsson and others, 2016) and newly emplaced lavas (Fimmvörðuháls; Edwards and others, 2012). (4) Gross errors higher than 4 standard deviations of the deduced elevation difference in areas presumed unchanged were masked out. (5) An automatic outlier removal was applied, comparing the dDEM versus a filtered dDEM with a windows size of 500 m, and excluding the cells for which the difference between filtered and unfiltered exceeded 1 standard deviation. (6) A random pick of 100 points every 500×500 m was selected, to speed up computation of the geostatistical method, after verifying that the impact of the subsampling was negligible. Steps (3) to (5) were iterated once, after visual inspection of the results, adding an extra mask of unfiltered but clear outliers.

The grids of the off-glacier areas were piped into the GSLib routines in the same steps as described by Magnússon and others (2016): (1) The *nscore* function was used to transform the grid of the off-glacier areas into a dataset fitting a normal distribution. (2) A semivariogram was calculated with the routine *gamv*, and the result was manually fitted into a modeled semivariogram, either spherical or Gaussian, following the shape of the semivariogram. (3) 1000 realizations of simulated errors propagated onto the ice cap were computed, using as input the normalized data and the modeled semivariogram. From the result, the mean of the 1000 realizations at each pixel was calculated. The mean map (Fig. S3 and S4) revealed the simulated propagation of the maps of errors onto the ice cap. From the simulation we obtained the mean of the 1000 realizations of glacier-wide bias of the dDEM analyzed along with a 95% interval confidence based on the histogram on the simulations.

The texture of snow might produce different effects in the correlation compared to bare ground. This was studied in Magnússon and others (2016) showing similar semivariograms of the dDEMs on- and off-glacier over short distances. The high-frequency errors produced in low contrast in snow therefore had low impact in the SGSim, while the main errors that needed to be modeled were the low-frequency, spatially-variable errors produced by the residuals in image orientation.

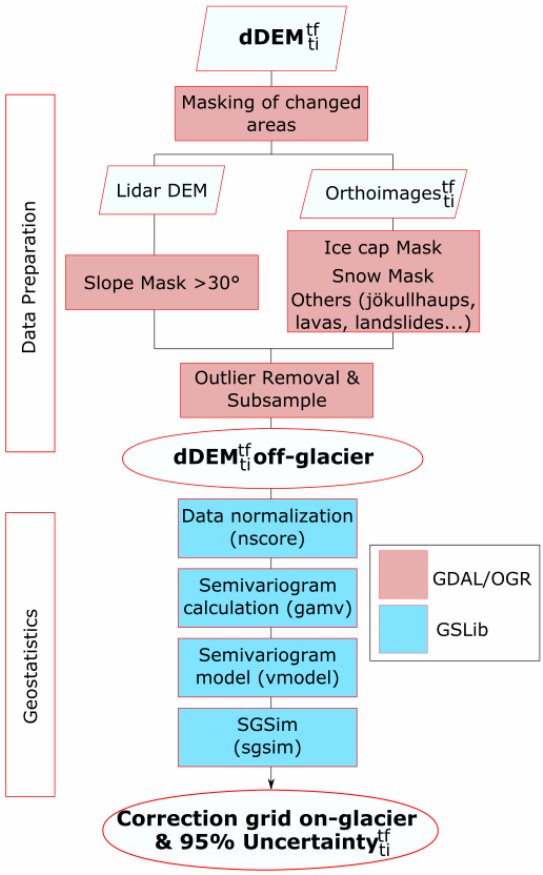

Fig. S3: Pipeline used for uncertainty analysis, inspired by Magnússon and others (2016) but using here script-based, open-source routines.

The archives of stereo images included two datasets at relatively close dates of survey for the years 1960 and 1980. On 5 August 1960 a full survey of the ice cap was carried out by AMS, and on the same day ~20% of the ice cap was surveyed by LMÍ. The LMÍ survey of Eyjafjallajökull was completed on 13 August 1960 (1 week later). The 1980 datasets were taken approximately 1 month apart, on 28 July 1980 by LMÍ and on 22 August 1980 by the KH-9 declassified satellite.

These datasets provided a comparison of independently acquired elevation data and served as validation of the concept, showing the reliability of SGSim in relationship with other proxies commonly used to correct glacier-wide elevation changes and associated uncertainty.

The four datasets (1960 LMÍ, 1960 DMA, 1980 LMÍ and 1980 KH-9) were compared with the 2010 lidar DEM, and two values of glacier-wide mean elevation difference were obtained for 1960–2010 and 1980–2010 (Table S1). The calculations excluded the areas where either of the datasets of each pair contained data gaps, e.g. the 1960 LMÍ dataset contains gaps due to poor overlap between flight lines, which could skew the glacier-wide mean elevation difference. The three following possibilities were tested for bias correction and precision of the dDEM: (1) median (dDEM bias) and NMAD (dDEM precision) of the off-glacier areas, Fig. S3), (2) median and NMAD of the off-glacier areas over a 1 km buffer around the ice cap, and (3) SGSim.

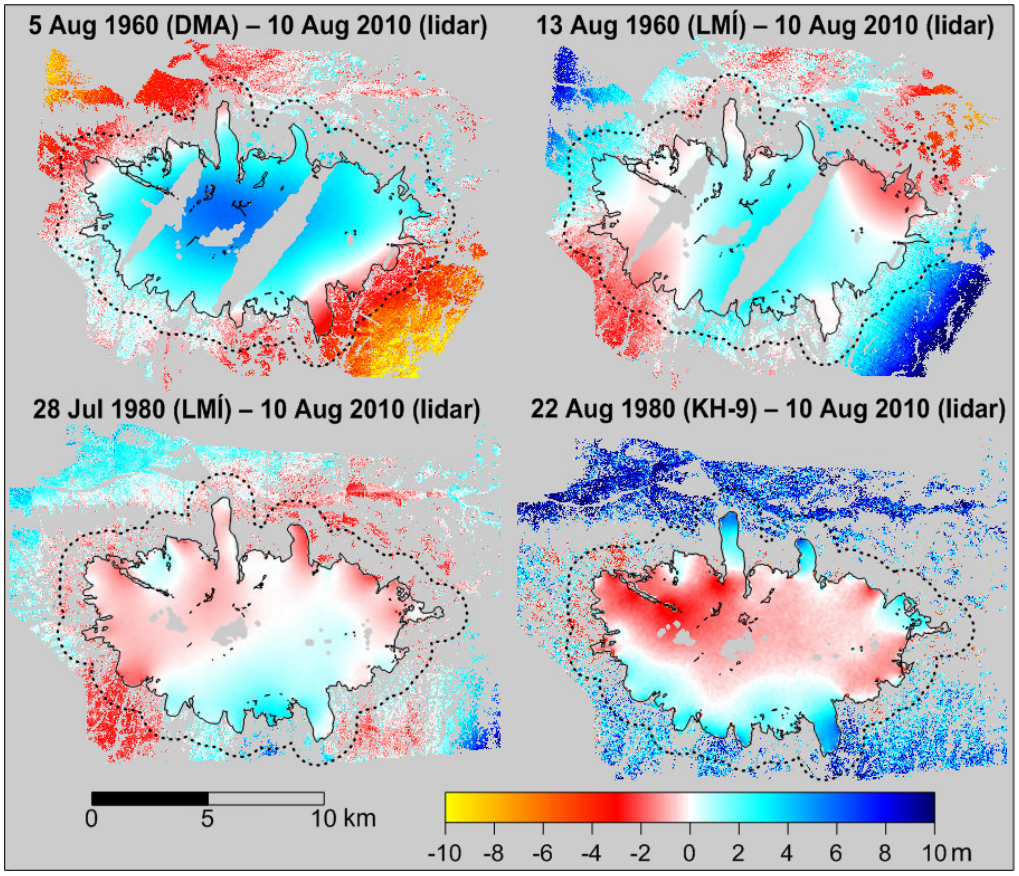

Fig. S4: Maps of off-glacier (snow- and ice-free) areas and SGSim-simulated spatially-variable errors inside the ice cap (solid black lines) of each DEM of 1960 and 1980 compared to the 2010 lidar DEM. Red colors indicate negative errors, and blue, positive errors. Buffer areas used for statistics are marked in dashed black lines.

Table S1. Comparison of three methods for bias correcting the glacier-wide mean elevation change, using the off-glacier error map, along with different proxies of uncertainty of the corrected glacier-wide mean elevation change (Δh_ice). The approaches are: 1) Bias correction and uncertainty estimate using respectively the median and NMAD of the off-glacier areas. 2) The same proxies derived from the off-glacier areas extending 1 km buffer from the glacier margin 3) bias correction and uncertainty assessment (95% confidence level) extracted from SGSim.

		Descriptive statistics			**SGSim (Geostatistics)**	
dDEM	Median ± NMAD off-glacier (m)	Δh_{ice} (m)	Median ± NMAD buffer off-glacier (m)	Δh_{ice} (m)	Glacier-wide mean ± 95% Unc. (m) of simulated errors	Δh_{ice} (m)
5 Aug 1960 (DMA)–2010	–1.3±2.5	–10.1±2.5	–0.6±1.8	–10.8±1.8	2.42±0.31	–13.83±0.31
13 Aug 1960 (LMÍ)–2010	0.8±2.6	–13.5±2.6	0.6±1.7	–13.3±1.7	0.67±0.41	–13.38±0.41
28 Jul 1980 (LMÍ)–2010	0.5±2.1	–20.7±2.1	–0.5±1.4	–19.7±1.4	–0.04±0.41	–20.13±0.41
22 Aug 1980 (KH-9)–2010	4.7±4.1	–24.2±4.1	3.0±4.2	–22.5±4.2	–0.14±0.99	–19.35±0.99

The results from Table S1 for the two series of 1960 reveal a similar glacier-wide mean elevation change when the SGSim correction is applied. We calculated a seasonal correction over 80% of the ice cap between 5 August and 13 August 1960, yielding -0.36 ± 0.14 m of elevation change due to melt. This melt explained the discrepancy in SGSim-based glacier-wide mean elevation changes and provided an excellent fit of results. The bias-corrected elevation difference on-glacier based on the two other proxies (median off-glacier and median over 1 km buffer off-glacier) yielded a higher disparity in the results (>3 m), although it still fitted within their respective error bars (NMAD values of the respective input).

Analogously, the two series of 1980 indicated that the best agreement is when bias-correcting using SGSim. The seasonal correction between 28 July and 22 August 1980 was -1.43 ± 0.44 m, which again explained why the mean elevation change of the ice cap using the dataset in late July was higher than the one in late August. It also yielded a fit with a few decimeters of difference, well within the error bars. On the other hand, the two other proxies gave a much higher (>4 m) disparity of results that could not be justified by seasonal differences but by erroneous bias correction.

S5. Finalizing the dDEMs: Filtering and interpolation of gaps inside the ice cap

To calculate the volume change, the bias-corrected dDEMs were masked using the maximum overlapping extent of the ice cap between the dates of survey. The result was filtered using the same median filter applied for the preparation of the maps of errors, but excluding areas at the glacier margins (500 m in-glacier from margin) and the 2010 eruption site; in these areas the filter would reject good data due to high variability in the elevation changes. An additional manual mask was applied for any remaining clear artifacts due to lack of image texture.

Gaps in the dDEMs (Fig. 4 of the main text) had multiple causes, insufficient stereo overlap, cloud coverage and, to a lesser extent, matching errors. In order to fill in the gaps for accurate volume calculations we combined three different approaches:

1) Most of the gaps were small (<5% of the ice cap) and fairly evenly distributed, which allowed simple linear interpolation from the edges of the gap area.

2) The dDEMs involving the 2014 Pléiades DEM contained gaps in the SW margin due to clouds at the time of acquisition. These gaps were filled based on 50 m elevation bands. Each of these bands

contained the mean elevation difference of the respective dDEM at each analyzed elevation range, after excluding values larger than 3*NMAD of the analyzed elevation range (Brun and others, 2017).

3) The largest gaps amounted to a maximum of 15% of the ice cap in the southern area (S_{1989}) of the 1989 series (Fig. 4 of main text). We fitted a linear function of the volume changes of S_{1989} as a function of the volume changes on the rest (85%) of the ice cap in ten time periods without gaps in this area (e.g. Magnússon and others, 2016). The result yielded a clear linear fit (R^2 = 0.98), which permitted obtaining the volume changes at S_{1989} in the periods 1984–1989 and 1989–1994. This was used to complete the volume changes dV_{1984}^{1989} and dV_{1989}^{1994}.

S6. Seasonal corrections of the geodetic mass balance

Table S2: Summary of parameters and 95% uncertainties utilized for modelling summer melt and summer snowfall until 1 October

Abbreviation	Parameter	Value
T	Daily temperature at 2m above ground	
T_+	Positive degree-day	
P	Daily precipitation	
$ddf_{f\&i}$	Degree-day factor of firn and ice	6.5 ± 0.5 mm w.e. °C^{-1}
ddf_s	Degree-day factor of snow	5.5 ± 0.5 mm w.e. °C^{-1}
$c_{f\&i}$	Conversion factor of firn and ice to water equivalent	0.75 ± 0.1
c_s	Conversion factor of snow to water equivalent	0.5 ± 0.1
α, β	Binary switches between snow and firn or ice	
$P_{(T<1°C)}$	Threshold between rain and snow precipitation	

Table S3. Seasonal corrections applied to each series of DEMs

Date of DEM	Area-average elevation difference (m)
29 Sept 1945	N/A
5 Aug 1960	–1.79 ± 0.69
13 Aug 1960	–1.36 ± 0.56
28 Jul 1980	–1.98 ± 0.80
22 Aug 1980	–0.56 ± 0.51
4 Sept 1984	+0.04 ± 0.34
31 Jul 1989	–0.79 ± 0.90
6 Aug 1994	–1.14 ± 0.65
12 Aug 1998	–1.21 ± 0.57
5 Oct 2004	N/A
7 Oct 2009	N/A
10 Aug 2010	–1.83 ± 0.72
11 Aug 2014	–1.13 ± 0.70

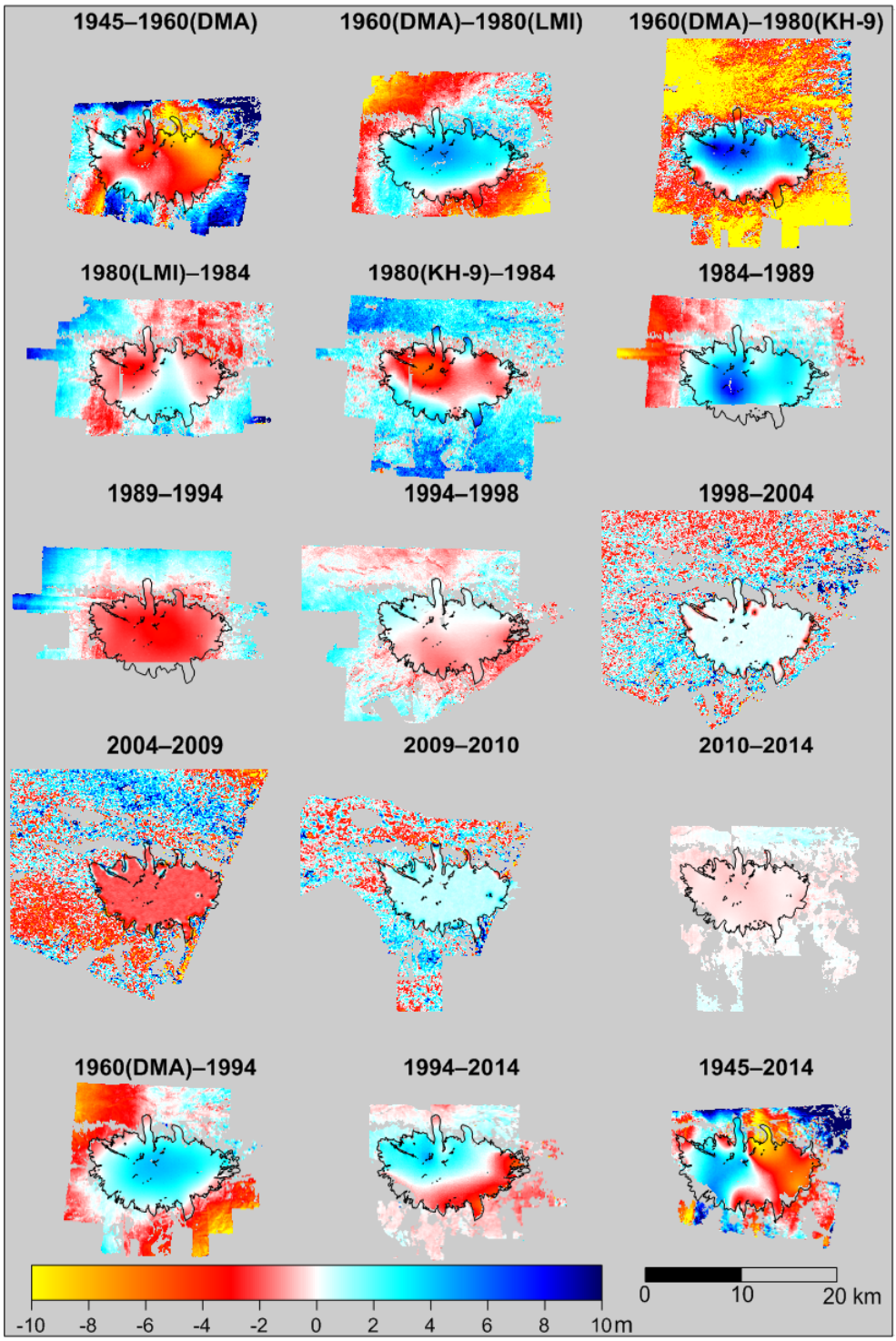

Fig. S5: Map of off-glacier errors for each dDEM and maps of the spatially-variable errors within Eyjafjallajökull, obtained from SGSim.Outlines are shown with a black solid line.

References

Belart JMC, Berthier E, Magnússon E, Anderson LS, Pálsson F, Thorsteinsson T, Howat IM, Aðalgeirsdóttir G, Jóhannesson T and Jarosch AH (2017) Winter mass balance of Drangajökull ice cap (NW Iceland) derived from satellite sub-meter stereo images. *The Cryosphere* **11**(3), 1501–1517 (doi:10.5194/tc-11-1501-2017)

Brun F, Berthier E, Wagnon P, Kääb A and Treichler D (2017) A spatially resolved estimate of High Mountain Asia glacier mass balances from 2000 to 2016. *Nat. Geosci.* **10**(9), 668 (doi:10.1038/ngeo2999)

Dall J (2003) Cross-calibration of interferometric SAR data. *Sonar Navig. IEE Proc. - Radar* **150**(3), 177–183 (doi:10.1049/ip-rsn:20030448)

Deutsch CV (1998) GSLIB - Geostatistical Software Library and User"s Guide. https://infoscience.epfl.ch/record/51514

DeWitt BA and Wolf PR (2000) *Elements of Photogrammetry(with Applications in GIS).* McGraw-Hill Higher Education

Edwards B., Magnússon E., Thordarson T., Guðmundsson M. T., Höskuldsson A., Oddsson B. and Haklar J. (2012) Interactions between lava and snow/ice during the 2010 Fimmvörðuháls eruption, south-central Iceland. *J. Geophys. Res. Solid Earth* **117**(B4) (doi:10.1029/2011JB008985)

GDAL/OGR contributors (2018) *The GDAL/OGR Geospatial Data Abstraction software Library.* The Open Source Geospatial Foundation http://gdal.org

Guðmundsson S, Björnsson H, Magnússon E, Berthier E, Pálsson F, Guðmundsson MT, Högnadóttir T and Dall J (2011) Response of Eyjafjallajökull, Torfajökull and Tindfjallajökull ice caps in Iceland to regional warming, deduced by remote sensing. *Polar Res.* **30**(7282) (doi:10.3402/polar.v30i0.7282)

Hirschmuller H (2008) Stereo Processing by Semiglobal Matching and Mutual Information. *IEEE Trans. Pattern Anal. Mach. Intell.* **30**(2), 328–341 (doi:10.1109/TPAMI.2007.1166)

Jóhannesson T, Björnsson H, Magnússon E, Guðmundsson S, Pálsson F, Sigurðsson O, Thorsteinsson T and Berthier E (2013) Ice-volume changes, bias estimation of mass-balance measurements and changes in subglacial lakes derived by lidar mapping of the surface of Icelandic glaciers. *Ann. Glaciol.* **54**(63), 63–74 (doi:10.3189/2013AoG63A422)

Jóhannesson T, Björnsson H, Pálsson F, Sigurðsson O and Þorsteinsson Þ (2011) LiDAR mapping of the Snæfellsjökull ice cap, western Iceland. *Jökull* **61**, 19–32

Kjartansson G (1967) The Steinsholtshlaup, central-south Iceland on January 15th, 1967. *Jökull* **17**, 249–262

Lacroix P (2016) Landslides triggered by the Gorkha earthquake in the Langtang valley, volumes and initiation processes. *Earth Planets Space* **68**(1), 46 (doi:10.1186/s40623-016-0423-3)

Lowe DG (2004) Distinctive Image Features from Scale-Invariant Keypoints. *Int. J. Comput. Vis.* **60**(2), 91–110 (doi:10.1023/B:VISI.0000029664.99615.94)

Magnússon E (2003) Airborne SAR data from S-Iceland: analyses, DEM improvements and glaciological application. *MSc Thesis Dep. Phys. Univ. Icel.*

Magnússon E, Belart JMC, Pálsson F, Ágústsson H and Crochet P (2016) Geodetic mass balance record with rigorous uncertainty estimates deduced from aerial photographs and lidar data – Case study from Drangajökull ice cap, NW Iceland. *The Cryosphere* **10**(1), 159–177 (doi:10.5194/tc-10-159-2016)

Magnússon E, Björnsson H, Dall J and Pálsson F (2005) Volume changes of Vatnajökull ice cap, Iceland, due to surface mass balance, ice flow, and subglacial melting at geothermal areas. *Geophys. Res. Lett.* **32**(5) ://000227640800003

Marti R, Gascoin S, Berthier E, de Pinel M, Houet T and Laffly D (2016) Mapping snow depth in open alpine terrain from stereo satellite imagery. *The Cryosphere* **10**(4), 1361–1380 (doi:10.5194/tc-10-1361-2016)

Oddsson B, Guðmundsson MT, Edwards BR, Thordarson T, Magnússon E and Sigurðsson G (2016) Subglacial lava propagation, ice melting and heat transfer during emplacement of an intermediate lava flow in the 2010 Eyjafjallajökull eruption. *Bull. Volcanol.* **78**(7), 48 (doi:10.1007/s00445-016-1041-4)

Pedersen G. B. M., Belart J. M. C., Magnússon E., Vilmundardóttir O. K., Kizel F., Sigurmundsson F. S., Gísladóttir G. and Benediktsson J. A. (2018) Hekla Volcano, Iceland, in the 20th Century: Lava Volumes, Production Rates, and Effusion Rates. *Geophys. Res. Lett.* **45**(4), 1805–1813 (doi:10.1002/2017GL076887)

Pope A, Willis IC, Rees WG, Arnold NS and Pálsson F (2013) Combining airborne lidar and Landsat ETM+ data with photoclinometry to produce a digital elevation model for Langjökull, Iceland. *Int. J. Remote Sens.* **34**(4), 1005–1025 (doi:10.1080/01431161.2012.705446)

Rott H and Davis RE (1993) Multifrequency and polarimetric SAR observations on alpine glaciers. *Ann. Glaciol.* **17**, 98–104 (doi:10.3189/S0260305500012672)

Shean DE, Alexandrov O, Moratto ZM, Smith BE, Joughin IR, Porter C and Morin P (2016) An automated, open-source pipeline for mass production of digital elevation models (DEMs) from very-high-resolution commercial stereo satellite imagery. *ISPRS J. Photogramm. Remote Sens.* **116**, 101–117 (doi:10.1016/j.isprsjprs.2016.03.012)

Surazakov AB and Aizen VB (2010) Positional accuracy evaluation of declassified Hexagon KH-9 mapping camera imagery. *Photogramm. Eng. Remote Sens.* **76**(5), 603–608

Paper III

Spatially distributed mass balance of selected Icelandic glaciers, 1945–2015. Trends and link with climate.

Joaquín M.C. Belart, Eyjólfur Magnússon, Etienne Berthier, Águst Þ. Gunnlaugsson, Finnur Pálsson, Guðfinna Aðalgeirsdóttir, Helgi Björnsson.

Manuscript to be submitted to Frontiers in Earth Science.

Spatially distributed mass balance of selected Icelandic glaciers, 1945–2015. Trends and link with climate

Joaquín M.C. Belart, Eyjólfur Magnússon, Etienne Berthier, Águst Þ. Gunnlaugsson, Finnur Pálsson, Guðfinna Aðalgeirsdóttir, Helgi Björnsson

ABSTRACT:

Excluding the three largest ice caps, Icelandic glaciers have received until recently limited attention in terms of mass balance observations over the last century. In this study, estimates of glacier-wide geodetic mass balance from 1945 to 2015 are presented, in decadal time spans, for 14 glaciers (total area >1000 km^2) spatially distributed in all quarters of Iceland and subject to different climatic forcing. The estimates are derived from numerous sources of elevation data: historical aerial photographs, declassified spy satellite images, modern satellite stereo imagery and airborne lidar. The obtained mass balances are correlated with precipitation and air temperature by a first order equation including a reference-surface correction term. This permits statistical modelling of annual mass balances and to temporally homogenize the mass balances for a region-wide, multitemporal mass balance study. The mean and standard deviation (mean±SD) of mass balances of the target glaciers were –0.44±0.16 m w.e. a^{-1} in 1945–1960, 0.00±0.21 m w.e. a^{-1} in 1960–1980, 0.11±0.25 m w.e. a^{-1} in 1980–1994, –1.01±0.50 m w.e. a^{-1} in 1994–2004, –1.27±0.56 m w.e. a^{-1} in 2004–2010 and –0.14±0.51 m w.e. a^{-1} in 2010–2015. High decadal mass-balance variability is found on glaciers located at the south and west coasts, in contrast to the glaciers located inland, north and northwest. The fit between mass balance and climate substantially improves by applying a reference-surface correction. Yet this fit reveals in some cases an unrealistic mass balance sensitivity to temperature and precipitation changes, and for Mýrdalsjökull the fit is poor (R^2=0.69). This could be attributed to: (1) inaccuracies in the estimates of summer temperature and winter precipitation obtained from the climate model, (2) an oversimplified model relating mass balance and climate. Moreover, the reference-surface correction is applied under assumption of a linear relationship between area and volume changes. This failed at specific time periods due to substantial lowering in the accumulation area while the glacier fronts were advancing. This is likely related to changes in the ice flux towards the ablation area, possibly linked to periods of high precipitation. This study provides unique data for studies of coupled mass balance to ice dynamics, especially aiming at reproducing an increased ice flux forced by precipitation changes.

Keywords: Region-wide mass balance, glacier–climate relationship, remote sensing.

Keypoints:

A ~70-year record of mass balances was extracted over 14 glaciers located around Iceland, improving the estimates of mass loss and allowing a region-wide mass balance intercomparison. Glaciers in the south and west coasts show higher mass balance fluctuations than the inland or northern glaciers.

These observations were linearly fitted with records of temperature and precipitation using statistical relations. This led to some misfits, which may be explained by an incomplete climate model and the linearity assumptions utilized.

The long records of mass balances and DEMs add constraints to the discussion of mass balance changes in relation with climate. Observed patterns of elevation change between 1960s and 1990s indicate significant variations in ice dynamics, likely controlled mainly by fluctuations in precipitation, that may call for new challenges in glacier modelling.

INTRODUCTION

Glacier mass balance is an ideal proxy to describe climate variability (Ahlmann, 1940; Ohmura, 2011; Vaughan et al., 2013; Bojinski et al., 2014). Mass balance is related to winter precipitation (winter snow) and summer temperature (a proxy for available energy to melt snow and ice). Mountain glaciers and small ice caps have a relatively rapid response, in decadal timescales, to adjust their geometry to a new climate (Nye, 1960; Jóhannesson et al., 1989 Bahr et al., 1998; Aðalgeirsdóttir et al., 2006). Glaciers therefore act as low pass filters to climatic variables with a time delay (e.g. Elsberg et al., 2001; Marzeion et al., 2012).

Mass balance observations from in situ measurements are sparse and costly; they are only available for about 450 glaciers around the world (Zemp et al., 2015, updated in WGMS, 2017), whereas mass balance inferred from remote sensing observations, e.g. geodetic mass balance (Cogley et al., 2011) is achievable for most glacierized regions without demanding field logistics. The remote sensing era started as early as the 1900s, and the mapping cameras rapidly developed in the 1930s, giving way to numerous airborne and spaceborne photogrammetric and photoreconnaissance surveys worldwide (Livingston, 1963; Spriggs, 1966; Bindschadler and Vornberger, 1998), providing valuable sources to create Digital Elevation Models (DEMs) with the potential for geodetic mass balance measurements (e.g. Bolch and others, 2011; Magnússon and others, 2016; Fieber and others, 2018).

Despite the vast amount of historical archives of stereo images, the geodetic records of the first half of the 20th century are scarce and based on contour maps (e.g. Bauder et al., 2007). Observations become fairly common after the 1980s (e.g. Fischer et al., 2015) and have been very frequent since the 2000s (WGMS, 2017) due to the rapid development and availability of sensors with capabilities to retrieve the glacier surface geometry (e.g. optical stereoscopic imagery, radar, lidar).

Geodetic mass balances are especially useful if they are spatially distributed, as they are the basis for region-wide mass balance studies. These studies have been carried out in several glacierized regions, such as the Alps (Bauder et al., 2007; Fischer et al., 2015; Berthier et al., 2016), Andes, (Soruco et al., 2009), Greenland (Bolch et al., 2013), or High Mountain Asia, (Kääb et al., 2012; Gardelle et al., 2013; Brun et al., 2017). These studies advance the understanding the relation between glacier and climate, improve regional and global climate models and constrain the regional glacier mass loss and sea-level rise (e.g. Marzeion et al., 2014; Huss and Hock, 2015).

In Iceland, mass balance observations have mostly focused on the three largest ice caps: Vatnajökull (~8000 km^2), Langjökull (~900 km^2) and Hofsjökull (~890 km^2), with a 25-year record of in situ measurements (Björnsson and Pálsson, 2008; Pálsson et al., 2012; Björnsson et al., 2013; Jóhannesson et al., 2013). These account for about 90% of the total glacierized area, and their mass balance records have been used to estimate the glacier mass loss and sea-level rise contribution of the entirety of Icelandic glaciers (Björnsson et al., 2013). Other glaciers are less significant for the total Icelandic mass loss, but they are spatially distributed in all quarters of Iceland and have the potential to provide insights into regional climate variations.

The aim of this study is to produce a catalogue of maps of elevation difference and a 70-year record of geodetic mass balance of spatially distributed glaciers in Iceland. These mass balances are statistically correlated to records of temperature and precipitation to infer their static sensitivity to

climate fluctuations, and the mass balances are homogenized for a region-wide multitemporal mass balance study. Results are discussed in a context of climate-driven changes in the analyzed glaciers.

STUDY AREAS

For the current study, 14 glaciers and ice caps were selected, distributed in all quarters of Iceland, with different regional climatic regimes (Björnsson et al., 2013). They are shown in Fig. 1. Geodetic mass balance estimates have been recently obtained for three of the target glaciers: Drangajökull, Eyjafjallajökull and Tungnafellsjökull (Gunnlaugsson, 2016; Magnússon et al., 2016a; Belart et al., in review). In situ mass balance observations have been carried out at a few locations on Mýrdalsjökull since 2001 (Ágústsson et al., 2013), and on Drangajökull during 2005–2015 (e.g. Belart et al., 2017; Anderson et al., 2018). Previous studies have also calculated geodetic mass balance over 1–2 decades on Snæfellsjökull (Jóhannesson et al., 2011), Eyjafjallajökull, Tindfjallajökull and Torfajökull (Guðmundsson et al., 2011). The rest of the targets have very limited or completely lack previous mass-balance observations.

The size of the target glaciers varies from ~3.5 km^2 for Hofsjökull Eystri to ~560 km^2 for Mýrdalsjökull, and sum up to a total of >1000 km^2 (year 2010). Their elevation range is from ~200 m at Hofsjökull Eystri, to ~2000 m at Öræfajökull. The ice thickness is known for five of the glaciers, being on average ~100 m for Drangajökull (Magnússon et al., 2016b), ~230 m for Mýrdalsjökull (Björnsson et al., 2000), ~120 m for Öræfajökull (Magnússon et al., 2012b), ~50 m for Snæfellsjökull (Björnsson, 2017) and ~60 m for Tungnafellsjökull (Gunnlaugsson, 2016).

The three largest ice caps, Vatnajökull (V), Langjökull (L) and Hofsjökull (H) (Fig. 1), were excluded from this study with the exception of Öræfajökull, which is a part of Vatnajökull. This was due to the complexity of the processing scheme: the relatively small footprint of the historical aerial photographs in comparison with the glacierized area would limit the bare ground areas used as reference (i.e. vicinity of the ice cap and nunataks) over large amounts of aerial photographs, causing large distortions in the resulting DEMs. The surveys of these ice caps were also carried out over multiple dates (months to years), complicating the mosaicking and interpretation of the results.

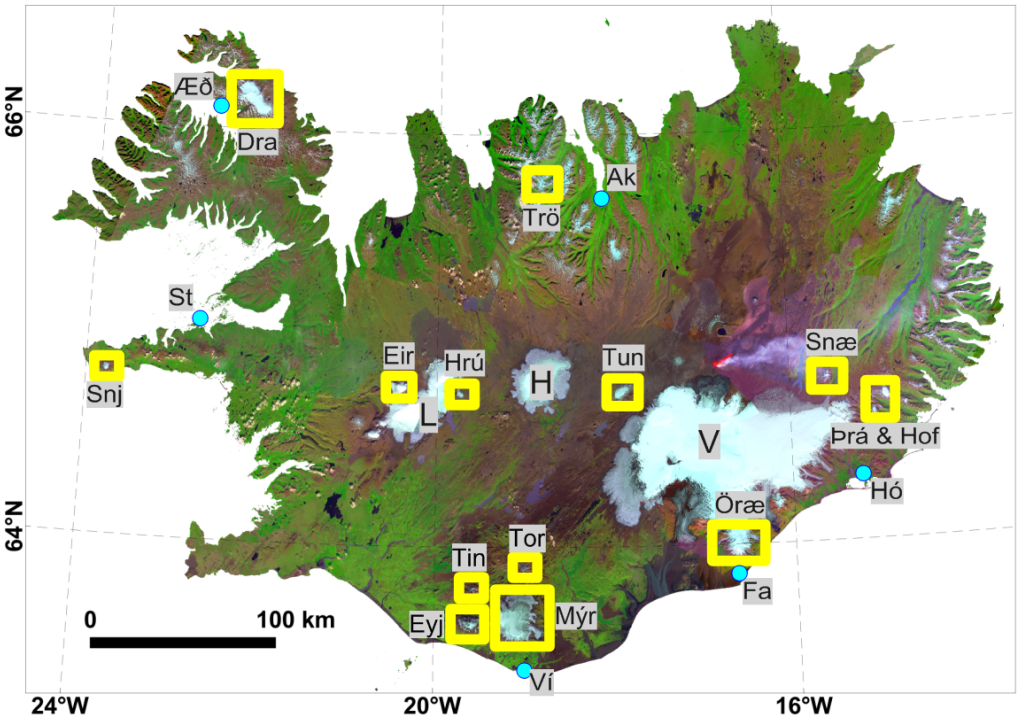

Fig 1: Target glaciers of this study, surrounded by a yellow box: Drangajökull (Dra), Snæfellsjökull (Snj), Eyjafjallajökull (Eyj), Tindfjallajökull (Tin), Torfajökull (Tor), Mýrdalsjökull (Mýr), Öræfajökull (Öræ), Þrándarjökull (Þrá), Hofsjökull Eystri (Hof), Snæfell (Snæ), Tungnafellsjökull (Tun), Hrútfell (Hrú), Eiríksjökull (Eir) and Barkárdals- and Tungnahryggsjökull, considered as one glacier unit on Tröllaskagi (Trö). Blue dots show the six weather stations with long time series: Stykkishólmur (St), Vík (Ví), Fagurhólsmýri (Fa), Hólar í Hornafirði (Hó), Akureyri (Ak) and Æðey (Æð).

DATA AND METHODS:

The data used in this study is described in Belart et al. (in review), and consists on the dense catalogue of stereoscopic imagery available in Iceland from 1945 to 2015, from airborne and spaceborne, frame (pinhole) camera and pushbroom sensors, together with airborne lidar data (Jóhannesson et al., 2013). Fig. 2 gives an overview of the datasets used, and further information on individual datasets is given in the supplement S1. In addition, daily gridded climatic records were used: linearly modelled precipitation from 1958–2007 (LT, 1×1 km, Crochet et al., 2007), numerically modelled precipitation from 1980–2016 (HARMONIE, 2.5×2.5 km, Nawri et al., 2017) and interpolated temperature from 1948–present (1×1 km, Crochet and Jóhannesson, 2011) as well as records from selected weather stations with long time series (>50 year) (Fig. 1, data available at www.vedur.is).

For each target glacier, the methods described by Belart et al. (in review) were followed, consisting on: (1) DEM and ortho creation using photogrammetric processing in a semi-automated workflow. (2) Bias correction and uncertainty estimates using Sequential Gaussian Simulation (SGSim, Magnússon et al., 2016). (3) Filtering, gap filling and volume calculation (4) Seasonal corrections between the date of each survey and 1 October of the respective year. (5) Glacier-wide geodetic

mass balance ($\dot{B}$) using the conversion factor 0.85±0.06 Huss (2013). This resulted in two values of ($\dot{B}$), one relative to the survey dates and one fixed to the start of the hydrological year (1 October).

Gaps in the DEMs on the glacier surface occurred because of incomplete glacier surveys, cloud presence and lack texture in the images. An interpolation of the elevation difference on the gap areas was done as a function of elevation bands (e.g. Brun et al., 2017), and the uncertainty of these areas was enlarged based on the amount of datapoints and variations in elevation the difference retrieved for each elevation band (Supplement S2).

The seasonally-corrected mass balance was then correlated with the mean summer temperature (Ts, defined from 21 May to 30 Sep) and winter precipitation (Pw, defined form 1 Oct to 20 May) averaged over the same years as the geodetic mass balance. This required a correction to reference-surface mass balance (Elsberg et al., 2001; Harrison et al., 2001) for correlation of mass-balance with climate (Cogley et al., 2011; Huss et al., 2012), simplified by approximating the changes in area (ΔA) and volume as a linear function for the analyzed time period, as previously observed in Pálsson et al. (2012) and Belart et al. (in review). This resulted in a first order equation that can be solved by weighted least-squares (Belart et al., in review)

$$\dot{B} = \varphi Ts + \omega Pw + \gamma \Delta A + k \quad (1)$$

Solving Eq.1 yielded static sensitivities of mass balance to summer temperature (φ, m w.e. a^{-1} K^{-1}) and winter precipitation (ω, m w.e. a^{-1} $(10\%)^{-1}$). The model was used to calculate annual mass balances as a function of summer temperature, winter precipitation and area changes. The model was not applied to Snæfell due to limited geodetic observations (Fig. 2).

For a decadal, region-wide comparison, we selected the years 1945, 1960, 1980, 1994, 2005, 2010 and 2015, as a median of the most common survey years (Fig.2). The geodetic mass balance of each glacier was temporally homogenized (e.g. Lambrecht and Kuhn, 2007; Fischer et al., 2015) to these years when needed, by using the annual mass balance modelled using temperature and precipitation records (Eq. 1). The annual correction was not applied to datasets acquired in 1946 and 2017 due to lack of climate data.

Further remarks for processing individual target glaciers, are described in the supplement S2.

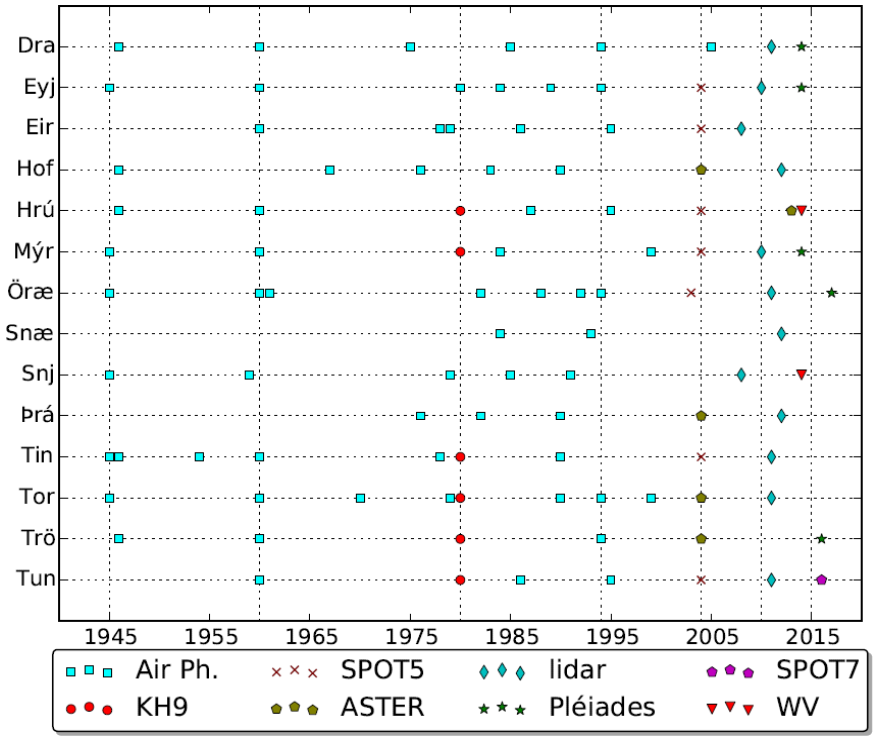

Fig. 2: Temporal distribution of the datasets for each target glacier. Vertical lines are emplaced at the most repeated survey times, based on airborne (1945, 1960, 1994) and spaceborne (1980) stereo images. 2004 contained abundant measurements from SPOT5 (SPIRIT, Korona et al., 2009) and ASTER (GLIMS, Raup et al., 2007). The airborne lidar surveys are spread over 5 years and adjusted to year 2010 (Jóhannesson et al., 2013). Recent satellite sub-meter stereo images from Pléiades, and WorldView DEMs (ArcticDEM, Noh and Howat, 2015, data available at http://arcticdemapp.s3-website-us-west-2.amazonaws.com/explorer/) were acquired during 2014–2017 and adjusted to 2015.

RESULTS

Spatial pattern of elevation changes

Over 100 DEMs were utilized in this study, 70 of which were processed using photogrammetric techniques. The area gaps on the glacierized areas were on average 15% of the total area, and seven $dDEMs$ contained gaps > 30% of the glacierized area, with a maximum of 40% for gaps in Snæfellsjökull between 1945–1959.

A chronological time series of $dDEMs$ for each target glacier is shown in the supplement (S3). This supplement also includes remarks on the evolution of the debris-covered glacier of Klofajökull (N-Eiríksjökull) between 1960–2008, and a landslide occurred in the pro-glacier areas of Tindfjallajökull.

Overview of geodetic mass balances

We computed the geodetic mass balances for 70 time periods in total (85 including the results from Belart et al. (in review) and Magnússon et al. (2016a)), i.e. on average six time periods for each of the 14 target glaciers, nine of them starting from 1945 (Fig.3). Uncertainties were typically <0.1 m w.e. a^{-1} (95% confidence level) for periods longer than 10 years, but increased for the shorter time periods (e.g. Huss, 2013) or if the DEMs contained significant gaps. The maximum and minimum values were, respectively, 0.84±0.21 m w.e. a^{-1} on Snæfellsjökull in 1985–1991 and –2.55±0.48 m w.e. a^{-1} on Torfajökull in 2004–2009. The seasonal correction was generally small (<0.1 m w.e. a^{-1}) over ~10 years periods, but increased significantly for the shorter time periods (e.g. Belart et al., in review). Details on each glacier analyzed, including geodetic mass balance fixed to the survey dates and seasonally corrected, are given in supplements S3 and S4.

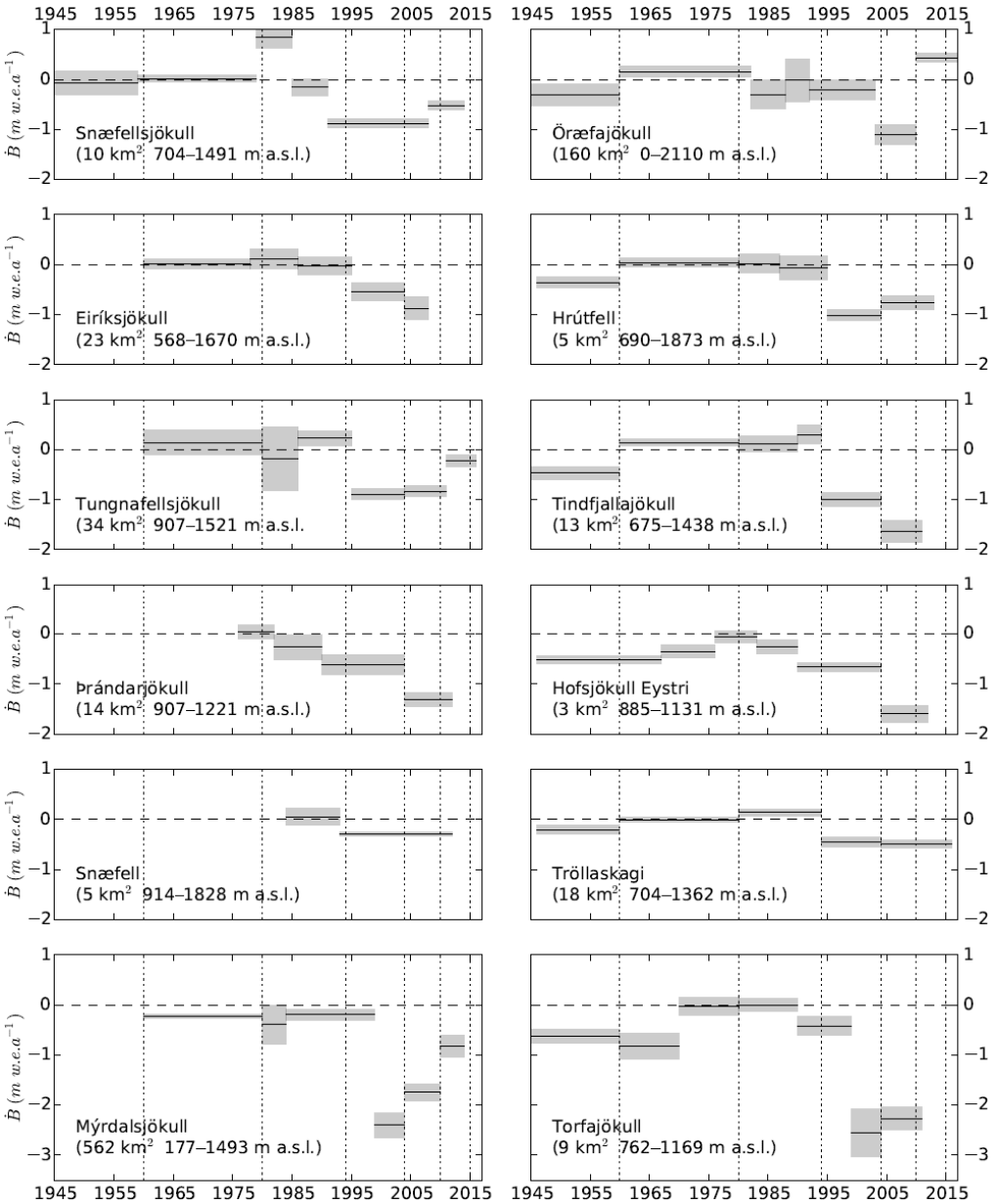

Fig. 3. Geodetic mass balance of 12 of the analyzed glaciers. The dates are fixed to 1 October, based on seasonal corrections. Grey bands indicate uncertainty at 95% confidence level. Note the extended Y axis in the lowermost panels. Dashed vertical lines show the years selected for region-wide intercomparisons. The numbers in parenthesis indicate the area in 2010 and the range of elevation of each glacier.

Mass balance and climate records: correlation and sensitivities

The least-square fit between reference-surface mass balance and climatic variables (Eq. 1) yielded a robust fit with $R^2 > 0.90$ on eight of the targets, and $R^2 > 0.80$ on 10 targets (Table 1). The fit however was not as strong for Mýrdalsjökull ($R^2 = 0.69$) or Tungnafellsjökull ($R^2 = 0.74$).

The calculated mass-balance sensitivity to summer temperature ranges from –0.21±0.10 (Þrándarjökull) to –3.85±1.05 m w.e.a^{-1} K^{-1} (Snæfellsjökull). The highest sensitivity to winter precipitation was found on Mýrdalsjökull with 0.56±0.92 m w.e.a^{-1} $(10\%)^{-1}$. The validity of these extreme sensitivities is addressed in the discussion section.

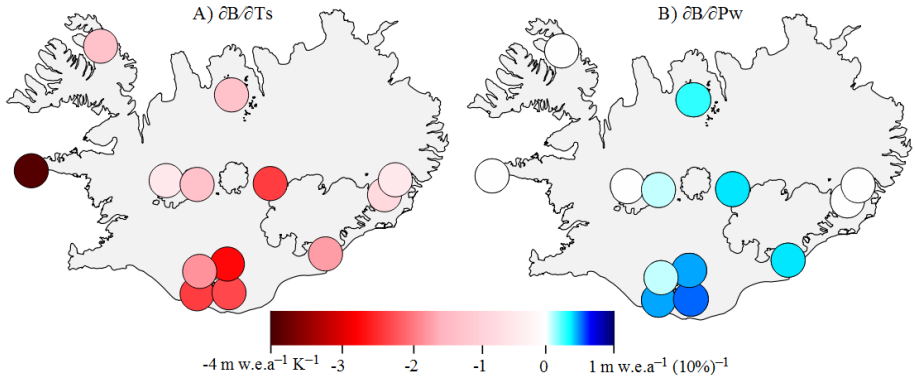

Fig. 4: Mass-balance sensitivities to summer temperature (left) and winter precipitation (right).

In five of the analyzed glaciers, we found that the variations in winter precipitation yielded negative sensitivity (–0.1 to 0 m w.e. a^{-1} $(10\%)^{-1}$) to mass balance (Table 2) (further addressed in the following discussion). In these cases we considered $\omega = 0$, when solving Eq.1 by least squares, assuming that its contribution was insignificant to mass balance changes (e.g. Leclercq and Oerlemans, 2012).

Table 1: Mass balance sensitivities of the analyzed glaciers to a 1°C rise in temperature and to a 10% increase in precipitation. Uncertainties (1σ) were extracted from the variance matrix by the least squares adjustment. No uncertainties (N/A) were computed for Barkárdals- and Tungnahryggsjökull as the mass-balance measurements were minimum (four observations) to solve the least square adjustment. *Target glaciers for which the sensitivity to precipitation was set to zero ($\omega = 0$).

	$\partial\dot{B}/\partial Ts$ (m w.e.a^{-1} K^{-1})	$\partial\dot{B}/\partial Pw$ (m w.e. a^{-1} $(10\%)^{-1}$)	R^2	R^2 ($\gamma = 0$)
Barkárdals- and Tungnahryggsjökull	–0.81±N/A	0.26±N/A	N/A	N/A
Drangajökull*	–0.84±0.32	0	0.81	0.70
Eiríksjökull*	–0.32±0.11	0	0.98	0.85
Eyjafjallajökull (Belart et al., in review)	–2.08±0.45	0.51±0.25	0.81	0.81
Hofsjökull Eystri*	–0.52±0.01	0	0.99	0.44
Hrútfell	–0.83±0.04	0.05±0.05	0.99	0.99
Mýrdalsjökull	–2.05±1.06	0.56±0.92	0.69	0.65
Öræfajökull	–1.02±0.46	0.38±0.16	0.95	0.95
Snæfellsjökull*	–3.85±1.05	0	0.91	0.63
Þrándarjökull*	–0.21±0.10	0	0.99	0.38
Tindfjallajökull	–1.38±0.48	0.03±0.14	0.96	0.76
Torfajökull	–2.69±0.99	0.46±0.38	0.95	0.93
Tungnafellsjökull	–2.10±0.72	0.32±0.26	0.74	0.68

Region-wide mass balance at the selected time periods

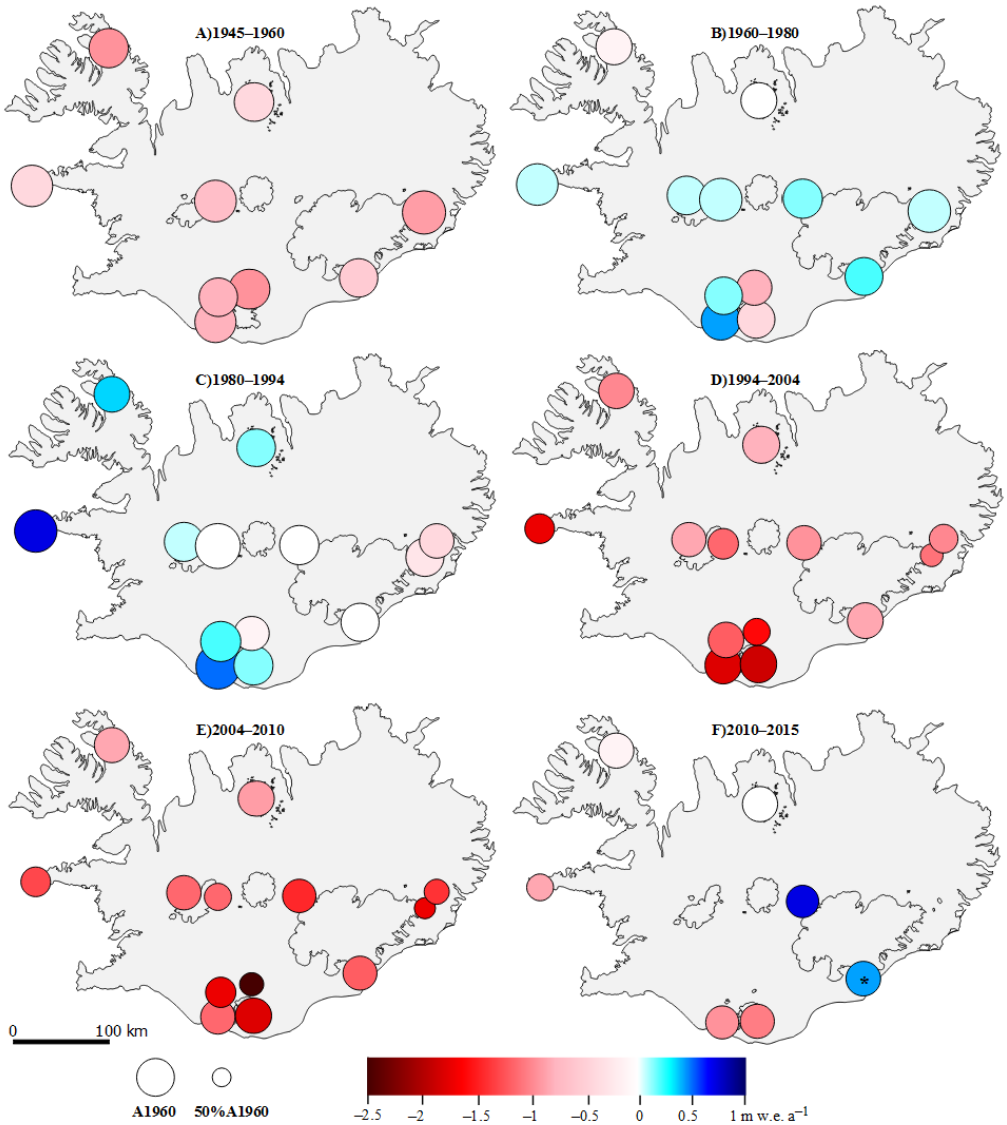

Fig. 5: Glacier-wide geodetic mass balance for six time periods between 1945 and 2015. Red and blue colors indicate negative and positive mass balance, respectively. The size of each circle shows the ratio of area changes relative to 1960. *The temporal homogenization was not applied to Öræfajökull between 2010–2017, due to the lack of gridded climate data after 2016.

For the six time periods temporally homogenized, the maximum mass loss was found on Torfajökull, –2.5 m w.e. a^{-1} in the period 2004–2010. The maximum mass gain occurred on Snæfellsjökull in 1980–1994, accumulating at a rate of 0.7 m w.e. a^{-1}. Without area-weighting, the mean and standard deviation (mean±SD) of mass balances of the target glaciers were –0.44±0.16 m w.e. a^{-1} in 1945–1960, 0.00±0.21 m w.e. a^{-1} in 1960–1980, 0.11±0.25 m w.e. a^{-1} in 1980–1994, –1.01±0.50 m w.e. a^{-1} in

1994–2004, –1.27±0.56 m w.e. a^{-1} in 2004–2010 and –0.14±0.51 m w.e. a^{-1} in 2010–2015. The range of obtained mass balance therefore becomes more disperse in the last two time periods (Fig. 6).

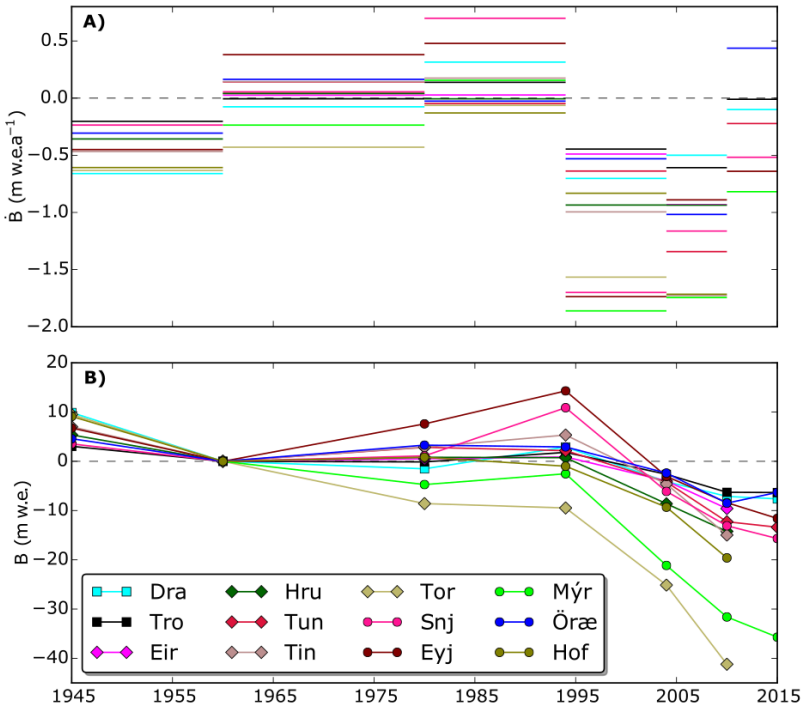

Fig. 6: A) Average mass balance after temporal homogenization at the six time periods analyzed. B) Cumulative absolute mass balance centered in 1960 (common year for the selected glaciers). Squares indicate glaciers located at the north, diamonds glaciers inland and circles represent glaciers at the south and west coast.

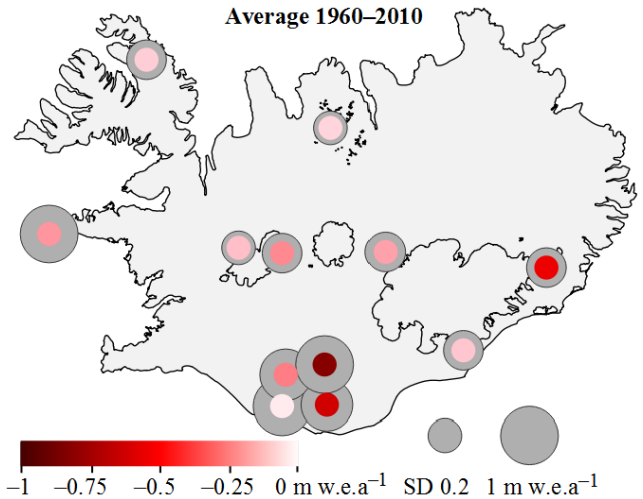

Fig. 7: Glacier-wide mass balance average during 1960–2010. The size of the grey circles shows the temporal variability, estimated for each glacier as the standard deviation of the temporally homogenized glacier-wide mass balance, using a weight based on each time period.

Total mass changes and contribution to sea-level rise

We divided the target glaciers into four subgroups >100 km^2 to estimate total glacier mass change: Drangajökull, Mýrdalsjökull, Öræfajökull and the group of other glaciers and ice caps (<100 km^2) (Table 1). Most of the mass loss occurred in 1994–2010: 23.75±1.61 Gt (1.48±0.1 Gt a^{-1}), or 0.066±0.004 mm Sea Level Equivalent (SLE). Mýrdalsjökull contributed about 70% to the total mass loss ($\dot{B}_{1994}^{1910}$), even though its area is about half of the total of studied glaciers. The group of glaciers <100 km^2 contributed to the mass loss significantly more than some larger (>100 km^2) ice caps such as Öræfajökull, and more than twice as much as Drangajökull (Table 1).

Table 2: Area, area-weighted mass balance (m w.e. a^{-1}) and mass loss (Gt) for the analyzed areas in 1945–1960, 1960–1994 and 1994–2010. *Values used for Mýrdalsjökull, Eiríksjökull and Tungnafellsjökull reach only back to 1960. **Þrándarjökull and Snæfell are excluded in this analysis, due to limited data coverage.

	Area 2010 (km^2)	$\dot{B}_{1945}^{1960}$ (m w.e. a^{-1}) [Gt]*	$\dot{B}_{1960}^{1994}$ (m w.e. a^{-1}) [Gt]	$\dot{B}_{1994}^{2010}$ (m w.e. a^{-1}) [Gt]
Drangajökull	143.6	–0.66±0.17 [–1.46±0.37]	0.06±0.05 [0.30±0.25]	–0.61±0.04 [–1.42±0.10]
Mýrdalsjökull*	562.4	N/A N/A	–0.07±0.07 [–1.53±1.50]	–1.82±0.17 [–16.97±1.55]
Öræfajökull	160.2	–0.31±0.23 [–0.82±0.57]	0.09±0.10 [0.52±0.63]	–0.71±0.15 [–1.94±0.39]
Others**	187.9	–0.42±0.07 [–1.03±0.17]	0.16±0.04 [1.23±0.28]	–1.01±0.05 [–3.42±0.17]
Total	1054.1	N/A N/A	0.01±0.04 [0.52±1.67]	–1.34±0.09 [–23.75±1.61]

DISCUSSION

Spatio-temporal mass balance and climate distribution

The temperature record from Stykkishólmur indicates a maximum in the 1930s followed by gradual cooling until the 1960s (Fig. 8). During 1945–1960, all the analyzed glaciers show mass loss (Fig. 3 and 5a). During 1960–1980 most glaciers were on average in equilibrium, with the exception of slightly negative values for Torfajökull and Mýrdalsjökull. Most glaciers were gaining mass or close to equilibrium in 1980–1994, with the highest mass gain on Snæfellsjökull (W) and Eyjafjallajökull (S) (Fig. 3 and 5b,c). These results agree with the regional mass balance trends described prior to the 1990s based on reduced previous observations (Björnsson et al., 2013).

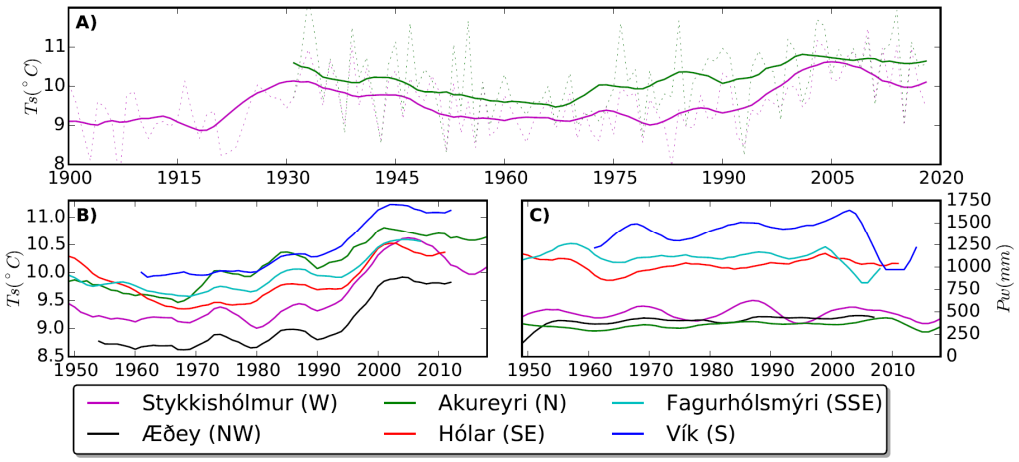

Fig. 8: A) Long time series of average summer temperatures (June, July, August) at Stykkishólmur and Akureyri. B) Summer temperatures at the six stations selected around Iceland. C) Winter precipitation (October-April). The solid lines are obtained by applying 11-year wide triangular filters (e.g. Pálsson et al., 2012; Björnsson et al., 2013). The location of each station is shown in Fig. 1.

In 1994–2010, a significant mass loss is observed in all the analyzed glaciers (Fig. 5d,e). The highest mass loss is found at coastal glaciers in the south and west and glaciers located at lower elevations (ca <1200 m a.s.l., Fig. 2). The area-weighted mass balance of the studied glaciers was $\dot{B}_{1994}^{2010}$ =–1.34±0.09m w.e. a^{-1} (Table 2), similar to the mass balance measured in situ at Hofsjökull and Langjökull (–1.4 m w.e. a^{-1}), but more negative than for Vatnajökull (–0.8 m w.e. a^{-1}) (Pálsson et al., 2012; Björnsson et al., 2013; Jóhannesson et al., 2013).

After 2010, glacier mass balance has been less negative than the previous two decades, and Öræfajökull has been gaining mass, showing 0.44±0.08 m w.e. a^{-1} in 2010–2017. It covers the largest elevation range (0–2100 m a.s.l.), collects the highest amount of precipitation in Iceland (Crochet et al., 2007) with likely summer snowfalls and has steep outlets leading to rapid mass transport. The modelled precipitation used in our study (Nawri et al., 2017) indicates increased winter precipitation in recent years on Öræfajökull.

The decadal variability of mass balances is strongly related to the proximity of the glaciers to the coasts (Fig. 6,7). Glaciers located at the south and west coasts are classified as maritime (e.g. De Woul and Hock, 2005) and show high mass balance variations during the study period. Öræfajökull is an exception, which can possibly be explained by its aforementioned topographic characteristics and large precipitation rates. The inland glaciers have a more continental regime (e.g. Hock et al., 2009). They are subject to rain shadows and have a more stable precipitation. Their differences in mass balance may be explained by differences in elevation, which can explain the larger decadal variability of Torfajökull and Tindfjallajökull, being these more sensitive to temperature changes than other glaciers inland (Fig. 4). Glaciers further north, like Drangajökull and the glaciers on Tröllaskagi, have significantly lower decadal variations, probably explained by colder oceanic currents affecting their climate (Björnsson et al., 2013).

We observed high intraregional variability of mass balances, particularly clear for Tindfjallajökull, Torfajökull, Eyjafjallajökull and Mýrdalsjökull (S-Iceland, maximum 40 km away from each other). Analogously, different catchments of some of the analyzed glaciers can exhibit substantial mass

balance differences: (1) Drangajökull shows a strong E-W trend of mass balance, probably associated with effects of precipitation and snow drift (Magnússon et al., 2016a; Belart et al., 2017). (2) In Mýrdalsjökull the northern (inland) outlets show a homogeneous lowering trend, as opposed to the southern (coastal) outlets, which reveal high decadal variability in elevation (Fig. S3.5). This pattern is observed on Vatnajökull (Björnsson et al., 2013) and can be explained by the maritime regime of the southern outlets, with most precipitation falling at these locations, while the northern outlets are located in a rain shadow (Crochet et al., 2007; Ágústsson et al., 2013). (3) Two of the outlets of Öræfajökull are calving at their terminus (Magnússon et al., 2012), also resulting in a more negative mass balance than the rest of the ice cap (Fig. S3.6).

The intraregional variability can additionally explain why Mýrdalsjökull contributes 70% of the mass loss of the study areas in 1994–2010, despite it covering only about 50% of their total area (Table 2). This shows that the interpolation of mass balance from a few glaciers to the entire region (e.g. Björnsson et al., 2013) can lead to erroneous estimates of mass loss from small glaciers. In this context, Mýrdalsjökull and the southern small glaciers contribute more than the northern glaciers, like Drangajökull or the cluster of glaciers in Tröllaskagi. Nevertheless, the small glaciers only cover 10% of the total glacierized area of Iceland, and their mass loss is close to one order of magnitude smaller than for the entire country (9.5 Gt a^{-1} vs 1.5 Gt a^{-1}).

In comparison to long-term (>50 year) mass balance observations in other glaciarized regions, the evolution of Icelandic glaciers during the last 70 years follows similar trends as observed in the Alps (Huss et al., 2010), Pyrénees (Marti et al., 2015) or in tropical glaciers as in Cordillera Real (Soruco et al., 2009). The intraregional variability observed in Iceland during 1994–2004 (SD= 0.56 m w.e. a^{-1}) and 2004–2010 (SD=0.51 m w.e. a^{-1}), indicate a similar variability compared to the Himalayas in 2000–2016 (Brun et al., 2017). Other glacierized regions, however, have experienced more homogeneous decay during the last decades, such as the Alps (Berthier et al., 2016; Fischer et al., 2015) or Svalbard (Moholdt et al., 2010).

Statistical estimation of mass balance from precipitation and temperature records

The mass balance correlates well with climatic variables using a reference-surface correction (Cogley et al., 2011; Huss et al., 2012). This correction improves the fit (R^2, Table 1), typically by 10% and up to 50% for glaciers exhibiting large area changes (Fig. 5). A first order equation (Eq.1) can be used to estimate the annual mass balance as a function of summer temperature, winter precipitation and area, permitting a practical temporal homogenization of geodetic mass balance (e.g. Lambrecht and Kuhn, 2007; Fischer et al., 2015).

Torfajökull, with DEMs acquired in 1979 and 1980, and Tindfjallajökull, with DEMs acquired in 1978 and 1980, served as a test to contrast the temporal homogenization. In both cases, using a DEM 1–2 years apart from 1980, with temporal homogenization based on annually modelled mass balance, led to similar results when using the 1980 DEM, with differences between 0.02 and 0.14 m w.e. a^{-1}, that are within the uncertainties of the geodetic estimates (Supplement S2). On the other hand, it was observed that the temporal homogenization applied for Tungnafellsjökull when shifting from 2011–2016 to 2010–2015 (Fig. 6f) caused a substantial increase in the homogenized mass balance, as result of a very positive mass balance in 2010–2011 in combination with a very negative mass balance in 2015–2016 from the simple model (Eq. 1). This result should be considered with caution.

In some cases, the obtained mass-balance sensitivities indicate unrealistic estimates of the glaciers' responses to climate, in particular the extreme sensitivity to summer temperature estimated in Snæfellsjökull and a slightly negative correlation between winter precipitation and mass balance for

some glaciers, which was subsequently assumed as zero sensitivity to winter precipitation when the homogenization was carried out. In other cases the fit was poor, as for Mýrdalsjökull. Both cases are further described below. The parameters $\partial \dot{B}/\partial Pw$ and $\partial \dot{B}/\partial Ts$ (Fig. 4 and Table 1) should therefore be considered as statistically-derived correlators rather than actual sensitivities. Two questions arise from this method: is the climate model incomplete, or is the linear fit an over-simplification?

Measuring and modelling of winter precipitation is challenging (e.g. Jarosch et al., 2012); the modelled precipitation used was found to be overestimated in coastal areas like Öræfajökull, resulting in unrealistically high modelled-derived winter mass balance (Schmidt et al., 2017). Moreover, the mass balance is controlled by other variables neglected in our simple climate model. Full energy balance models can better reproduce glaciers' response to climate, (e.g. Arnold et al., 1996; Hock and Holmgren, 2005) accounting, for example, for albedo changes, which can accelerate the melt if dust (e.g. Arnalds et al., 2016; Wittmann et al., 2017) or thin tephra (e.g. Möller et al., 2014; Gascoin et al., 2017) are emplaced on the glacier, or can decrease the melt if snow events occur during the summer.

The energy balance models, however, do not account for some mass balance forcing, for example: (1) Wind-drifted snow can significantly contribute to winter accumulation in individual catchments, as demonstrated for Drangajökull (Magnússon et al., 2016a; Belart et al., 2017) and also glacier-wide, for small glaciers surrounded by mountains (e.g. Dadic et al., 2010). (2) Debris (either rock or tephra), present in Icelandic glaciers like Eiríksjökull (Fig. S3.1), enhances or reduces the melt rate depending on the thickness (e.g. Östrem, 1959). (3) Volcanic forcing can affect the mass balance observations, typically at most to one hydrological year (Björnsson et al., 2013). (4) Local changes in thermal power underneath the glacier, as observed on Mýrdalsjökull (Guðmundsson et al., 2007), can locally also affect the mass balance (Björnsson, 2003).

The reference-surface correction term in the mass balance model (Eq. 1) was generalized by (Elsberg et al., 2001; Harrison et al., 2001), and further in Belart et al. (in review) by assuming a linear relationship between the volume changes and area changes of the glacier. This linearity is generally observed in this study's glaciers, with a typical fit R^2>0.8 between volume changes and area changes (e.g. Pálsson et al., 2012; Belart et al., in review), but is questioned for Mýrdalsjökull (R^2=0.3) and Öræfajökull (R^2=0.5).

A non-linear relationship between area and volume changes can be observed occasionally by the obtained maps of elevation changes: the period 1960s to 1990s reveal abnormal elevation changes with significant lowering of the accumulation area, while the margins are advancing. This led to a rapid area increase, while the volume remained close to zero. This effect is particularly visible in observed at five of the target glaciers during the 1960s to 1990s: Snæfellsjökull (W), Eyjafjallajökull (Belart et al., in review) and Mýrdalsjökull (S), Öræfajökull (SSE) and Eiríksjökull (inland). This scenario therefore disagrees with the described linear assumption, and it helps explaining the misfit found in Eyjafjallajökull during 1980–1984, where the statistical model overestimated the mass balance (Belart et al., in review), possibly related to significant area increase with limited volume increase.

Some of these events correlate well with periods of increased winter precipitation observed at nearby stations (Fig 9). For example in 1945–1960 Öræfajökull (SSE) experienced elevation gain at high elevation, and two southern outlets had slight advances (Fig. 9 and S3.6). This coincides with increased precipitation at Fagurhólsmýri before and around 1960 (Fig. 8 and 9). The following period analyzed (1960/61–1982) reveals a substantial lowering in the accumulation area. Higher subsidence of the accumulation can be observed in Mýrdalsjökull in 1980–1984, which could be associated with increased precipitation in the early 1970s (Fig. 9)

This suggests that the ice motion was accelerated from the increased mass input after periods of high winter precipitation. After a series of winters of increased precipitation, the deficit of input compared to previous years, together with high submergence rates, could lead to the significant lowering of the accumulation area. During 1960–1990 the temperature was relatively stable (Fig. 8), which suggests that these changes in geometry were substantially forced by precipitation changes.

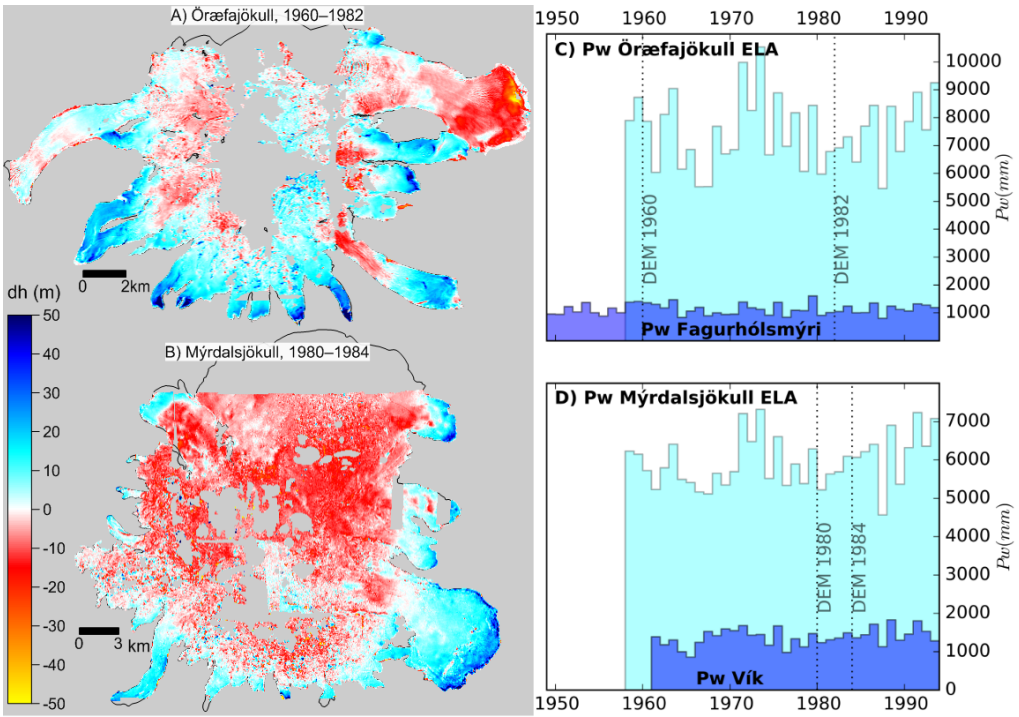

Fig 9. A) Maps of elevation changes of Öræfajökull (23 August 1960 (West side) mosaicked with 07 July 1961 (East side) – 20 August 1982), B) Mýrdalsjökull (23 August 1980 – 09 September 1984). C) Winter precipitation, as extracted from the gridded models (cyan) at the Equilibrium Line Altitued (ELA) of Öræfajökull in 1957–1994. In blue, the winter precipitation is obtained from Fagurhólsmýri, ~1 km away from the ice cap. D) Analogous data for Mýrdalsjökull at the ELA, from the gridded models (cyan) and in blue from a weather station nearby (Vík, ~20km away from Mýrdalsjökull).

These observations indicate that coupling mass balance with ice dynamics is a key for fully describing the mass balance – climate relationship (e.g. Jóhannesson, 1997; Aðalgeirsdóttir et al., 2006). The presented series of DEMs, volume changes and geodetic mass balance, in combination with available bedrock maps, like that of Mýrdalsjökull and Öræfajökull (Björnsson et al., 2000; Magnússon et al., 2012), stimulate the development and further improvement of models capable to reproduce the observed behaviour of glaciers in 1960–1990, a period with limited observation, yet interesting as it presents a climate substantially different than the climate after the 1990s. This will also help understand the future evolution of glaciers as Öræfajökull, which has started a new period of increased accumulation and probably an increase in the ice dynamics.

CONCLUSIONS

This study presents a 70-year extensive dataset of elevation changes and geodetic mass balances of glaciers distributed in all quarters of Iceland, most of them previously lacking mass balance measurements. The mean and standard deviation (mean±SD) of mass balances of the target glaciers were –0.44±0.16 m w.e. a^{-1} in 1945–1960, 0.00±0.21 m w.e. a^{-1} in 1960–1980, 0.11±0.25 m w.e. a^{-1} in 1980–1994, –1.01±0.50 m w.e. a^{-1} in 1994–2004, –1.27±0.56 m w.e. a^{-1} in 2004–2010 and –0.14±0.51 m w.e. a^{-1} in 2010–2015. The period 1994–2010, the most negative mass balance period, yielded a mass loss of 23.75±1.61 Gt (1.48±0.1 Gt a^{-1}), or 0.066±0.004 mm SLE.

The region-wide, multitemporal intercomparison of mass balances revealed spatial trends over Iceland: glaciers located close to the south and west coast experience higher decadal oscillations in mass balance than the internal and northern glaciers. This trend can probably be explained by different local climate, related to oceanic currents surrounding Iceland, rain shadows and elevation of the glaciers. Due to a large intraregional variability, particular care should be taken when extrapolating mass balance from one glacier to another, even at close distances.

The correction for reference-surface improved substantially the fit between mass balance and the climate model. Yet, in some of the studied glaciers, a simple linear model could not explain the mass balance as function of summer temperatures and winter precipitations; this model required the assumption of linearity between area and volume changes, which was contradicted at specific time periods when observing substantial lowering in the accumulation area while the glacier fronts were advancing. This was attributed to changes in ice flux towards the ablation area, possibly explained by high precipitation events. This study provides unique data for studies of coupled mass balance to ice dynamics, especially aiming at reproducing an increased ice flux forced by precipitation changes.

Acknowledgements:

This study was funded by the University of Iceland (UI) Research Fund and the Icelandic research council (Rannís) through the project Katla Kalda. Karsten Kristinsson is greatly acknowledged for scanning the aerial photographs stored at Landmælingar Íslands. Pléiades images were acquired at research price thanks to the CNES ISIS program (http://www.isis-cnes.fr). WorldView DEMs were obtained through the ArcticDEM project. This study uses the lidar mapping of the glaciers in Iceland, funded by the Icelandic Research Fund, the Landsvirkjun research fund, the Icelandic Road Administration, the Reykjavík Energy Environmental and Energy Research Fund, the Klima- og Luftgruppen research fund of the Nordic Council of Ministers, the Vatnajökull National Park, the organization Friends of Vatnajökull, LMÍ, IMO and the UI research fund. EB acknowledges support from the French Space Agency (CNES) though the TOSCA program. This study uses the GLIMS database of the outlines of Icelandic glaciers. Michelle Koutnik is thanked for fruitful discussions about potential from the datasets and rock and debris covered glaciers.

References

Aðalgeirsdóttir, G., Jóhannesson, T., Björnsson, H., Pálsson, F. and Sigurðsson, O.: Response of Hofsjokull and southern Vatnajökull, Iceland, to climate change, J. Geophys. Res.-Earth Surf., 111(F3), 2006.

Ágústsson, H., Hannesdóttir, H., Thorsteinsson, T., Pálsson, F. and Oddsson, B.: Mass balance of Mýrdalsjökull ice cap accumulation area and comparison of observed winter balance with simulated precipitation, Jökull, 63, 91–104, 2013.

Ahlmann, H. W.: The relative influence of precipitation and temperature on glacier regime, Geogr. Ann., 22(3–4), 188–205, doi:10.1080/20014422.1940.11880689, 1940.

Anderson, L. S., Flowers, G. E., Jarosch, A. H., Aðalgeirsdóttir, G. T., Geirsdóttir, Á., Miller, G. H., Harning, D. J., Thorsteinsson, T., Magnússon, E. and Pálsson, F.: Holocene glacier and climate variations in Vestfirðir, Iceland, from the modeling of Drangajökull ice cap, Quat. Sci. Rev., 190, 39–56, doi:10.1016/j.quascirev.2018.04.024, 2018.

Arnalds, O., Dagsson-Waldhauserova, P. and Olafsson, H.: The Icelandic volcanic aeolian environment: Processes and impacts — A review, Aeolian Res., 20, 176–195, doi:10.1016/j.aeolia.2016.01.004, 2016.

Arnold, N. S., Willis, I. C., Sharp, M. J., Richards, K. S. and Lawson, W. J.: A distributed surface energy-balance model for a small valley glacier. I. Development and testing for Haut Glacier d' Arolla, Valais, Switzerland, J. Glaciol., 42(140), 77–89, doi:10.3189/S0022143000030549, 1996.

Bahr, D. B., Pfeffer, W. T., Sassolas, C. and Meier, M. F.: Response time of glaciers as a function of size and mass balance: 1. Theory, J. Geophys. Res.-Solid Earth, 103(B5), 9777–9782, 1998.

Bauder, A., Funk, M. and Huss, M.: Ice-volume changes of selected glaciers in the Swiss Alps since the end of the 19th century, Ann. Glaciol., 46, 145–149, 2007.

Belart, J. M. C., Magnússon, E., Berthier, E., Pálsson, F., J., Aðalgeirsdottir, G. and Jóhannesson, T.: The geodetic mass balance of Eyjafjallajökull ice cap in 1945-2014. Processing guidelines and relation to climate., J. Glaciol., in review.

Belart, J. M. C., Berthier, E., Magnússon, E., Anderson, L. S., Pálsson, F., Thorsteinsson, T., Howat, I. M., Aðalgeirsdóttir, G., Jóhannesson, T. and Jarosch, A. H.: Winter mass balance of Drangajökull ice cap (NW Iceland) derived from satellite sub-meter stereo images, The Cryosphere, 11(3), 1501–1517, doi:10.5194/tc-11-1501-2017, 2017.

Berthier, E., Cabot, V., Vincent, C. and Six, D.: Decadal Region-Wide and Glacier-Wide Mass Balances Derived from Multi-Temporal ASTER Satellite Digital Elevation Models. Validation over the Mont-Blanc Area, Front. Earth Sci., 4, doi:10.3389/feart.2016.00063, 2016.

Bindschadler, R. and Vornberger, P.: Changes in the West Antarctic ice sheet since 1963 from declassified satellite photography, Science, 279(5351), 689–692, 1998.

Björnsson, H.: Subglacial lakes and jokulhlaups in Iceland, Glob. Planet. Change, 35(3–4), 255–271, 2003.

Björnsson, H.: The glaciers of Iceland, Atlantis Press, 2, 613, doi:10.2991/978-94-6239-207-6, 2017.

Björnsson, H. and Pálsson, F.: Icelandic glaciers, Jökull, 58, 365–386, 2008.

Björnsson, H., Pálsson, F. and Guðmundsson, M.: Surface and bedrock topography of the Mýrdalsjökull ice cap, Iceland, Jökull, 49, 29–46, 2000.

Björnsson, H., Pálsson, F., Guðmundsson, S., Magnússon, E., Aðalgeirsdóttir, G., Jóhannesson, T., Berthier, E., Sigurðsson, O. and Thorsteinsson, T.: Contribution of Icelandic ice caps to sea level rise: trends and variability since the Little Ice Age, Geophys. Res. Lett., 40, 1–5, doi:10.1002/grl.50278, 2013.

Bojinski, S., Verstraete, M., Peterson, T. C., Richter, C., Simmons, A. and Zemp, M.: The Concept of Essential Climate Variables in Support of Climate Research, Applications, and Policy, Bull. Am. Meteorol. Soc., 95(9), 1431–1443, doi:10.1175/BAMS-D-13-00047.1, 2014.

Bolch, T., Pieczonka, T. and Benn, D. I.: Multi-decadal mass loss of glaciers in the Everest area (Nepal Himalaya) derived from stereo imagery, The Cryosphere, 5(2), 349–358, doi:10.5194/tc-5-349-2011, 2011.

Bolch, T., Sandberg Sørensen, L., Simonsen, S. B., Mölg, N., Machguth, H., Rastner, P. and Paul, F.: Mass loss of Greenland's glaciers and ice caps 2003–2008 revealed from ICESat laser altimetry data, Geophys. Res. Lett., 40, 1–7, doi:10.1002/grl.50270, 2013.

Brun, F., Berthier, E., Wagnon, P., Kääb, A. and Treichler, D.: A spatially resolved estimate of High Mountain Asia glacier mass balances from 2000 to 2016, Nat. Geosci., 10(9), 668, doi:10.1038/ngeo2999, 2017.

Cogley, J. G., Hock, R., Rasmussen, L. A., Arendt, A. A., Bauder, A., Braithwaite, R. J., Jansson, P., Kaser, G., Möller, M., Nicholson, L. and Zemp, M.: Glossary of glacier mass balance and related terms, IHP-VII Technical Documents in Hydrology No. 86, IACS Contribution No. 2, UNESCO-IHP, Paris, , 114, 2011.

Crochet, P. and Jóhannesson, T.: A dataset of daily temperature in Iceland for the period 1949–2010, Jökull, 61, 1–17, 2011.

Crochet, P., Jóhannesson, T., Jonsson, T., Sigurðsson, O., Björnsson, H., Pálsson, F. and Barstad, I.: Estimating the spatial distribution of precipitation in Iceland using a linear model of orographic precipitation, J. Hydrometeorol., 8(6), 1285–1306, 2007.

Dadic, R., Mott, R., Lehning, M. and Burlando, P.: Wind influence on snow depth distribution and accumulation over glaciers, J. Geophys. Res. Earth Surf., 115(F1), doi:10.1029/2009JF001261, 2010.

De Woul, M. and Hock, R.: Static mass-balance sensitivity of Arctic glaciers and ice caps using a degree-day approach, Ann. Glaciol. Vol 42 2005, 42, 217–224, 2005.

Elsberg, D. H., Harrison, W. D., Echelmeyer, K. A. and Krimmel, R. M.: Quantifying the effects of climate and surface change on glacier mass balance, J. Glaciol., 47(159), 649–658, 2001.

Fieber, K. D., Mills, J. P., Miller, P. E., Clarke, L., Ireland, L. and Fox, A. J.: Rigorous 3D change determination in Antarctic Peninsula glaciers from stereo WorldView-2 and archival aerial imagery, Remote Sens. Environ., 205(Supplement C), 18–31, doi:10.1016/j.rse.2017.10.042, 2018.

Fischer, M., Huss, M. and Hoelzle, M.: Surface elevation and mass changes of all Swiss glaciers 1980–2010, The Cryosphere, 9(2), 525–540, doi:10.5194/tc-9-525-2015, 2015.

Gardelle, J., Berthier, E., Arnaud, Y. and Kääb, A.: Region-wide glacier mass balances over the Pamir-Karakoram-Himalaya during 1999–2011, The Cryosphere, 7, 1263–1286, doi:10.5194/tc-7-1263-2013, 2013.

Gascoin, S., Guðmundsson, S., Adalgeirsdottir, G., Pálsson, F., Schmidt, L., Berthier, E. and Björnsson, H.: Evaluation of MODIS Albedo Product over Ice Caps in Iceland and Impact of Volcanic Eruptions on Their Albedo, , doi:10.3390/rs9050399, 2017.

Guðmundsson, M. s T., Högnadóttir, Þ., Kristinsson, A. B. and Guðbjörnsson, S.: Geothermal activity in the subglacial Katla caldera, Iceland, 1999–2005, studied with radar altimetry, Ann. Glaciol., 45, 66–72, doi:10.3189/172756407782282444, 2007.

Guðmundsson, S., Björnsson, H., Magnússon, E., Berthier, E., Pálsson, F., Guðmundsson, M. T., Högnadóttir, T. and Dall, J.: Response of Eyjafjallajökull, Torfajökull and Tindfjallajökull ice caps in Iceland to regional warming, deduced by remote sensing, Polar Res., 30(7282), doi:10.3402/polar.v30i0.7282, 2011.

Gunnlaugsson, Á. Þ.: The geodetic mass balance and ice thickness of Tungnafellsjökull ice cap, Univ. Icel., (M.Sc. Thesis), 1–67, 2016.

Harrison, W. D., Elsberg, D. H., Echelmeyer, K. A. and Krimmel, R. M.: On the characterization of glacier response by a single time-scale, J. Glaciol., 47(159), 659–664, 2001.

Hock, R. and Holmgren, B.: A distributed surface energy-balance model for complex topography and its application to Storglaciaren, Sweden, J. Glaciol., 51(172), 25–36, 2005.

Hock, R., de Woul, M., Radic, V. and Dyurgerov, M.: Mountain glaciers and ice caps around Antarctica make a large sea-level rise contribution, Geophys Res Lett, 36, 2009.

Huss, M.: Density assumptions for converting geodetic glacier volume change to mass change, The Cryosphere, 7(3), 877–887, doi:10.5194/tc-7-877-2013, 2013.

Huss, M. and Hock, R.: A new model for global glacier change and sea-level rise, Front. Earth Sci., 3, doi:10.3389/feart.2015.00054, 2015.

Huss, M., Hock, R., Bauder, A. and Funk, M.: 100-year mass changes in the Swiss Alps linked to the Atlantic Multidecadal Oscillation, Geophys. Res. Lett., 37, 2010.

Huss, M., Hock, R., Bauder, A. and Funk, M.: Conventional versus reference-surface mass balance, J. Glaciol., 58(208), 278–286, doi:10.3189/2012JoG11J216, 2012.

Jarosch, A. H., Anslow, F. S. and Clarke, G. K. C.: High-resolution precipitation and temperature downscaling for glacier models, Clim. Dyn., 38(1), 391–409, doi:10.1007/s00382-010-0949-1, 2012.

Jóhannesson, T.: The response of two Icelandic glaciers to climatic warming computed with a degree-day glacier mass-balance model coupled to a dynamic glacier model, J. Glaciol., 43(144), 321–327, doi:10.3189/S0022143000003270, 1997.

Jóhannesson, T., Raymond, C. F. and Waddington, E. D.: A Simple Method for Determining the Response Time of Glaciers, in Glacier Fluctuations and Climatic Change, pp. 343–352, Springer, Dordrecht., 1989.

Jóhannesson, T., Björnsson, H., Pálsson, F., Sigurðsson, O. and Þorsteinsson, Þ.: LiDAR mapping of the Snæfellsjökull ice cap, western Iceland, Jökull, 61, 19–32, 2011.

Jóhannesson, T., Björnsson, H., Magnússon, E., Guðmundsson, S., Pálsson, F., Sigurðsson, O., Thorsteinsson, T. and Berthier, E.: Ice-volume changes, bias estimation of mass-balance measurements and changes in subglacial lakes derived by lidar mapping of the surface of Icelandic glaciers, Ann. Glaciol., 54(63), 63–74, doi:10.3189/2013AoG63A422, 2013.

Kääb, A., Berthier, E., Nuth, C., Gardelle, J. and Arnaud, Y.: Contrasting patterns of early 21st century glacier mass change in the Himalaya, Nature, 488(7412), 495–498, doi:10.1038/nature11324, 2012.

Korona, J., Berthier, E., Bernard, M., Remy, F. and Thouvenot, E.: SPIRIT. SPOT 5 stereoscopic survey of Polar Ice: Reference Images and Topographies during the fourth International Polar Year (2007-2009), ISPRS J. Photogramm. Remote Sens., 64, 204–212, doi:10.1016/j.isprsjprs.2008.10.005, 2009.

Lambrecht, A. and Kuhn, M.: Glacier changes in the Austrian Alps during the last three decades, derived from the new Austrian glacier inventory, Ann. Glaciol., 46, 177–184, 2007.

Leclercq, P. W. and Oerlemans, J.: Global and hemispheric temperature reconstruction from glacier length fluctuations, Clim. Dyn., 38(5–6), 1065–1079, 2012.

Livingston, R. G.: A history of military mapping camera development, USAF Liaison Off. US Army Eng. Geod. Intell. Mapp. R Agency, 79–110, 1963.

Magnússon, E., Pálsson, F., Björnsson, H. and Guðmundsson, S.: Removing the ice cap of Öræfajökull central volcano, SE-Iceland: Mapping and interpretation of bedrock topography, ice volumes, subglacial troughs and implications for hazards assessments, Jökull, 62, 131–150, 2012.

Magnússon, E., Belart, J. M. C., Pálsson, F., Ágústsson, H. and Crochet, P.: Geodetic mass balance record with rigorous uncertainty estimates deduced from aerial photographs and lidar data – Case study from Drangajökull ice cap, NW Iceland, The Cryosphere, 10(1), 159–177, doi:10.5194/tc-10-159-2016, 2016a.

Magnússon, E., Belart, J. M. C., Pálsson, F., Anderson, L., Gunnlaugsson, Á. Þ., Berthier, E., Ágústsson, H. and Geirsdottir, A.: The subglacial topography of Drangajökull ice cap, NW-Iceland, deduced from dense RES-profiling, Jökull, 66, 1–26, 2016b.

Marti, R., Gascoin, S., Houet, T., Ribière, O., Laffly, D., Condom, T., Monnier, S., Schmutz, M., Camerlynck, C., Tihay, J. P., Soubeyroux, J. M. and René, P.: Evolution of Ossoue Glacier (French Pyrenees) since the end of the Little Ice Age, The Cryosphere, 9(5), 1773–1795, doi:10.5194/tc-9-1773-2015, 2015.

Marzeion, B., Hofer, M., Jarosch, A. H., Kaser, G. and Mölg, T.: A minimal model for reconstructing interannual mass balance variability of glaciers in the European Alps, The Cryosphere, 6(1), 71–84, doi:10.5194/tc-6-71-2012, 2012.

Marzeion, B., Cogley, J. G., Richter, K. and Parkes, D.: Attribution of global glacier mass loss to anthropogenic and natural causes, Science, 345(6199), 919–921, 2014.

Moholdt, G., Nuth, C., Hagen, J. O. and Kohler, J.: Recent elevation changes of Svalbard glaciers derived from repeat track ICESat altimetry, Remote Sens. Environ., 114(11), 2756–2767, 2010.

Möller, R., Möller, M., Björnsson, H., Guðmundsson, S., Pálsson, F., Oddsson, B., Kukla, P. A. and Schneider, C.: MODIS-derived albedo changes of Vatnajökull (Iceland) due to tephra deposition from the 2004 Grímsvötn eruption, Int. J. Appl. Earth Obs. Geoinformation, 26, 256–269, doi:10.1016/j.jag.2013.08.005, 2014.

Nawri, N., Pálmason, B., Petersen, G. N., Björnsson, H. and Þorsteinsson, Á. Þ.: The ICRA atmospheric reanalysis project for Iceland, Icel. Meteorol. Off., VÍ 2017-005, 1–39, 2017.

Noh, M.-J. and Howat, I. M.: Automated stereo-photogrammetric DEM generation at high latitudes: Surface Extraction with TIN-based Search-space Minimization (SETSM) validation and demonstration over glaciated regions, GIScience Remote Sens., 52(2), 198–217, doi:10.1080/15481603.2015.1008621, 2015.

Nye, J. F.: The response of glaciers and ice-sheets to seasonal and climatic changes, Proc. R. Soc. Lond. Ser. Math. Phys. Sci., 256(1287), 559, doi:10.1098/rspa.1960.0127, 1960.

Ohmura, A.: Observed Mass Balance of Mountain Glaciers and Greenland Ice Sheet in the 20th Century and the Present Trends, Surv. Geophys., 32(4–5), 537–554, 2011.

Östrem, G.: Ice Melting under a Thin Layer of Moraine, and the Existence of Ice Cores in Moraine Ridges, Geogr. Ann., 41(4), 228–230, 1959.

Pálsson, F., Guðmundsson, S., Björnsson, H., Berthier, E., Magnússon, E., Guðmundsson, S. and Haraldsson, H.: Mass and volume changes of Langjökull ice cap, Iceland, ~1890 to 2009, deduced from old maps, satellite images and in situ mass balance measurements, Jökull, 62, 81–96, 2012.

Raup, B., Racoviteanu, A., Khalsa, S. J. S., Helm, C., Armstrong, R. and Arnaud, Y.: The GLIMS geospatial glacier database: A new tool for studying glacier change, Glob. Planet. Change, 56(1–2), 101–110, 2007.

Schmidt, L. S., Aðalgeirsdóttir, G., Guðmundsson, S., Langen, P. L., Pálsson, F., Mottram, R., Gascoin, S. and Björnsson, H.: The importance of accurate glacier albedo for estimates of surface mass balance on Vatnajökull: evaluating the surface energy budget in a regional climate model with automatic weather station observations, The Cryosphere, 11(4), 1665–1684, doi:10.5194/tc-11-1665-2017, 2017.

Soruco, A., Vincent, C., Francou, B. and Gonzalez, J. F.: Glacier decline between 1963 and 2006 in the Cordillera Real, Bolivia, Geophys. Res. Lett., 36, 2009.

Spriggs, R. M.: The calibration of Military Cartographic Cameras, Technical Note, Wright-Patterson Air Force Base Ohio USA, 1966.

Vaughan, D. G., Comiso, J. C., Allison, J., Carrasco, J., Kaser, R., Kwok, R., Mote, P., Murray, T., Paul, F., Ren, J., Rignot, E., Solomina, O., Steffen, K. and Zhang, T.: Observations: Cryosphere, in Climate Change 2013: The Physical Science Basis. Contribution of Working Group I to the Fifth Assessment Report of the Intergovernmental Panel on Climate Change, Cambridge University Press, Cambridge, United Kingdom and New York, NY, USA., 2013.

WGMS: Global Glacier Change Bulletin No. 2 (2014-2015), World Glacier Monit. Serv. WGMS, 244 pp, doi:10.5904/wgms-fog-2017-10, 2017.

Wittmann, M., Groot Zwaaftink, C. D., Steffensen Schmidt, L., Guðmundsson, S., Pálsson, F., Arnalds, O., Björnsson, H., Thorsteinsson, T. and Stohl, A.: Impact of dust deposition on the albedo of Vatnajökull ice cap, Iceland, The Cryosphere, 11(2), 741–754, doi:10.5194/tc-11-741-2017, 2017.

Zemp, M., Frey, H., Gärtner-Roer, I., Nussbaumer, S. U., Hoelzle, M., Paul, F., Haeberli, W., Denzinger, F., Ahlstrøm, A. P., Anderson, B., Bajracharya, S., Baroni, C., Braun, L. N., Cáceres, B. E., Casassa, G., Cobos, G., Dávila, L. R., Delgado Granados, H., Demuth, M. N., Espizua, L., Fischer, A., Fujita, K., Gadek, B., Ghazanfar, A., Hagen, J. O., Holmlund, P., Karimi, N., Li, Z., Pelto, M., Pitte, P., Popovnin, V. V., Portocarrero, C. A., Prinz, R., Sangewar, C. V., Severskiy, I., Sigurðsson, O., Soruco, A., Usubaliev, R. and Vincent, C.: Historically unprecedented global glacier decline in the early 21st century, J. Glaciol., 61(228), 745–762, doi:10.3189/2015JoG15J017, 2015.

Supplement for Spatially distributed mass balance of selected Icelandic glaciers, 1945–2015. Trends and link with climate.

This supplement includes:

S1-Supplementary information on the datasets

S2-Supplementary information on the data processing

S3-Time series of elevation changes and mass balance of target glaciers

S4-Geodetic mass balances fixed to the survey dates and seasonally corrected

S5-Mass balance over large (>50 year) time period

S1-Supplementary information on the datasets

The historical datasets used in this study consist on series of aerial photographs acquired in Iceland since 1945 and stored at Landmælingar Íslands (www.lmi.is). For a typical area in Iceland, this includes aerial photographs taken in 1945/46 (American Mapping Service, AMS), 1960/61 (Defense Mapping Agency, DMA), and 1950s to 1990s (Landmælingar Íslands, LMI). The data is available online (https://www.lmi.is/landupplysingar/loftmyndasafn-2-2/) or scanned upon request (Magnússon et al., 2016; Pedersen et al., 2018; Belart et al., in review). The DMA surveys in 1960/61 did not reach the east of Iceland and hence did not cover Snæfell, Þrándarjökull nor Hofsjökull Eystri. An additional dataset was obtained from Loftmyndir efh. from Mýrdalsjökull and Torfajökull in 1999.

The Hexagon KH9 imagery acquired in August 1980 covered 8 of the target areas, (from south to north) Eyjafjallajökull, Mýrdalsjökull, Tindfjallajökull, Torfajökull, Hrútfell, Tungnafellsjökull, Barkádals- and Tungnahryggsjökull.

In the years 2000–2010 numerous acquisitions took place in glacierized areas, in Iceland and elsewhere with SPOT5, through the SPIRIT project (Korona et al., 2009), This provided datapoints through the 2000s in Eyjafjallajökull, Mýrdalsjökull, Tindfjallajökull, Eiríksjökull, Hrútfell, Tungnafellsjökull and Öræfajökull. The last mentioned includes two acquisitions, in 2003 and 2010. ASTER, with modified gain setup especially for surveying glaciers through the GLMIS project (Raup et al., 2007), provided datapoints in 2004 for Barkárdals- and Tungnahryggsjökull, Torfajökull, Þrándarjökull and Hofsjökull Eystri, and in 2013 for Hrútfell.

The lidar datasets were collected between 2008 and 2012, being the earliest one in Snæfellsjökull and Eiríksjökull, the latest ones in Snæfell and Þrándarjökull (Jóhannesson et al., 2013). They covered the glacierized areas and their vicinities (up to 10 km in some cases). At particular locations they had gaps due to low energy of the pulse return, in particular in wet areas covered by tephra, as Kötlujökull (SW-Mýrdalsjökull).

The Pléiades data was scheduled and acquired over the summers 2014 (Eyjafjallajökull, Mýrdalsjökull and Drangajökull, the last one described in Belart et al. (2017)), 2016 (Tungnahryggsjökull and Barkárdalsjökull) and 2017 (Öræfajökull). Mýrdalsjökull and Öræfajökull are relatively large ice caps, >150 km^2 and >20 km width, larger than the satellite swath, hence they were covered in two acquisitions over the course of two weeks. Analogously, Barkárdals- and Tungnahryggsjökull were

surveyed among a larger cluster of glaciers in Tröllaskagi peninsula, hence they were acquired in two separate scenes over the course of two weeks.

WorldView data was used via ArcticDEM (Noh and Howat, 2015), http://arcticdemapp.s3-website-us-west-2.amazonaws.com/explorer/), in Hrútfell as reference for processing other datasets, and in Snæfellsjökull to update the lidar survey. Both datasets were collected in October 2014, and processed into 2×2 m DEMs (Noh and Howat, 2015). The Hrútfell DEM contained significant gaps on the glacier surface, and the Snæfellsjökull DEM included some clear artifacts that were manually masked out.

A dataset was acquired from SPOT7, covering Tungnafellsjökull in 2016. Despite the availability of Pléiades data in 2013 (Berthier et al., 2014; Gunnlaugsson, 2016), the more recent dataset was used in this study since the density assumptions in the geodetic estimates become more robust over longer time periods (Huss, 2013).

The majority of the surveys (55%) were carried out in August, very few in July (5%) and the rest of the surveys were collected between September and October. Most of the surveys from 1945/46 were done in late September or early October.

S2-Supplementary information on the data processing

The photogrammetric processing of the datasets in order to obtain DEMs and orthoimages uses the workflow described in Belart et al., (in review). For each target area, we defined a reference dataset to co-register the rest of the datasets. We used the lidar data in all cases where it was available. In Barkárdals- and Tungnahryggsjökull, we defined the Pléiades dataset as reference (Papasodoro et al., 2015). In Hrútfell we defined a WV DEM as reference.

The stereo images with pinhole camera model were processed using MicMac (Pierrot Deseilligny and Clery, 2011; Rupnik et al., 2017), using Ground Control Points (GCPs) extracted from common areas with the reference dataset. The pushbroom stereo images, from Pléiades, ASTER, SPOT5/7 and WV were processed and co-registered to the reference dataset using the ASP software (Shean et al., 2016). We re-processed the datasets from Tungafellsjökull (Gunnlaugsson, 2016) for consistency with the methodology carried out in the rest of datasets.

The workflow required delineation of the glacier outlines for the glacier-wide calculations. The glacier margins were initially extracted from the GLIMS inventory (Raup et al., 2007) and other previous studies of Icelandic glaciers (Guðmundsson et al., 2011; Magnússon et al., 2012) and subsequently modified to fit the outlines at the selected time period, using thus a systematic definition of the areas to be included or excluded (e.g. debri-covered ice or snowfields). We modified the definition of margins for N-Eiríksjökull, where we included the debri-covered ice at the low areas, in order to visualize the processes affecting debris-covered glaciers (Fig. S3.2).

The delineation of margins by a single operator also minimized errors in area definition. When gaps were present at particular locations of the margins, due to clouds or bad stereo coverage, the outline was filled using the archives of Landsat or ASTER images relative to the analyzed year, or up to two years apart from the analyzed year if there were no images suitable. In the case of the oldest datasets, margins with gaps were digitized from the closest time available. Margins of Eiríksjökull were also obtained relative to 2010 based on Landsat7, for calculation of annually modelled mass balance for the period 2008–2010.

At specific locations and times, mosaics out of two surveys were needed due to incomplete coverage from a single survey. This was the case for: Tindfjallajökull Sep 1945 (70%) & Sep 1946 (30%),

Öræfajökull Aug 1960 (60%) & July 1961 (40%), Eiríksjökull Aug 1978 (80%) and Aug 1979 (20%) and Öræfajökull Aug 1992 (50%) & Aug 1994 (30%). In these cases, mosaics of each two bias-corrected dDEMs was done, after shifting the underlaying dDEM with the mean difference at the overlapping areas of the mosaic, in order to correct the elevation difference caused by the time difference.

Remaining gaps on the maps of elevation difference were filled using mean elevation difference at each 100 m elevation bands, after excluding values larger than three times the Normalized Median Absolute Deviation of each analyzed band. (e.g. Brun et al., 2017). These gaps, in some cases, accounted for a significant percentage of the total ice cap analyzed (up to 40% in the dDEMs in Snæfellsjökull, Figs. S3.7). We established three categories of errors based on the area coverage of each band each elevation band for filling the entirety of the band: we assigned ±1NMAD of the analyzed band if this contained for 60%–80% of grid points, 2NMADSD for 40%–60% of grid points and 3NMAD for elevation bands with less than 40% of grid points. These uncertainties were applied to the gaps at each band, which was added *in quadrature* with an area-weight to the total uncertainty of the dDEM analyzed.

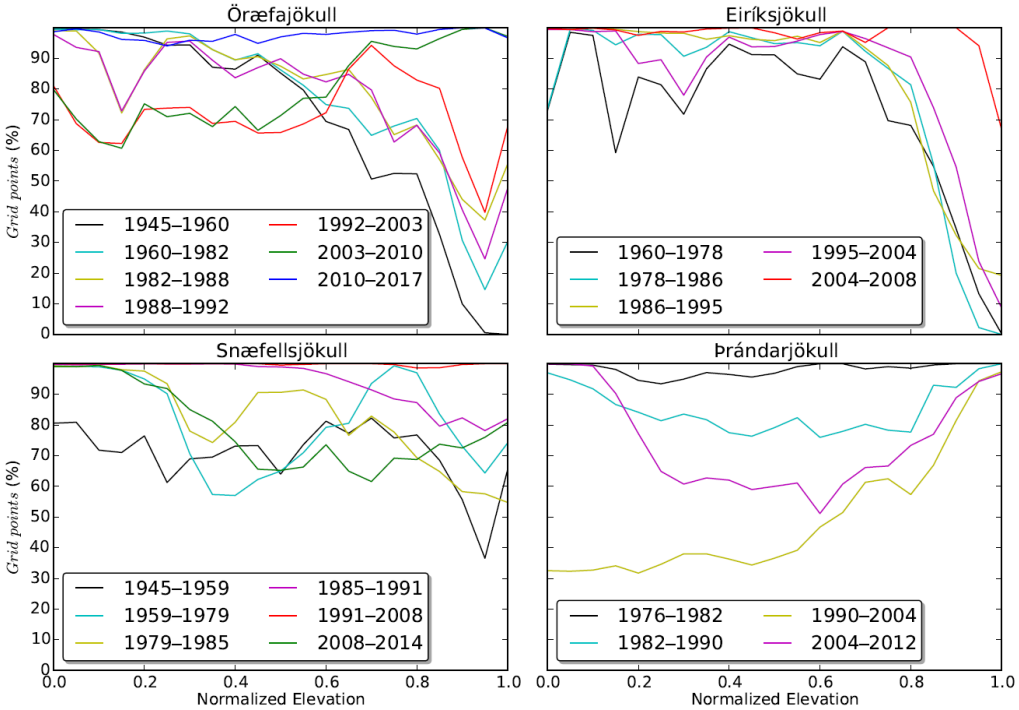

Figure S1. Percentage of grid nodes of the dDEM on-glacier, at the four target areas with the largest data gaps, plotted versus the normalized elevation from lidar. Normalized elevation was calculated as $(z-z_{2.5})/(z_{97.5}-z_{2.5})$, where z is elevation and the sub-indexes indicate percentiles of the entire range of elevation (Brun et al., 2017).

We calculated mass balance $\dot{B}_{t1}^{t2}$ and seasonally corrected $\dot{B}_{EOS}{}_{t1}^{t2}$ (Belart et al., in review) for each chronologically consecutive DEM, using the conversion factor c=0.85±0.6 (Huss, 2013) in all cases.

For correlation of mass balance with climatic parameters (Belart et al., in review), we extracted mean summer temperature (MST) and mean winter precipitation (MWP) annually and averaged over the

time periods defined by the DEMs, from the gridded climatic records, extracted at the equilibrium line altitude (ELA) on each target glacier. The ELA was extracted using the snow line as proxy, in one dataset acquired close to the end of summer, with a clearly defined ablation and accumulation zone. Summer was defined from 21 May to 30 Sep and winter from 1 Oct to 20 May.

To verify the robustness of the temporal homogenization, we calculated independent geodetic mass balances for Torfajökull and Tindfjallajökull using DEMs acquired 1–2 years apart from 1980, allowing to contrast the results of the temporal homogenization for shifting geodetic mass balances to an origin or an end in 1980 (Table S1).

Table 1: Geodetic mass balances of Torfajökull measured using DEMs acquired in 1970,1979,1980 and 1990. Using the annually modelled mass balance from 1979-1980 we calculated the homogenized mass balance without the 1980 DEM. This was done analogously for Tindfjallajökull using the DEMs of 1960,1978,1980 and 1990, contrasted with the annually modelled mass balance from 1978-1980.

Torfajökull			Tindfjallajökull		
Period	Measured	Homogenized	Period	Geodetic	Homogenized
	m w.e. a^{-1}	m w.e. a^{-1}		m w.e. a^{-1}	m w.e. a^{-1}
$\dot{B}_{1970}^{1979}$	0.14±0.18		$\dot{B}_{1960}^{1978}$	0.09±0.04	
$\dot{B}_{1970}^{1980}$	–0.03±0.15	–0.05±0.18	$\dot{B}_{1960}^{1980}$	0.14±0.06	0.12±0.04
$\dot{B}_{1979}^{1990}$	–0.03±0.11		$\dot{B}_{1978}^{1990}$	0.29±0.10	
$\dot{B}_{1980}^{1990}$	0.00±0.14	0.14±0.11	$\dot{B}_{1980}^{1990}$	0.12±0.12	0.14±0.10

S3-Elevation changes and mass balance of individual target glaciers

In this section we show the elevation changes obtained for each target glacier analyzed. Similar maps can be found for Drangajökull in (Magnússon et al., 2016), and Eyjafjallajökull (Belart et al., in review).

S3.1 Barkárdals- and Tungnahryggsjökull

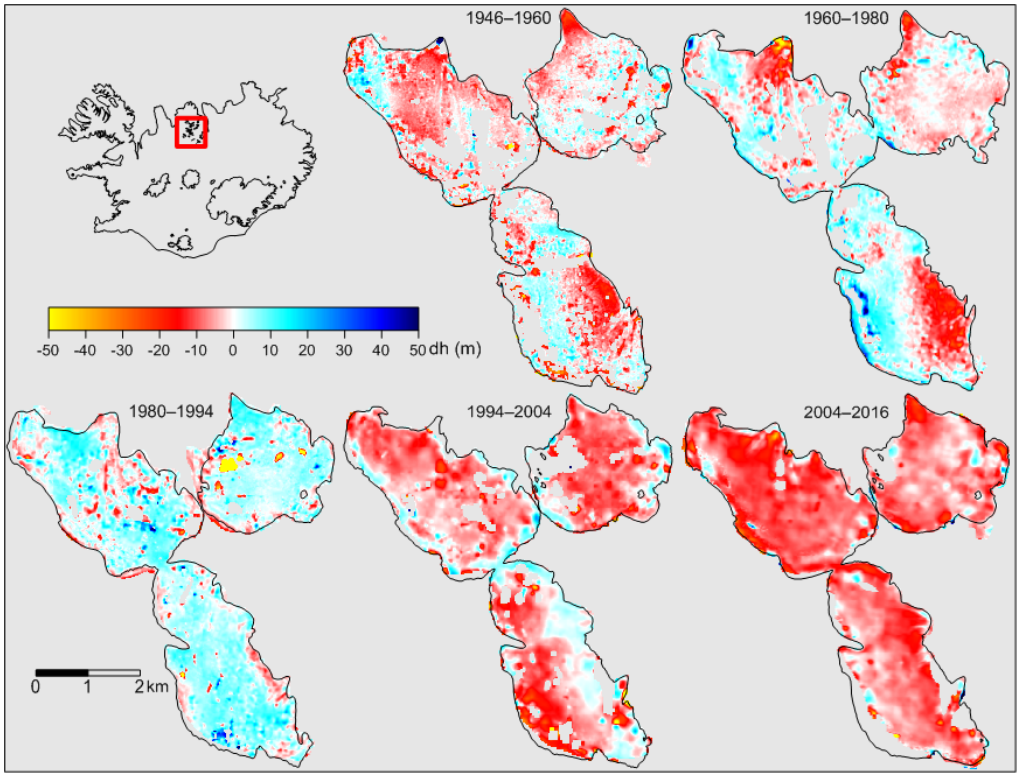

S3.2 Eiríksjökull

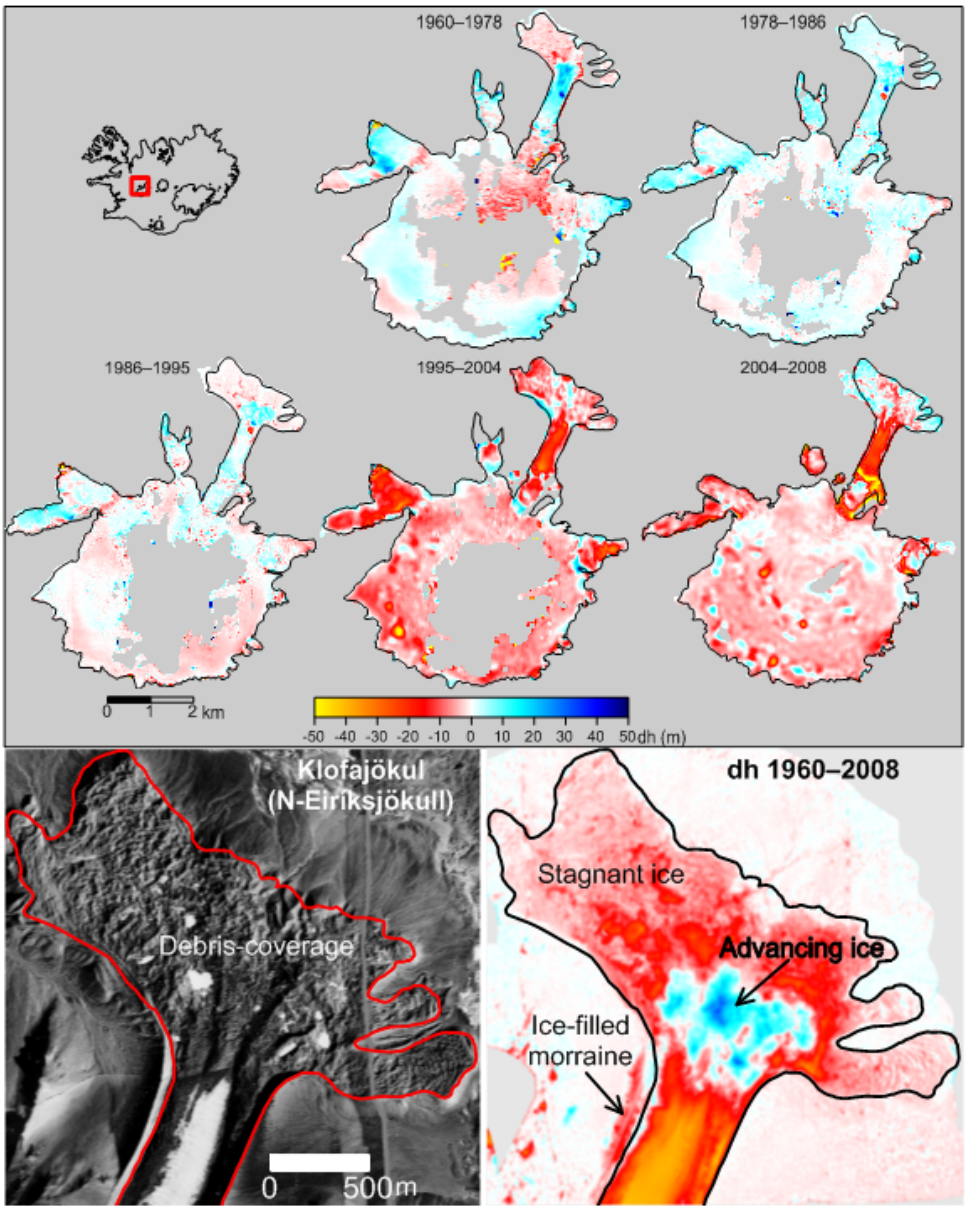

Low left: Orthorectified aerial photograph from 1960, showing the debris-covered margin at the northern glacier snout in Eiríksjökull. Low right: Elevation difference between 1960 and 2008. Stagnant ice at the boundaries of the glacier slowly melted at the analyzed time period, while new ice has flown to lower elevation and remained insulated due to the debris coverage

S3.3 Hofsjökull Eystri

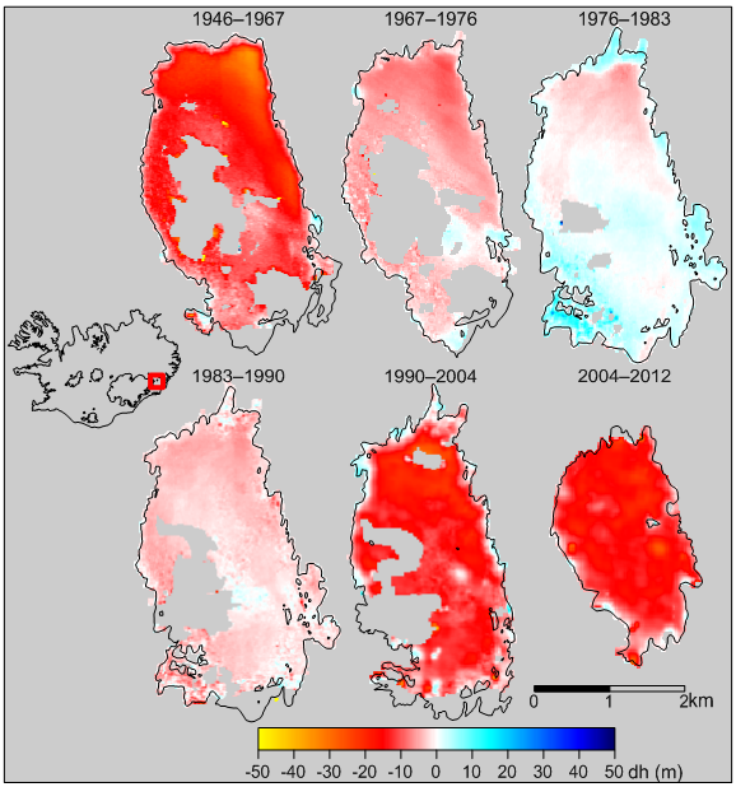

S3.4 Hrútfell

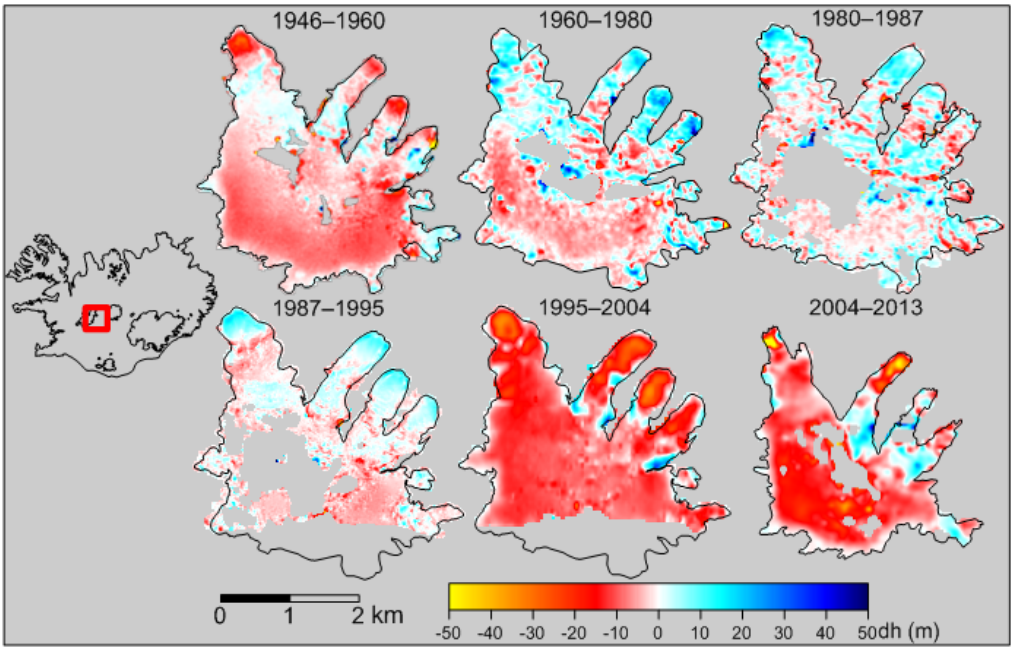

S3.5 Mýrdalsjökull

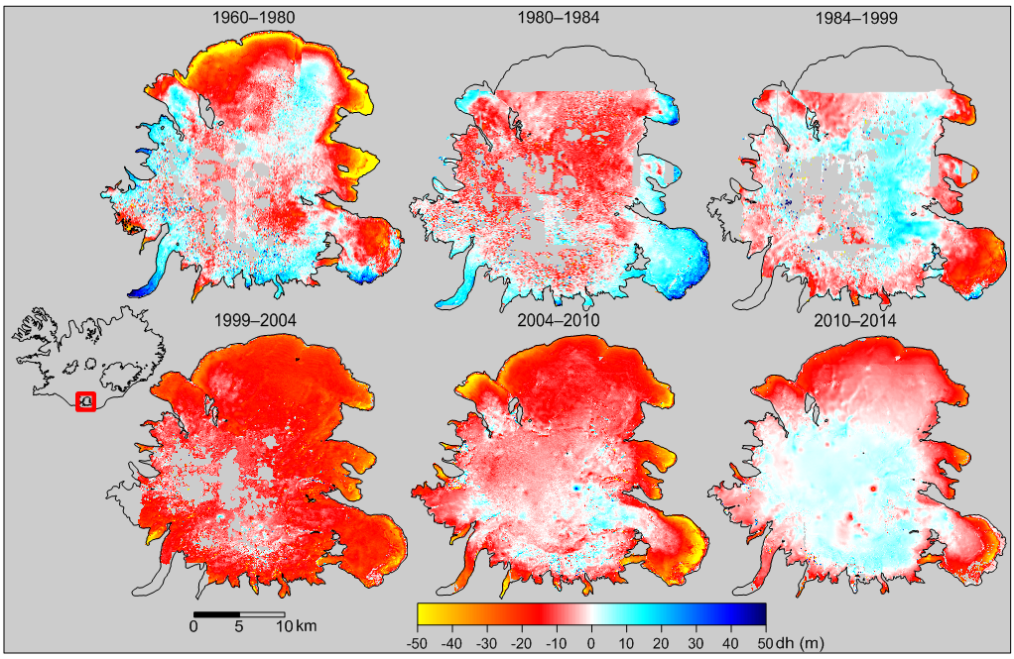

S3.6 Öræfajökull

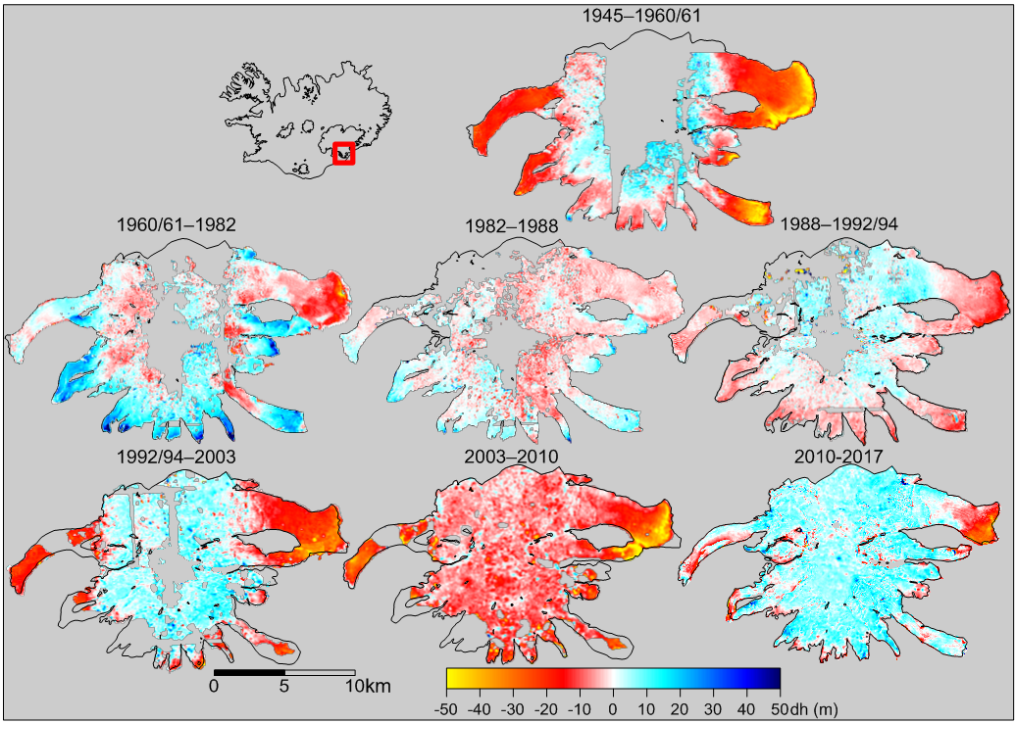

S3.7 Snæfellsjökull

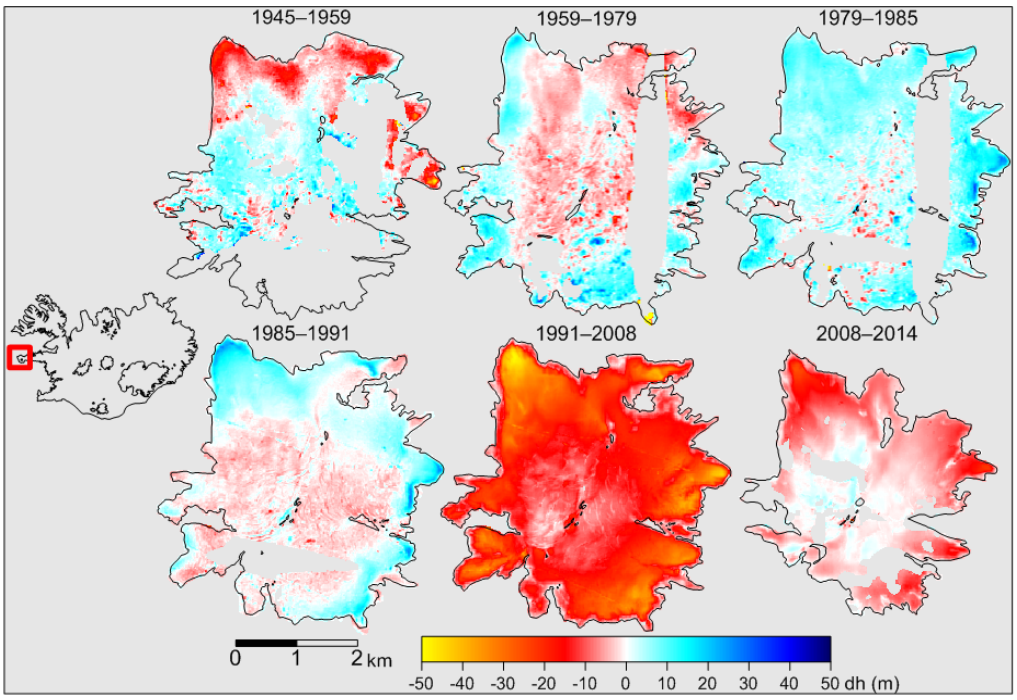

S3.8 Snæfell

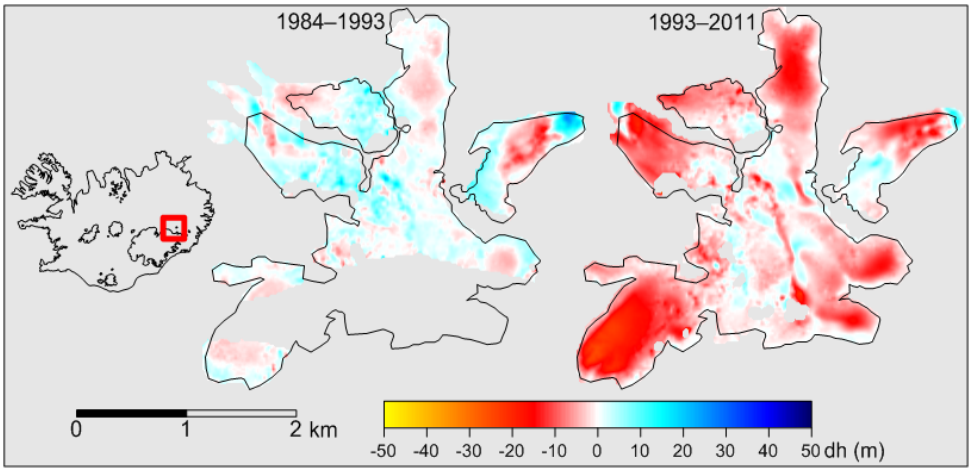

S3.9 Þrándarjökull

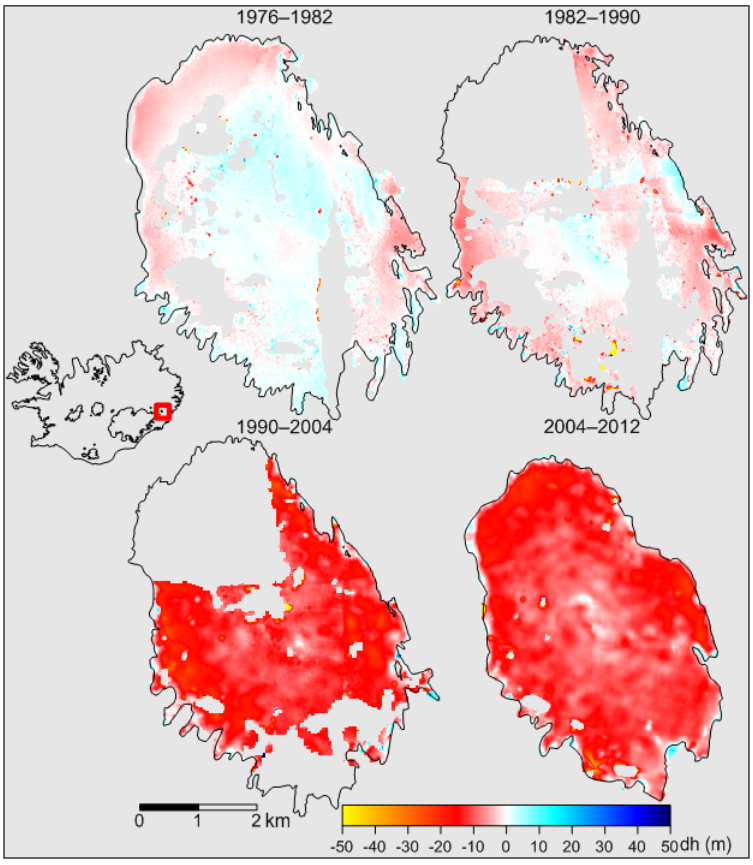

S3.10 Tindfjallajökull

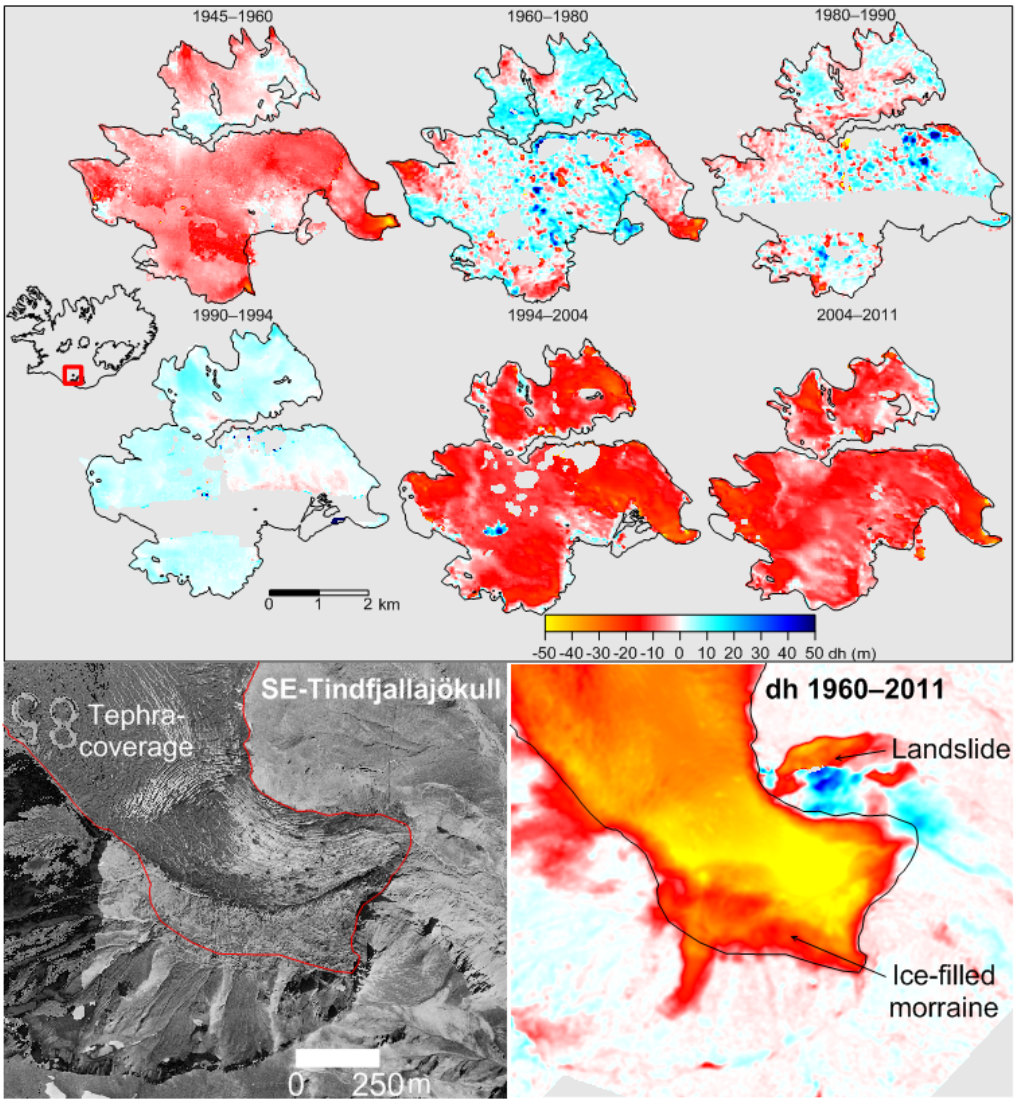

Low left: Orthorectified aerial photograph from SE-Tindfjallajökull in 1960. The glacier margin is heavily affected by tephra from the Hekla 1947 eruption. Glaciers outlines are marked in red lines. Low right: Elevation difference 1960–2011. Besides the lowering of the glacier tongue, stagnant ice on the southern side has melted, and a landslide occurred at the northern side of the glacier margin. Glacier outlines are marked in black lines.

S3.11 Torfajökull

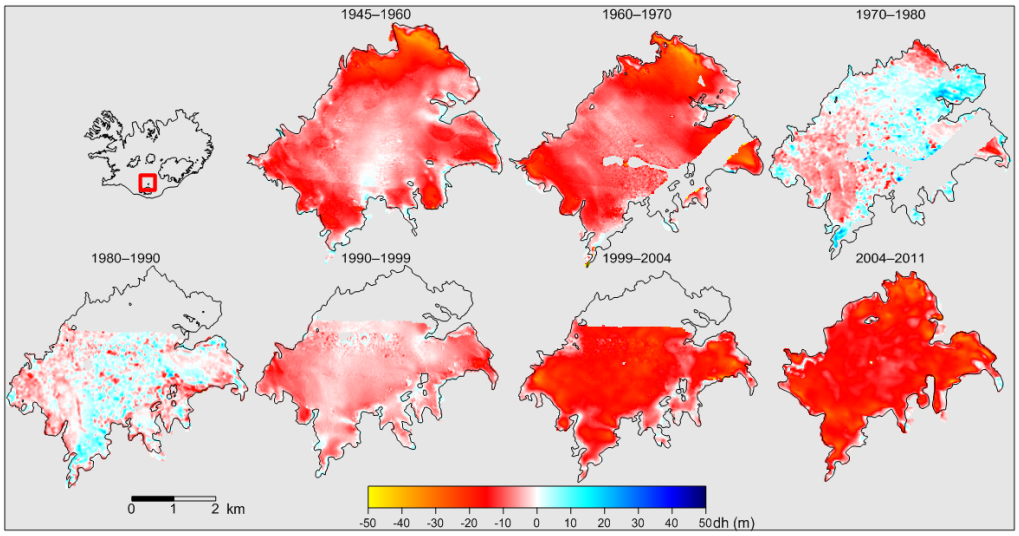

S4.12 Tungnafellsjökull

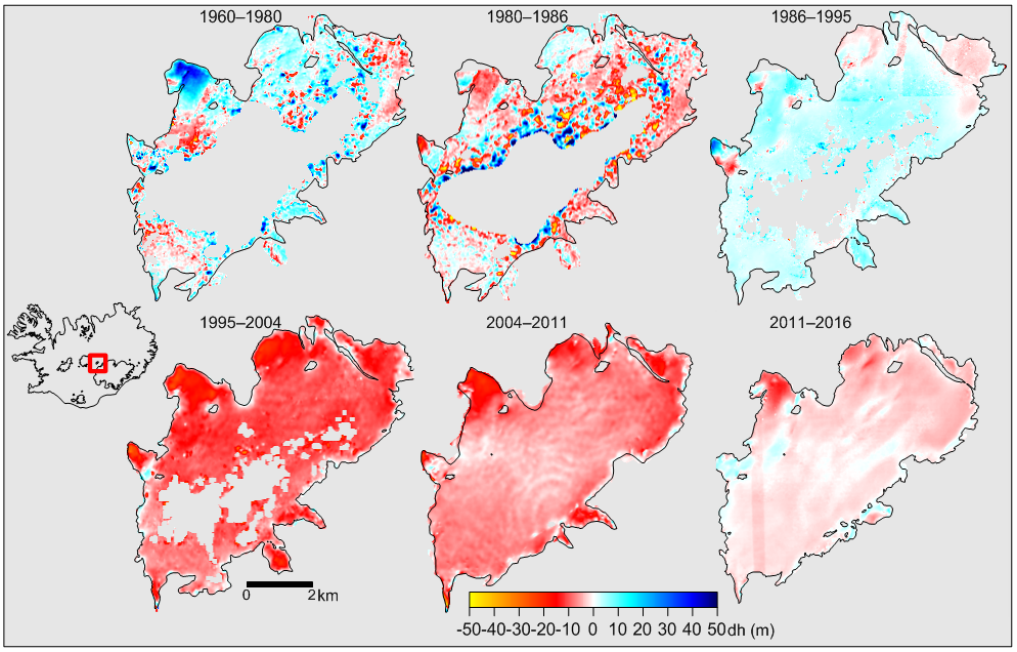

S4-Table of geodetic mass balances, relative to the survey dates and fixed to 1 October

#	t_1	t_2	$\dot{B}$	$\dot{B}_{EOS}$	#	t_1	t_2	$\dot{B}$	$\dot{B}_{EOS}$
Eir	1960	1978	-0.02 ± 0.10	0.01 ± 0.10	Snj	1945	1959	0.05 ± 0.24	-0.07 ± 0.24
Eir	1986	1995	-0.01 ± 0.17	-0.03 ± 0.18	Snj	1959	1979	0.02 ± 0.05	0.01 ± 0.07
Eir	1995	2004	-0.55 ± 0.17	-0.55 ± 0.18	Snj	1979	1985	0.69 ± 0.15	0.84 ± 0.21
Eir	1978	1986	0.13 ± 0.19	0.12 ± 0.20	Snj	1985	1991	0.13 ± 0.05	-0.15 ± 0.17
Eir	2004	2008	-0.95 ± 0.19	-0.88 ± 0.22	Snj	1991	2008	-1.02 ± 0.08	-0.88 ± 0.09
Hof	1946	1967	-0.49 ± 0.08	-0.51 ± 0.08	Snj	2008	2014	-0.64 ± 0.07	-0.52 ± 0.09
Hof	1967	1976	-0.34 ± 0.12	-0.35 ± 0.13	Tin	1945	1960	-0.36 ± 0.12	-0.47 ± 0.13
Hof	1976	1983	0.11 ± 0.04	-0.06 ± 0.12	Tin	1960	1978	0.01 ± 0.01	0.09 ± 0.04
Hof	1983	1990	-0.31 ± 0.05	-0.26 ± 0.14	Tin	1960	1980	0.09 ± 0.06	0.14 ± 0.07
Hof	1990	2004	-0.78 ± 0.08	-0.66 ± 0.09	Tin	1980	1990	0.06 ± 0.15	0.12 ± 0.16
Hof	2004	2012	-1.49 ± 0.15	-1.60 ± 0.17	Tin	1978	1990	0.27 ± 0.07	0.29 ± 0.07
Hrú	1946	1960	-0.27 ± 0.11	-0.36 ± 0.11	Tin	1990	1994	0.54 ± 0.15	0.31 ± 0.19
Hrú	1960	1980	0.01 ± 0.08	0.04 ± 0.09	Tin	1994	2004	-1.09 ± 0.14	-1.00 ± 0.15
Hrú	1980	1987	0.09 ± 0.15	0.02 ± 0.19	Tin	2004	2011	-1.45 ± 0.19	-1.63 ± 0.21
Hrú	1987	1995	-0.10 ± 0.22	-0.06 ± 0.24	Tor	1945	1960	-0.54 ± 0.13	-0.63 ± 0.14
Hrú	1995	2004	-1.02 ± 0.10	-1.01 ± 0.11	Tor	1960	1970	-0.95 ± 0.25	-0.83 ± 0.26
Hrú	2004	2013	-0.78 ± 0.11	-0.76 ± 0.13	Tor	1970	1979	0.21 ± 0.19	0.14 ± 0.19
Mýr	1960	1980	-0.29 ± 0.02	-0.24 ± 0.04	Tor	1970	1980	0.01 ± 0.18	-0.03 ± 0.18
Mýr	1980	1984	-0.57 ± 0.36	-0.40 ± 0.39	Tor	1979	1990	-0.10 ± 0.09	-0.03 ± 0.10
Mýr	1984	1999	-0.10 ± 0.10	-0.19 ± 0.11	Tor	1980	1990	-0.05 ± 0.12	0.00 ± 0.13
Mýr	1999	2004	-2.64 ± 0.21	-2.40 ± 0.25	Tor	1990	1999	-0.43 ± 0.15	-0.42 ± 0.19
Mýr	2004	2010	-1.42 ± 0.10	-1.74 ± 0.17	Tor	1999	2004	-2.56 ± 0.43	-2.55 ± 0.48
Mýr	2010	2014	-0.98 ± 0.07	-0.82 ± 0.22	Tor	2004	2011	-2.07 ± 0.20	-2.27 ± 0.23
Öræ	1945	1960	-0.25 ± 0.22	-0.31 ± 0.23	Trö	1946	1960	-0.16 ± 0.10	-0.20 ± 0.10
Öræ	1960	1982	0.10 ± 0.10	0.16 ± 0.10	Trö	1960	1980	-0.02 ± 0.05	-0.01 ± 0.05
Öræ	1982	1988	-0.12 ± 0.27	-0.30 ± 0.29	Trö	1980	1994	0.19 ± 0.05	0.14 ± 0.06
Öræ	1988	1992	-0.04 ± 0.32	-0.02 ± 0.42	Trö	1994	2004	-0.44 ± 0.08	-0.45 ± 0.10
Öræ	1992	2003	-0.16 ± 0.17	-0.21 ± 0.20	Trö	2004	2016	-0.59 ± 0.07	-0.49 ± 0.08
Öræ	2003	2010	-1.28 ± 0.16	-1.10 ± 0.19	Tun	1960	1980	0.13 ± 0.25	0.14 ± 0.25
Öræ	2010	2017	0.44 ± 0.07	0.44 ± 0.08	Tun	1980	1986	-0.20 ± 0.64	-0.18 ± 0.64
Sna	1984	1993	0.09 ± 0.16	0.06 ± 0.16	Tun	1986	1995	0.24 ± 0.15	0.23 ± 0.16
Sna	1993	2012	-0.22 ± 0.02	-0.29 ± 0.04	Tun	1995	2004	-0.86 ± 0.09	-0.89 ± 0.11
Þrá	1976	1982	0.02 ± 0.08	0.04 ± 0.14	Tun	2004	2011	-0.82 ± 0.07	-0.83 ± 0.11
Þrá	1982	1990	-0.16 ± 0.23	-0.26 ± 0.25	Tun	2011	2016	-0.32 ± 0.04	-0.22 ± 0.11
Þrá	1990	2004	-0.71 ± 0.20	-0.61 ± 0.20					
Þrá	2004	2012	-1.24 ± 0.12	-1.31 ± 0.14					

References

Belart, J. M. C., Magnússon, E., Berthier, E., Pálsson, F., J., Aðalgeirsdottir, G. and Jóhannesson, T.: The archives of stereoimages in Iceland: processing guidelines, geodetic mass balance and glacier–climate interaction in Eyjafjallajökull ice cap, 1945–2014, Journal of Glaciology, in review.

Belart, J. M. C., Berthier, E., Magnússon, E., Anderson, L. S., Pálsson, F., Thorsteinsson, T., Howat, I. M., Aðalgeirsdóttir, G., Jóhannesson, T. and Jarosch, A. H.: Winter mass balance of Drangajökull ice cap (NW Iceland) derived from satellite sub-meter stereo images, The Cryosphere, 11(3), 1501–1517, doi:10.5194/tc-11-1501-2017, 2017.

Berthier, E., Vincent, C., Magnússon, E., Gunnlaugsson, Á. Þ., Pitte, P., Le Meur, E., Masiokas, M., Ruiz, L., Pálsson, F., Belart, J. M. C. and Wagnon, P.: Glacier topography and elevation changes derived from Pléiades sub-meter stereo images, The Cryosphere, 8(6), 2275–2291, doi:10.5194/tc-8-2275-2014, 2014.

Björnsson, H., Pálsson, F., Sigurðsson, O. and Flowers, G. E.: Surges of glaciers in Iceland, Annals of Glaciology, Vol 36, 82–90, 2003.

Brun, F., Berthier, E., Wagnon, P., Kääb, A. and Treichler, D.: A spatially resolved estimate of High Mountain Asia glacier mass balances from 2000 to 2016, Nature Geoscience, 10(9), 668, doi:10.1038/ngeo2999, 2017.

Guðmundsson, S., Björnsson, H., Magnússon, E., Berthier, E., Pálsson, F., Guðmundsson, M. T., Högnadóttir, T. and Dall, J.: Response of Eyjafjallajökull, Torfajökull and Tindfjallajökull ice caps in Iceland to regional warming, deduced by remote sensing, Polar Research, 30(7282), doi:10.3402/polar.v30i0.7282, 2011.

Gunnlaugsson, Á. Þ.: The geodetic mass balance and ice thickness of Tungnafellsjökull ice cap, University of Iceland, (M.Sc. Thesis), 1–67, 2016.

Huss, M.: Density assumptions for converting geodetic glacier volume change to mass change, The Cryosphere, 7(3), 877–887, doi:10.5194/tc-7-877-2013, 2013.

Jóhannesson, T., Björnsson, H., Magnússon, E., Guðmundsson, S., Pálsson, F., Sigurðsson, O., Thorsteinsson, T. and Berthier, E.: Ice-volume changes, bias estimation of mass-balance measurements and changes in subglacial lakes derived by lidar mapping of the surface of Icelandic glaciers, Annals of Glaciology, 54(63), 63–74, doi:10.3189/2013AoG63A422, 2013.

Korona, J., Berthier, E., Bernard, M., Remy, F. and Thouvenot, E.: SPIRIT. SPOT 5 stereoscopic survey of Polar Ice: Reference Images and Topographies during the fourth International Polar Year (2007-2009), ISPRS J Photogramm, 64, 204–212, doi:10.1016/j.isprsjprs.2008.10.005, 2009.

Krüger, J., Kjaer, K. H. and Meer, J. J. M. V. D.: From push moraine to single-crested dump moraine during a sustained glacier advance, Norsk Geografisk Tidsskrift - Norwegian Journal of Geography, 56(2), 87–95, doi:10.1080/002919502760056404, 2002.

Magnússon, E., Pálsson, F., Björnsson, H. and Guðmundsson, S.: Removing the ice cap of Öræfajökull central volcano, SE-Iceland: Mapping and interpretation of bedrock topography, ice volumes, subglacial troughs and implications for hazards assessments, Jokull, 62, 131–150, 2012.

Magnússon, E., Belart, J. M. C., Pálsson, F., Ágústsson, H. and Crochet, P.: Geodetic mass balance record with rigorous uncertainty estimates deduced from aerial photographs and lidar data – Case

study from Drangajökull ice cap, NW Iceland, The Cryosphere, 10(1), 159–177, doi:10.5194/tc-10-159-2016, 2016.

Noh, M.-J. and Howat, I. M.: Automated stereo-photogrammetric DEM generation at high latitudes: Surface Extraction with TIN-based Search-space Minimization (SETSM) validation and demonstration over glaciated regions, GIScience & Remote Sensing, 52(2), 198–217, doi:10.1080/15481603.2015.1008621, 2015.

Papasodoro, C., Berthier, E., Royer, A., Zdanowicz, C. and Langlois, A.: Area, elevation and mass changes of the two southernmost ice caps of the Canadian Arctic Archipelago between 1952 and 2014, The Cryosphere, 9(4), 1535–1550, doi:10.5194/tc-9-1535-2015, 2015.

Pedersen G. B. M., Belart J. M. C., Magnússon E., Vilmundardóttir O. K., Kizel F., Sigurmundsson F. S., Gísladóttir G. and Benediktsson J. A.: Hekla Volcano, Iceland, in the 20th Century: Lava Volumes, Production Rates, and Effusion Rates, Geophysical Research Letters, 45(4), 1805–1813, doi:10.1002/2017GL076887, 2018.

Pierrot Deseilligny, M. and Clery, I.: Apero, AN Open Source Bundle Adjusment Software for Automatic Calibration and Orientation of Set of Images, ISPRS - International Archives of the Photogrammetry, Remote Sensing and Spatial Information Sciences, 3816, 269–276, doi:10.5194/isprsarchives-XXXVIII-5-W16-269-2011, 2011.

Raup, B., Racoviteanu, A., Khalsa, S. J. S., Helm, C., Armstrong, R. and Arnaud, Y.: The GLIMS geospatial glacier database: A new tool for studying glacier change, Global and Planetary Change, 56(1–2), 101–110, 2007.

Rupnik, E., Daakir, M. and Pierrot Deseilligny, M.: MicMac – a free, open-source solution for photogrammetry, Open Geospatial Data, Software and Standards, 2, 14, doi:10.1186/s40965-017-0027-2, 2017.

Shean, D. E., Alexandrov, O., Moratto, Z. M., Smith, B. E., Joughin, I. R., Porter, C. and Morin, P.: An automated, open-source pipeline for mass production of digital elevation models (DEMs) from very-high-resolution commercial stereo satellite imagery, ISPRS Journal of Photogrammetry and Remote Sensing, 116, 101–117, doi:10.1016/j.isprsjprs.2016.03.012, 2016.